EVOLUTION OF A CENTRIFUGAL COMPRESSOR
From turbocharger to micro gas turbine applications

Proefschrift

ter verkrijging van de graad van doctor
aan de Technische Universiteit Delft,
op gezag van de Rector Magnificus prof. ir. K. C. A. M. Luyben,
voorzitter van het College voor Promoties,
in het openbaar te verdedigen op woensdag 21 november 2012 om 10:00 uur

door

Mattia OLIVERO

Laurea specialistica in ingegneria aerospaziale
Politecnico di Torino

geboren te Carmagnola (Torino), Italië

Dit proefschrift is goedgekeurd door de promotor:

Prof. ir. J. P. van Buijtenen

Copromotor: Dr. ir. P. Colonna

Samenstelling promotiecommissie:

Rector Magnificus	voorzitter
Prof. ir. J. P. van Buijtenen	Technische Universiteit Delft, promotor
Dr. ir. P. Colonna	Technische Universiteit Delft, copromotor
Dr.-ing. R. Pecnik	Technische Universiteit Delft
Prof. dr. ir. B.-J. Boersma	Technische Universiteit Delft
Prof. dr. ir. F. Scarano	Technische Universiteit Delft
Prof. dr. ir. H. W. M. Hoeijmakers	Universiteit Twente
Dr. ir. S. Rebay	Università degli Studi di Brescia, Italië
Prof. dr. ir. A. H. M. Verkooijen	Technische Universiteit Delft, reservelid

This work has been financially supported by Senter-Novem (now Agentschap NL, under the Dutch Ministry of Economic Affairs, Agriculture, and Innovation) and Micro Turbine Technology B.V., grant number # HTAS.08001.

ISBN 978-94-6191-419-4

Published by Mattia Olivero, Italy.

Printed by Ipskamp Drukkers, the Netherlands.

[1] Author's email: mattia.olivero@gmail.com

Dedicated to
Luisella, with love and gratitude,
and Mum and Dad, who made this possible.

What chance had the scandal-ridden CIA to resist a force with enough power to build pipelines through tundra that had been demonstrated to be ecologically fragile? Who could stand against the organization that had reduced government research spending on solar, wind, tidal, and geothermal energy to a placating trickle, so as to avoid competition with their own atomic and fossil-fuel consortia? How could CIA effectively oppose a group with such overwhelming dominance that She was able, in conjunction with its Pentagon flunkies, to make the American public accept the storage of atomic wastes with lethal half-lives so long that failure and disaster were absolutely assured by the laws of anti-chance?

Trevanian, 1979, *Shibumi*.

Summary

Fossil fuels are non-renewable resources which take millions of years to form, and whose reserves are being depleted much faster than new ones are being generated. Furthermore, fossil fuels utilization raises environmental concerns, particularly regarding the global climate change, while the increasing price trend indicates that the fossil-fuels-based energy is becoming a scarce commodity. Therefore, the current energy situation cannot be maintained indefinitely and future energy conversion systems have to be sustainable.

One of the options for a more efficient and sustainable use of fossil fuels as energy sources is arguably distributed generation (DG). Among the various technologies which are currently proposed for DG, micro combined heat and power (μCHP), defined as the process of producing both electricity and usable thermal energy at high efficiency and near the point of use, could play a very relevant role, because it positively integrates technological as well as cultural and institutional components, related to the potential for reducing the ecological impact of electricity conversion.

Micro gas turbines offer many potential advantages in comparison to other conversion technologies suitable for μCHP applications, such as compact size and high specific power; small number of moving parts; low vibrations and noise; low maintenance requirements, which lead to low maintenance costs; high fuel flexibility; possibly short delivery time and very low emissions; modularity; high-grade residual thermal energy.

The main components of a CHP unit based on a micro turbine are the compressor, the turbine, the combustor, the recuperator, the generator, and the heat recovery unit. In the size range of micro gas turbines, radial-flow components are usually adopted for the turbomachinery, since they offer minimum surface and end-wall losses, and provide the highest efficiency. Centrifugal compressors also provide very high pressure ratio per stage, are less expensive to manufacture, and are similar in terms of design and volume flow rate to those adopted for automotive turbochargers, whose market is currently around two millions units per year, and is therefore characterized by relatively low production costs.

The use of single-shaft radial turbomachinery for micro turbines allows thus for simple designs, with satisfiying aerothermodynamic and economic constraints, thanks to the evolution that automotive turbochargers have experienced in the past seventy years. Furthermore, the introduction of advanced computational fluid dynamics (CFD) tools and of innovative materials in recent years has led to a marked improvement in the current state-of-the-art technology of small turbochargers. However, according to some authors, the efficiency levels of centrifugal compressors have almost "stalled" after years of development, while further improvements by means of CFD methodologies would likely to be only incremental.

Nevertheless, improvements in micro turbines performance through suitable modifications of turbocharger technology are to be expected, especially considering that turbochargers usually employ centrifugal compressors with vaneless diffusers in order to maximize the flow range and minimize production costs, wherelse gas turbines require higher efficiency and pressure ratio for a much narrower operating range. Moreover, further engineering challenges are related to the so-called small-scale effects. These are due to i) relatively high viscous losses because of low Reynolds numbers; ii) high relative tip clearance (i.e., the ratio of the tip clearance to the blade height at the impeller outlet) due to manufacturing tolerances; iii) high heat losses, because of large area-to-volume ratios; iv) relative large size-independent losses, such as those from bearings and auxiliaries, given the low power output.

As a consequence, the main objectives of this work are

1. To develop novel methodologies which allow understanding the flow structure and loss mechanisms of very small centrifugal compressors, and identifying those aspects whose improvement can lead to higher micro compressor performance.

2. To analyze and quantify the influence of the tip clearance on the performance and flow properties of micro compressors, since the unshrouded impellers used in automotive turbochargers suffer from efficiency decrements, because of the pressure losses and secondary flows caused by very large clearance gaps.

3. To design and build a test-rig for the automatic acquisition of the performance maps of very small centrifugal compressors, and for testing either future, new configurations which aim to improve the performance of an exemplary micro turbine compressor, or other very small centrifugal compressors.

4. To develop an original optimization methodology for turbomachinery components, to be further utilized for the improvement of the performance of an exemplary micro turbine compressor, through the investigation of vaned diffusers, which are claimed to exhibit higher static pressure recovery and efficiency than vaneless diffusers, at the expenses of a narrower operating range.

In this study, the recuperated micro gas turbine developed by the Dutch company Micro Turbine Technology B.V. (MTT) has been utilized as an illustrative example. The MTT micro turbine delivers electrical and thermal power output up to 3 and 14 kW, respectively, and will be primarily applied in μCHP units for domestic dwellings. The turbomachinery consists of a commercial off-the-shelf automotive turbocharger, made of a centrifugal compressor, a radial turbine, and oil-lubricated bearings. A cycle study of the MTT recuperated micro gas turbine has been carried out in order to assess the impact of the centrifugal compressor performance on the system performance. The analysis proved that increasing the performance of the centrifugal compressor adopted for the MTT micro turbine is pivotal in order to achieve higher performance levels of the μCHP system.

The main conclusions of the work presented here are summarized as follows:

- A fully automated optimization methodology has been developed by integrating an optimization algorithm, a geometry generator, a grid generator, a CFD solver, and a

post processor. This methodology can be used for the optimization of turbomachinery components, but has been applied here to the design and optimization of vaned diffusers for the exemplary micro compressor. The optimized vaned diffusers led to increased static pressure recovery, but the compressor efficiency was lower than that of the vaneless configuration, because of larger total pressure losses.

- The test-rig, which has been designed and built for the automatic acquisition of the performance maps of very small, high-speed centrifugal compressors, proved to be robust, reliable, and versatile. An experimental campaign has been carried out in order to quantify the aerodynamic performance of the exemplary compressor, and the test data, summarized in the form of performance maps and tables, have been used to validate the results of the numerical analyses shown in this dissertation. Furthermore, the test-rig will be a useful tool in the development of future, new designs which aim at improving the performance of the exemplary micro turbine compressor, and will be utilized to test other very small centrifugal compressors for a variety of different applications.

- A new one-dimensional (1D) method for the assessment of the performance (i.e., stage total-to-total pressure ratio and isentropic efficiency; impeller inlet and outlet velocity triangles; impeller internal, external, and mixing losses; vaneless diffuser losses; volute losses) of very small centrifugal compressors has been developed on the basis of two very well-known design methodologies, namely the single- and two-zone model. This novel tool combines the advantages of the two, since it distinguishes between high- and low-momentum flows within the impeller bladed passages as possible with the two-zone model, and allows evaluating the impeller loss mechanisms, as possible with the single-zone model.

This dissertation is structured as follows. **Chapter 1** illustrates the concept, potential, and technology of μCHP within the framework of different energy scenarios. The motivation and scope of this work, and the outline of the dissertation are also given here.

Chapter 2 presents the new 1D method for the assessment of the performance and loss mechanisms of very small centrifugal compressors. The novel methodology has been applied here to the exemplary micro centrifugal compressor. The numerical results computed by this tool have been validated against the experimental results obtained with the test-rig. The comparison has been performed at 190 and 220 krpm, and varying mass flow rate, respectively, and shows a good agreement, since the model is able to capture the pressure ratio and efficiency trends. However, in proximity of the choking condition the difference between the numerical and test data is higher. Furthermore, at the micro turbine design point (i.e., mass flow rate equal to 50 g/s and rotational speed equal to 240 krpm), the model overpredicts the pressure ratio, but underpredicts the efficiency. At the micro turbine design point, it has been calculated that the skin friction losses contribute to the largest efficiency decrease, followed by the mixing losses, and the vaneless diffuser losses.

Chapter 3 describes the experimental set-up which has been designed and built for the acquisition of the performance maps of very small, high-speed centrifugal compressors.

The compressor impeller is driven by a turbine powered by pressurized air coming from a buffer tank, pressurized in turn by two screw compressors. The shaft speed is varied by a turbine control valve, while further equipment necessary to operate the test-rig was also integrated into the set-up, as well as the instrumentation and data acquisition system. The test-rig can currently accomodate impellers with diameters up to 20 mm, and rotational speeds up to 220 krpm. However, rotational speeds up to 240 krpm (i.e., the micro turbine design point) are deemed within reach with suitable improvements of the compressor test-rig. The uncertainty propagation analysis has also been performed. The results show that for the exemplary micro compressor the static pressure uncertainty highly influences both the pressure ratio and efficiency uncertainties. In particular, the uncertainty of the compressor inlet static pressure is preponderant with respect to that of the outlet static pressure. Substituting the actual pressure transmitters with ones having better accuracy and lower full scale would therefore reduce the uncertainties of the final results. On the contrary, the total temperature uncertainty contributes to the efficiency uncertainty to a lower degree, while the mass flow rate uncertainty does not have any impact at all on the uncertainties of the final results.

Chapter 4 shows the numerical study performed with a commercial CFD code which solves the three-dimensional (3D) Reynolds averaged Navier-Stokes (RANS) equations. Steady-state simulations of the exemplary centrifugal compressor have been carried out to approximate the real, time-dependent flow physics with satisfactory results and shorter computational time with respect to an unsteady approach. The results of the numerical analysis, which has been performed at the micro turbine design point, show that the flow separates due to the supersonic relative Mach number at the impeller blades tip. Subsequently, a low-velocity region develops on the blades suction side, enlarges along the streamwise direction, and leads to the generation of high losses in proximity of the impeller outlet, at the shroud. Furthermore, the calculated static pressure recovery coefficient of the vaneless diffuser of the exemplary compressor stage is equal to 0.4. It is thus located at the lower end of the ranges documented in the literature. Finally, it has been calculated that for every 1%-increase of the impeller tip clearance, the stage total-to-total pressure ratio and isentropic efficiency decrease by 1.3% and 0.6%, respectively. The impeller efficiency drop due to the impeller tip clearance is two times larger than the loss documented in the literature for larger centrifugal impellers.

Chapter 5 describes the influence of the diffuser on the compressor performance. Firstly, an overview of the impeller outlet flow phenomena is given, in order to identify their effects on the downstream flow field. A brief description of the two main categories of diffusers (i.e., vaneless and vaned) follows. Finally, the most important design parameters of a vaned diffuser are highlighted.

Chapter 6 illustrates the developed optimization methodology. Firstly, the optimization of vaned diffusers has been performed by coupling a genetic algorithm (GA) to a in-house two-dimensional Euler CFD code, in order to test this optimization strategy. Secondly, the GA has been coupled to a commercial 3D RANS CFD code, in order to account for the viscous effects and the impeller-diffuser interaction. In this case, the GA has been assisted by a Kriging metamodel, in order to reduce the computational costs, while a multi-objective problem has been solved by minimizing, separately and simulta-

neously, a function of the stage total-to-static pressure ratio, and a function of the stage total-to-total isentropic efficiency. The relative position of the vanes between the diffuser inlet and outlet, their inclination with respect to the radial direction at the leading and trailing edges, the diffuser outlet radius, and the vane number have been selected as design variables. At first, the optimization methodology has been utilized to design vaned diffusers for the exemplary compressor, at the micro turbine design point. In this case, the efficiency of the simulated most efficient optimized vaned diffuser is 1.9% lower than that of the vaneless diffuser. The vaned diffuser however exhibits a 7.4%-higher static pressure recovery. Subsequently, a larger impeller diameter, which delivers a higher pressure ratio at the same rotational speed, has been considered. At the micro turbine design point, the efficiency and static pressure recovery of the simulated most efficient optimized vaned diffuser are respectively 1.8% and 16.6% higher than those of the vaneless configuration. As a consequence, the use of vaned diffusers with a low-pressure pressure ratio compressor is beneficial only in terms of static pressure recovery, while a reduction of the friction losses, leading to increased efficiencies, can be achieved only in the case of high dinamic heads available at the diffuser inlet, due to larger impellers.

Chapter 7 draws the conclusions regarding the work presented in this dissertation, while recommendations are suggested for future research activities.

Samenvatting

Fossiele brandstoffen zijn niet-hernieuwbare energiebronnen gevormd over een periode van miljoenen jaren, waarvan de reserves tegenwoordig sneller worden verbruikt dan worden gegenereerd. Verder gaat het verbruik van fossiele brandstoffen gepaard met milieueffecten; onder wetenschappers is er consensus dat met name de uitstoot van koolstofdioxide die bij de verbranding van de genoemde koolwaterstofverbindingen ontstaat, bijdraagt aan een verhoogd broeikasgaseffect en daardoor verandering van het klimaat bewerkstelligt. Bovendien duidt de stijgende prijs van fossiele brandstoffen op het feit dat zij schaarser worden. De huidige situatie kan derhalve niet gehandhaafd kan worden en toekomstige energieomzettingsystemen dienen daarom duurza(a)m(er) te zijn.

Binnen het geschetste context is gedistribueerde vermogens-opwekking een optie voor het efficient(er) en duurzaam verbruik van fossiele brandstoffen. In het geheel aan huidige technologische opties voor gedistribueerde vermogens-opwekking speelt microwarmtekracht - een proces voor de simultane productie van warmte (thermisch vermogen) en elektrisch vermogen met een hoog rendement daar waar deze energievermogensvormen benodigd zijn - een belangrijke rol, omdat het technologische, maar tevens culturele en institutionele aspecten integreert - om zodoende de potentiële ecologische impact bij energieomzettingen (waaronder elektriciteitsopwekking) te reduceren.

Microgasturbines bieden in vergelijking met andere, soortgelijke energieomzettingstechnologieën voor microwarmtekrachttoepassingen een veelheid aan voordelen, waaronder een compacte bouw, een hoog specifiek-vermogen en een gering aantal bewegende delen. Verder vertonen ze weinig trillingen, hebben ze een lage geluidsproductie, zijn ze makkelijk en goedkoop in onderhoud, hebben ze een hoge flexibiliteit in brandstoftype, lage (toelaatbare) emissies, zijn ze modulair, en is de residuale thermische energie (de zogenaamde restwarmte) van een hoge kwaliteit.

De belangrijke componenten van een microwarmtekrachtsysteem gebaseerd op een microturbine zijn de compressor, de turbine, de verbrandingskamer, de interne warmtewisselaar, de generator en een systeem voor restwarmtewinning. Voor de gangbare grootte van microgasturbines wordt veelal gebruik gemaakt van radiale stromingscomponenten, omdat het rendement (het) hoog(st) is en de stromingsverliezen langs het oppervlak en de wand minimaal zijn. Centrifugale compressoren hebben tevens een hoge drukverhouding per trap en zijn goedkoop te fabriceren, en, omdat de gangbare compressoren qua ontwerp en volumedebiet soortgelijk zijn aan drukvullers in auto's (voor de auto-industrie worden jaarlijks rond de twee miljoen drukvulleréénheden gefabriceerd) zijn de productiekosten laag. Dankzij de ontwikkelingen van en de ervaringen met drukvullers in de auto-industrie in de afgelopen zeventig jaar, is het mogelijk, om binnen de gebruikelijke aerothermodynamis-

che en economische condities, éénassige radiale stromingsmachines voor microturbines te gebruiken. Daar bijkomend heeft het gebruik van "computational fluid dynamics" (CFD) tools en van nieuwe materialen gedurende de laatste jaren geresulteerd in verbetering van de technologie van kleine drukvullers. Doch, zoals door enkele bronnen is aangegeven, is na jaren van successieve toename van het rendementsniveau van centrifugale compressoren bijna een maximum bereikt; potentiële verbeteringen die kunnen voortkomen uit CFD analyses zullen maar in minieme rendementsverbeteringen resulteren.

Desalniettemin is verbetering van de prestatie van microturbines te verwachten door geschikte aanpassingen te plegen aan drukvuller technologie. Immers, drukvullers maken gebruik van centrifugale compressoren met zogenaamde schoeploze diffusors om zodoende het stromingsbereik te maximaliseren en de productiekosten te minimaliseren, terwijl gas turbines een hoger rendement en drukverhouding nodig hebben in een beperkter werkingsgebied. Daarnaast zijn er technische uitdagingen wegens effecten die zich manifesteren op en door de kleine schaal. Deze effecten zijn het gevolg van: i) de relatief hoge visceuze verliezen vanwege de lage Reynolds waarden; ii) een grote relatieve speling bij de schoeptip (gedefinieerd als de verhouding van de speling tussen schoeptip en behuizing en de schoephoogte ter plaatse van de schoepenuitlaat) wegens toleranties bij de vervaardiging van de waaier (het schoepenrad); iii) hoge warmteverliezen door de hoge verhouding tussen het oppervlak en het volume; iv) relatief hoge, grootte-onafhankelijke verliezen zoals de verliezen bij de lagering en overige componenten, gegeven het laag vermogen.

De doelstellingen van dit onderzoek, beschouwende het bovenstaande, zijn

1. Om methodologieën te ontwikkelen die het mogelijk maken om de structuur van de stroming en de verliesmechanismen bij kleine centrifugale compressoren beter te begrijpen en om (zodoende) aspecten te identificieren die kunnen bijdragen aan een betere prestatie van een microcompressor.

2. Om de invloed van de relatieve speling tussen de tip en de compressorbehuizing op de prestatie van de compressor en op de stromingseigenschappen te analyseren en te kwantificeren, omdat de zogenaamde waaiers zonder behuizing die in de autoindustrie gebruikt worden, rendementsverliezen hebben wegens de drukverliezen en secundaire stromingen als gevolg van de (relatief) grote spelingen.

3. Om een testopstelling te ontwerpen en bouwen die automatische acquisitie van de prestatiekarakteristieken van kleine compressoren mogelijk maakt, en die bovendien flexibel is voor het testen van een aangepaste compressor met bijvoorbeeld een andere configuratie (ter verbetering van de prestatie van een microturbine compressor) of een andere kleine centrifugale compressor.

4. Om een optimalisatie methodologie voor turbomachinecomponenten te ontwikkelen die in de toekomst gebruikt kan worden om de prestatie van de compressor te verbeteren middesl onderzoek verricht aan diffusors met schoepen. Van het laatstgenoemde wordt beweerd dat zij voor een betere statische drukopbouw zorgdragen en een hoger rendement mogelijk maken dan schoeploze diffusors, doch voor een kleiner werkgebied van de compressor.

Voor dit onderzoek is een warmtegeïntegreerde (gerecupereerde) microgasturbine gebruikt, welke is ontwikkeld door Micro Turbine Technology B.V. (MTT). Deze MTT microturbine levert een elektrisch vermogen van 3 kW en een thermisch vermogen van 14 kW en is primair ontwikkeld om gebruikt te worden als microwarmtekrachtsysteem voor huishoudelijke toepassingen. De stromingsmachinecomponenten ziin een standaard "off-the-shelf" drukvuller zoals gebruikt in de auto-industrie, welke bestaat uit een centrifugale compressor, een radiale turbine en olie-gesmeerde lagers. Een studie is uitgevoerd op de thermodynamische cyclus in de MTT warmtegeïntegreerde microgasturbine, zodat de invloed van de prestatie van de centrifugale compressor op the prestatie van het gehele systeem kan worden gekwantificeerd. Uit deze genoemde analyse volgt dat een verbetering van de prestatie van de centrifugale compressor van de MTT microgasturbine van eniment belang is om betere prestatie van het microwarmte-krachtsysteem te krijgen.

De belangrijke conclusies uit dit onderzoek staan hieronder vermeld

- Een volledig geautomatiseerde optimalisatie methodologie is ontwikkeld door een optimalisatie algoritme, een geometriegenerator, een gridgenerator, een CFD solver, en een zogenaamde "post-processor" te integreren. De ontwikkelde methodologie kan worden toegepast voor de optimalisatie van diverse componenten van stromingsmachines. In dit onderzoek is het optimalisatiesysteem gebruikt voor het ontwerpen en optimaliseren van de zogeheten diffusors met schoepen van de gebruikte microcompressor. De geoptimaliseerde diffusors met schoepen resulteerden in een verhoogde statische drukopbouw, echter vanwege de hogere totale-drukverliezen was het compressor rendement lager dan dat van de zogenaamde schoeploze configuratie.

- The testopstelling welke ontwikkeld is voor automatische data-acquisitie van grootheden van de prestatiekarakteristiek van zeer kleine en snel-roterende centrifugale compressoren, bleek robuust, betrouwbaar en veelzijdig bruikbaar te zijn. Een testronde is uitgevoerd om de aerodynamische prestatie van de onderhavige compressor te kwantificeren, en de gemeten data (die vewerkt zijn in prestatiekarakteristieken en prestatietabellen), zijn gebruikt geworden om de numerieke resultaten die verkregen zijn en hierin gedocumenteerd zijn, te valideren. Verder zal de testopstelling een zeer bruikbare tool zijn in de ontwikkeling van toekomstige, nieuwe ontwerpen met als doel het verbeteren van de prestatie van de microturbine compressor en zal gebruikt worden om andere micro centriugale compressoren te testen voor diverse toepassingen.

- Een nieuwe één-dimensionale (1D) methode voor de evaluatie van de prestatie (bijvoorbeeld de verhouding tussen de totale-tot-totale drukverhouding per trap, het isentropisch rendement, de snelheidsdriehoeken aan de schoepinlaat en -uitlaat, interne, externe en mengverliezen, verliezen in de schoeploze diffusor) van zeer kleine centrifugale compressoren is ontwikkeld op basis van twee bekende ontwerpmethodologieën, namelijk het zogenaamde enkele- en het twee-zone model. Deze nieuwe tool combineert de voordelen van de beide genoemde methodologieën, omdat onderscheid gemaakt wordt tussen hoge en lage impulsstromingen binnen de passages

van het schoepenrad, zoals bij het twee-zone model, en de mogelijkheid ingebouwd is om de verliesmechanismen in de waaier te evalueren, zoals bij het enkele-zone model.

Dit proefschrift is als volgt gestructureerd. **Hoofdstuk 1** illustreert het concept, het potentiëel en de technologie van microwarmtekracht binnen het raamwerk van verschillende energiescenarios. De uitgangspunten (motivatie) en de scope van dit werk, en de structuur van het proefschrift zijn ook genoemd.

Hoofdstuk 2 presenteert de nieuwe 1D-methode voor het evalueren van de prestatie en verliesmechanismen in zeer kleine centrifugale compressoren. De ontwikkelde methode is in dit onderzoek toegepast op een micro centrifugale compressor. De verkregen numerieke resultaten door de ontwikkelde tool zijn gevalideerd middels experimentele data verkregen uit een test. De vergelijking is uitgevoerd voor 190,000 en 220,000 rpm en variërende massadebiet. De overeenstemming tussen de twee datasets is goed, omdat het model in staat is om het verloop van de drukverhouding en het rendement correct te voorspellen. Echter, nabij de conditie waarbij choking optreedt, is er een groter verschil tussen de gemeten en gesimuleerde (numerieke) waarden. Verder, bij de werkingstoestand waarvoor de microturbine is ontworpen (massastroom gelijk aan 50 g/s en rotatiesnelheid gelijk aan 240,000 rpm) blijkt dat het model een te hoge druk verhouding voorspelt, terwijl het rendement verkregen uit het model juist lager uitvalt. Bij deze toestand wordt middels berekeningen aangetoond dat de grootste bijdrage aan de afname van het rendement komt door wrijvingsverliezen langs de wand, gevolgd door mengverliezen en verliezen in de schoeploze diffusor.

Hoofdstuk 3 beschrijft de testopstelling voor de data-acquisitie van de prestatiekarakteristieken van zeer kleine, zeer-snel-draaiende centrifugale compressoren. De compressor wordt aangedreven door een turbine waar doorheen lucht uit een buffervat onder druk stroomt. De drukopbouw en vulling van dit buffervat geschiedt middels twee schroef compressoren. De snelheid van de as wordt geregeld door de klep die de massastroom naar de turbine bepaalt. Daarnaast zijn de componenten benodigd om het systeem te draaien geïntegreerd in het systeem, alsmede is er het data-acquisitie systeem. De ontworpen opstelling kan waaiers met een afmeting tot maximaal 20 mm accomoderen bij toerentallen tot 220,000 rpm. Hogere toerentallen tot 240,000 rpm worden mogelijk geacht indien noodzakelijke aanpassingen worden gepleegd aan de opstelling. Er is tevens een onzekerheidsanalyse uitgevoerd. De resultaten tonen aan dat voor de beproefde microcompressor, de onzekerheid in gemeten statische druk, sterk de onzekerheid in de drukverhouding en die in het rendement beïnvloedt. In het bijzonder is de onzekerheid in de statische druk aan de compressorinlaat uitermate belangrijk of in ieder geval belangrijker dan die van de statische druk aan de compressoruitlaat. Gebruikmaking van nauwkeurigere instrumenten (drukmeters) en met een kleiner (beter op de drukken afgestemd) meetbereik, zal dus tot lagere onzekerheden leiden in de uiteindelijke resultaten. Daar tegenover staat dat de onzekerheid in de totale temperatuur veel minder bijdraagt aan de onzekerheid in het rendement, en die van de massastroom al helemaal niet.

Hoofdstuk 4 beschrijft de numerieke studie welke is verricht middels een commerciëel verkrijgbaar CFD code die de drie-dimensionale (3D) zogenaamde Reynolds averaged

Navier-Stokes (RANS) vergelijkingen oplost. Simulaties onder stationaire condities zijn met succes uitgevoerd op de centrifugale compressor om een redelijke benadering te krijgen van de tijdsafhankelijke physica van de stroming. Hierdoor is de simulatietijd korter dan wanneer de niet-stationaire simulatie wordt gepleegd. Numerieke simulaties bij ontwerpcondities van de microturbine tonen aan dat de stroming los laat vanwege de relatief hoge Mach getallen bij de schoeptip. Vervolgens ontstaat er een gebied aan de zuigzijde van de schoepen met lage stromingssnelheden, die dan in de stromingsrichting groter wordt en resulteert in grote verliezen nabij de rotoruitlaat bij de zogenaamde behuizing. Verder is de berekende waarde voor de coëfficiënt die de statische druk opbouw aangeeft voor de schoeploze diffusor van de werkelijke compressor trap 0.47, en deze waarde ligt dus in een lagere interval dan de waarden uit de literatuur. Verder is getoond dat voor elke 1% toename in de speling tussen de tip en de behuizing, de totale-tot-totale drukverhouding per trap en de afname van het isentropisch rendement respectievelijk 1.3% en 0.6% zijn. De daling van het rendement van de rotor door de genoemde speling is twee keer hoger dan het verlies welke in de literatuur gedocumenteerd staat voor grotere centrifugale waaiers.

Hoofdstuk 5 beschrijft de invloed van de diffusor op de prestatie van de compressor. Ten eerste wordt een overzicht gegeven van de stroming aan de uitlaat van het schoepenrad om de effecten die deze stroming heeft op het stromingsveld verder te identificeren. Er wordt ook een kort overzicht gegeven van twee diffusor categorieën (schoeploze en met schoepen). Als laatst worden de van belang zijnde ontwerpparameters van de diffusors met schoepen benadrukt.

Hoofdstuk 6 illustreert het gebruik en de werking van de ontwikkelde optimalisatie methodologie. Ten eerste wordt de optimalisatie strategie getest door voor de optimalisatie van diffusors met schoepen een koppeling te plegen tussen een genetische algoritme (GA) en een twee-dimensionale Euler academische CFD code. Vervolgens is het GA gekoppeld aan een commerciele 3D RANS CFD code om zodoende de visceuze effecten en de interactie tussen de diffusor en de waaier in beschouwing te nemen. In deze situatie is het GA aangevuld met een Kriging metamodel om zodoende de berekeningen minder computationele-intensief te maken, terwijl een multi-objectief probleem is opgelost door apart en simultaan te minimaliseren een functie van de totale-tot-totale drukverhouding per trap en een functie van de totale-tot-totale isentropisch rendement per trap. De positie van de schoepen tussen de diffusorinlaat en -uitlaat, hun helling ten opzichte van de radiale richting bij de rand van de schoep bij de in- and uitlaat, de straal bij de diffusoruitlaat en de schoepnummer zijn als ontwerpvariabelen gekozen. Als eerste stap is de optimalisatie methodologie gebruikt om de diffusors met schoepen van de gekozen compressor te ontwerpen (bij de ontwerpcondities van de microturbine). In dit geval is het rendement van de meest optimale diffusor met schoepen 1.9% lager dan dat van de schoeploze diffusor. De diffusor met schoepen heeft echter een 7.4% hogere statische drukopbouw. Vervolgens is een grotere waaier diameter beschouwd die een hogere drukverhouding geeft bij een zelfde toerental. Bij de ontwerptoestand van de microturbine is het rendement en statische drukopbouw van de gesimuleerde, meest efficient geoptimaliseerde diffusor met schoepen, respectievelijk 1.8% en 16.6% hoger dan die van de schoeploze configuratie. Het gevolg is dat het gebruik van een diffusor met schoepen met een lage-drukverhouding

compressor voordelig is alleen in termen van statische drukopbouw, terwijl een reductie van de wrijvingsverliezen, resulterende in verhoogde rendementen, alleen verkregen kan worden in het geval van hogere dynamische drukken aan de diffusorinlaat wegens grotere waaiers.

Hoofdstuk 7 geeft conclusies betrekking hebbende op dit onderzoek en aanbevelingen voor verder relevant onderzoek op het gebied.

Table of Contents

List of Figures

List of Tables

Nomenclature

Latin symbols

A	Area $[m^2]$
a	Constant; coefficients of the polinomial regression function
AR	Area ratio
AS	Aspect ratio
b	Height $[m]$; total systematic uncertainty
C	Absolute flow velocity $[m/s]$
c	Tip clearance $[m]$; chord length $[m]$
c_f	Friction coefficient
c_p	Specific heat capacity at constant pressure $[J/kg \cdot K]$
c_v	Specific heat capacity at constant volume $[J/kg \cdot K]$
CP	Static pressure recovery coefficient
D	Design
DR	Diffusion ratio
$\tilde{f}$	Pseudo-objective function
F	Tangential velocity factor
f	Objective function
g	Inequality constraint
h	Specific enthalpy $[J/kg]$; equality constraint
i	Incidence angle $[°]$
K	Total pressure loss coefficient
L	Diffuser length $[m]$
LWR	Length-to-width ratio
$\dot{m}$	Mass flow rate $[kg/s]$
M	Mach number
$\mathbf{n}$	Vector normal to the outlet area
N	Rotational speed $[rpm]$
n	Number of design variables; number of sample points
P	Power $[W]$
p	Pressure $[Pa]$; probability; polinomial regression function
R	Specific gas constant $[J/kg \cdot K]$; correlation function between any two sample points
r	Radius $[m]$; radial coordinate; result
RC	Relative tip clearance

RR	Radius ratio
s	Specific entropy $[\mathrm{J/kg \cdot K}]$; total random uncertainty; pitch; tournament size
T	Temperature $[\mathrm{K}]$
t	Time $[\mathrm{s}]$; student's factor; number of generations
U	Blade speed $[\mathrm{m/s}]$; total combined expanded uncertainty
u	Total combined uncertainty
$\mathbf{v}$	Velocity vector
VTA	Vane turning angle
$\dot{W}$	Loss expressed as specific enthalpy change $[\mathrm{J/kg}]$
$\mathbf{w}$	Vector of the weight coefficients
W	Relative flow velocity $[\mathrm{m/s}]$
w	Diffuser width $[\mathrm{m}]$; weight coefficient
$\mathbf{x}$	Vector of the design variables; vector of the sample points
X	Measured quantity; design matrix of the sample points
x	Axial coordinate; design variable; sample point
y	Unknown function of interest; column vector containing the response values at each sample point
Z	Impeller blade number; diffuser vane number; realization of a Gaussian random process

Acronyms

AC	Alternate current
BPS	Bowman Power Systems
CEE	Central and Eastern Europe
CFD	Computational fluid dynamics
CHP	Combined heat and power
COTS	Commercial off-the-shelf
CVD	Conventional vaned diffuser
DC	Direct current
DG	Distributed generation
DOE	Design of experiments
EA	Evolutionary algorithm
EC	European Commission
EES	Elliott Energy Systems
EU-15	European Union fifteen Member States up to May 1, 2004
EU-27	European Union twenty-seven Member States up to July 1, 2013
FB	Full blade
FS	Full scale
GA	Genetic algorithm
GHG	Greenhouse gases
I/O	Input/output
IPCC	International Panel on Climate Change
IR	Ingersoll-Rand

ISA	International Standard Atmosphere
LE	Leading edge
LSVD	Low-solidity vaned diffuser
μTURCO-rig	Micro turbine radial compressor test-rig
MOGA	Multi-objective genetic algorithm
MTT	Micro Turbine Technology B.V.
NI	National Instruments
NURBS	Non-uniform rational B-spline
OEM	Original equipment manufacturer
PARC-1	One-dimensional performance analysis code for radial compressors
PID	Proportional-integral-derivative
PS	Pressure side
R	Reading
R&D	Research and development
RANS	Reynolds averaged Navier-Stokes
SB	Splitter blade
SS	Suction side
SST	Shear stress transport
T&D	Transmission and distribution
TE	Trailing edge
TPES	Total primary energy supply
TSM	Taylor series method
UMF	Uncertainty magnification factor
UPC	Uncertainty percentage contribution
VD	Vaned diffuser

Greek symbols

α	Absolute flow angle [°]
β	Relative flow angle [°]
γ	Ratio of specific heat capacities
ε	Secondary flow area fraction
η	Efficiency [%]; effectiveness [%]
θ	Tangential coordinate; sensitivity factor; divergence angle [°]; stagger angle [°]
λ	Swirl parameter
ξ	Pressure losses [%]
π	Pressure ratio
ρ	Density $\left[\mathrm{kg/m^3}\right]$
σ	Slip factor; solidity
τ	Unknown correlation parameter
ϕ	Diffuser inclination [°]; diameter [m]
φ	Objective function
χ	Secondary flow mass fraction
ψ	Constraint

ω	Angular velocity [rad/s]

Subscripts

0	Total state
1	Compressor inlet; impeller inlet
2	Compressor outlet; impeller outlet
3	Cold side recuperator outlet; diffuser vane leading edge
4	Combustor outlet; diffuser vane trailing edge
5	Turbine outlet; diffuser outlet
6	Hot side recuperator outlet; flow collection point in the volute
7	Heat recovery unit outlet; volute throat
8	Combustor fuel inlet; volute outlet
∞	Refers to the tangential velocity for zero slip velocity
a	Refers to the first element of the two-element in series model; ambient condition; arbitrary location within the vaneless diffuser
b	Refers to the second element of the two-element in series model; blade
c	Compressor; curvature; current
corr	Corrected
D	Diffuser
d	Design
df	Disk friction
el	Electrical
eul	Euler
ext	External
f	Fuel
h	High
I	Impeller
int	Internal
is	Isentropic
l	Low; larger
leak	Leakage
m	Meridional component of the flow velocity; mutation
mech	Mechanical
mix	Mixing
o	Overall
out	Outlet
p	Primary; preliminary
r	Radial component of the flow velocity; result
rec	Recuperator; recirculation
ref	Reference
rel	Relative
s	Secondary; sample
sh	Shaft
sl	Slip

t	Turbine
TE	Trailing edge
th	Thermal
thr	Throat
ts	Total-to-static
tt	Total-to-total
u	Tangential component of the flow velocity
V	Volute
v	Vane
vnl	Vaneless
x	Axial component of the flow velocity

Superscripts

’	Refers to the cut at the diffuser vane leading edge
*	Refers to the specific entropy gain

"The air we receive at our birth and resign only when we die is the first necessity of our existence."

The Times, 1881.

1 Introduction

This chapter provides an overview of the concept, potential, and various technologies of micro cogeneration, in the framework of different energy scenarios. Micro cogeneration is one of the available options for the abatement of CO_2 and NO_x emissions. The motivation and scope of this work, and the outline of the dissertation are also given.

1.1 World energy and emissions trends

Fossil fuels (i.e., coal, oil, and natural gas) are of great importance because their combustion allows for the conversion of significant amounts of energy per unit of mass. The use of coal as a fuel pre-dates recorded history, while commercial exploitation of oil began in the 19th century to light lamps. Natural gas, once flared-off as an unneeded by-product of oil production, is now considered a very valuable resource.

The wide-scale use of fossil fuels, coal at first and oil later, to fire steam engines enabled the Industrial Revolution, and in the past two centuries their exploitation for transportation, energy conversion, and as feedstock for the petrochemical industry greatly increased.

Since the global energy consumption is predicted to increase by 37% from 2008 to 2035, rising from 12.3 billion tonnes of oil equivalent (Gtoe) to 16.7 Gtoe [127], the demand for fuel sources is expected to continue to grow in the coming years as well (Fig. 1.1a). In particular, fossil fuels account for 53% of that increment, and continue to supply the bulk of global energy consumption, though their share is predicted to fall from 81% in 2008 to 74% in 2035.

Oil remains the dominant fuel in the primary energy mix during the period 2008-2035, but its share drops from 33% to 28%, while the demand for coal increases by 18%. The growth of natural gas demand overtakes by far that of all the other fossil fuels, as its consumption increases by 43%. At that point, natural gas will be close to surpassing coal as the second most important fuel in the primary energy mix. The share of nuclear power increases from 5.8% to 7.6%, while the energy conversion from renewable sources (e.g., biomass, geothermal heat, hydro, rain, sunlight, tides, and wind) is expected to grow faster than any other energy source, at an average rate equal to 7.9% per year.

Figure 1.1b shows the total primary energy supply (TPES) in the Netherlands in the period 1973-2030, with a focus on the year 2007. The TPES includes electricity generation, industrial consumption (included non-energy use), transport, residential, commercial, public service, agricultural, fishing, and other non-specified sectors. The Netherlands' TPES was over 83 Mtoe in 2007, representing a 9%-increase from 2000, and a 24%-increase from 1990 [125]. The TPES grew steadily since the mid-1980s, with a few ups and downs. In 2007, coal summed up to over 9% of the TPES, showing a 4.6%-increase from 1973, while the share of oil has fallen to 40% from 50% in 1973, then started growing again. The share of natural gas grew from around 45% in 1973 to over 52% in 1985, and gradually declined to 40% in 2007. Biomass made up over 3% of the TPES.

Because of the wide-spread utilization of fossil fuels since the Industrial Revolution, the atmospheric concentration of greenhouse gases (GHG) has increased dramatically [119]. The Intergovernmental Panel on Climate Change (IPCC) stated that "changes in atmospheric concentrations of GHG and aerosols, land cover, and solar radiation alter the energy balance of the climate system", and concluded that the "increase in anthropogenic GHG concentrations is very likely to have caused most (i.e., more than 50%) of the increase in the global average temperature since the mid-20th century" [121]. Furthermore, anthropogenic warming, such as that due to elevated GHG levels, has a discernible influence on many physical and biological systems, and it is projected to affect various issues such as freshwater resources, industry, food, and health [121].

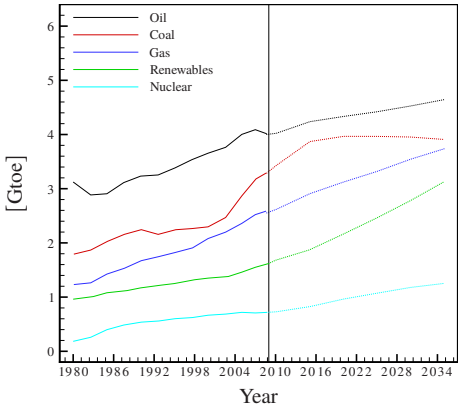

(a) *World primary energy demand by fuel. Renewables include biomass, geothermal heat, hydro, rain, sunlight, tides, and wind. Data taken from Ref. [127].*

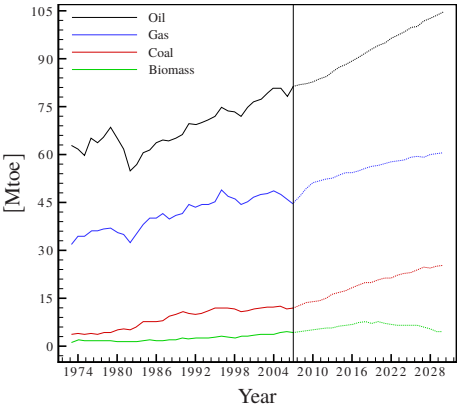

(b) *Total primary energy supply by fuel for the Netherlands. The term "total" includes electricity generation, industrial consumption, transport, residential, commercial, public service, agricultural, fishing, and other non-specified sectors. Data taken from Ref. [125].*

Figure 1.1: *Energy demand and supply by fuel.*

Among the GHG present in the Earth's atmosphere, carbon dioxide (CO_2) is the most abundant, and its concentration increased from approximately 280 ppmv in pre-industrial times to 385 ppmv in 2008 [122]. The IPCC asserted that "the present atmospheric CO_2 increase is caused by anthropogenic emissions of CO_2" [120], which are due to fossil fuels combustion, forest clearing, biomass burning and other non-energy production processes, and cause "most of the observed increase in global average temperatures since the mid-20^{th} century" [122]. Figure 1.2 shows the variation of the CO_2 concentration in the past 1,000 years. The dramatic increase of CO_2 emissions since the Industrial Revolution is clearly visible.

The rising demand of fossil fuels will continue to drive up the world energy-related CO_2 emissions from 29.3 Gt to 35.4 Gt (representing a 21%-increase), in the period 2008-2035 [126]. Nonetheless, the average growth rate of 0.7% per year represents a notable improvement with respect to previous predictions. In the Netherlands, total CO_2 emissions from fuel combustion rose by 29% between 1990 and 2006, mainly because of the larger use of oil and natural gas, and without additional policies emissions are projected to increase by more than 44% in 2030 [125].

Nitrogen oxides (NO_x) as well can have a strong environmental impact and cause severe health problems. They originate from combustion processes, and include nitrogen dioxide (NO_2) and nitrous oxide (N_2O). NO_x play an important role in the creation of ozone, which cause acute respiratory problems, reduce the agricultural production, and can react further to produce undesired pollutants, and in the formation of acid rains. Furthermore, NO_x emissions can contribute to the formation of particles which are dangerous

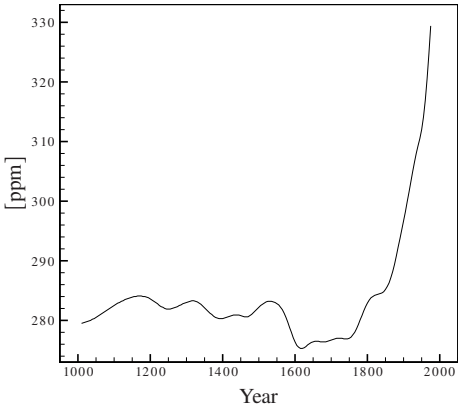

(a) *Variation of CO_2 concentration since the year 1000. Data taken from Ref. [79].*

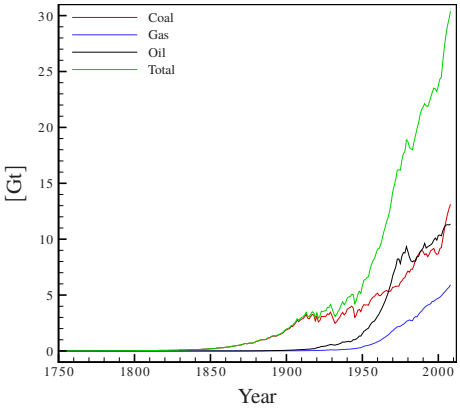

(b) *Variation of CO_2 concentration by fossil fuel since the year 1750. Data taken from Ref. [175].*

Figure 1.2: *Variation of CO_2 concentration.*

to the health of human beings and animals, wherelse the NO_x present in the air can react with organic chemicals to form a wide variety of toxic products. NO_x emissions can also cause water quality deterioration and eutrophication, which leads to oxygen depletion and fish kills, and may also change the pH of water, with the effect of lowering the buffering capacity leading to higher levels of dissolved metals. Finally, N_2O accumulates in the atmosphere with other GHG, causing a gradual rise in the Earth's temperature, and leading to increased sea levels, expansion of desert lands, and changes in the rain patterns and microclimate conditions.

1.2 Distributed generation of electricity

Fossil fuels are non-renewable resources, since they take millions of years to form, and reserves are being depleted much faster than new ones are being generated, because of the exponentially growing world primary energy consumption. The increasing price trend and the prominent role in geopolitics indicate thus that the fossil-fuels-based energy is becoming a scarce commodity. Furthermore, fossil fuels utilization raises environmental concerns, particularly regarding the global climate change. As a consequence, the current energy situation cannot be maintained indefinitely and future energy conversion systems have to be sustainable.

One of the options for a more efficient and sustainable use of fossil fuels as energy sources is arguably distributed generation (DG), which is defined as "the production of electricity at, or near, the point of use, irrespective of size, fuel, and technology" [281]. It is also known as "embedded generation", "dispersed generation", and "decentralised generation" [2]. Various technologies are used in DG [115, 124, 216, 281], such as micro cogeneration systems for the on-site simultaneuos conversion of the fuel into electrical

and thermal energy (e.g., reciprocating engines, fuel cells, Stirling engines, Rankine cycle turbines operated with steam or organic compounds as working fluid, and micro gas turbines), on-site renewable energy systems (e.g., photovoltaic and biomass conversion systems, and wind and water turbine generators), and energy recycling technologies that capture otherwise wasted energy (e.g., systems powered by gas pressure drop, exhaust heat from industrial processes, and low energy content combustibles from various processes).

In the last decade, several major factors contributed to a renewed interest into DG, and therefore to its evolution. On the one hand, environmental concerns, depletion of fossil fuels reserves, and increasing dependency on politically unstable regions for the supply of fossil fuels have raised the issue of developing sustainable energy technologies, which has thus moved to the foreground of many governments' agendas. Therefore, in 2008 the European Commission (EC) published the "20 20 by 2020 package" [83, 84] in order to pursue by 2020 a 20%-reduction of GHG emissions, a 20%-share of renewable energy in the overall energy mix, and a 20%-energy efficiency improvement. Each Member State has set its individual targets, and the Dutch government pursues by 2020 a 30%-reduction of GHG emissions (compared to 1990 levels), an increased share of renewable energies in the overall energy use from 2% to 20%, and an annual energy efficiency improvement of 2% [184].

On the other hand, technological innovations and a changing economic and regulatory environment have heavily influenced such interest as well. This has been confirmed by the International Energy Agency [123], which listed four factors (other than climate change concerns) that contributed to the DG evolution, i.e., developments in DG technologies, constraints on the construction of new transmission and distribution (T&D) lines, increased customer demand for highly reliable electricity, and the electricity market liberalisation.

Decentralization is thus a current trend, but it is interesting to point out that in the late 19^{th} century the inventor and businessman T. A. Edison anticipated a highly dispersed electricity system, with individual businesses generating their own power. He thus envisioned a dynamic, decentralized power industry, with dozens of companies generating and delivering electricity close to where it was used, or even putting systems on site in customers' basements [64]. Furthermore, in the early 1970's the economist and writer E. F. Schumacher wrote that the technological development should be given "a direction that shall lead it back to the real needs of man, and that also means: to the actual size of man. Man is small, and, therefore, small is beautiful. To go for giantism is to go for self-destruction" [228].

The benefits of DG are mutiple and can be divided in three main categories [70, 115, 123, 204, 265]. From an environmental point of view, DG can exploit renewable energy sources as fuel inputs; reduces emissions; guarantees increased systems efficiency; reduces the amount of the land required for electricity-conversion facilities and of rights-of-way for T&D corridors. From an operational point of view, DG reduces T&D losses, loads requirements, and power fluctuations; improves electric systems reliability and power quality; provides ancillary services, on-site power in case of emergency or systems outages, and modularity; decreases the vulnerability and increases the resilience of critical infrastructures. From an economical point of view, DG reduces the construction of new T&D

networks, the upgrade of existing lines, peak power requirements, and energy prices; has a positive influence on the energy prices due to its location flexibility; shows a flexible reaction to energy prices fluctuations; can exploit cheap fuel opportunities.

1.3 Micro cogeneration

Micro cogeneration, also known as micro combined heat and power (μCHP) or domestic cogeneration, is generally defined as "the process of producing both electricity and usable thermal energy (either heat or cooling, or both) at high efficiency and near the point of use" [281]. It is important to stress out that the definition incorporates the simultaneuos conversion of the fuel into electrical and thermal energy, a performance criterion of high efficiency, and a location criterion which places the unit close to the customer. In contrast with the currently dominant pattern of producing the electricity in large, centralised power plants, μCHP would then make a fundamental difference in electricity systems, because it integrates technological as well as cultural and institutional components, but also entails the potential for reducing the ecological impact of electricity conversion from the fuel [202].

There is however no clear consensus about what "micro" actually means. Ackerman *et al.* [2] suggested to use the latter term for DG units with power output up to 5 kW_{el}, and to define as "small" those systems in the range from 5 kW_{el} to 5 MW_{el}. Other studies [72, 202] defined energy conversion units below 15 kW_{el} as "micro". A further distinction has been given in a summary report by FaberMaunsell [87], where a CHP system was defined as "mini" if capable of supplying between 10 and 100kW_{el}, and as "micro" if able to supply less than 10 kW_{el}. Pilavachi [208] stated that "micro" CHP systems were in the range up to 150 kW_{el}, and "mini" CHP applications in the range from 150 kW_{el} to 1 MW_{el}. The diatribe was finally clarified by the European Union (EU) through the Directive 2004/8/EC of the European Parliament and of the Council, according to which "micro cogeneration unit shall mean a cogeneration unit with a maximum capacity below 50 kW_{el}, and small scale cogeneration shall mean cogeneration units with an installed capacity below 1 MW_{el}" [82].

1.3.1 Benefits

As a quantitative example, Fig. 1.3 shows the comparison between cogeneration and conventional generation. The data have been taken from the work of Lee [169], are based on average values for the United Kingdom, and refer to the year 2010. According to the author, a typical U.K. coal-fired central power plant has an efficiency equal to about 40%, while the T&D losses on average are around 8% of the trasmitted power.

The left-hand side of Fig. 1.3 shows a conventional generation system, with electricity generated by a coal-fired central power plant, and heat generated by a local boiler. That system requires 3.9 units of energy input to meet the customer's requirements (i.e., one unit of electrical energy and one unit of thermal energy). On the right-hand side, the same electricity and heat requirements are supplied by just 2.5 units of energy input through a

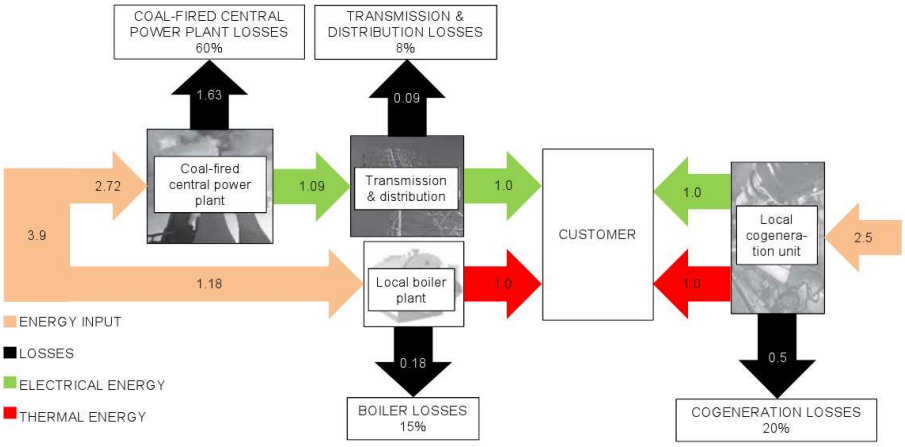

Figure 1.3: *Cogeneration versus conventional generation. The data are based on average values for the United Kingdom and refer to the year 2010. Data taken from Ref. [169].*

local CHP unit.

By introducing the overall (η_{o}), electrical (η_{el}), and thermal (η_{th}) efficiency defined as

$$\eta_{\mathrm{o}} = \frac{\text{Electrical energy + thermal energy}}{\text{Energy input}}, \tag{1.1}$$

$$\eta_{\mathrm{el}} = \frac{\text{Electrical energy}}{\text{Energy input}}, \tag{1.2}$$

$$\eta_{\mathrm{th}} = \frac{\text{Thermal energy}}{\text{Energy input}}, \tag{1.3}$$

the corresponding values have been calculated for the cogeneration and conventional generation (Table 1.1). The overall efficiency is equal to 51.3% for the conventional generation, and to 80.0% for cogeneration. The local CHP unit is thus 55.9% more efficient than the conventional generation system. The electrical efficiencies are slightly different (40.0% for cogeneration and 36.8% for the conventional generation), while the thermal efficiency calculated for the conventional generation is 52.8% higher than the value for cogeneration (40.0% for cogeneration and 84.7% for the conventional generation). Finally, the saving of the energy input due to the use of the local CHP unit is equal to 35.9%.

The values given in Table 1.1 refer to the United Kingdom, and might differ from the average efficiencies for the Netherlands. In particular, most of the Dutch central power plants are gas-fired units, since the Netherlands are presently the second largest natural gas producer in Europe and the ninth in the world, accounting for 46.7% of the EU-27 total annual gas production, and for 2.5% of the world total annual gas production [37]. Modern combined-cycle gas turbine plants, which currently dominate the gas-based technology for intermediate and base-load power generation, feature an electrical efficiency

Table 1.1: *Comparison of overall* (η_o)*, electrical* (η_{el})*, and thermal* (η_{th}) *efficiency between cogeneration and conventional generation. Data taken from Ref. [169].*

	η_o [%]	η_{el} [%]	η_{th} [%]
Cogeneration	80.0	40.0	40.0
Conventional generation	51.3	36.8	84.7

that is expected to increase to about 64% by 2020 from the actual values in the range 52-60% [75]. Furthermore, in the Netherlands the electrical T&D losses account for 4% of the distributed volumes [1], while the electrical efficiency achieved with local CHP units might be lower than the 40%-value calculated by Lee [169], especially in the case of a low power output which is more suited for μCHP. Therefore, when using the average values for the Netherlands, the difference between the overall efficiency obtained with cogeneration and the value achieved with the conventional generation would be lower than those calculated for the United Kingdom, whereby electricity is mainly generated by means of coal-fired power plants.

Furthermore, the values mentioned above for the United Kingdom and the Netherlands will vary from those relative to other countries, based on the fuels burned in central power plants for the electricity production, the electrical T&D losses, and the electrical efficiencies of the local micro CHP system. As a consequence, the advantages of using cogeneration instead of the conventional generation can vary significantly from country to country, although appropriately sized CHP units are generally more efficient than conventional generation systems, and allow making substantial savings of the energy input.

Micro cogeneration systems will also have a beneficial impact for reducing GHG emissions, mainly due to the reduction of CO_2 and NO_x emissions [63, 86, 103, 169, 203], although gas-fired power plants are indeed less polluting than their coal-fired counterparts. According to a report published by the Energy Information Administration [74], combustion of natural gas produces about 44% less CO_2 and about 80% less NO_x than coal combustion, per unit of energy produced.

Moreover, since μCHP systems require the energy conversion unit to be located close to the customer in order to supply the required thermal energy, their application also reduces the electrical T&D losses. Micro cogeneration also offers concrete costs savings to the customers, by reducing imported electricity, by selling surplus electricity back to the grid, and by providing affordable heat. Increased cost-effectiveness might also be achieved by using biomass and/or waste materials as fuels for μCHP applications [80].

1.3.2 Market potential

Buildings with central heating systems represent the main potential for the application of micro cogeneration technology. Furthermore, although μCHP systems are very flexible

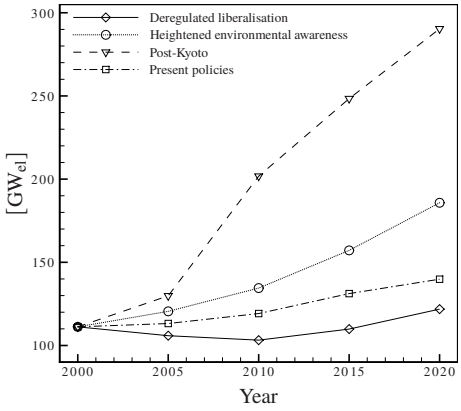

(a) *Cogeneration capacity in EU-15, Cyprus, Norway, and Switzerland.*

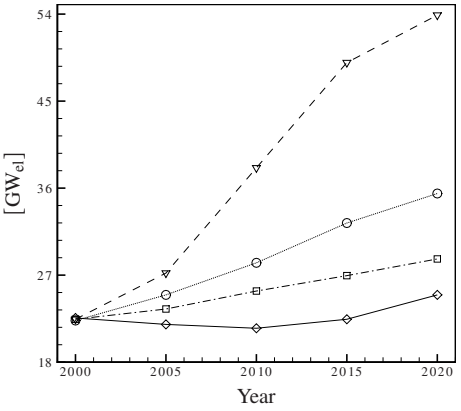

(b) *Cogeneration capacity in CEE countries.*

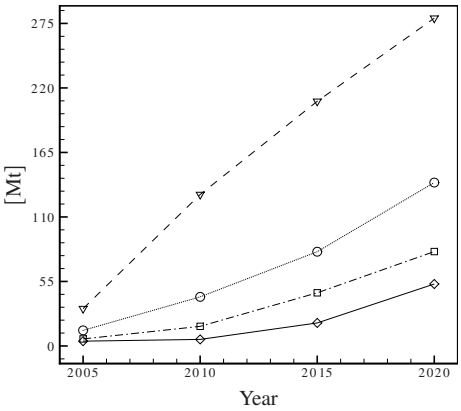

(c) *CO_2 emissions reduction in EU-15, Cyprus, Norway, and Switzerland.*

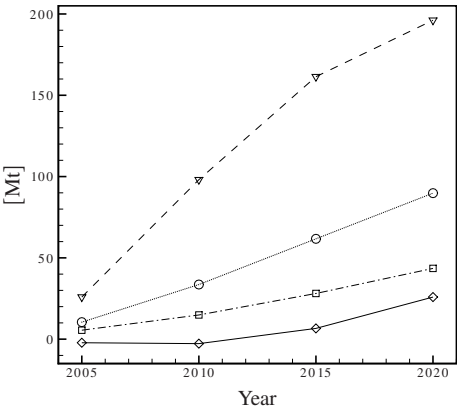

(d) *CO_2 emissions reduction in CEE countries.*

Figure 1.4: *Prediction of European cogeneration capacity and CO_2 emissions reduction by scenario. Data taken from Ref. [73].*

in terms of fuel input, natural gas is likely to be the primary fuel utilized in micro cogeneration. This means that conventional heating systems such as natural gas-fired condensing boilers will likely be replaced by μCHP units, which are thus seen as a promising next generation heating technology for countries with extensive natural gas infrastructures.

In the last decade, several studies have been carried out in order to determine the market potential of micro cogeneration in Europe, and more specifically in the Netherlands. In 2001, the potential application of cogeneration (both domestic and industrial) in 28 European countries (i.e., EU-15, Cyprus, Norway, Switzerland, and 10 Central and Eastern Europe (CEE) countries) was assessed with a modelling process which involved four different scenarios [73]. Three of these scenarios assumed ratification of the Kyoto Pro-

tocol within the EU and implementation of the GHG emission targets. Only the best case scenario ("Post-Kyoto") included full world-wide Kyoto ratification, while the worst case scenario ("Deregulated liberalisation") assumed failure of the Protocol, with the whole process delayed by ten years. The report concluded that only under the Post-Kyoto scenario significant growth of the application of cogeneration occured until the year 2020, in order to fulfill the target set by the EC of doubling the cogeneration output as a proportion of electricity generation from 9% to 18% by 2010 [81]. Alternatively, a continuation of the current status quo was unlikely to lead to much, if any, growth over the same period. Under the Post-Kyoto scenario, in the period 2000-2020 cogeneration was projected to almost triple the capacity from 74 GW_{el} to 195 GW_{el} in the EU-15 (Fig. 1.4a), and from 22 GW_{el} to 54 GW_{el} in the CEE countries (Fig. 1.4b). At the same time, in 2020 the total annual CO_2 emissions saving was predicted to be approximately 270 Mt in the EU-15 (Fig. 1.4c), and almost 200 Mt in the CEE countries (Fig. 1.4d).

An econometric model was developed in 2002 to estimate the potential size of the European market of μCHP (with electrical power $P_{el} < 3$ kW) under various scenarios, for the period 2001-2020 [87]. The selected scenarios were the "business as usual" approach, where current conditions were assumed, the "medium effort" scenario, where reasonable efforts were made with regard to legislation, policy, and financial incentives, and the "maximum effort" scenario, whereby considerable initiatives were taken to promote micro cogeneration. The investigation for both market potential and CO_2 emissions reduction was carried out for the EU-15, eleven CEE countries, and Norway. The model indicated that under the best scenario a total of 11.5 million μCHP units could be sold by 2020 across the twenty-seven countries, leading to an equivalent reduction of 7.3 Mt of CO_2 emissions (Fig. 1.5). For the CEE countries in particular, the prediction revealed that by 2020 around 670,000 units could be sold, with an equivalent reduction of 1 Mt of CO_2 emissions. Furthermore, among the EU-15 countries, Sweden, the United Kingdom, and Germany exhibited the greatest market potential in 2002 under the optimal scenario, followed by Austria, Norway, and Spain.

In 2003, Dentice d'Accadia *et al.* [60] reported a forecast for the year 2006, based on which Germany, the United Kingdom, and the Netherlands would become the largest markets for μCHP installations ($P_{el} < 15$ kW), thanks to the climate, a tradition of DG on both supplier and end-user sides, and a large diffusion of gas connection. A second group of countries (i.e., Italy, Austria, Switzerland, and Belgium) would play a less important, but still significant, role in the micro cogeneration diffusion. The rest of Europe, both for the lack of gas connection and the moderate climate, were not expected to play a pivotal role.

Slowe [240] gave a commercial outlook for μCHP ($P_{el} < 6$ kW) in the period 2005-2010. According to the author, the European market was dominated by 5-kW_{el} units sold in Germany. He claimed that while these markets were growing steadily, it was unlikely that sales would rise above 10,000 units per year by 2010. On the contrary, Slowe saw a greater interest for μCHP units with an electrical power lower than 3 kW, designed for single-family homes. The initial markets for these products were likely to be the United Kingdom, the Netherlands, and Germany, although the market potential could be constrained by product availability, engagement by utilities and boiler manufacturers, and regulatory barriers and issues.

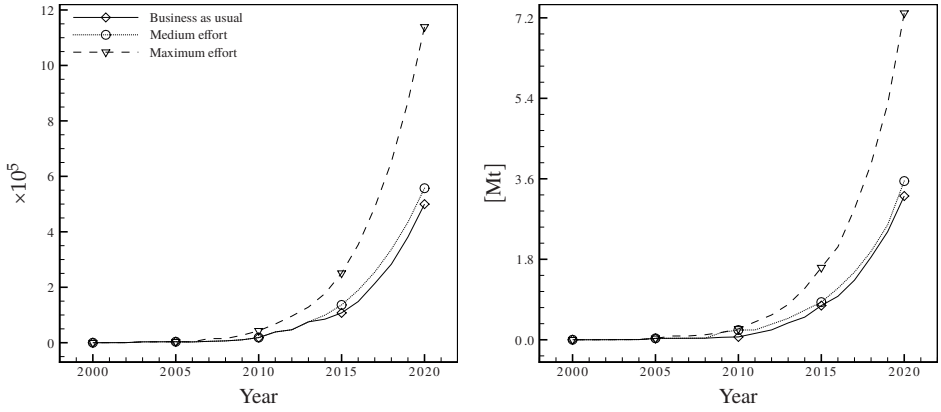

(a) *Cumulative sales.* **(b)** *CO_2 emissions reduction.*

Figure 1.5: *Prediction of micro cogeneration potential in twenty-seven European countries by scenario. Data taken from Ref. [87].*

An investigation about the mass market introduction of micro cogeneration ($P_{el} < 15$ kW) in the Netherlands was carried out in 2006 by Colijn [48], according to whom Dutch μCHP systems would use natural gas for heating purposes. Since 95% of the 7 million domestic and light industrial sites have a connection to the gas network, Colijn firstly estimated the theoretical potential for micro cogeneration in more than 6.65 million units. However, a more practical method for analyzing the market potential was based on the number of central heating boilers mounted each year. Of the 385,000 central heating boilers placed in homes in the Netherlands, up to 80,000 were for new homes, while the rest were replacements. Therefore, about 300,000 boilers could be replaced by micro cogeneration units every year. That number dropped down to 150,000 per year considering as limiting factors the heat and electricity demands in the average Dutch home, which could make micro cogeneration uneconomical and not attractive to the end-users. Finally, taking into account comfort as a further requirement, domestic CHP could directly replace heating boilers in about 50,000 homes per year.

Another assessment of the micro cogeneration market penetration in the Netherlands in the period 2010-2030 has been performed in 2008 by de Jong *et al.* [53]. The authors considered the μCHP systems having an electrical power equal to 1kW, and based their predictions on two different scenarios. "Scenario 1" was provided by the Smart Power Foundation, which is the Dutch foundation within which μCHP developers cooperate, and assumed a maximum payback period of 5 years, based on adequate support and feed-in tariffs. "Scenario 2" was a more pessimistic approach, which involved a slower market penetration. The term "slower" was interpreted as a slower growth after successful launch in the introductory phase (2008-2013). The two scenarios are shown in Figs. 1.6a and 1.6b. According to Scenario 1, the annual sales of μCHP units could increase fourfold in the period 2013-2023, from about 75,000 to about 325,000, and then stabilize around 350,000 in

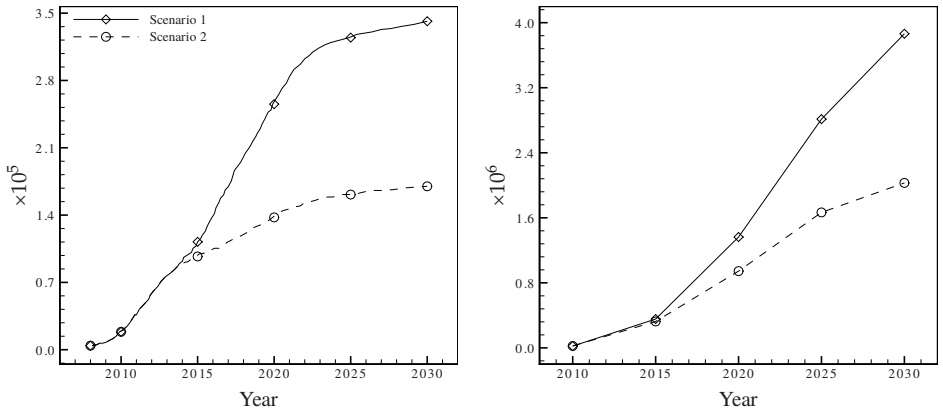

(a) *Sales.* **(b)** *Cumulative installed units.*

Figure 1.6: *Prediction of micro cogeneration potential in the Netherlands by scenario. Data taken from Ref. [53].*

2030. On the basis of Scenario 2, during the first period (2008-2013) the market developed at the same rate as that of Scenario 1, then the development was delayed due to several factors (e.g., profitability, success of μCHP units launch, unfavourable distribution of gas and electricity prices, high initial costs, and lack of interest among consumers), such that the large-scale sales held each year at about 50% of the level of Scenario 1. As a consequence, in Scenario 1 almost 4 millions of μCHP units would be installed in the Netherlands in 2030, while that number dropped to less than 2 millions according to Scenario 2.

More recently, two reports have been published by COGEN Europe [44] and Delta Energy & Environment [59]. In 2010, COGEN Europe has developed two long-term scenarios (i.e., "baseline" and "advanced" scenario), reflecting the influence of several key factors in shaping the outlook for cogeneration. Under the baseline scenario, the installed cogeneration capacity rises gradually to the period 2035-2040 at a slightly higher rate of 2.25% than historically, such that by 2040 it will be equal to about 175 GW_{el}, of which 60 GW_{el} due to micro and mini CHP installations ($P_{el} < 50$ kW). Under the advanced scenario, the installed CHP capacity will be equal to 200 GW_{el}, of which 35% generated through micro and mini units. Furthermore, the analysis of the European opportunity for mini and micro CHP systems ($P_{el} < 100$ kW) performed in 2011 by Delta Energy & Environment suggests that the annual sales could reach over 200,000 units by 2015, and over 600,000 units by 2020.

1.3.3 Conversion technologies

Micro cogeneration systems usually consist of four basic elements, namely a prime mover or conversion unit, an electricity generator, a heat recovery system, and a control system. The prime mover converts the chemical energy stored within a fuel into useful forms of energy (i.e., electrical and thermal), and drives the electricity generator, while

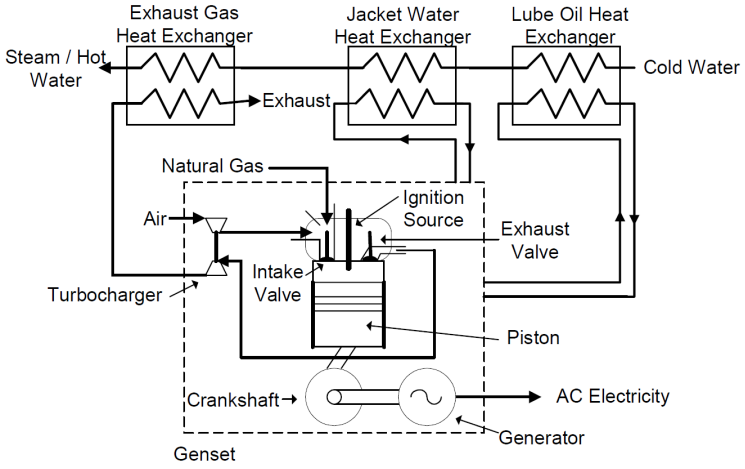

Figure 1.7: *A micro cogeneration system based on a spark ignition engine [197].*

the residual thermal energy is recovered through the heat recovery system, and distributed to the surroundings. The main conversion technologies that can be applied to μCHP are reciprocating engines, Stirling engines, fuel cells, Rankine cycle systems, and micro gas turbines [71, 80, 197, 202, 235, 264, 281].

Reciprocating engine In a reciprocating engine the prime mover is a piston-driven internal combustion engine. Spark ignition engines, which make use of a spark plug to ignite an air-fuel mixture introduced into the cylinder at high pressure, and mostly run on natural gas, propane, gasoline, or landfill gas, are usually employed in μCHP applications [71, 80, 197, 235, 264, 281]. In such systems, the most important features required by a spark ignition engine are long service intervals, maintenance-friendly design, and prolonged life of all the components, due to the extensive periods of continuous operation; high recovery of the thermal energy available in the exhaust gases and cooling systems; lean-burn or stoichiometric combustion in order to minimize emissions, while maintaining stable operating conditions; operational safety and reliability; low fuel consumption [71, 197, 264].

Figure 1.7 shows a typical arrangement for a micro cogeneration system based on a spark ignition engine. In such system, the fuel is mixed with air and compressed in a cylinder. This mixture is then ignited by an externally supplied spark and the hot, expanding gas moves a piston, thereby causing the crankshaft to rotate. The mechanical energy is then used to drive a generator, while the thermal energy from the exhaust gases, from the lubricating air cooler, and from the jacket water cooler of the engine is recovered using heat exchangers, and then supplied to the heating system.

The overall efficiency of μCHP systems based on reciprocating engines is in the range of 85-90%, with electrical efficiencies in the range between 28% and 39% [197], although

the latter generally does not exceed 26% at sizes below 15 kW_{el} [202].

Reciprocating engines are commercially available and produced in large numbers by a variety of companies worldwide. The German company SenerTec GmbH [230] produces the μCHP unit Dachs, which delivers 5.5 kW_{el} and 12.5 kW_{th}, respectively. The overall, electrical, and thermal efficiency are respectively equal to 88%, 27%, and 61%, with a fuel input equal to 20.6 kW. The Japanese company Honda Motor Company, Ltd. [114] has been developing a 1-kW_{el} household cogeneration unit since 2002. The ECOWILL model currently exhibits an electrical efficiency equal to 26%, and an overall efficiency equal to 92%. PowerPlus Technologies GmbH [209], currently a subsidiary of Vaillant GmbH, produces the ecoPOWER system in three different sizes (1, 3, and 4.7 kW_{el}). The smallest unit is based on the ECOWILL model, while the two larger systems show overall and electrical efficiency equal to 90% and 25%, respectively.

Stirling engine Unlike internal combustion engines, for which combustion takes place inside the engine, Stirling engines are piston-driven machines powered by an external thermal energy source. In this engine, a working gas flows between a high-temperature chamber and a low-temperature cooling chamber by means of a displacer piston. On the way from the hot to the cold chamber, the gas flows through a regenerator (made of wire, ceramic mesh, or porous metal), which captures the heat of the hot gas and returns it to the cold gas as the latter flows back to the hot chamber.

Stirling engines can be classified on the basis of either the arrangement or the drive method. Alpha, Beta, and Gamma Stirling engines are distinguished by the position and number of pistons and cylinders, while the drive methods are based on kinematic drive and free-piston drive [198, 222, 263].

Overall efficiences in micro cogeneration applications based on Stirling engines can be in the range from 65% to 85% [197], while so far electrical efficiency values of 20% have been achieved in large systems, with predicted efficiencies for future models higher than 24% [202] or even close to 50% [197]. Small Stirling engines achieve lower electrical efficiency than larger units, typically around 12% [202].

Stirling engines are in between the research and development (R&D) phase and marketing. Field tests are still being carried out, but initial commercial products are available. Whisper Tech Ltd. [274], from New Zealand, is now a joint venture with Spanish Mondragón Cooperative Corporation, and manufactures and distributes its WhisperGen μCHP system in Europe. The system has a nominal electrical output up to 1 kW, while the maximum thermal output is equal to 14 kW. Requiring a nominal heat input equal to 16 kW, the overall, electrical, and thermal efficiency are respectively equal to 94%, 6%, and 88%. Cleanenergy AB [39] from Sweden produces and markets μCHP engines based on Stirling technology for biogas, landfill gas, and natural gas use. These engines have an electrical power output in the range 2-9 kW, while the thermal power output is in the range 8-25 kW. The overall efficiency is larger than 90%, while the electrical efficiency is in the range 22-25%. Stirling Systems Ltd. [255] is a Swiss corporation which has developed it module based on a Stirling engine for more than ten years. It delivers an electrical power of approximately 1.2 kW, while the peak thermal power is equal to about 15 kW. The overall

efficiency is larger than 90%, and the electrical efficiency is equal to 18%. The English company Baxi Heating U.K. Ltd. [21] developed the first wall-hung domestic μCHP boiler in the United Kingdom. The Baxi Ecogen produces up to 1kW of electrical energy, and up tp 6 kW of thermal energy. The energy input is equal to 7.7 kW, such that the overall, electrical, and thermal efficiency are respectively equal to 91%, 13%, and 78%. The Dutch company Remeha B.V. [213] developed eVita, the world's first μCHP "combined" boiler. The eVita boiler operates in the same way as high-performance boilers, but can also generate up to 1 kW_{el} and 5 kW_{th} by means of a Stirling engine. The overall, electrical, and thermal efficiency of the eVita system are respectively equal to 92%, 13%, and 66%.

Fuel cell A fuel cell is a device that converts the chemical energy stored within a fuel into electricity, through an electrochemical reaction with oxygen or another oxidizing agent. In the simplest case, hydrogen is used as fuel, although hydrocarbons such as natural gas and alcohols like methanol can also be utilized. Water and thermal energy are by-products of this process, and the latter can be recuperated for space and water heating since the reaction is exothermic.

A fuel cell consists of a sandwich of layers, called a fuel cell stack, that are placed around a central electrolyte. The fuel is oxidized on the anode, and the oxygen is reduced on the catode, while bipolar plates feed the gases, collect the electrons, and conduct the reaction heat. To achieve higher capacities, a number of single fuel cells can be connected in series. There are various types of fuel cells, which differ on the basis of the type of the electrochemical reaction taking place, the type of electrolyte, and the type of catalyzer. The most common fuel cells are alkaline fuel cells, direct methanol fuel cells, molten carbonate fuel cells (MCFC), phosphoric acid fuel cells (PAFC), polymer electrolyte membranes fuel cells (PEMFC), and solid oxide fuel cells (SOFC).

PEMFC used for low-power electricity conversion can currently reach electrical efficiencies from 28% to 33%, while in the future it may be possible to achieve 36%-efficiencies for domestic systems [202]. Furthermore, advanced high-temperature MCFC and SOFC systems are projected to achieve overall efficiencies in the range from 50% to 55%, while hybrid combined fuel cell-heat engine systems are calculated to achieve overall efficiencies above 60% in DG applications [264]. Micro cogeneration systems based on fuel cells have the potential to reach overall efficiencies of about 80%.

In 2007, MCFC and PAFC units were available on the market for commercial and industrial CHP, and afterwards fuel cells began to be commercialized in a wider variety of applications [92, 264]. However, fuel cells for micro cogeneration are still in the R&D phase, with a number of pilot plants currently being tested, although in some cases the transition from the R&D phase to commercialisation is already in progress. The Swiss company Hexis AG [108] has developed a μCHP system based on a SOFC, with electrical and thermal power output equal to 1 kW and 1.8 kW, respectively. It has an overall efficiency of 95%, while the electrical efficiency is in the range 30-35%. Vaillant GmbH, in cooperation with the New York-based Plug Power, has developed a micro cogeneration unit based on a PEMFC. The fuel cell heating appliance targets a maximum electrical power output equal to 4.6 kW, and a maximum thermal power output equal to 7 kW, showing

overall and electrical efficiency respectively equal to 85% and 35%. The U.S. company IdaTech, LLC. [117], together with RWE AG and Buderus USA, is developing a PEMFC system with an electrical power output up to 5 kW, targeting an electrical efficiency up to 30%.

Rankine cycle system Among other technologies which are currently under development for micro cogeneration, systems based on the Rankine thermodynamic cycle are arguably one of the most advanced concepts. The most familiar Rankine power plants make use of the steam turbine, which is one of the most versatile and oldest conversion technologies used in power generation, still widely utilized for industrial CHP applications, with power output up to several MW_{el}.

Large steam power plants typically exhibit electrical efficiency in the range from 36-38%, which decrease to 7-10% for small cogeneration plants [71, 264, 281], while overall efficiencies can be as high as 80% [80, 264, 281].

As a consequence, for applications up to a few hundred kW_{el}, steam power plants are inappropriate in order to achieve acceptable performance levels. An important number of new solutions have been proposed to efficiently overcome this drawback, among which organic Rankine cycle (ORC) systems are the most widely used. The difference between the ORC and the steam Rankine cycle lies in the working fluid, which for the former is an organic fluid (e.g., a refrigerant, a hydrocarbon, a silicon oil, a perfluorocarbon) exhibiting favourable thermodynamic properties [25, 129, 167, 192]. When compared to steam power plants, ORC plants show high overall efficiency and very high turbine efficiency; low mechanical stress of the turbine blades and direct coupling between the turbine and the generator, due to low rotational speeds; no corrosion of the turbine blades, due to the absence of moisture in the vapour nozzles; long life and minimum maintenance requirements; oil-free operation, due to the use of the working fluid as lubricant; quiet and leakage-free operation; very high reliability; cost-effective designs [7, 25, 65, 167, 173, 174, 192]

The electrical efficiency of an ORC-based μCHP system is estimated to be between 10% and 20%, depending on temperature levels, while overall efficiencies can be as high as 90% [71, 202].

ORC technology has been very well-known since the early 1970's, while the first commercial applications appeared in the 1980's in the medium-scale power range. Nowadays, ORC power plants are quickly spreading around the world in the power output range from few hundreds kW_{el} to 2.5 MW_{el}. However, while in the latter case many units are commercially available, in the former only few solutions are actually suitable. Amovis GmbH, Climate Energy, LLC., Cogen Microsystems, Eneftech Innovation, Energetix Genlec, Ltd., and OTAG Vertriebs GmbH & Co. KG are among the various companies currently involved in the development of μCHP units based on the Rankine cycle, with a power output lower than 10 kW_{el}.

Summary Table 1.2 compares the abovementioned conversion technologies for micro cogeneration, on the basis of selected performance criteria. Operational life and reliability

Table 1.2: *Comparison of performance characteristics for micro cogeneration (power output < 50 kW_{el}) conversion technologies. η_o and η_{el} are the overall and electrical efficiency, respectively.*

	Reciprocating engine	Stirling engine	Fuel cell	Rankine cycle system	Micro gas turbine
η_o [%]	85-90	80-90	80-85	80-90	70-90
η_{el} [%]	20-25	10-25	25-33	8-15	14-23
Emissions	High	Very low/moderate	Zero/almost zero	N.a.	Low
Part-load efficiency	Very good	Good	Excellent	Excellent	Good
Noise level	High	Moderate	Low	Moderate	Low/moderate
Fuel flexibility	Good	High	Good	Very high	Good
Market availability*	+++	++	+	+	+++

*+ R&D phase, ++ R&D phase/near to market, +++ Commercially available.

have not been included because of the difficulty to assess them at this stage of the development of the various technologies. Micro gas turbines, which are discussed in detail in Sec. 1.4, are also listed in the table for comparison purposes. Reciprocating engines are commercially available in large numbers, can achieve high overall and electrical efficiencies, and exhibit high electrical efficiencies at part-load operating conditions. They also have relatively low investment costs, but require frequent maintenance, produce significant emissions, and have high noise levels. Due to the fact that combustion takes place in a separate combustor, Stirling engines offer low emissions as well as a high fuel flexibility. They also have the potential to achieve high overall efficiency values with moderate electrical efficiencies, though smaller Stirling engines have even lower electrical efficiencies. Stirling engines have less moving parts than internal combustion engines [80], thus they exhibit lower friction losses, wear, and vibrational levels, and require less maintenance. Some of the drawbacks are the currently very high investment costs and the lack of design and operational experience in the low-power range. Fuel cells are still in the R&D and field testing phases, but they offer the potential benefit of the highest electrical efficiency and the lowest emissions. They also exhibit low noise levels, an excellent behaviour at part-load conditions, and require less frequent maintenance intervals. On the contrary, fuel cells have moderate fuel flexibility, very high investment (i.e., material and manufacturing) costs, and low durability and power density. Systems based on the Rankine cycle for μCHP are still mainly in the R&D phase, but few solutions are actually commercially available. Potentially, they offer low emissions and high fuel flexibility, but electrical efficiencies are expected to be low. In addition, some steam engine concepts will allow higher power-to-heat ratios.

1.4 Micro gas turbines

Micro gas turbines are small-scale gas turbines, which thus operate on the same Brayton cycle as their bigger counterparts, although miniaturisation leads to increased internal losses in the turbomachinery, because of large relative tip clearances (i.e., the ratio of the tip clearance to the blade height at the impeller outlet) due to manufacturing tolerances, and high viscous effects because of low Reynolds numbers. There are no established guidelines to categorise small gas turbines for CHP applicationse, therefore a gas turbine has been defined in the literature as "micro" if it has a power output up to 150 kW_{el} [208], 200 kW_{el} [80, 180], 250 kW_{el} [264], 300 kW_{el} [235], 400 kW_{el} [242], and 500 kW_{el} [281].

They offer many potential advantages in comparison to other conversion technologies used for μCHP applications [80, 168, 197, 208, 242, 264, 281]. These include compact size and high specific power; small number of moving parts; low vibrations, noise, and maintenance requirements, which lead to low investment and maintenance costs; high fuel flexibility; possibly short delivery time; modularity. Furthermore, when utilized in micro cogeneration applications, micro turbines generate high-grade residual thermal energy (suitable for supplying a variety of building and light industrial thermal needs), potential for very low emissions, and overall efficiencies that can reach 80% and above [208, 235, 281]. On the contrary, micro turbines still exhibit low electrical efficiencies [208, 235, 281],

and suffer from lower power output and efficiency at high ambient temperatures and at part-load operating conditions.

1.4.1 The micro turbine package

Figure 1.8 shows a schematic of a recuperated micro turbine CHP unit and the temperature-entropy diagram of the corresponding thermodynamic air cycle. The main components of such a system are the compressor, the turbine, the combustor, the recuperator, the generator, and the heat recovery unit. At point 1, the compressor sucks air in at ambient conditions ($T_1 = T_a$ and $p_1 = p_a$), and pressurizes it to point 2 (T_2, p_2). Downstream of the compressor, the air flows into the recuperator cold side, where the flue gases raise its temperature from T_2 at point 2 to T_3 at point 3. The pressure at point 3 drops to $p_3 < p_2$ because of the pressure losses across the recuperator on the high-pressure side (i.e., the cold side). Subsequently, the air enters the combustor, where it is burned with the natural gas, causing a further temperature increase from T_3 at point 3 to T_4 at point 4. The pressure at point 4 drops to $p_4 < p_3$ because of the pressure losses across the combustor. At the combustor exit, the flue gases expand through the turbine from point 4 (T_4, p_4) to point 5 (T_5, p_5), and then flow in the recuperator low-pressure side (i.e., the hot side), where they are cooled from T_5 to T_6. Due to the pressure losses of the recuperator on the low-pressure side, the pressure p_6 at point 6 is lower than p_5. Finally, the flue gases are further used in the heat recovery unit for either water or space heating, and afterwards they are exhausted to ambient pressure.

Turbomachinery In a micro gas turbine, the compressor and turbine are commonly mounted on a single-shaft, which is supported by two sets of bearings. Although large, axial-flow turbines and compressors are typically more efficient than radial-flow components, in the size range of micro gas turbines the latter offer minimum surface and end-wall losses, and provide the highest efficiency [242]. Centrifugal compressors also provide very high pressure ratios per single stage. Furthermore, centrifugal machines are less expensive to manufacture, and are similar in terms of design and volume flow rate to automotive turbochargers, which have been used for almost fifty years to increase the power of reciprocating engines.

Today's world market for automotive turbochargers is around two millions units per year [242], and is therefore characterized by relatively low production costs. Moreover, small gas turbines, of the size and power rating of micro turbines, serve as auxiliary power units on airplanes, such that decades of experience with these applications constitute the basis for the technological development of micro turbines.

Compressor wheels can be made of aluminium or titanium, wherelse turbine wheels are made of alloys like Inconel, since they operate at much higher temperatures, but a constant R&D work is underway to introduce ceramic materials for turbines, as well as the other hot components (e.g., the combustor and the recuperator), in order to increase the operating temperatures.

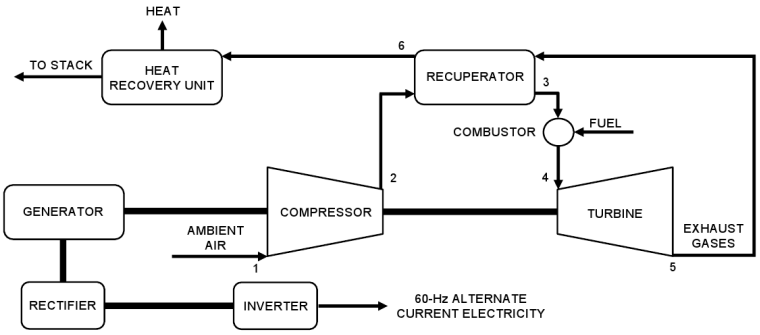

(a) *Major components.*

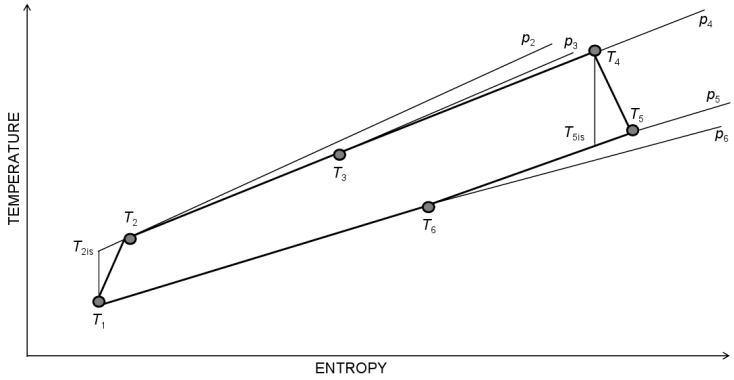

(b) *Temperature-entropy diagram of the thermodynamic air cycle.*

Figure 1.8: *A micro cogeneration system based on a recuperated micro gas turbine.*

Bearings In a micro gas turbine, the shaft is most commonly supported by either oil-lubricated or air bearings [242]. The former are mechanical bearings that can be made of high-speed metal rollers, floating sleeves or ceramic surfaces, which offer the most attractive benefits in terms of life, operating temperature and lubricant flow. Although their technology is well-known, they require an oil system that adds costs and maintenance.

Air bearings allow the shaft to spin on a thin layer of air, so friction is low and the rotational speed can be increased to higher values. No oil system is necessary, such that air bearings offer simplicity of operation without the cost, reliability concerns, and maintenance requirements of oil bearings. Concerns however do exist about the reliability of air bearings under repeated start-ups, shut-downs, and load changes, while they also lengthen micro turbines start-up time up to two minutes.

Active magnetic bearings are an alternative to rolling element bearings [38]. Their technology is well-established, but only in the last decade became practical in the gas turbines field, thanks to high-speed micro processing that allows stable control and dynamic

stiffness and damping. The active magnetic bearing uses the magnetic force to hold the rotor in place as opposed to the forces of a rolling element or air foil bearings, resulting in three major technological advantages, namely oil-free operation with no air requirements, operation in extreme temperature environments, and active control.

Recuperator In order to be financially viable and to achieve the efficiency levels needed to be competitive in the μCHP market, micro turbines often have a recuperator, which is a heat exchanger that uses the turbine exhaust gases to pre-heat the pressurized air, prior to the combustor. This leads thus to increased efficiencies, to fuel savings up to 40% [159, 208, 242], and to lower temperatures of the exhaust gases which enter the heat recovery unit [242].

The two main performance parameters of a recuperator are the effectiveness and the pressure drop. The former is the ratio of the actual temperature increase of the air flowing through the compressor side of the recuperator, to the maximum theoretical temperature increase. By referring to Fig. 1.8, the recuperator effectiveness is defined as

$$\eta_{\text{rec}} = \frac{h_3 - h_2}{h_5 - h_2}, \tag{1.4}$$

where h is the specific enthalpy. As the heat transfer approaches reversibility, h_2 approaches h_3 and η_{rec} tends to unity (i.e., 100%). In pratice, recuperator effectiveness values typically range from 60 to 80%, but very high-performance recuperators can achieve effectiveness of 90% and beyond [242].

A further increase of the recuperator effectiveness would require a larger heat transfer area, resulting in equipment costs that might cancel any advantage due to fuel savings, and in a significant pressure drop through the recuperator, thereby reducing the net power production, and consequently increasing the micro turbine cost per kW_{el}. As a consequence, the design and optimization of recuperators is a challenge that must be a balance of performance and costs, as well as reliability and durability. Additional requirements for micro turbines recuperators have been identified by McDonald [179] and by Muley and Sundén [188].

A wide variety of efficient surface geometries can be considered for high-effectiveness recuperators, but the most representative types for micro turbines are the primary surface, plate-fin, and tubular geometries (Fig. 1.9). Details of the three kind of recuperators can be found in the work of McDonald [180]. The most common materials used for the recuperator of a micro turbine are Type 347 stainless steel for temperatures below 675°C, Type 347 super stainless steel for a temperature limit of 750°C, Inconel 625 for temperatures up to 800°C, and superalloys (e.g., Haynes 214 and 230) for temperatures up to 900°C [180].

Generator The design of high-speed generators that could spin at the same rotational speed of the turbomachinery components, eliminating thus the need for a reduction gearbox, has been a crucial milestone in the development of micro turbines. In single-shaft micro turbines, the high-speed generator is directly driven by the shaft, and can also serve

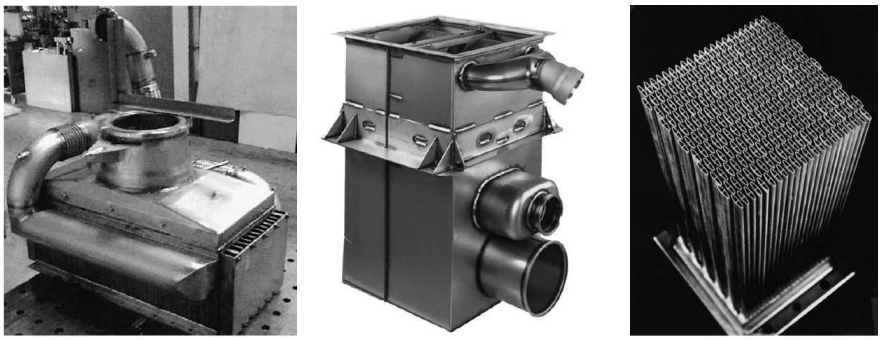

Figure 1.9: *Primary surface (left), plate-fin (center), and tubular (right) micro turbines recuperators [180].*

as a motor turning the shaft until sufficient rotational speed is reached to allow the compressor to supply enough air for self-sustaining combustion.

The generator design makes use of either permanent magnet alternators, which have an efficiency as high as 95%, or permanent magnet discs, which remove iron and eddy current losses, and whose efficiency levels can reach 98% [172]. Generators however require the conversion of the high-frequency alternate current (AC) output to 50 Hz or 60 Hz for general use. This involves rectifying the high-frequency AC to direct current (DC), then inverting the DC to 50 Hz AC or 60 Hz AC, and finally filtering to reduce harmonic distortion. These operations usually cause an efficiency penalty of the order of 5% [242].

Digital power controllers are generally mounted on single-shaft micro turbines to convert the high- frequency AC power into commercially viable electricity. Power electronics are therefore a critical component and represent significant design challenges, specifically in matching the micro turbine output to the required load. They are generally designed to handle seven times the nominal voltage, to allow for transients and voltage spike, and to generate three-phase electricity [242].

Furthermore, electronic components control all of the engine/generator operating and start-up functions. Micro turbines are generally equipped with controls that allow the unit to be operated either in parallel with or independent of the grid, and they incorporate many of the grid and system protection features required for interconnection. The controls usually also allow for remote monitoring and operation.

1.4.2 Major manufacturers

Micro turbines technology dates back to the 1950's, since they evolved from automotive turbochargers, small jet engines, and auxiliary power units for airplanes, and has developed rapidly during the last two decades for the electricity conversion. It finally became commercially available at the end of the 1990's [33, 159, 242, 264].

U.S. companies have exploited their experience from these fields from early on, and were the first to produce commercial products that were at the cutting edge of micro tur-

bines technology. The most important U.S. micro turbine manufacturers are nowadays Capstone Turbine Corporation, Elliott Energy Systems, and Ingersoll-Rand Energy Systems, while two other major developers are the European Bowman Power Systems and Turbec AB.

Capstone Turbine Corporation, founded in 1988, is the world's leading producer of low-emission micro turbine systems, and was the first to enter the market with commercially viable air bearings technology. Capstone micro turbines are manufactured in the range from 30 kW_{el} to 1 MW_{el}, and run on both gaseous and liquid fuels.

Elliott Energy Systems (EES) is now a fully-owned subsidiary of Ebara Corporation, Japan, and was established in 1993. The micro turbines produced by EES are in the range from 35 kW_{el} to 200 kW_{el}, and make use of high-speed oil-lubricated bearings, in contrast to the air bearings utilized by Capstone micro turbines.

Ingersoll-Rand (IR) Energy Systems is a division of the IR Company which commercializes its micro turbine since 2001, under the name PowerWorks. IR micro turbines have a power output equal to either 70 kW_{el} or 250 kW_{el}. The latter has been the largest micro turbine available, prior to the commercialization of the 1-MW_{el} micro turbine by Capstone. The main characteristic of the IR micro turbine is the two-shaft design, which offers a free turbine for multiple purposes and is expected to double the life expectancy of the product, as a consequence of the fact that the mechanical stress is shared between the two turbines. This design however increases costs and requires a starting mechanism, because the generator cannot start the micro turbine, as in single-shaft configurations. Furthermore, the micro turbine does not incorporate power electronics for transforming the power, but uses a reduction gearbox which converts the power to the grid frequency. At the beginning of 2011, IR Energy Systems was acquired by FlexEnergy.

Bowman Power Systems (BPS) is headquartered in the United Kingdom and was established in 1994, while its first units emerged in 1999. Initially, BPS produced micro cogeneration systems in three different sizes (45, 60, and 80 kW_{el}), but rather quickly it focused exclusively on the 80-kW_{el} model. BPS uses Elliott Energy Systems' engine for its micro turbines, and produces the power electronics itself. The main feature of BPS products is the integration of the heat recovery unit with the micro turbine package.

Turbec AB is a Swedish company which was founded in 1998 as a joint venture between Volvo Aero and ABB, which cooperated in the development of a micro turbine-based hybrid system for vehicles. At the end of the 1990's, Turbec AB redesigned the vehicle-based micro turbine into a more robust industrial product suited for stationary applications and serial production. The first commercial 100-kW_{el} unit was delivered in September 2000. Turbec micro turbines are only produced in this size and mostly runs on natural gas, although the company installed some units which run on waste and biomass gases, and show similarities to the Capstone and Elliott/Bowman systems, as they make use of the single-shaft design with a built-in recuperator. However, the package also incorporates the heat recovery unit, which was introduced in Capstone micro turbines only in 2003. Turbec AB has been acquired by the Italian company API Com s.r.l. at the end of 2003.

Table 1.3 provides the performance characteristics of commercial micro turbine CHP systems. They are the C30 of Capstone, the TA-100 of EES, the PowerWorks 70 of IR

Table 1.3: *Comparison of performance characteristics for commercial micro turbine cogeneration systems. Fuel input (P_f); electrical (P_{el}) and thermal (P_{th}) power output; overall (η_o), electrical (η_{el}), and thermal (η_{th}) efficiency; power-to-heat ratio (P_{el}/P_{th}); NO_x and CO emissions are compared for the C30 of Capstone, the TA-100 of EES, the PowerWorks 70 of IR Energy Systems, the TG80 of BPS, and the T100 of Turbec AB.*

	C30	TA-100	PowerWorks 70	TG80	T100
P_f [kW]	124	363	267	319	384
P_{el}^* [kW]	28	100	67	76	100
P_{th} [kW]	54	172	95	121	136
η_o [%]	66.1	74.9	60.7	63	61.5
η_{el} [%]	22.6	27.5	25.1	25	26.0
η_{th} [%]	43.5	47.4	35.5	38	35.4
P_{el}/P_{th}	0.52	0.58	0.71	0.63	0.74
NO_x [g/kWh]†	0.23	0.68	0.20	0.57	0.33
CO [g/kWh]†	0.63	0.66	0.12	0.69	0.20

*Net of parasitic and conversion losses.

†Levels guaranteed by the manufacturers.

Energy Systems, the TG80 of BPS, and the T100 of Turbec AB. The data show that the electrical efficiency generally increases as the micro turbine becomes larger, leading to a lower absolute quantity of the thermal energy available per unit of power output. Therefore, the power-to-heat ratio for the CHP system increases. In turn, this influences the economy of the micro turbine project, and may affect the decisions that customers would make in terms of CHP acceptance, sizing, and other characteristics. Furthermore, each micro turbine manufacturer listed in Table 1.3 uses a different type of recuperator, and each one has made individual trade-offs between costs and performance. The latter involves the extent to which the recuperator effectiveness increases cycle efficiency, the extent to which the recuperator pressure drop decreases cycle power, and the choice of what cycle pressure ratio to use. Consequently, the listed micro turbines have different overall efficiencies and different power-to-heat ratios. The values of NO_x and CO emissions reflect the levels guaranteed by the manufacturers.

Parallel to the development and commercialization of "large" micro turbines, research is being carried out to develop units with a very small power output ($\leq$10 kW_{el}), whose development involves major technological challenges related to so-called small-scale effects. Moreover, further engineering challenges are related to so-called small-scale effects. These are due to i) relatively high viscous losses because of low Reynolds numbers; ii) high relative tip clearance due to manufacturing tolerances; iii) high heat losses, because of the

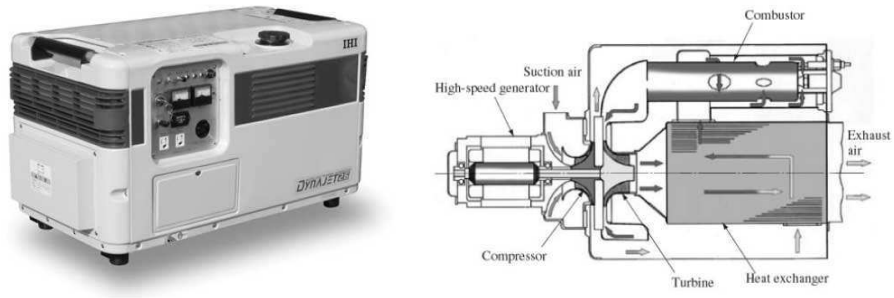

Figure 1.10: *A picture (left) and the layout (right) of the Dynajet 2.6 micro gas turbine [26].*

large area-to-volume ratios; iv) relative large size-independent losses, such as those from bearings and auxiliaries, given the low power output.

The Japanese Dynajet 2.6 produced by Nissan Motors Co., Ltd. was the first micro turbine in that range to enter the market of single households at the end of 2002 [165]. The Dynajet 2.6 (Fig. 1.10) is a single-shaft micro turbine, featuring compact and light-weight configuration, high-quality electricity, and low noise and vibrations. It has an electrical power output of 2.6 kW and a thermal efficiency of 12%. The compressor and turbine are based on Nissan automotive turbochargers, are mounted in a back-to-back layout, and can rotate up to 100,000 rpm. The high-speed generator is directly connected to the shaft on the compressor side and can be used as a motor in start-up applications, while a recuperator is utilized to increase the thermal efficiency and decrease the exhaust gases temperature. The electrical part consists of a constant-voltage/constant-frequency inverter, an engine controller, and a battery charger. The Nissan micro turbine can run both on kerosene and Diesel, and has half the size and weight of reciprocating engine generators with the same power output level. Furthermore, it emits respectively 1/7 and 1/60 of the NO_x and CO emissions of a reciprocating engine of the same class.

In the United States, a 3-kW_{el} micro gas turbine to be used as a portable power generator system has been developed by Barber-Nichols Inc. for military use [18]. The compact-size, low-weight unit operates on JP-8 fuel and relies on the Brayton cycle to generate 120/240 V AC. The compressor and turbine are commercial off-the-shelf (COTS) items that are mass-produced for automotive turbochargers, and the generator is a 2-pole, high-speed, permanent-magnet alternator. The recuperator is a commercial product that has been modified for this application, wherelse the combustor has been built in-house. The igniter, fuel pump, and controller are COTS components as well.

The Dutch company Micro Turbine Technology B.V. (MTT) is developing a recuperated micro gas turbine with electrical and thermal power output up to 3 and 14 kW, respectively [270]. The MTT micro turbine will be primarily applied in CHP units for domestic dwellings, but further conceptual studies have shown that it could also be used on long-distance trucks as an auxiliary power unit combined with the parking heater, and as a range extender mounted on electric vehicles.

In the μCHP application, the system pay-back time target is from 2 to 4 years depend-

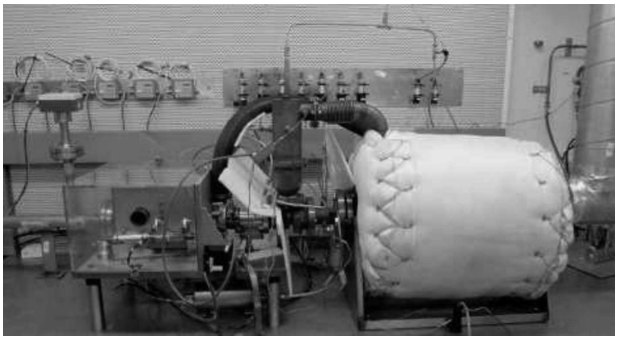

Figure 1.11: *The test-rig built for the recuperated micro gas turbine developed by Micro Turbine Technology B.V. [270].*

ing on the customers' profile, while CO_2 emissions savings are pojected to achieve six tons per year. Furthermore, although natural gas is the chosen fuel, a separated program has been started for the development of a combustor for liquid fuels.

The turbomachinery part of the MTT micro turbine consists of a COTS automotive turbocharger, made of a centrifugal compressor, a radial turbine, and oil-lubricated bearings. The single-can layout combustor and the fuel control system have been developed in-house, wherelse the stainless steel, primary surface recuperator has been specifically customized by a manufacturer. The high-speed, permanent-magnet generator is coupled to the turbocharger through a special coupling shaft. This rotor configuration allows thus the use of COTS components and shows an excellent thermal insulation of the generator, although the concept with two coupled rotors and two bearings sets exhibits some drawbacks with respect to mass production [270].

Figure 1.11 shows the test-rig built for the MTT recuperated microturbine. The inlet duct with the mass flow meter is located on the left, while the compressor inlet is placed at the right-hand side of the transparent plastic receiver-box. The vertical combustor is in the middle and connected to the turbine, while the insulated recuperator is located on the right. A first experimental campaign has been performed in the period 2008-2009, at the end of which electrical power and efficiency equal to 2.7 kW and 12.3%, respectively, were obtained at International Standard Atmosphere (ISA) conditions and 240,000 rpm [270]. At the end of 2010, an electrical efficiency of 16% has been achieved at ISA conditions with a new micro CHP demonstrator. A prototype has been built and extensively tested in 2011, while field tests have been planned at the end of 2012. The commercial launch is foreseen one year later.

1.5 Influence of the centrifugal compressor on the micro gas turbine performance

The use of single-shaft radial turbomachinery for micro turbines allows for simple designs, with satisfiying aerothermodynamic and economic constraints, thanks to the evolution that automotive turbochargers have experienced in the past seventy years. Furthermore, the introduction of advanced computational fluid dynamics (CFD) tools and of innovative materials in the recent years has led to a marked improvement in the current state-of-the-art technology of small turbochargers [218, 219].

However, according to McDonald [180], the efficiency levels of centrifugal compressors and radial turbines have almost "stalled" after years of development, while further improvements by means of CFD methodologies would likely to be only incremental. The author claims that combustion, mechanical, and generator efficiencies are already at high levels as well, such that he envisages the turbine inlet temperature and the recuperator effectiveness as the only two parameters having potential for increasing micro turbines efficiency.

Nevertheless, improvements in micro turbines performance through suitable modifications of turbocharger technology are to be expected, especially considering that turbochargers usually employ centrifugal compressors with vaneless diffusers in order to maximize the flow range and minimize production costs, wherelse gas turbines require higher efficiency and pressure ratio for a much narrower operating range.

As a consequence, a cycle study of the MTT recuperated micro gas turbine has been carried out in order to assess the impact of the centrifugal compressor performance on the system performance. A simplified model of the micro turbine has been developed with a tool for the thermodynamic analysis and optimization of systems for the production of electricity, heat, and refrigeration [259], coupled to a program which calculates the thermodynamic and transport properties for a large variety of fluids and fluid mixtures, using many modern physical models [260]. Figure 1.12 shows a simplified model of the micro gas turbine developed by MTT. Station 1 is the compressor inlet; station 2 is the compressor outlet/cold side recuperator inlet; station 3 is the cold side recuperator outlet/combustor inlet; station 4 is the combustor outlet/turbine inlet; station 5 is the turbine outlet/hot side recuperator inlet; station 6 is the hot side recuperator outlet/heat recovery unit inlet; station 7 is the heat recovery unit outlet.

The input data for modelling the components of the thermodynamic cycle have been taken from the work of Visser *et al.* [270], and two scenarios have been studied. In the reference scenario, the total-to-total pressure ratio (p_{02}/p_{01}) and the isentropic efficiency $(\eta_{c,is})$ of the centrifugal compressor are equal to 2.4 and 0.7, respectively. The compressor pressure ratio and efficiency, the turbine and mechanical efficiencies, the recuperator effectiveness, and the recuperator and combustor pressure losses have been assumed by the authors on the basis of manufacturers' specifications, literature, and engineering considerations. In the best-case scenario, the compressor pressure ratio and isentropic efficiency have been increased to 3.2 and 0.75, respectively. The other components as well perform better than what specified by the manufacturers. Table 1.4 summarizes the specifications

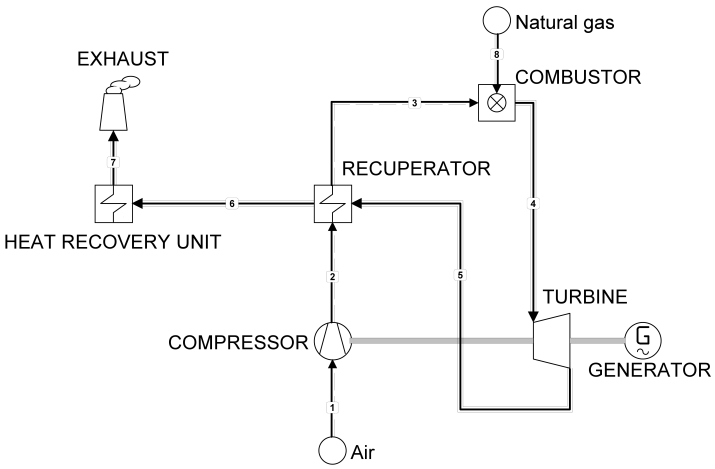

Figure 1.12: *A simplified model of the recuperated micro gas turbine developed by Micro Turbine Technology B.V.*

of the micro turbine components, for the two scenarios.

For each scenario, at first the thermodynamic cycle has been modelled at the design point, represented by the corresponding values given in Table 1.4. Afterwards, for each scenario further calculations have been carried out by varying the compressor isentropic efficiency from the design value, wherelse the specifications of all the other components, as well as the compressor pressure ratio, have been kept constant. All the calculations have been performed with an air mass flow rate equal to 45 g/s, while natural gas has been used as fuel. The generator, rectifier, and inverter losses have not been considered, such that the power output is the power delivered by the shaft. The shaft efficiency has been calculated as the ratio between the shaft power and the fuel input.

Figures 1.13a and 1.13b show the influence of the compressor isentropic efficiency on the MTT micro turbine shaft power (P_{sh}) and shaft efficiency (η_{sh}), for the two scenarios. In the reference scenario, at design point the micro turbine delivers 2.6 $\mathrm{kW_{el}}$ with a shaft efficiency equal to 15.5%. With increasing $\eta_{\mathrm{c,is}}$, P_{sh} increases, so does η_{sh}. The power available at the generator would be equal to 3.3 $\mathrm{kW_{el}}$ with an 80%-efficient compressor, with a consequent shaft efficiency equal to 19.5%. Therefore, in the reference scenario, P_{sh} and η_{sh} increase on average by 2.1% for every 1%-increase of $\eta_{\mathrm{c,is}}$.

In the best-case scenario, at design point the micro turbine delivers 4.96 $\mathrm{kW_{el}}$ with a shaft efficiency equal to 29.6%. Although this analysis is intended for assessing only the impact of the compressor performance on the micro turbine power and efficiency, Figs. 1.13a and 1.13b show how large is the influence of better components on the micro turbine performance, since in the best-case scenario P_{sh} and η_{sh} have almost doubled, in comparison with the values calculated for the reference scenario. However, in the best-case scenario $\eta_{\mathrm{c,is}}$ affects the micro turbine performance to a minor extent, as P_{sh} and η_{sh}

Table 1.4: *Components specifications for the cycle study of the recuperated micro gas turbine developed by Micro Turbine Technology B.V. p_{02}/p_{01} and $\eta_{c,is}$ are the compressor pressure ratio and isentropic efficiency; ξ_{a1} and ξ_{34} are the pressure losses trough the inlet pipe and combustor; T_{04} and $\eta_{t,is}$ are the turbine inlet temperature and isentropic efficiency; η_{mech} is the mechanical efficiency; η_{rec} is the recuperator effectiveness; ξ_{23} and ξ_{56} are the pressure losses through the recuperator cold and hot sides.*

	p_{02}/p_{01}	$\eta_{c,is}$	ξ_{a1} [%]	ξ_{34} [%]	T_{04} [K]	$\eta_{t,is}$	η_{mech}	η_{rec}	ξ_{23} [%]	ξ_{56} [%]
Reference	2.4	0.70	0.5	1	1300	0.65	0.97	0.8	1.5	3
Best	3.2	0.75	0.2	0.5	1350	0.70	0.98	0.9	1.5	3

increase on average by 1.4% for every 1%-increase of $\eta_{c,is}$.

Figure 1.13c illustrates the influence of the compressor total-to-total pressure ratio on the MTT micro turbine shaft efficiency. For each scenario, at first the thermodynamic cycle has been modelled at the design point, represented by the corresponding values given in Table 1.4. Afterwards, for each scenario further calculations have been carried out by varying the compressor pressure ratio from the design value, wherelse the specifications of all the other components, as well as the compressor isentropic efficiency, have been kept constant. As before, all the calculations have been performed with an air mass flow rate equal to 45 g/s, using natural gas as fuel, and by considering the power delivered by the shaft as the system power output. The shaft efficiency has thus been calculated as the ratio between the power output and the fuel input.

Firstly, by looking at Fig. 1.13c, it is possible to estimate the large influence of better components on the micro turbine performance, since in the best-case scenario the η_{sh}-values are about two times larger than those calculated for the reference scenario. Secondly, for both scenarios the trend of η_{sh} shows the existence of an optimum p_{02}/p_{01}, in correspondence of which η_{sh} is the highest. For both the reference and best-case scenarios, it occurs at a pressure ratio in the range 2.6-2.8. Therefore, for the reference scenario the optimum p_{02}/p_{01} is higher than that utilized for the previous calculations, wherelse for the best-case scenario it is lower.

In conclusion, increasing the performance of the current centrifugal compressor adopted for the MTT micro turbine is indeed pivotal in order to achieve higher performance levels of the μCHP system.

1.6 Motivation and scope

The performance of turbocharger centrifugal compressors are typically very well-known, thanks to the seven-decade-long technological development in the automotive field, and to the high-degree of reliability achieved by the current CFD methodologies. However, differences may be seen in the compressor flow field, and different compressor performance may be required, if turbochargers are employed in applications other than in

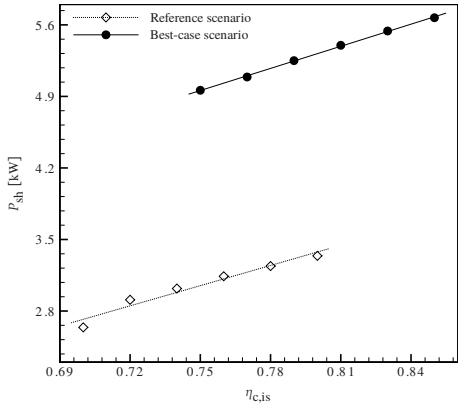

(a) *Compressor total-to-total isentropic efficiency versus shaft power at constant micro turbine inlet conditions; compressor total-to-total pressure ratio; turbine isentropic efficiency and inlet temperature; recuperator effectiveness.*

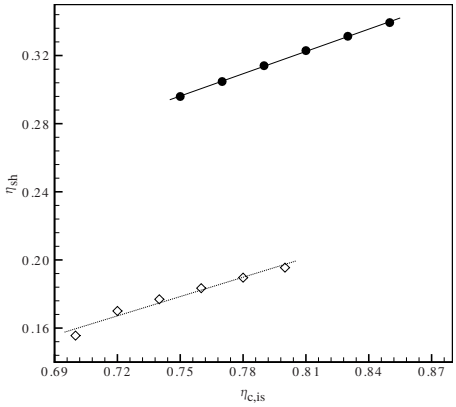

(b) *Compressor total-to-total isentropic efficiency versus shaft efficiency at constant micro turbine inlet conditions; compressor total-to-total pressure ratio; turbine isentropic efficiency and inlet temperature; recuperator effectiveness.*

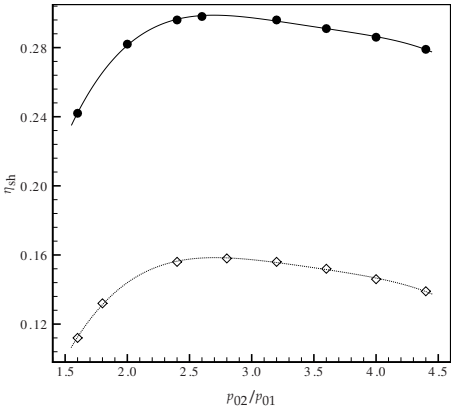

(c) *Compressor total-to-total pressure ratio versus shaft efficiency at constant micro turbine inlet conditions; compressor total-to-total isentropic efficiency; turbine isentropic efficiency and inlet temperature; recuperator effectiveness.*

Figure 1.13: *The influence of the compressor total-to-total isentropic efficiency and pressure ratio on the performance of the recuperated micro gas turbine developed by Micro Turbine Technology B.V.*

vehicle engines.

This is the case of the centrifugal compressor studied in this work, since it is part of an automotive turbocharger which has been utilized in a micro gas turbine for micro cogeneration applications. As a consequence, the objectives of this work are

1. To provide a better understanding of the compressor flow structure and loss mechanisms, through the use of novel methodologies which allow identifying those aspects whose improvement can lead to higher compressor performance.

2. To analyze and quantify the influence of the tip clearance on the compressor performance and flow properties, since the unshrouded impellers used in automotive turbochargers suffer from efficiency decrements, because of the pressure losses and secondary flows caused by very large clearance gaps.

3. To design and build a test-rig for the automatic acquisition of the performance maps of very small centrifugal compressors, and for testing either future, new configurations which aim to improve the performance of the current micro turbine compressor, or other very small centrifugal compressors.

4. To improve the compressor performance through the development of an original optimization methodology, which allows investigating the use of vaned diffusers, since they are claimed to exhibit higher static pressure recovery and efficiency than vaneless ones, at the expenses of a narrower operating range.

1.7 Thesis outline

This dissertation is structured as follows. **Chapter 2** presents a new one-dimensional methodology which predicts the design and off-design performance of very small single-stage centrifugal compressors, which operate with fluids obeying to the ideal gas law, by combinining a thorough analysis of the two-zone model to a set of empirical loss correlations, which are integrated in the secondary zone. This approach sequentially evaluates the flow properties in the impeller, vaneless diffuser, and volute. In particular, it allows estimating the source of the impeller losses and the impeller two-zone flow features, representing thus an alternative to the models available in the literature. The numerical results computed by this tool have been validated against the data collected throughout an experimental campaign, as described in Chap. 3, and allowed the acquisition of further knowledge about the centrifugal compressor performance and losses.

Chapter 3 describes the test-rig which has been designed and built for the automatic acquisition of the performance maps of very small centrifugal compressors, and used to characterize the compressor of the micro gas turbine investigated in this dissertation. In the future, the test-rig will also be employed for testing optimized components of the compressor stage. Furthemore, the uncertainty propagation analysis has also been carried out, in order to assess the potential error sources and their effects on the test data. The main elements of the uncertainty propagation analysis are also described here.

Chapter 4 presents the numerical study performed with a commercial CFD code which solves the three-dimensional (3D) Reynolds averaged Navier-Stokes (RANS) equations. Steady-state simulations have been carried to approximate the real, time-dependent flow physics with satisfactory results and shorter computational time with respect to an unsteady approach. The results of the CFD computations have been validated against the

experimental data described in Chap. 3, and allowed to understand the tip clearance influence on the compressor flow field and performance, and to acquire further knowledge about the compressor flow structure and loss mechanisms.

Chapter 5 illustrates the influence of the diffuser on the compressor stage performance. An overview of the flow phenomena which occur at the impeller outlet, and therefore affect the flow field in the downstream diffuser, is firstly given. A brief description of the two main categories of diffusers (i.e., vaneless and vaned) follows. Finally, the most important design parameters of a vaned diffuser are highlighted.

Chapter 6 shows the optimization of vaned diffusers. A genetic algorithm has been firstly coupled to a in-house CFD code which solves the two-dimensional Euler equations, and secondly to a commercial code which solves the 3D RANS equations. In the latter case, a metamodel has been used to reduce the computational costs. The position of the vanes between the diffuser inlet and outlet, their inclination with respect to the radial direction at the leading and trailing edges, the diffuser vane number, and the diffuser outlet radius have been selected as design variables. The maximization of the static pressure recovery and the minimization of the total pressure losses have been chosen as objective functions.

Chapter 7 draws the conclusions regarding the current work, while recommendations are suggested for future research activities.

"All models are wrong, but some models are useful."

George E. P. Box.

2

One-dimensional performance analysis

This chapter presents a new one-dimensional methodology which predicts the design and off-design performance of very small single-stage centrifugal compressors, which operate with fluids obeying to the ideal gas law, by combinining a thorough analysis of the two-zone model to a set of empirical loss correlations, which are integrated in the secondary zone. This approach sequentially evaluates the flow properties in the impeller, vaneless diffuser, and volute. In particular, it allows estimating the source of the impeller losses and the impeller two-zone flow features, representing thus an alternative to the models available in the literature.

Excerpts of this chapter appeared in:

Javed A., Yang S.-Y., Olivero M., Pecnik R., and van Buijtenen J. P., 2011, "Performance Evaluation of a Microturbine Centrifugal Compressor Using a Novel Approach," *Proc. International Gas Turbine Congress 2011*, IGTC2011-0144.

Javed A., Olivero M., Pecnik R., and van Buijtenen J. P., 2011, "Performance Analysis of a Microturbine Centrifugal Compressor From a Manufacturing Perspective," *Proc. ASME Turbo Expo 2011*, GT2011-46374.

2.1 Introduction

Three-dimensional (3D) computational fluid dynamics (CFD) codes are nowadays commonly used to analyze in great detail the flow through a centrifugal compressor stage. As a result of the growth and sophistication of CFD techniques, it may be imagined that the need for one-dimensional (1D) performance prediction methods has been largely superseded. However, although over the last decade the role of 1D techniques has clearly changed, from being a major design tool to a support role for more sophisticated techniques, in the foreseeable future those methodologies are still expected to have a definite presence in centrifugal compressors design.

Such methods generally require the use of empirical data and correlations, which allow the inadequate fluid definition to better agree with the real phenomena. These methodologies are then only as good as the experimental data they rely upon, therefore it is inevitable that the families of compressors from which the data have been obtained will be better predicted, especially when limited geometric data have been used to establish the empirical correlations.

As a consequence, the idea behind the development of any 1D model is to provide compressors performace maps which can be used in the preliminary design phase with a minimum amount of input information. This chapter thus presents a 1D performance analysis code for radial compressors (PARC-1), which allows estimating the design and off-design performance of very small single-stage centrifugal compressors operated with fluids obeying to the ideal gas law. This tool predicts the compressor performance (i.e., stage total-to-total pressure ratio and isentropic efficiency; impeller inlet and outlet velocity triangles; impeller internal, external, and mixing losses; vaneless diffuser losses; volute losses) on the basis of its geometry and operating conditions, and relies on the "level-three approach" [136], which makes use of a comprehensive set of models to represent the internal flow physics, and to predict the flow conditions at the stage outlet.

The main components of the compressor stage (i.e., the rotating impeller, the stationary vaneless diffuser, and the stationary volute) are modeled separately. They are shown in Fig. 2.1. In particular, by considering the impeller as divided into an inducer, where the fluid approaches the impeller blades, and an exducer, where the impeller blades transfer the energy to the fluid before it flows to the downstream component, different approaches to model the latter are available. Two of the most utilized methods are the single- and two-zone techniques, wherelse the new model introduced here combines the advantages of the two well-known approaches, since it predicts the impeller entropy generation through the losses models used in the single-zone methodology, while maintaining the features of the two-zone method.

In the following, firstly the main components and operating principles of a centrifugal compressor stage are described. Secondly, the two methodologies for impellers analysis available in the literature are briefly introduced, alongside with the vaneless diffuser and volute models. The description of the PARC-1 approach follows. Finally, the performance and losses of the centrifugal compressor adopted for the micro turbine developed by Micro Turbine Technology B.V. (MTT) are assessed by means of the three 1D methods.

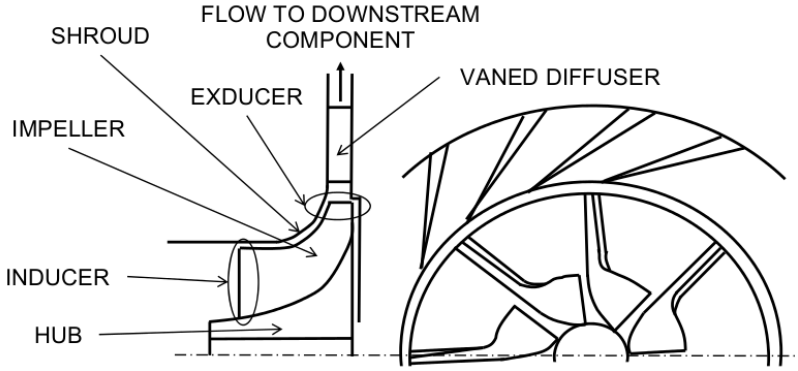

Figure 2.1: *Meridional (left) and front (right) views of a centrifugal compressor.*

2.2 The centrifugal compressor

Stage components Figure 2.1 shows the schematic of a single-stage centrifugal compressor. The stage consists of a rotating impeller which energizes the fluid, a stationary vaned diffuser to recover some of the fluid kinetic energy, and a stationary volute to collect the fluid and deliver it further downstream. Throughout this dissertation, the impeller inlet and outlet are referred to as stations 1 and 2, respectively. For vaned diffusers, station 3 is located at the vane leading edge, while station 4 represents the vane trailing edge. The diffuser outlet is placed at station 5. In a vaneless diffuser, stations 3 and 4 are not used. Station 6 is the plane in the volute where all the flow is collected, whereas stations 7 and 8 represent the volute throat and outlet, respectively.

Flow path The flow usually approaches the impeller through an inlet duct in the axial direction, unless prewhirl has been used to impose a non-zero tangential velocity. One of the functions of the impeller is to create under-pressure at the inducer, so that the flow proceeds through the inlet duct and then enters the impeller.

Figure 2.2a shows the impeller inlet velocity triangle. The flow is being conveyed to the inducer at the meridional velocity C_{m1}, and encounters the impeller rotating at the blade speed U_1. If no prewhirl is applied, the absolute flow angle α_1 and the tangential velocity C_{u1} are zero. The relative velocity W_1 and flow angle β_1 are then determined by the meridional component of the absolute velocity and the local blade speed. When β_1 is equal to the blade angle β_{b1}, the flow approaches the blades "dead-on". Under many operating conditions, however, β_1 will differ from β_{b1}, such that the blades will be subject to the angle of incidence

$$i = \beta_{b1} - \beta_1. \tag{2.1}$$

Afterwards, the flow enters the rotating impeller, is propelled through it, and is continuously energized while passing through the bladed passages. When the impeller bends

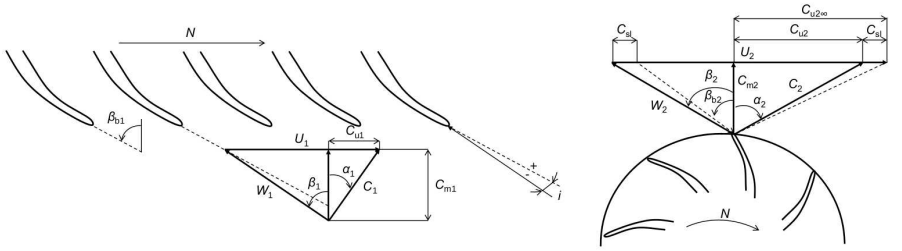

(a) *Inlet.* **(b)** *Outlet.*

Figure 2.2: *Impeller velocity triangles. C and W are the absolute and relative flow velocities, while* C_m *and* C_u *are the tangential and meridional components of the absolute velocity.* α *and* β *are the absolute and relative flow angles , while* β_b *is the blade angle. U is the blade speed, while the rotational speed N indicates the direction of rotation. At the inlet, i is the incidence angle. At the outlet,* C_{sl} *is the slip velocity, while* $C_{u2\infty}$ *is the tangential component of absolute velocity for* $C_{sl} = 0$.

from the axial to the radial direction, very complex forces come to act on the fluid, generating a complicated flow field in the passages. At the impeller outlet, in the relative frame of reference, the flow leaves the rotating impeller almost according to the blade angle. In the absolute frame of reference, the fluid flows in the tangential direction, due to the very large tangential component of absolute velocity, as a consequence of the impeller rotation. Therefore, it is fundamental that great care is taken to diffuse this high-velocity flow as efficiently as possible, in order to achieve the maximum static pressure rise. Finally, on leaving the stage, the flow is collected and delivered to the downstream components by means of a volute.

Figure 2.2b shows the impeller outlet velocity triangle. The meridional velocity C_{m2} is dictated by the conservation of mass equation, while the absolute velocity C_2 and flow angle α_2 result from the relative flow angle β_2 and the blade speed U_2. Under ideal conditions, the relative flow angle would precisely follow the blades, thus it would be equal to the blade angle β_{b2} (i.e., the backsweep angle). In practice, the two angles differ by an appreciable amount, which is quantified through the slip velocity

$$C_{sl} = C_{u2\infty} - C_{u2}, \tag{2.2}$$

where $C_{u2\infty}$ is the tangential component of absolute velocity which would exist if the flow exactly followed the blades. A slip factor is usually derived as

$$\sigma = 1 - \frac{C_{sl}}{U_2} = 1 - \frac{C_{u2\infty} - C_{u2}}{U_2}, \tag{2.3}$$

such that the slip reduces the magnitude of the tangential component of the absolute velocity from that attainable in the ideal case

$$C_{u2} = \sigma U_2 + C_{m2} \tan \beta_{b2}. \tag{2.4}$$

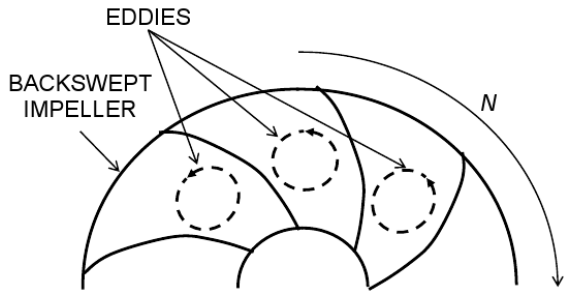

Figure 2.3: *The concept of relative eddy in a backswept centrifugal impeller. The rotational speed N indicates the direction of rotation.*

From a physical point of view, the slip factor can be understood by means of the so-called concept of relative eddy (Fig. 2.3), which is an inviscid flow effect. According to this theory, a fluid element entering the impeller does not rotate around its own axis with an angular velocity equal to that of the impeller, but moves around the compressor axis while maintaining a constant orientation relative to the stationary shroud. However, in the relative frame of reference, the fluid element rotates at an angular velocity equal in magnitude to that of the impeller, but opposite in direction. The relative vorticity of the flow entering the impeller will thus set up a recirculating flow pattern relative to the impeller itself and affect the primary flow by causing underturning across the impeller outlet plane. Several correlations have been used to calculate the slip factor [29, 205, 252, 256], but in this work the empirical expression introduced by Wiesner [277] has been used

$$\sigma = 1 - \frac{\sqrt{\cos \beta_{b2}}}{Z_I^{0.7}}, \tag{2.5}$$

where Z_I is the impeller blade number.

Performance A centrifugal compressor performance is usually given by means of maps in which the stage total-to-total pressure ratio (π_{tt}) and isentropic efficiency ($\eta_{tt,is}$) are plotted as a function of the corrected mass flow rate and rotational speed, which are respectively defined as

$$\dot{m}_{corr} = \frac{\dot{m}\sqrt{\dfrac{T_{01}}{T_{ref}}}}{\dfrac{p_{01}}{p_{ref}}}, \tag{2.6}$$

$$N_{corr} = \frac{N}{\sqrt{\dfrac{T_{01}}{T_{ref}}}}, \tag{2.7}$$

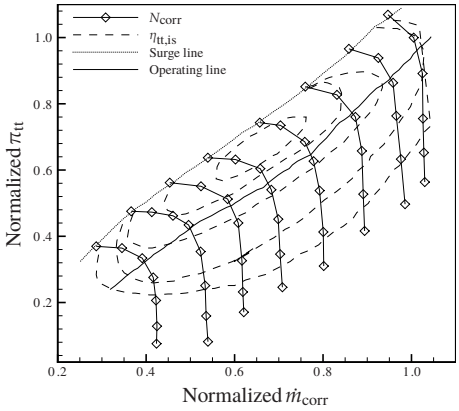

Figure 2.4: *An illustrative performance map of a centrifugal compressor.* π_{tt} *is the stage total-to-total pressure ratio,* $\dot{m}_{corr}$ *is the corrected mass flow rate,* N_{corr} *is the corrected rotational speed, and* $\eta_{tt,is}$ *is the stage total-to-total isentropic efficiency.*

where T_{ref} =288.15 K and p_{ref} =101,325 Pa. The stage total-to-total pressure ratio and isentropic efficiency are respectively defined as

$$\pi_{tt} = \frac{p_{08}}{p_{01}}, \tag{2.8}$$

$$\eta_{tt,is} = \frac{\left(\frac{p_{08}}{p_{01}}\right)^{\frac{\gamma-1}{\gamma}} - 1}{\frac{T_{08}}{T_{01}} - 1}. \tag{2.9}$$

Figure 2.4 shows a generic compressor performance map. On the one hand, as the mass flow rate through the compressor is reduced, at constant rotational speed, the pressure ratio increases until the surge margin is reached. Surge or stall is an extremley unstable operating region where the flow pulsates violently through the compressor stage and represents the stability limit to the lowest mass flow rate that the compressor can accomodate. On the other hand, the highest values of mass flow rate are limited by choking, which is a thermodynamic limit to compressible flow occurring when the local velocity is equal to the speed of sound. This means that no further increase of the mass flow rate is possible, neither by decreasing the back pressure nor by increasing the rotational speed.

2.3 The impeller model

2.3.1 The inducer

The impeller analysis begins with the estimation of the flow properties at the inducer, which increases the angular momentum of the fluid without increasing the radius. By considering total atmospheric flow conditions at the impeller inlet, the flow properties across the inducer can be established for any operating condition through an iterative procedure which proceeds until the value of the inlet relative Mach number has reached convergence. Afterwards, the impeller inlet velocity triangles are determined at hub, mid-span, and shroud.

A blockage factor equal to 2% and an axial velocity ratio parameter equal to 1.02 in the case of axial inlet have been used [136], while span-averaged incidence losses has been determined using the correlation given by Oh *et al.* [193].

2.3.2 The exducer

Subsequently, the flow properties at the impeller outlet can be estimated by either the single-zone or the two-zone models.

The single-zone model This method, also known as meanline method, is still the most practical approach for the design and performance analysis of centrifugal compressors. It consists of 1D equations for fluids which obey to the ideal gas law, empirical flow models, and loss correlations; assumes that there is no flow separation across the impeller; makes use of the impeller efficiency, slip factor, and governing equations to evaluate the flow properties and compressor performance [134, 135]. However, both the strength and weakness of such method lie in the empirical correlations used to calculate the efficiency and slip factor. As a consequence, a considerable amount of work has been done to derive such correlations using hundreds of test cases and experimental data [12, 166, 275, 276].

The single-zone model developed for the current study uses the set of loss correlations introduced by Oh *et al.* [193], and is primarily based on the theory provided by Whitfield and Baines [275]. The analysis begins by assuming the passage flow to be isentropic, and an iterative procedure is then applied to calculate the impeller outlet relative Mach number $(M_{2\text{rel}})$ using the non-dimensional mass flow equation

$$\frac{\dot{m}\sqrt{RT_{01\text{rel}}/\gamma}}{A_2 p_{01\text{rel}}} = s^* \cos\beta_2 M_{2\text{rel}} \left(1 + \frac{\gamma-1}{2} M_{2\text{rel}}^2\right)^{-\frac{\gamma+1}{2\gamma-2}} \left(1 + \frac{U_2^2 - U_1^2}{2c_p T_{01\text{rel}}}\right)^{\frac{\gamma+1}{2\gamma-2}}, \qquad (2.10)$$

where $\dot{m}$ is the mass flow rate; R is the specific gas constant; γ is the ratio of specific heat capacities; $p_{01\text{rel}}$ and $T_{01\text{rel}}$ are the impeller inlet relative total pressure and temperature; A_2 and β_2 are the impeller outlet area and relative flow angle; s^* is the impeller entropy gain; U_1 and U_2 are the impeller inlet and outlet blade speeds; c_p is the specific heat capacity at constant pressure. Equation 2.10 combines the continuity, energy, and entropy equations, and is solved by means of additional sub-models necessary to calculate A_2, β_2, and s^*.

Once $M_{2\text{rel}}$ has been calculated, the computation of the other flow properties follows, but an additional iteration is performed to determine the slip factor. Subsequently, the impeller entropy gain is computed by considering the impeller internal losses (i.e., blade loading, skin friction, clearance, and mixing losses), and the impeller outlet relative total temperature ($T_{02\text{rel}}$)

$$s^* = \exp^{-\Delta s/R} = \left[1 - \left(\frac{\gamma - 1}{\gamma R}\right) \frac{\sum \Delta h_{\text{int}}}{T_{02\text{rel}}}\right]^{\frac{\gamma}{\gamma-1}}, \tag{2.11}$$

where Δs is the entropy change of the actual process, and $\sum \Delta h_{\text{int}}$ is the summation of the impeller internal losses. Furthermore, the impeller enthalpy gain calculation involves the external losses (i.e., disc friction, recirculation, and leakage losses), which give rise to an increase in the impeller outlet total enthalpy without any corresponding increase in pressure [275].

Finally, the impeller total-to-total pressure ratio and isentropic efficiency are calculated as

$$\pi_{\text{tt}} = \left[\frac{\Delta h_{\text{eul}} - (\sum \Delta h_{\text{int}} + \Delta h_{\text{D}} + \Delta h_{\text{V}})}{c_p T_{01}} + 1\right]^{\frac{\gamma}{\gamma-1}}, \tag{2.12}$$

$$\eta_{\text{tt,is}} = \frac{\Delta h_{\text{eul}} - (\sum \Delta h_{\text{int}} + \Delta h_{\text{D}} + \Delta h_{\text{V}})}{\Delta h_{\text{eul}} + \sum \Delta h_{\text{ext}}}, \tag{2.13}$$

where Δh_{eul} is the total enthalpy rise calculated by means of the turbomachinery Euler equation; Δh_{D} and Δh_{V} are the vaneless diffuser and volute losses; T_{01} is the impeller inlet total temperature; $\sum \Delta h_{\text{ext}}$ is the summation of all the external losses.

The two-zone model The fluid dynamics of centrifugal compressors is one of the most complicated arrays of flow processes routinely encountered in engineering. At subsequent impeller locations, the boundary layers and the core flow are influenced by the Coriolis force, which is a very strong cross-passage force selective according to the velocity, and acts as a pseudo-centrifuge to separate the high- and low-velocity fluid elements. Hence, a low-momentum, secondary flow develops around the core and gathers near the shroud/suction side corner, wherelse the high-momentum, primary flow constitutes the rest of the flow field. The flow field at the impeller outlet is thus very complex, 3D, and turbulent, because of the blades curvature and the rotation.

Although the meanline method is still the most practical approach for predicting compressors performance [12], it lacks the capability of predicting the performance of separated flows, and considerably relies upon experimental data due to the extensive use of empirical flow models and loss correlations. On the contrary, the two-zone model assumes a portion of the fluid to pass through the secondary flow, carrying the losses, and the rest to be the isentropic primary zone. This methodology does not require any correlation based on experimental data to calculate the impeller losses, and proper mixing calculations are performed at the impeller outlet to estimate the mixed-out state flow properties.

The two-zone model is then a fine and reliable alternative to the single-zone technique.

It applies to fluids obeying to the ideal gas law, and consists of diffusion ratio calculations, primary and secondary flow calculations, and mixed-out state calculations.

The diffusion ratio is defined as

$$DR = \frac{W_1}{W_{2p}}, \tag{2.14}$$

and connects the impeller inlet flow conditions, represented by the relative velocity W_1, to the impeller outlet primary flow conditions, represented by the relative velocity W_{2p}. The amount of diffusion in the impeller passage has been estimated by means of the two-element in series model [136]. According to this model, the impeller passage is considered to be made of an inlet portion (element "a") and a rotating, diffusing passage (element "b"), for which the effectiveness values η_a and η_b have been specified equal to 0.4 and 0.3, respectively [136]. The effectiveness is defined as the ratio of the ideal to the actual pressure recovery coefficients, where the former is computed from the known impeller geometry and inducer flow conditions, such that the latter yields as a consequence. Due to their definitions, the ideal pressure recovery coefficient of element "b" is constant over the whole range of flow conditions, while the ideal pressure recovery coefficient of element "a" varies with the incidence angle.

Once the diffusion through the impeller passage has been calculated, the primary and secondary flows properties have to be estimated. To do so, the division of the mass and passage area between the primary and secondary flow zones, like two separate streamtubes extending from inlet to outlet, has to be established. This is done by means of the secondary flow mass fraction (χ) and the secondary flow area fraction (ε), which are defined as

$$\chi = \frac{\dot{m}_s}{\dot{m}}, \tag{2.15}$$

$$\varepsilon = \frac{A_s}{A_2}, \tag{2.16}$$

where $\dot{m}_s$ is the secondary flow mass flow rate, $\dot{m}$ is the overall mass flow rate, and A_s is the area occupied by the secondary flow. Many researchers often used a constant value for χ, which varied from 0.25 to 0.35 for small impellers [136], but further relationships can be seen in Fig. 2.5, which shows simple data-driven physical models representing the variation of χ and ε at different operating conditions, for three large and nine small impellers. In this work, the correlation given for the CETI impellers

$$\chi = 0.5\varepsilon^2 + 0.05\varepsilon, \tag{2.17}$$

has been initially considered, but it led to unsatisfactory results, because χ and ε were overpredicted, resulting in increased impeller losses and considerably lower efficiencies. This is due to the fact that the impeller investigated in this dissertation is 35% smaller than the smallest CETI impeller. As a consequence, the following new relationship has been derived through CFD investigations [140] to substitute Eq. 2.17

$$\chi = 0.282\varepsilon^2 + 0.0489\varepsilon. \tag{2.18}$$

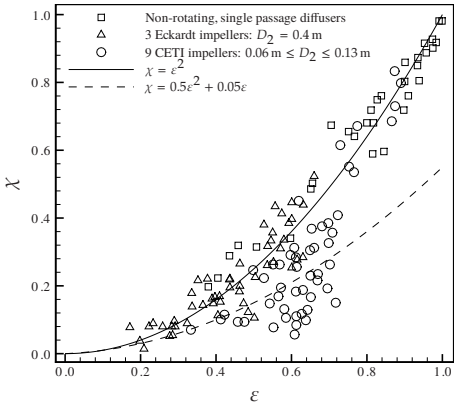

Figure 2.5: *Secondary flow mass fraction* (χ) *and secondary flow area fraction* (ε) *for different centrifugal impellers. Data taken from Ref. [136].*

Subsequently, the outlet flow conditions of the primary zone have been calculated based on work of Oh *et al.* [194], and on the jet-wake model introduced by Japikse [135, 136]. This part of the impeller model does not contain any iterative procedure, while the secondary flow properties have been calculated by means of successive iterations, which begin with the estimation of the secondary flow relative Mach number at the impeller oulet $(M_{2\text{rel,s}})$. The secondary flow is modelled assuming that

1. the fluid is perfectly guided by the blades,
2. the primary and secondary flow static pressures are equal to each other (i.e., unloaded tip condition), and
3. the front cover friction is negligible.

However, Rohne and Banzhaf [221] revealed that the first assumption is not correct, and introduced the tangential velocity factor

$$F_{\text{u,s}} = \frac{C_{\text{u2s}}}{C_{\text{u2p}}}, \tag{2.19}$$

where C_{u2p} and C_{u2s} are the tangential velocities of the primary and secondary flows, respectively. The authors found $F_{\text{u,s}}$ to be in the range 0.81-0.99, and specifically in the range 0.92-0.94. Following their measurements of unshrouded centrifugal impeller with backswept blades, a value equal to 0.93 has been used here.

The second and third assumptions provide the means to calculate the impeller entropy gain of the secondary flow

$$s^* = \exp^{-\Delta s/R} = \left[\frac{T_{2\text{p}}}{T_{02\text{rel,s}}}\left(1 + \frac{\gamma - 1}{2} M^2_{2\text{rel,s}}\right)\right]^{\frac{\gamma}{\gamma-1}}, \tag{2.20}$$

where T_{2p} is the impeller outlet static temperature of the primary flow , and $T_{02rel,s}$ is the impeller outlet relative total temperature of the secondary flow. In order to establish the secondary zone fluid properties at the impeller outlet, Eq. 2.20 is solved simultaneously with the non-dimensional mass flow equation given by Eq. 2.10, where the impeller outlet area, relative flow angle, and relative Mach number have been substitued with those relative to the secondary flow. When convergence is reached, the secondary flow properties and velocity triangle at the impeller outlet can be finally computed.

Subsequently, the primary and secondary zones are assumed to undergo rapid mixing. The mixed-out state is an effective state which allows establishing the thermodynamic state point of the flow leaving the impeller, on a mass-averaged basis. The mixing of the isentropic and non-isentropic flows leads thus to a static pressure rise and a total pressure drop, and the mixing losses have been calculated in terms of enthalpy change as the difference between the mass-averaged total properties at the impeller outlet and those at the mixing station. An iterative process has been carried out to calculate the mixed-out zone outlet properties, until convergence is reached for the energy equation

$$T_{02mix} = (1-\chi)\, T_{02p} + \chi T_{02s} + \frac{\gamma - 1}{\gamma R}\left(\dot{W}_{df} + \dot{W}_{rec} + \dot{W}_{leak}\right), \tag{2.21}$$

where T_{02mix}, T_{02p}, and T_{02s} are the impeller outlet total temperature of the mixed-out, primary, and secondary flows, while $\dot{W}_{df}$, $\dot{W}_{rec}$, and $\dot{W}_{leak}$ are the disk friction, recirculation, and leakage losses, expressed as specific enthalpy change.

2.4 The vaneless diffuser model

The vaneless diffuser has been analyzed by means of detailed 1D flow equations for vaneless diffusers given by Stanitz [251]. They represent a model to analyze compressible flows, considering also wall friction effects and area changes. The effects of the mixing losses due to non-uniform flow conditions at the impeller outlet/diffuser inlet and the heat transfer are not considered. The variations of the fluid properties are determined as a function of the radius for a prescribed variation of the diffuser height, by a succession of states through the vaneless diffuser.

Figure 2.6 shows the coordinates system for a point on the mean surface of revolution generated about the rotation axis by the centerline between the shroud and hub diffuser walls. The cylindrical coordinates r, θ, and x give the radial, tangential, and axial positions of the point, respectively. The diffuser effective height b (Fig. 2.6b) measured across the passage in the normal direction is function of the radius only, and is equal to the diffuser geometric height minus the boundary layer displacement thickness on the diffuser walls. The use of b is required by continuity considerations in order to calculate the proper velocity component normal to the cross-sectional flow area of the vaneless diffuser. As a consequence, no investigation of the boundary layer thickness in the vaneless diffuser has been performed.

A fluid particle on the mean surface of revolution is shown in Fig. 2.6a. It has the dimensions $rd\theta$ and $dr/\sin(\phi)$ on the surface of revolution, while the height is equal to b

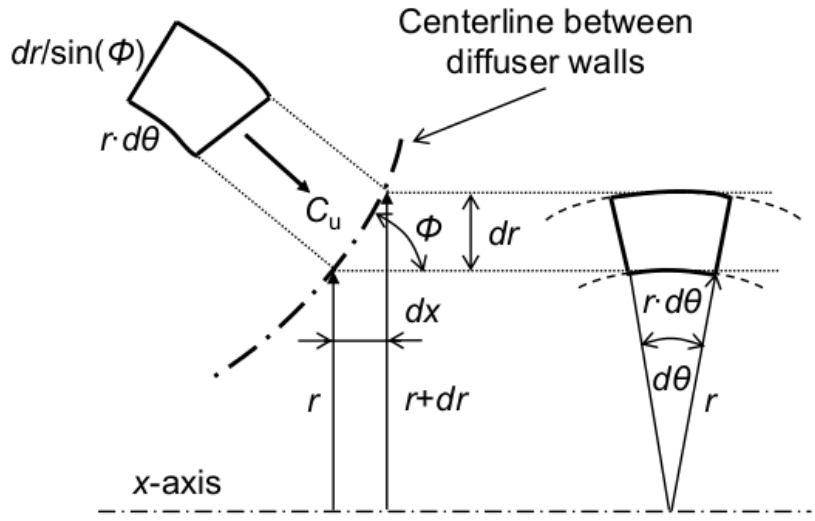

(a) *A fluid particle on the surface of revolution generated by the centerline between the diffuser walls. It has the dimensions* $rd\theta$ *and* $dr/\sin(\phi)$*, and flows with tangential velocity* C_u*.* ϕ *represents the diffuser inclination.*

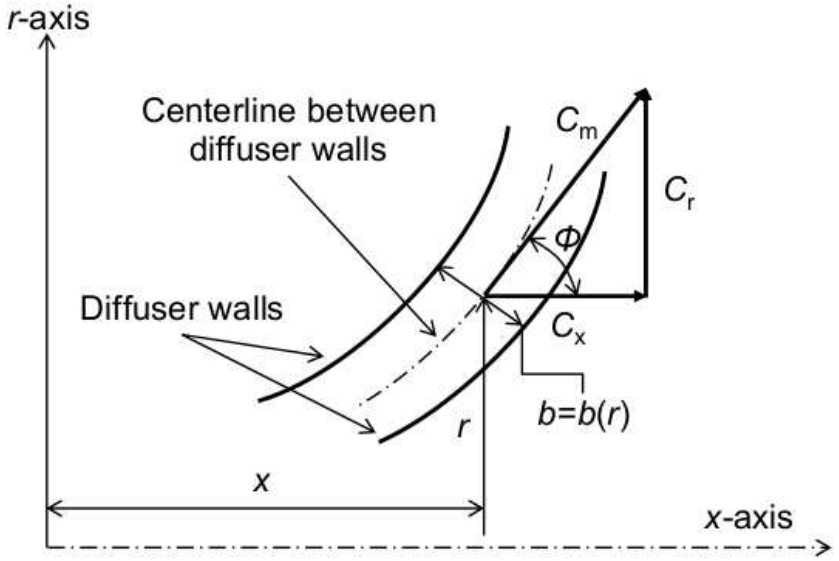

(b) *Diffuser profile, velocity components, and coordinates in the meridional plane.* C_m*,* C_r*, and* C_x *are the meridional, radial, and axial components of the absolute velocity.* b *is the diffuser effective height, while* ϕ *represents the diffuser inclination.*

Figure 2.6: *The coordinates system for the one-dimensional model for the vaneless diffuser.*

on a plane normal to that surface. The slope of the centerline between the shroud and hub diffuser walls (i.e., the diffuser inclination) is represented by the angle ϕ

$$\phi = \arctan \frac{dr}{dx} = \phi(r). \tag{2.22}$$

For the vaneless diffuser mounted on the centrifugal compressor investigated here, ϕ is equal to 90°.

The motion on the mean surface of revolution is assumed to be steady and, since the flow conditions are assumed to be uniform along b and θ, mixing losses resulting from non-uniform flow conditions in the tangential direction at the impeller outlet can be neglected. Since experiments [28] indicate that these losses take place in the immediate vicinity of the impeller outlet, they can be neglected in the rest of the vaneless diffuser.

Finally, the velocity C of a point on the mean surface of revolution is tangent to the surface and has component C_r, C_u, and C_x in the r-, θ-, and x-direction, respectively. In this analysis, however, it is more convenient to consider the meridional velocity C_m, which is tangent to the centerline between the diffuser walls in the meridional plane, and is defined as

$$C_m = \sqrt{C_r^2 + C_x^2}. \tag{2.23}$$

From Eq. 2.23, the flow angle on the mean surface of revolution is defined as

$$\alpha = \arctan \frac{C_u}{C_m}. \tag{2.24}$$

The fluid state at any radius on the mean surface of revolution is then described by the thermodynamic properties, the fluid velocity, and the flow direction, which are calculated by solving the following equations:

- Radial momentum equation

$$\frac{1}{\rho}\frac{dp}{dr} + C_m \frac{dC_m}{dr} - \frac{C_u^2}{r} + c_f \frac{C^2 \cos\alpha}{b \sin\phi} = 0. \tag{2.25}$$

- Tangential momentum equation

$$C_m \frac{dC_u}{dr} + \frac{C_m C_u}{r} + c_f \frac{C^2 \sin\alpha}{b \sin\phi} = 0. \tag{2.26}$$

- Continuity equation

$$\frac{1}{\rho}\frac{d\rho}{dr} + \frac{1}{C_m}\frac{dC_m}{dr} + \frac{1}{b}\frac{db}{dr} + \frac{1}{r} = 0. \tag{2.27}$$

- Energy equation for adiabatic flows

$$T_0 = T + \frac{\gamma - 1}{2\gamma R} C^2. \tag{2.28}$$

- Equation of state for ideal gases

$$p = \rho RT. \tag{2.29}$$

Equations from 2.25 to 2.29 have been solved with a step-by-step integration by means of the fourth-order Runge-Kutta method.

The results obtained with this model are quite accurate, provided that the inlet flow conditions are uniform. This is not usually the case, so the value of the skin friction coefficient c_f which appears in Eq. 2.26 has been adapted to increase the precited losses. In this work, the friction factor recommended by Japikse [133] has been used

$$c_f = 0.01 \left(\frac{1.8 \times 10^5}{Re} \right)^{0.2}. \tag{2.30}$$

2.5 The volute model

The volute is simulated with a 1D model which takes into account the realistic effects of diffusion and losses in this component [136, 137]. The key geometric parameter is the outlet-to-inlet area ratio

$$AR_{\mathrm{V}} = \frac{A_8}{A_5} = \frac{\pi \phi_8^2/4}{2\pi r_5 b_5}, \tag{2.31}$$

where ϕ_8 is the volute outlet diameter, and r_5 and b_5 are the diffuser outlet radius and height, respectively.

The aerodynamic losses can be estimated through three simple assumptions. Firstly, the meridional component of the kinetic energy entering the volute is assumed to be completely lost, so that it can be written as

$$K_{\mathrm{m}} = \frac{1}{1 + \lambda_{\mathrm{V}}^2}, \tag{2.32}$$

where $\lambda_{\mathrm{V}} = C_{\mathrm{u}5}/C_{\mathrm{m}5}$ is the volute inlet swirl parameter, being $C_{\mathrm{u}5}$ and $C_{\mathrm{m}5}$ the volute inlet tangential and meridional components of the absolute velocity.

The second and third assumptions are related to C_{u}. For an accelerating flow ($C_{\mathrm{u}5} < C_8$), it is assumed that no losses occur, wherelse for a decelerating flow ($C_{\mathrm{u}5} > C_8$), it is assumed that the pressure losses correspond to the total pressure losses in a sudden expansion mixing process. The losses due to flow deceleration are computed as

$$K_{\mathrm{u}} = \frac{\left(\lambda_{\mathrm{V}} - 1/AR_{\mathrm{V}}\right)^2}{1 + \lambda_{\mathrm{V}}^2}. \tag{2.33}$$

By introducing the total pressure loss coefficient $K_{\mathrm{V}} = K_{\mathrm{u}} + K_{\mathrm{m}}$, these three assumptions lead to two different values of the static pressure recovery coefficient CP, depending on whether the flow condition corresponds to a diffusing ($\lambda_{\mathrm{V}} AR_{\mathrm{V}} > 1$, Eq. 2.34) or an

accelerating flow ($\lambda_V AR_V < 1$, Eq. 2.35)

$$CP_V = \frac{2\left(\lambda_V - 1/AR_V\right)}{AR_V\left(1+\lambda_V^2\right)}, \tag{2.34}$$

$$CP_V = \frac{\left(\lambda_V^2 - 1/AR_V^2\right)}{\left(1+\lambda_V^2\right)}. \tag{2.35}$$

Once K_V and CP_V have been computed, the volute outlet flow conditions can be calculated, since

$$K_V = \frac{p_{05} - p_{08}}{p_{05} - p_5}, \tag{2.36}$$

$$CP_V = \frac{p_8 - p_5}{p_{05} - p_5}. \tag{2.37}$$

Finally, the stage total-to-total pressure ratio and isentropic efficiency are defined by Eqs. 2.8 and 2.9.

2.6 The one-dimensional performance analysis code for radial compressors

The computation of the impeller losses without using empirical loss correlations is the main advantage of the two-zone model described in Sec. 2.3. However, although that approach predicts the flow of centrifugal impellers with more accuracy than the single-zone model, it lacks the capability of providing information about the source of the impeller losses, since it calculates them lumped together.

As a consequence, a new analysis tool has been developed on the basis of the two-zone model, but with a different approach for predicting the secondary zone entropy generation, which now stems from the empirical loss correlations utililized in the single-zone model.

The empirical loss correlations have been taken from the work of Oh *et al.* [193], but the new methodology calculates the losses through the flow properties of the secondary zone, where all the losses are supposed to originate from. Therefore, differences in both losses magnitude and trend are expected, since the single-zone method usually employes the impeller outlet flow properties to calculate the losses.

As with the two-zone model, the flow properties of the secondary zone have been calculated using an iterative procedure, which starts by estimating the relative Mach number of the secondary flow at the impeller outlet, and then proceeds by calculating the velocity triangle at the impeller outlet. The change in enthalpy due to the internal losses is then computed through the single-zone loss correlations, while the entropy gain is calculated using Eq. 2.11, where the impeller outlet relative total temperature $T_{02\text{rel}}$ has been substituted by the impeller outlet relative total temperature of the secondary flow $T_{02\text{rel,s}}$. The iterative procedure is stopped when the continuity is conserved in Eq. 2.10.

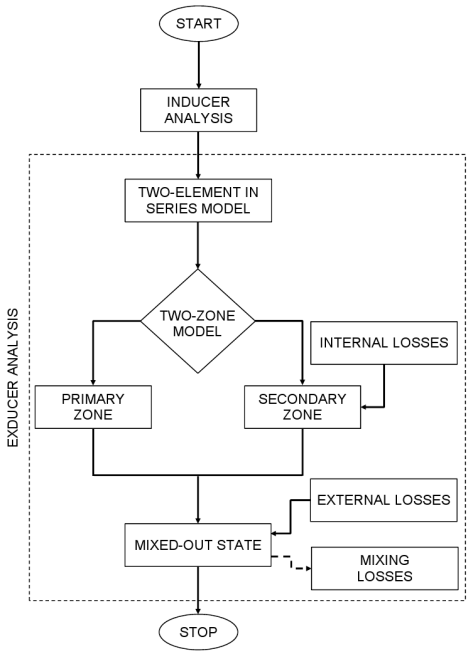

Figure 2.7: *Schematic of the one-dimensional performance analysis code for radial compressors operated with fluids obeying to the ideal gas law.*

Figure 2.7 shows a schematic of the novel 1D performance analysis code for radial compressors. The PARC-1 code allows estimating the design and off-design performance of very small single-stage centrifugal compressors operated with fluids obeying to the ideal gas law. This new methodology has been implemented in a programming environment for algorithm development, data analysis, visualization, and numerical computation [178].

2.7 Results and discussion

This section shows the numerical results computed by the single-zone, two-zone, and PARC-1 models. The models have been utilized for the analysis of the centrifugal compressor adopted for the MTT recuperated micro gas turbine. The geometric details of the compressor can be found in Sec. 3.1. Firstly, the compressor stage performance as calculated by the three models are validated against the experimental data shown in Chap. 3. Secondly, the comparison of the impeller internal, external, and mixing losses as computed by the three methods follows. Finally, the compressor performance and losses have been calculated at the best efficiency point at 220 krpm, and at the micro turbine design point (i.e., $\dot{m}$ = 50 g/s and N = 240 krpm).

2.7.1 Comparison between experimental and numerical results

Figure 2.8 shows the comparison of the stage total-to-total pressure ratio and isentropic efficiency between the experimental and numerical results, at 190 and 220 krpm, and varying mass flow rate, respectively. The numerical results have been computed by the single-zone, two-zone, and PARC-1 models.

The 1D methods capture the stage total-to-total pressure ratio trend, but they show a poor capability in predicting it at high mass flow rates. This might be due to the fact that the geometric details of the impeller throat are not considered in the models. As a consequence, in proximity of the choking condition, the numerical models underpredict π_{tt}, with respect to the experimental results. At low mass flow rates, the two-zone and PARC-1 models exhibit a better agreement with the test data, while the single-zone model overpredict them to a large extent.

The numerical tools also capture the stage total-to-total isentropic efficiency trend, although they all overpredict it. The deviation between the numerical and experimental results decrease from the single-zone to the PARC-1 models, while the two-zone approach gives intermediate results. Therefore, the single-zone model underestimates the losses, while the PARC-1 methodology yields higher losses, which thus lead to lower efficiencies. As a consequence, although the mixing and external losses are calculated in the same way for the two-zone and PARC-1 methods, the summation of the internal losses computed with the latter is higher than the lumped losses computed by the former. Furthermore, the best efficiency point is calculated at a lower mass flow rate than the measured value. As for the pressure ratio, the single-zone model shows the worst behaviour at high mass flow rates, wherelse the two-zone and PARC-1 models exhibit a better agreement with the experimental results.

2.7.2 Internal losses

Figure 2.9 shows the impeller internal losses (i.e., incidence, blade loading, skin friction, and clearance losses) computed by the single-zone and PARC-1 models, at 190 and 220 krpm, and varying mass flow rate, respectively. The two-zone model does not provide the calculation of the individual loss mechanisms, so it has not been included in the comparison.

Incidence losses (Fig. 2.9a) are due to flow adjustments with respect to the impeller inlet blade angle. At off-design conditions, the flow enters the impeller at an incidence angle which is either positive or negative, causing the flow velocity to reduce or increase, respectively. In this work the incidence losses are the average of the values calculated at hub, mid-span, and shroud. The two models use the same relationship for calculating this loss, thus the trends are very similar. At both speeds, there is a point of minimum incidence loss, which occurs at higher mass flow rates with increasing rotational speed. When compared with Fig. 2.8, these points do not correspond to the best efficiency points in the compressor map at the same rotational speeds, indicating thus a non-optimum inducer blade angle. However, the incidence loss does not have a significant effect upon compressor performance as long as the impeller can operate reasonably well at different incidence

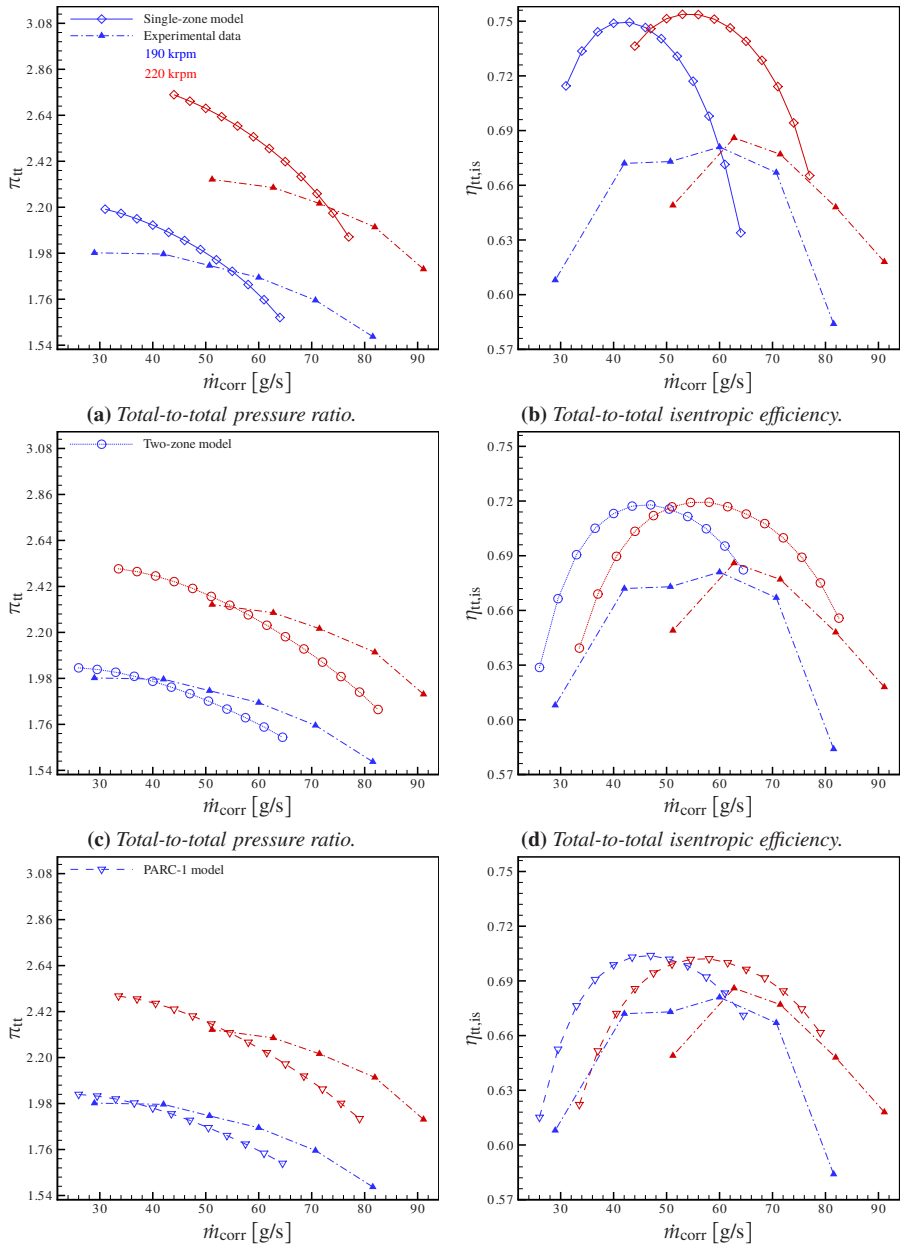

(a) *Total-to-total pressure ratio.*

(b) *Total-to-total isentropic efficiency.*

(c) *Total-to-total pressure ratio.*

(d) *Total-to-total isentropic efficiency.*

(e) *Total-to-total pressure ratio.*

(f) *Total-to-total isentropic efficiency.*

Figure 2.8: *Comparison of the stage total-to-total pressure ratio and isentropic efficiency between experimental (closed symbols) and one-dimensional numerical (hollow symbols) results at 190 and 220 krpm, and varying mass flow rate, respectively. The numerical results have been computed by the single- and two-zone models, and by the one-dimensional performance analysis code for radial compressors (PARC-1).*

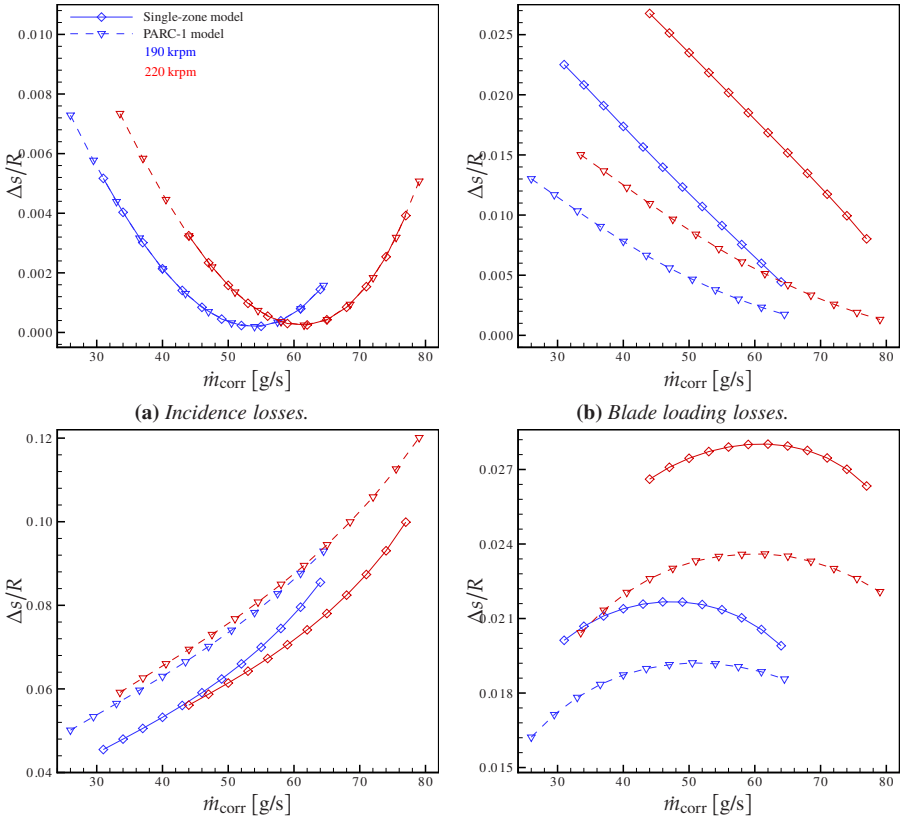

(a) *Incidence losses.*

(b) *Blade loading losses.*

(c) *Skin friction losses.*

(d) *Clearance losses.*

Figure 2.9: *Impeller internal losses (i.e., incidence, blade loading, skin friction, and clearance losses) computed by the single-zone model and the one-dimensional performance analysis code for radial compressors (PARC-1), at 190 and 220 krpm, and varying mass flow rate, respectively.*

values close to the design point value [136].

Blade loading losses (Fig. 2.9b) are generated because of the negative velocity gradients in the boundary layer, and the associated flow separation. They are directly related to the impeller diffusion factor (Eq. 2.14), since the amount of diffusion within the impeller influences the flow velocities, affecting thus the boundary layer development, and the eventual flow separation. For both models, the blade loading losses decrease with increasing mass flow rate, due to lower secondary flow and flow recirculation, although for the single-zone model the rate of decrease is higher. The latter also exhibit higher losses than the PARC-1 code. The discrepancy lies in the different diffusion behaviour, such that the velocity of the primary flow utilized by the PARC-1 model might be on average higher than the impeller outlet velocity used by the single-zone model, thus leading to lower blade loading losses because the flow separation is postponed, or even avoided.

Skin friction losses (Fig. 2.9c) originate from the shear forces which act on the impeller walls and are caused by turbulent friction. They are considered to be equivalent to those experienced by a fully developed flow in a pipe of circular cross-sectional area with a diameter and length equal to the average hydraulic diameter and length of the impeller flow passage, respectively. Skin friction losses increase for both models with increasing mass flow rate, since the fluid is flowing faster, leading to higher friction around protruding objects. Furthermore, the increase in mass flow rate causes an increase in the wetted area as the secondary zone reduces, resulting in higher skin friction losses. The PARC-1 code predicts slightly higher losses, as a consequence of higher flow velocities.

Clearance losses (Fig. 2.9d) result from the leakage flow through the clearance gap, due to the pressure gradient between the pressure and suction sides of the impeller blades. The clearance gap flow influences the secondary flow significantly. The tip clearance in running condition of the current centrifugal compressor is not known, but a value equal to 5% [195] of the impeller outlet blade height has been used to asses this type of losses. The clearance losses increase with increasing mass flow rate up to a maximum value, for both models, then they decrease while approaching the choking condition. Whitfield and Wallace [276] showed a similar trend, though no sign of losses reduction close to choking was visible. However, the impeller analyzed by those authors did not have any backsweep angle. A further reason of such difference could lie in the different tangential velocities at the impeller outlet. In this study, higher clearance losses are computed by the single-zone model, because of the higher impeller outlet tangential velocities utilized in the calculations.

2.7.3 Mixing losses

Figure 2.10 shows the impeller mixing losses computed by the single-zone, two-zone, and PARC-1 models, at 190 and 220 krpm, and varying mass flow rate, respectively. These losses result from the mixing of the wake with the isentropic stream, and depend on the downstream location at which the mixing station is considered. For the single-zone model, a correlation based on the jet-wake area distribution in the impeller passage is used [193], wherelse the two-zone and PARC-1 methods consider the mixing losses to be produced when the low-momentum, secondary flow is mixed with the high-momentum, primary flow.

The two-zone and PARC-1 models show very similar trend and values, at both speeds, as they perform proper flow mixing calculations. The mixing loss reduces as the operating point moves from the surge to choking condition, because the secondary area diminishes with increasing mass flow rates. On the contrary, the single-zone model exhibits an opposite trend, since the mixing loss increases with increasing mass flow rate, and has lower values as well. The strong discrepancy with the two other models might be due to assumption of the secondary flow area fraction which appears in the empirical correlation used by the single-zone model.

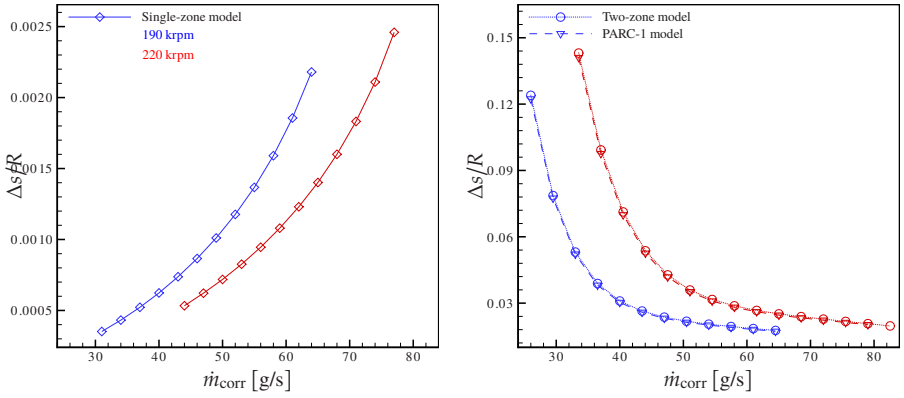

(a) *Single-zone model.* **(b)** *Two-zone and PARC-1 models.*

Figure 2.10: *Impeller mixing losses computed by the single- and two-zone models, and the one-dimensional performance analysis code for radial compressors (PARC-1), at 190 and 220 krpm, and varying mass flow rate, respectively.*

2.7.4 External losses

Figure 2.11 illustrates the impeller external losses (i.e., disk friction, recirculation, and leakage losses) computed by the single-zone, two-zone, and PARC-1 models at 190 and 220 krpm, and varying mass flow rate, respectively.

Disk friction losses (Fig. 2.11a) are represented by an enthalpy rise due to the work done on the fluid by the shear between the rear face of the impeller and any adjacent stationary surface. They consider rotating disks in a stationary housing, and depend on the Reynolds number, according to the correlation used by Oh *et al.* [193]. Disk friction losses decrease as the mass flow rate increases, at each rotational speed, since the secondary flow is reduced at higher mass flow rates, resulting then in a lower amount of flow leaking into the clearance gap between the impeller disk and the housing. However, with increasing rotational speed, they increase due to increased friction and blade speed. The three models predict the disk friction losses with similar trends and magnitude, although the small deviations among the results can be explained with the different flow velocities at the impeller outlet.

Recirculation losses (Fig. 2.11b) are caused by the recirculation of the low-momentum flow from the vaneless space back into the impeller passages. At low mass flow rates, the recirculation losses are high at both rotational speeds, because of high tangential velocities, which might force the flow to recirculate back into the rotating impeller. They diminish as the mass flow rate is increased at constant rotational speed, because of lower diffusion rates and absolute flow angles. The single-zone model predicts slightly higher recirculation losses because of higher velocities.

Finally, an additional enthalpy rise is due to the fluid flowing from the blades pressure to suction sides, reducing the energy transfer from the impeller to the fluid. However, for

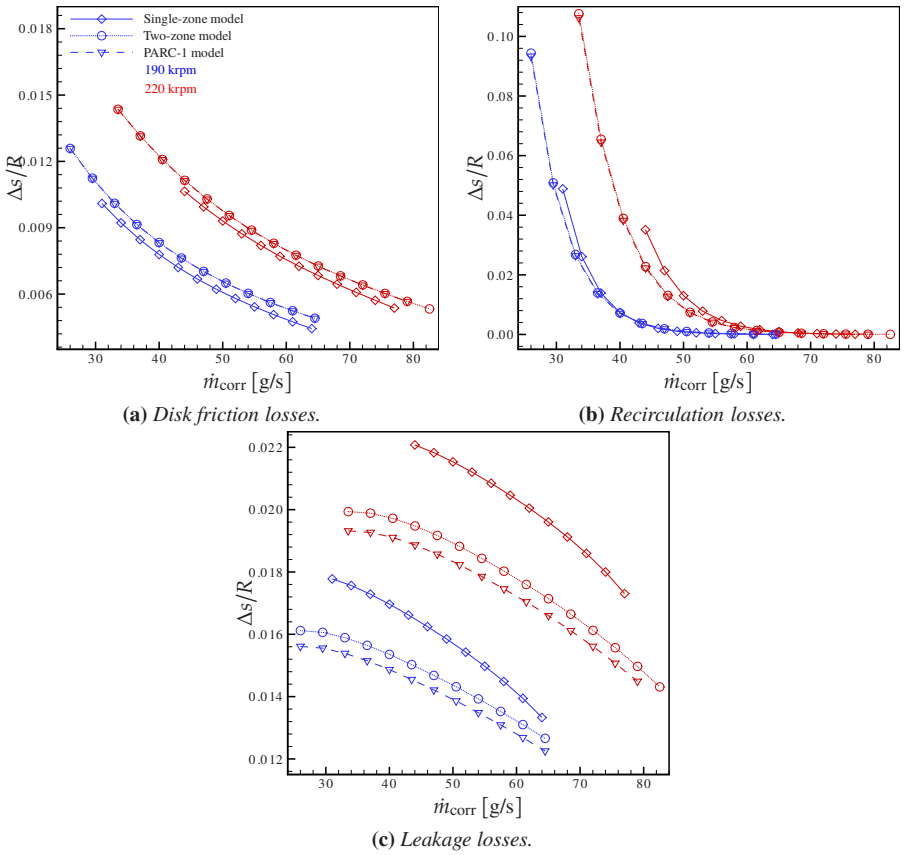

(a) *Disk friction losses.*

(b) *Recirculation losses.*

(c) *Leakage losses.*

Figure 2.11: *Impeller external losses (i.e., disk friction, recirculation, and leakage losses) computed by the single- and two-zone models, and the one-dimensional performance analysis code for radial compressors (PARC-1), at 190 and 220 krpm, and varying mass flow rate, respectively.*

unshrouded impellers, some leakage flow re-enters into the impeller bladed passages from the inducer/shroud gap, re-energizes the flow, and generates the so-called leakage losses (Fig. 2.11c). The two-zone and PARC-1 methods show similar results, while the values calculated with the single-zone model are higher. As the mass flow rate increases at constant rotational speed, the leakage losses decrease. However, the leakage losses increase as the rotational speed increases, because the fluid is flowing faster.

2.7.5 Performance and losses analysis

Table 2.1 shows the effects of the different loss mechanisms on the stage total-to-total isentropic efficiency, calculated with the single-zone, two-zone, and PARC-1 models. The comparison has been performed at the best efficiency point for a rotational speed equal to

Table 2.1: *Effects of the different loss mechanisms on the stage total-to-total isentropic efficiency at the best efficiency point at 220 krpm, computed by the single- and two-zone models, and the one-dimensional performance analysis code for radial compressors (PARC-1).*

Losses	Single-zone	Two-zone	PARC-1
Incidence	−0.0%	−0.0%	−0.0%
Blade loading	−1.7%	/	−0.7%
Skin friction	−6.5%	/	−9.9%
Clearance	−2.6%	/	−2.8%
Mixing	−0.1%	−1.6%	−3.3%
Disk friction	−0.7%	−0.5%	−1.0%
Recirculation	−0.3%	−0.1%	−0.3%
Leakage	−1.9%	−1.0%	−2.1%
Vaneless diffuser	−4.3%	−2.0%	−4.2%
Volute	−6.9%	−2.6%	−5.5%
Total	−25.0%	−28.2%	−29.8%
Efficiency	75.0%	71.8%	70.2%

220 krpm. The blade loading, skin friction, and clearance losses have not been calculated for the two-zone model, since it only allows for the computation of the impeller internal losses as lumped together in a single term.

The skin friction losses are the highest for both the single-zone and PARC-1 models, and the valuex calculated with the PARC-1 code are higher, due to a higher average velocity in the impeller bladed passages. On the contrary, the blade loading losses calculated with the single-zone model are higher, because of a higher diffusion factor. The clearance losses are of the same order of magnitude, while the incidence losses are negligible for the the three models.

Further differences can be noticed when comparing the mixing losses. Those calculated with the single-zone model are almost zero, as this approach does not consider the separation between high- and low-momentum flows. On the contrary, the mixing losses are higher for the two-zone and PARC-1 models. The latter calculates the highest mixing losses, because of a larger deviation between the flow properties at the mixing station and at the impeller blades trailing edge.

Among the impeller external losses, the leakage losses are the highest for all of the three models, as a consequence of a large amount of leakage flow which re-enters into the impeller bladed passages at the inducer. On the other hand, the recirculation flow at the impeller outlet is lower. Further losses are due to the flow deceleration in the vaneless diffuser and volute. The losses occurring in the latter component are higher than those due to the diffuser deceleration, as a consequence of a stronger diffusion taking place in

Table 2.2: *Effects of the different loss mechanisms on the stage total-to-total isentropic efficiency at the micro turbine design point (i.e., $\dot{m}$ = 50 g/s and N = 240 krpm), computed by the one-dimensional code for radial compressors.*

Losses	
Incidence	−0.3%
Blade loading	−1.1%
Skin friction	−7.3%
Clearance	−2.4%
Mixing	−5.9%
Disk friction	−1.2%
Recirculation	−2.6%
Leakage	−2.0%
Vaneless diffuser	−5.1%
Volute	−4.1%
Total	−32.0%
Efficiency	68.0%

the volute.

Overall, as visible in Fig. 2.8, the stage total-to-total isentropic efficiency calculated with the single-zone model is the highest, while that computed with the PARC-1 code is the lowest. The difference between the numerical and experimental results is equal to 8.5%, 4.5%, and 2.3% for the single-zone, two-zone, and PARC-1 models, respectively.

Finally, the PARC-1 tool has been used to estimate the design point performance of the centrifugal compressor adopted for the MTT micro turbine. The calculated stage total-to-total pressure ratio and isentropic efficiency are equal to 2.79 and 0.68, respectively, while the corresponding experimental data provided by MTT are equal to 2.69 and 0.71. Therefore, the PARC-1 model overpredicts the pressure ratio by 3.6%, and underpredicts the efficiency by 4.7%.

Table 2.2 illustrates the effects of the different loss mechanisms on the stage total-to-total isentropic efficiency, calculated by the PARC-1 method at the micro turbine design point. The skin friction losses account for the largest share, and contribute to decrease the efficiency by 7.3%, followed by the mixing losses (−5.9%), and the vaneless diffuser losses (−5.1%). Furthermore, at this operating condition the mixing, recirculation, and vaneless diffuser losses are higher than the values calculated at the best efficiency point at 220 krpm, because of a higher impeller outlet velocity, due to the increased rotational speed.

2.8 Conclusions

A new methodology for the assessment of the performance and loss mechanisms of very small centrifugal compressors has been presented in this chapter. The PARC-1 model has been implemented in a programming environment for algorithm development, data analysis, visualization, and numerical computation. The main features of the PARC-1 code, and the results of its application to the centrifugal compressor adopted for the MTT micro turbine can be summarized as follows:

- The model has been developed on the basis of the single- and two-zone methodologies, and combines the advantages of the two, since the loss correlations have been integrated in the secondary zone. In particular, this tool distinguishes between high- and low-momentum flows within the impeller bladed passages as the two-zone model, and allows evaluating the impeller loss mechanisms, as possible with the single-zone methodology.

- The numerical results obtained with the PARC-1 model at 190 and 220 krpm, and varying mass flow rate, have been compared to the experimental data related to the performance of the micro compressor for the MTT system, obtained with the μTURCO-rig (see Chap. 3). The comparison shows a good agreement, except close to the choking condition. This model is generally able to capture the stage total-to-total pressure ratio and isentropic efficiency trends, although it overpredicts the test data. However, in proximity of the choking condition the code underpredicts the pressure ratio, since the geometric details of the impeller throat have not been not considered. Furthermore, the best efficiency point is calculated at a lower mass flow rate than the measured value.

- The PARC-1 model has been used to estimate the loss mechanisms at 190 and 220 krpm, and varying mass flow rates. According to computed results, the skin friction losses are the highest among the internal losses, while the recirculation losses are the highest among the external losses. Furthermore, the mixing losses are very high at low mass flow rates, and rapidly decrease with increasing mass flow rates.

- The new model has been utilized as well for the compressor performance analysis at the micro turbine design point (i.e., $\dot{m}$ = 50 g/s and N = 240 krpm). The calculated stage total-to-total pressure ratio and isentropic efficiency are equal to 2.79 and 0.68, respectively, while the corresponding experimental data provided by MTT are equal to 2.69 and 0.71. Therefore, the PARC-1 methodology overpredicts the pressure ratio by 3.6%, and underpredicts the efficiency by 4.7%.

- On the basis of the computed results, at the micro turbine design point the skin friction losses contribute to the largest efficiency decrease (-7.3%), followed by the mixing losses (-5.9%), and the vaneless diffuser losses (-5.1%).

- The PARC-1 methodology has to be tested with other micro compressors, in order to further solidify its role as an efficient method to analyze very small centrifugal compressors.

- Further numerical simulations are required to improve the capability of this novel approach to properly quantify the diffusion ratio, the relationship between the secondary flow mass and area fractions, and the tangential velocity factor, which are employed in the model.

"There are two possible outcomes: if the result confirms the hypothesis, then you've made a measurement. If the result is contrary to the hypothesis, then you've made a discovery."

Enrico Fermi.

3
Experimental setup

A test-rig has been designed and built for the acquisition of the performance maps of very small centrifugal compressors, and used to characterize the micro turbine compressor, which is the object of investigation of this dissertation. Its operating principles, main components, and instrumentation are described in detail in this chapter. The data collected throughout an experimental campaign have been used to validate the numerical results documented in Chaps. 2 and 4. In the future, the test-rig will also be employed for testing optimized components of the compressor stage. Furthemore, the uncertainty propagation analysis has also been carried out, in order to assess the potential error sources and their effects on the test data. The main elements of the uncertainty propagation analysis are also described here.

3.1 Introduction

The possibility to perform experimental investigations is paramount in the design phases of centrifugal compressors, as well as in their optimization in subsequent development stages. Furthermore, having a flexible test facility where different compressor configurations can be tested with minor modifications leads to reduced costs and time. Besides, computational fluid dynamics (CFD) is nowadays a very important tool in the design of centrifugal compressors. However, due to the complexity of the flow field through the compressor, accurate analyses may be difficult to obtain. Therefore, the validation of the numerical solutions with experimental data is pivotal.

The turbomachinery part of the micro turbine developed by Micro Turbine Technology B.V. (MTT) currently consists of an automotive turbocharger. The performance maps of the centrifugal compressor were made available by the original equipment manufacturer (OEM), but the experimental data provided to the author by the OEM could not be considered sufficiently reliable for a proper validation of the numerical analyses (see Chaps. 2 and 4). In addition, in order to obtain a multi-purpose test-bench for very small compressors, it has been decided to design and build a specific set-up at the TU Delft Process & Energy Department.

The main goal of the experimental campaign successively conducted with the micro turbine radial compressor test-rig (μTURCO-rig) was then the acquisition of the performance maps (i.e., pressure ratio and efficiency as function of mass flow rate and rotational speed) of the centrifugal compressor adopted for the MTT micro gas turbine system.

The experiments were performed in parallel to CFD investigations which allowed gaining further knowledge about the flow structure, performance, and loss mechanisms of the centrifugal compressor stage. Therefore, the main use of the collected experimental data was the validation of the numerical models employed for those analyses.

Furthermore, the μTURCO-rig will be available for future tests of newly designed configurations which aim to improve the micro turbine compressor performance.

In this chapter, the operating principles, main components, and instrumentation of the the μTURCO-rig are firstly described. Subsequently, a brief introduction about the uncertainty propagation analysis is given, since the latter has been performed to assess the potential error sources and their effects on the test data. Finally, the experimental results are presented and discussed.

3.2 The experimental facility

The μTURCO-rig is shown in Fig. 3.1a, while the tested compressor stage is visible in Fig. 3.1b. The latter is equipped with an unshrouded centrifugal impeller, a vaneless diffuser, and a volute (Fig. 3.1c). It is designed for air and delivers a pressure ratio of about 2.7, at the design mass flow rate and rotational speed equal to 50 g/s and 240 krpm, respectively.

The impeller has 6 full and 6 splitter blades, with a backsweep angle equal to $-34°$. The blade angle at the inducer tip is equal to $-64°$. The blades thickness is constant from

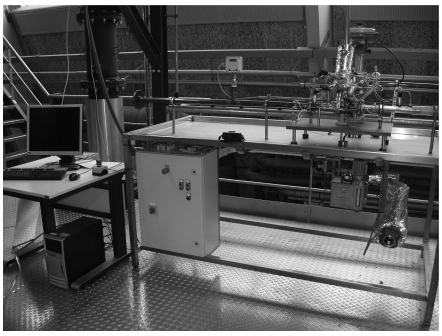

(a) *The whole test-rig.*

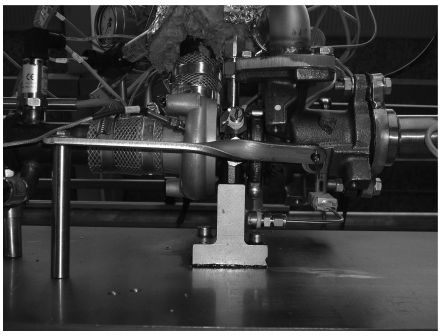

(b) *The centrifugal compressor stage.*

(c) *The impeller and vaneless diffuser.*

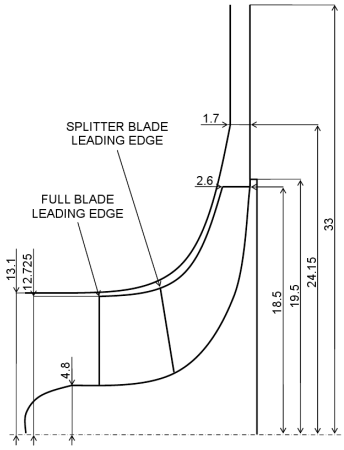

(d) *Main dimensions in mm of the impeller and vaneless diffuser.*

Figure 3.1: *The test-rig built at the TU Delft Process & Energy Department, and the tested centrifugal compressor.*

the leading to the trailing edges and equal to 0.5 mm. A tip clearance equal to 0.375 mm has been measured at the inducer, with the compressor standing still in ambient air, as the difference between the shroud and the blade tip diameters. The impeller and diffuser main dimensions are given in Fig. 3.1d. The impeller inlet hub and shroud diameters are equal to 9.6 and 26.2 mm, respectively, while the impeller outlet diameter is equal to 39 mm. The diameter at the impeller blades trailing edge is equal to 37 mm. The pinched vaneless diffuser is 2.6-mm-high at the inlet and 1.7-mm-high at the outlet, where the diameter is equal to 66 mm. The volute outlet diameter is equal to 27.6 mm.

Figure 3.2 shows an isometric view of the μTURCO-rig, whose major components can be identified. A turbine is used in order to power the compressor, as powering it with an electric motor was deemed more complex and costly. The turbine is supplied externally with pressurized air from two oil-free screw compressors that provide a total combined

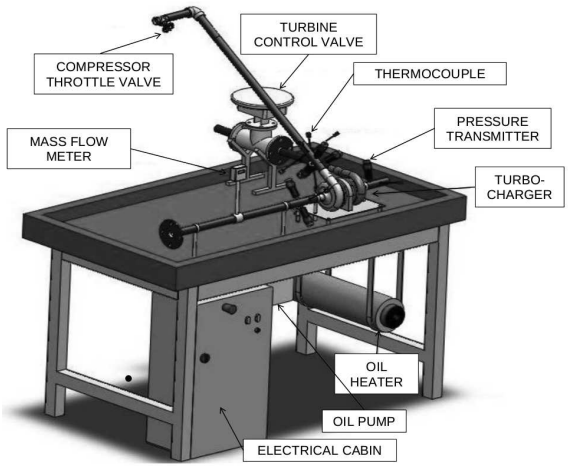

Figure 3.2: *An isometric view of the test-rig built at the TU Delft Process & Energy Department.*

capacity equal to 6.06 m^3/min at a nominal pressure equal to 8 bar and room temperature. A 4-m^3 buffer tank is located between the screw compressors and the turbine control valve, across which the pressure is decreased to about 3 bar. The turbine control valve is used to vary and control the compressor rotational speed, by changing the amount of air which flows through the turbine. It can be operated either manually or automatically.

The mass flow rate across the compressor stage is controlled by an adjustable throttle valve which is positioned downstream of the compressor outlet. The maximum rotational speed which has been reached as of 05-06-2012 is equal to 220 krpm, but a second buffer tank, with a 5-m^3 volume, has been recently placed downstream of the first tank. The larger system capacity would allow increasing the maximum rotational speed achievable by the compressor, and bring it to the design value equal to 240 krpm. The experimental results will be therefore updated as soon as they are available.

The test-rig is also equipped with an autonomous oil circuit that lubricates the shaft and bearings. The oil is stored in a tank, pumped through the circuit by an hydraulic pump, and heated up by means of an electrical heater, since it seems that a less viscous oil applies a lower pressure on the bearings. The heater can deliver a maximum thermal power equal to 2 kW and is placed upstream of the bearing arrangement. The oil pressure can be adjusted using a valve which allows the oil by-passing the bearings and flowing back into the oil tank. A filter located between the electrical heater and the bearing system is used to clarify the oil before it enters the bearings housing.

3.2.1 Instrumentation

Figure 3.3 shows a simplified process and instrumentation diagram of the μTURCO-rig. An immersible thermal gas mass flow meter is used for measuring the compressor mass flow rate. The mass flow meter has been calibrated to measure air and can stand

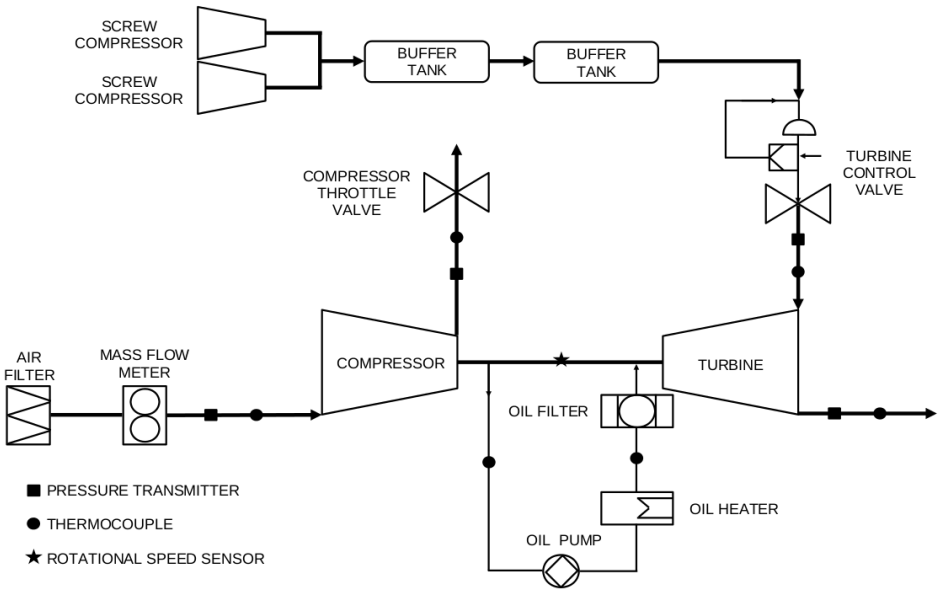

Figure 3.3: *The simplified process and instrumentation diagram of the test-rig built at the TU Delft Process & Energy Department.*

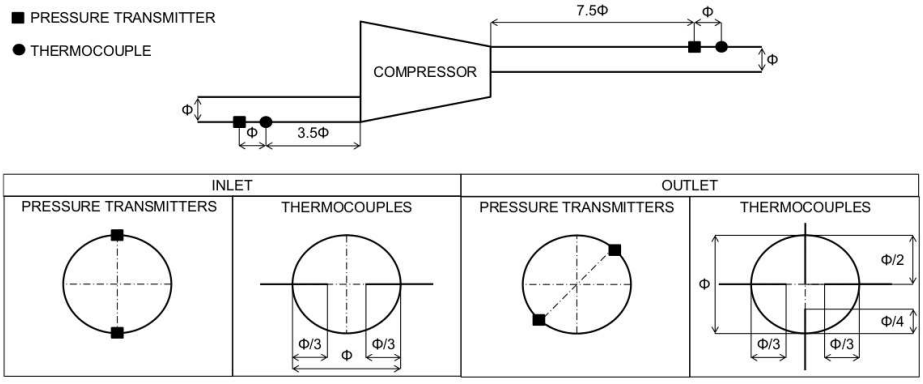

Figure 3.4: *Pressure transmitters and thermocouples installation at the compressor inlet and outlet.*

temperatures up to 400°C.

The compressor rotational speed is measured with a speed sensor whose functional principle is based on 1-MHz pulse induction and eddy current discrimination, performed with a solenoid sensor that is mounted in the compressor housing, through a bore. The sensor detects and counts the compressor vanes one by one.

Static pressure and total temperature measurements at the compressor inlet and outlet are performed following the SAE standards [243, 244]. The number and position of pressure transmitters and thermocouples following these standards are shown in Fig. 3.4. At the inlet, the pressure is measured with pressure transmitters that can stand media temperatures up to 125°C. At the outlet, the allowable media temperature is up to 155°C. The total temperature is measured with type K thermocouples.

The specifications of all the measuring instruments are summarized in Table 3.1.

3.2.2 The data acquisition system

The data acquisition hardware consists of a computer connected to a National Instruments (NI) cDAQ-9172 chassis through a USB interface. The NI cDAQ-9172 is an eight-slot chassis designed to be used with C-series input/output (I/O) modules and is capable of measuring a broad range of analog and digital I/O signals and sensors.

The analog input modules are the NI 9201, NI 9203, and NI 9211. They are connected to the rotational speed sensor, the pressure transmitters and the mass flow meter, and the thermocouples, respectively. The analog output module is the NI 9265, which is connected to the turbine control valve. The specification of all the modules mounted on the NI cDAQ-9172 chassis are given in Tables 3.2 and 3.3.

A data acquisition program has been developed in LabVIEW [191] for measuring, logging, and displaying the relevant data throughout the experiment, controlling the compressor rotational speed, and post-processing the measured data. Therefore, the main portion of the software consists of three loops running in parallel.

The *capture loop* senses events that are triggered when the user operates any kind of control on the front panel (Fig. 3.5a). When such an event occurs, it is cued and processed by the *process loop*. The *acquisition & control loop* runs according to a timer and continuously acquires data. Since the loop rate is equal to 100 ms, while the data acquisition task is set to continuously acquire samples at a frequency equal to 1 kHz, an average of 100 samples/channel per loop are stored and displayed on the front panel.

The static pressures and total temperatures at the compressor inlet and outlet and the mass flow rate are then used to calculate the compressor stage pressure ratio and efficiency. This happens when the operator presses the “Calc. parameters” button on the post-processing panel (Fig. 3.5b). The pressure ratio and efficiency are calculated through a running-average algorithm over a time span defined by the operator in terms of number of loops. A 10-loop interval has been adopted for the experimental campaign aimed at obtaining the compressor performance maps, thus 1000 samples are averaged for each variable each time that post-processing is performed. Furthermore, as redundant pressure transmitters and thermocouples are used at the compressor inlet and outlet, an additional averaged value is calculated on the basis of the sensors number at each location.

Table 3.1: *Specifications of the measuring instruments. R and FS stand for reading and full scale, respectively.*

Instrument	Company	Model	Location	Range	Accuracy	Output signal
Mass flow meter	Sierra Instruments	Steel-Mass Model 640S	Inlet	0-100 g/s	±1.0%R+0.5%FS	4-20 mA
Rotational speed sensor	Acam-Messelectronic	PicoTurn-SG	Shroud	0.39-320 krpm	±0.25%FS	0.4-4.5 V
Pressure transmitter	AE Sensors	AE-SML-10.0	Inlet	0-6 bar	±0.5%FS	4-20 mA
Pressure transmitter	STS Sensors	ATM (Ex)	Outlet	0-8 bar	±0.5%FS	4-20 mA
Thermocouple	Labfacility	Type K	Inlet and outlet	−40-+1100°C	±1.5°C or 0.4%R*	±10 mV

*Whichever is greater

Table 3.2: *Specifications of the National Instrument analog input modules. R and FS stand for reading and full scale, respectively.*

Module	Signal type	Channels	Resolution [bits]	Max sampling rate [S/s]	Signal input range	Accuracy
NI-9203	Current	8	16	200 k	±20 mA	±0.04%R±0.02%FS
NI-9201	Voltage	8	12	500 k	±10 V	±0.04%R±0.07%FS
NI-9211	Thermocouple	4	24	15	±80 mV	1.3°C

Table 3.3: *Specifications of the National Instrument analog output module.*

Module	Signal type	Channels	Resolution [bits]	Max update rate [S/s]	Range
NI-9265	Current	4	16	100 k/ch	0-20 mA

Since these values are averaged during a short period of time (i.e., one second), in accordance with the guidelines given by American Society of Mechanical Engineers [11] they can be utilized for further calculations. The averaged pressure, temperature, mass flow rate, and rotational speed used for the post-processing are visible on the top, left-hand side of the post-processing panel (Fig. 3.5b). The post-processed flow properties are visible on the bottom, left-hand side of the panel. The performance maps are immediately available to the operator on the right-hand side of the panel. The compressor stage pressure ratio and efficiency as functions of the corrected mass flow rate are shown above and below, respectively.

According to the SAE standards [243, 244], during a test "data shall not be taken until reasonable thermal stability is achieved". Those standard define a thermal condition to be stable when the normalized temperature difference across the compressor is lower than, or equal to, a defined ΔT, over a specified amount of time Δt

$$\frac{T_{02} - T_{01}}{T_{01}} \leq \Delta T, \tag{3.1}$$

where T_{01} and T_{02} are the total temperatures at the compressor inlet and outlet, respectively. In this case, ΔT has been set equal to 0.5°C and Δt has been specified equal to 60 s. An operator-definable watch-dog timer has been implemented in the software to allow the operator understanding when the thermal stability criterion is fulfilled. The watch-dog timer is always set to 0 every time the software is launched. This condition is indicated by the fact that the "Stability" LED on the post-processing panel is off. When the stability criterion is achieved, the timer is started and the LED switches on as soon as the specified Δt is elapsed. The operator can then reset to 0 the timer by means of a "Reset" button. The thermal stability block is located on the post-processing panel and is visible at the center of the left-hand side.

The turbine control valve can be operated either manually or automatically. The turbine control valve block is located on the front panel, at the bottom, right-hand side (Fig. 3.5a). In the manual mode, the operator can prescribe the valve opening percentage by moving the pointer up and down, or by directly typing the percentage in the white window at its right. In the automatic mode, a proportional-integral-derivative (PID) controller operates the μTURCO-rig when the "Auto Control" button is pressed by the operator, after that the desired valve opening percentage has been set. The PID controller is contained in the *acquisition & control loop* and is executed at the same speed of that loop (i.e., 100 ms). Its proportional, integral, and derivative values have been extrapolated after that numerous tests have been carried out at various settings and system disturbances.

3.3 Uncertainty propagation analysis

In this section, the main concepts related to the theory of uncertainty propagation are briefly recalled, together with the elements specifically applied in this case, while the results of the application of such analysis are reported in Sec. 3.4.

For each quantity X_i measured in any experimental facility, various elemental sources

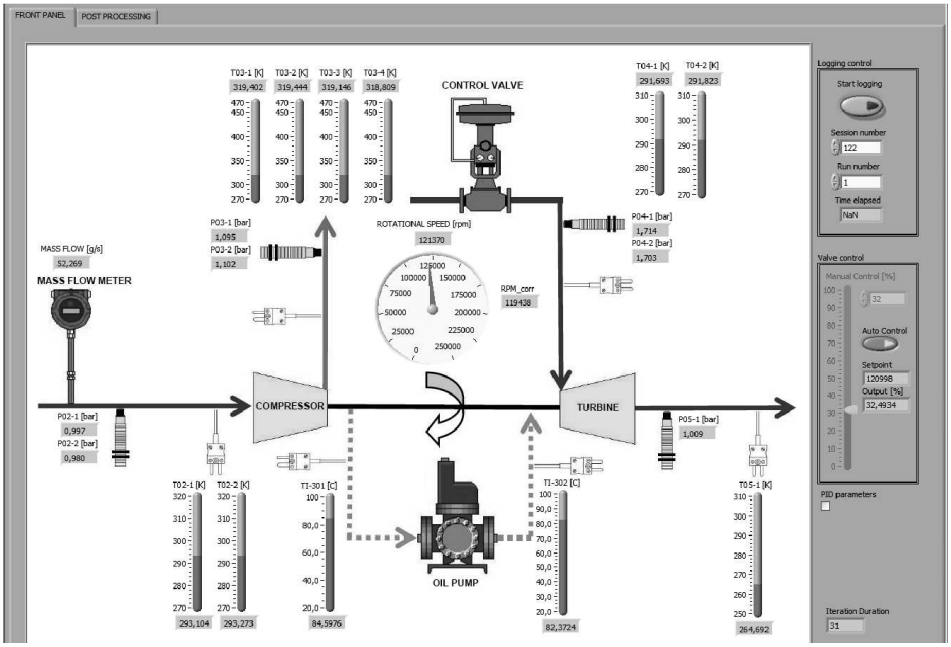

(a) *The front panel.*

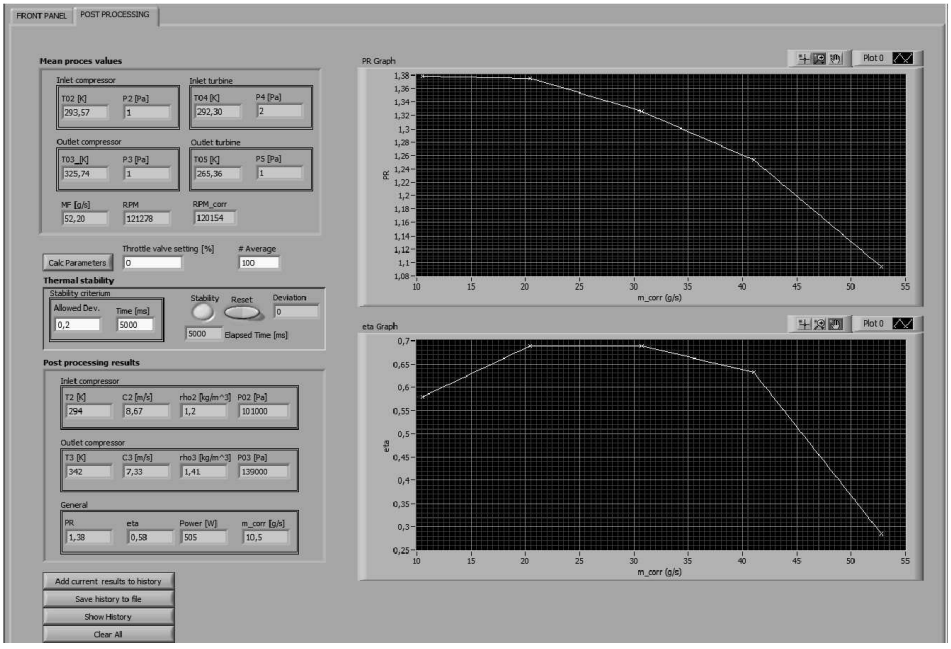

(b) *The post-processing panel.*

Figure 3.5: *The front and post-processing panels of the LabVIEW program developed for the test-rig built at the TU Delft Process & Energy Department.*

of systematic and random uncertainties exist, due the corresponding elemental systematic and random errors. All the elemental uncertainties are then summed up, such that for every X_i only the total systematic and random uncertainties are given. The mutual combination of the total systematic and random uncertainties gives the total combined uncertainty of X_i. All of the total combined uncertainties are then propagated in order to obtain the value of the uncertainty affecting the final engineering variable of interest, namely the pressure ratio and the efficiency of the compressor stage.

Errors, and thus uncertainties, may arise from different sources, such as calibration, data acquisition, and test techniques [46, 47]. Within each source, there may be several elemental sources of systematic and random uncertainties. If for the i-th variable X there are M elemental systematic and random errors identified as significant and whose uncertainties are respectively $b_{X_{i,1}}, b_{X_{i,2}}, \ldots, b_{X_{i,M}}$ and $s_{X_{i,1}}, s_{X_{i,2}}, \ldots, s_{X_{i,M}}$, then the total uncertainties of the measured parameter X_i are calculated as the root-sum-square combination of the elemental uncertainties

$$b_{X_i} = \sqrt{b_{X_{i,1}}^2 + b_{X_{i,2}}^2 + \ldots + b_{X_{i,q}}^2} = \sqrt{\sum_{q=1}^{M} b_{X_{i,q}}^2}, \tag{3.2}$$

$$s_{X_i} = \sqrt{s_{X_{i,1}}^2 + s_{X_{i,2}}^2 + \ldots + s_{X_{i,q}}^2} = \sqrt{\sum_{q=1}^{M} s_{X_{i,q}}^2}. \tag{3.3}$$

Once the total systematic (Eq. 3.2) and the random (Eq. 3.3) uncertainties have been calculated for each measured variable X_i, the total combined uncertainty u_{X_i} of X_i is given as

$$u_{X_i} = \sqrt{b_{X_i}^2 + s_{X_i}^2}, \tag{3.4}$$

from which the total combined expanded uncertainty yields

$$U_{X_i} = t u_{X_i}, \tag{3.5}$$

where t is called "student's factor". In this work, $t = 2$ for a 95% level of confidence has been assumed, since the large-sample assumption is appropriate for most engineering and scientific applications [11, 47].

Consequently, the total combined uncertainties of the elemental values have to be propagated to the so-called final results. The set of described assumptions and concepts is called "uncertainty propagation theory", and lies on the fact that if the relationship between the measured variables and the final results is known, then the uncertainties of the former can be propagated to compute the uncertainties of the latter [11].

One of the main approaches followed in order to incorporate the uncertainties of the measured values in the final results is the Taylor series method (TSM) [11, 128], which has been used here because the data available from the instruments specifications can be directly applied in the uncertainties calculation, the systematic and random uncertainties of each component can be calculated separately, the computational time for the systematic uncertainty calculation is low, and the computed sensitivity factors may be used for the

uncertainty analysis.

The use of the TSM for propagating the uncertainties of the measured variables into the final results has been extensively decribed in the literature [24, 45–47, 155], therefore in this dissertation only the equations used for the uncertainties propagation are briefly recalled. The total systematic b_r and random s_r uncertainties of the final result r are

$$b_r^2 = \sum_{i=1}^{J} \theta_i^2 b_{X_i}^2, \tag{3.6}$$

$$s_r^2 = \sum_{i=1}^{J} \theta_i^2 s_{X_i}^2, \tag{3.7}$$

where $\theta_i = \partial r/\partial X_i$ is the sensitivity factor. From Eqs. 3.6 and 3.7, the total combined expanded uncertainty of the final result is defined as

$$U_r^2 = 2u_r^2 = 2\left(b_r^2 + s_r^2\right). \tag{3.8}$$

The uncertainty propagation represents a very useful tool in all the phases of an experimental campaign, from the initial planning to the detailed design, debugging, testing of operational procedures, and data analysis [190]. It is also a crucial component of the performance assessment of flow measuring techniques.

Two of the parameters that help to know which variables are the most important or have more influence on the final result when an experimental investigation is planned, are the uncertainty magnification factor (UMF) and the uncertainty percentage contribution (UPC) [47].

The UMF is defined as the factor that, for a given measured variable X_i, indicates the influence of the uncertainty of that variable on the uncertainty of the final result. According to the TSM, the total combined uncertainty can be rewritten as

$$u_r^2 = \sum_{i=1}^{J} \left(\frac{\partial r}{\partial X_i}\right)^2 u_{X_i}^2, \tag{3.9}$$

where the partial derivative $\partial r/\partial X_i$ relates a variation in the result r to a variation in the measured variable X_i, and u_{X_i} is defined by Eq. 3.4. Each term of Eq. 3.9 is now divided by r^2, while the terms on the right-hand side are multiplied by $(X_i/X_i)^2$, yielding

$$\frac{u_r^2}{r^2} = \frac{1}{r^2}\sum_{i=1}^{J}\left(\frac{X_i}{X_i}\right)^2\left(\frac{\partial r}{\partial X_i}\right)^2 u_{X_i}^2 = \sum_{i=1}^{J}\left(\frac{X_i}{r}\frac{\partial r}{\partial X_i}\right)^2\left(\frac{u_{X_i}}{X_i}\right)^2. \tag{3.10}$$

It is therefore possible to define UMF from Eq. 3.10 as

$$UMF_i \equiv \frac{X_i}{r}\frac{\partial r}{\partial X_i}. \tag{3.11}$$

From Eq. 3.11, it can be seen that if UMF is greater than 1, the influence of the variable uncertainty is magnified as it propagates into the final result, while it diminishes if UMF is

lower than 1 [47]. Since the UMFs are squared in Eq. 3.10, their signs are of no importance, thus only the absolute values are considered.

The definition of UPC follows from Eq. 3.9. Dividing Eq. 3.9 u_r^2 gives

$$1 = \frac{\sum_{i=1}^{J} \left(\frac{\partial r}{\partial X_i} \right)^2 u_{X_i}^2}{u_r^2}, \tag{3.12}$$

which allows to define UPC as

$$UPC_i \equiv \frac{\left(\frac{X_i}{r} \frac{\partial r}{\partial X_i} \right)^2 \left(\frac{u_{X_i}}{X_i} \right)^2}{\left(\frac{u_r}{r} \right)^2} \times 100. \tag{3.13}$$

The UPC of a variable determines the percentage contribution of the uncertainty of that variable to the squared uncertainty of the final result. Since it contains the effects of both the UMF and the magnitude of the uncertainty of that variable u_{X_i}, it is useful in the planning phases once the variables uncertainties are estimated [47].

3.4 Results and discussions

Figure 3.6 shows the performance maps of the MTT micro turbine centrifugal compressor, obtained with the μTURCO-rig. The stage total-to-total pressure ratio and isentropic efficiency are plotted versus the corrected mass flow rate and rotational speed. Data have been acquired at 120, 160, 190, and 220 krpm. However, at 220 krpm, the data have not been acquired in thermally stable conditions, due to operational issues involving the screw compressors which power the turbine. In particular, the buffer tank is quickly exhausted, causing then pressure fluctuations which negatively affect the flow. This in turn leads to temperature fluctuations which do not allow reaching thermal stability. Nevertheless, a second buffer tank has been recently installed, in order to pressurize the 5-m^3-volume buffer tank. New experiments at 220 krpm will therefore be performed soon, in order to obtain experimental data that are not affected by flow temperature fluctuations.

The experiments have been conducted from high to low mass flow rates, for each rotational speed. The surge condition was identified when the characteristic sound produced by the vibrating impeller blades was heard. Multiple tests are instead required close to the choking condition in order to properly identify it. The maximum stage total-to-total isentropic efficiency is of the same order of magnitude at each rotational speed (~0.7), while the maximum pressure ratio was measured at 220 krpm, and it is equal to 2.3.

The average uncertainties for the calculated performance quantities (see Sec. 3.3) are summarized in Table 3.4 for all rotational speeds. The uncertainties decrease as the rotational speed increases, although the decrement is generally small. The efficiency uncertainty exhibits the highest values, but the largest decrease from low to high rotational

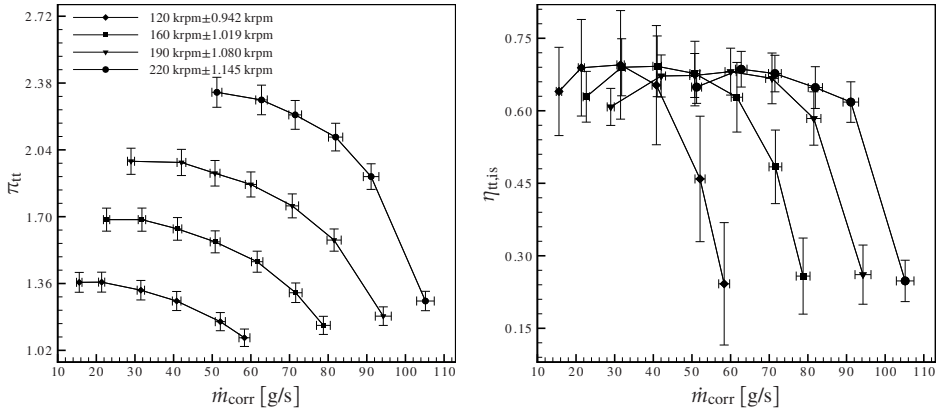

(a) *Total-to-total pressure ratio.* **(b)** *Total-to-total isentropic efficiency.*

Figure 3.6: *Performance maps of the centrifugal compressor adopted for the recuperated micro gas turbine developed by Micro Turbine Technology B.V.*

Table 3.4: *Average uncertainties affecting the engineering quantities of the final results (i.e., corrected mass flow rate $\dot{m}_{corr}$, corrected rotational speed N_{corr}, total-to-total pressure ratio π_{tt}, total-to-total isentropic efficiency $\eta_{tt,is}$).*

Quantity	120 krpm	160 krpm	190 krpm	220 krpm
$\dot{m}_{corr}$	3.05%	2.48%	2.34%	2.25%
N_{corr}	0.78%	0.63%	0.57%	0.52%
π_{tt}	3.69%	3.54%	3.41%	3.30%
$\eta_{tt,is}$	18.56%	12.07%	9.00%	7.11%

speeds.

The results of the uncertainty propagation from the test data to the final results are also shown in Fig. 3.6 in the form of error bars. The uncertainty of the rotational speed measurements increases with increasing rotational speed, since the accuracy of the rotational speed sensor is function of the full scale (i.e., 320 krpm, see Table 3.1), while the accuracy of the analog input module for the rotational speed measurements depends on both the reading and the full scale (see Table 3.2). The uncertainty of the corrected mass flow rate decreases from the choking to surge condition (i.e, decreasing mass flow rate), at all rotational speeds, because the accuracies of both the mass flow meter and the analog input module for the mass flow rate measurements depend on both the reading and the full scale (see Table 3.2).

On the contrary, the uncertainties of the calculated pressure ratios increase with de-

creasing mass flow rates, at all rotational speeds, because the measured static pressures are higher closer to the surge condition. At the same time, the uncertainties at high rotational speeds are higher than those computed at lower rotational speeds, as a consequence of larger measured static pressures. Furthermore, a speed increase results in a larger difference between the values calculated at low mass flow rates and those obtained at high mass flow rate rates. This deviation is equal to 12.3% at 120 krpm and to 35.4% at 220 krpm. Therefore, it can be observed that, for a given speed-line, the uncertainty difference between values at low and high mass flow rates is large if the rotational speed is high as well. The trends of the calculated pressure ratios uncertainties might be due to the fact that the pressure transmitters uncertainty is function of the full scale only (see Table 3.1), but the accuracy of the analog input module for the static pressure measurements depends on both the reading and the full scale (see Table 3.2).

The uncertainties of the calculated efficiencies decrease with decreasing mass flow rate at a given speed-line, for all the rotational speeds, while they decrease with increasing rotational speed at a given mass flow rate. This is due to the fact that the total temperature uncertainty exhibits a large influence as it is propagated, although its contribution is lower than that of the static pressure uncertainty. The difference between the uncertainties at low and high mass flow rates is of the same order of magnitude for all rotational speeds.

Tables 3.5 and 3.6 show the UMFs and UPCs for the stage total-to-total pressure ratio and isentropic efficiency, respectively. Only three operating points, corresponding to three values of mass flow rate, are reported at 120, 160, and 190 krpm, since these conditions are sufficient to obtain the trends affecting these two parameters.

According to the UMFs values for the stage total-to-total pressure ratio (Table 3.5), the influence of the uncertainties due to the static pressure at the compressor inlet $(\mathrm{UMF}_{\mathrm{p}_2})$ and outlet $(\mathrm{UMF}_{\mathrm{p}_5})$ does not increase while propagating the uncertainty, since these two variables have values close to 1. The UMFs corresponding to the other variables are of the order of magnitude of 1×10^{-4}, therefore the influence of their uncertainties decreases when the latter are propagated. The UPCs for the pressure ratio show that its uncertainty largely depends on the static pressures uncertainties. Furthermore, the UMF-values are not influenced neither by the rotational speed nor by the mass flow rate, wherelse the UPC-values vary with the rotational speed and mass flow rate. In particular, $\mathrm{UPC}_{\mathrm{p}_2}$ increases with increasing rotational speed and mass flow rate, while $\mathrm{UPC}_{\mathrm{p}_5}$ shows an opposite behaviour. The latter behaviour is noticeable for $\mathrm{UPC}_{\mathrm{T}_{05}}$ as well, while $\mathrm{UPC}_{\mathrm{T}_{02}}$ is directly proportional to the rotational speed, but inversely proportional to $\dot{m}$. As a consequence, at high rotational speeds and mass flow rates, the uncertainty due to the pressure transmitters located at the compressor inlet has a pivotal contribution to the pressure ratio uncertainty.

Table 3.6 shows the UMFs and UPCs for the stage total-to-total isentropic efficiency. The influence of the pressure and temperature uncertainties, both at the inlet and outlet, increase when they are propagated. This explains why the error bars in Fig. 3.6b are larger than those in Fig. 3.6a. The influence is however lower at high rotational speeds and flow mass rates, at which the UMF-values decrease for both the static pressure and total temperature. The efficiency uncertainties are therefore less influenced by the propagation of the pressures uncertainties with increasing mass flow rate and rotational speed. As a consequence, the vertical error bars visible in Fig. 3.6b are larger at low speeds. In addition,

Table 3.5: *Uncertainty magnification factors (UMFs) and uncertainty percentage contributions (UPCs) for the stage total-to-total pressure ratio.*

Quantity		120 krpm			160 krpm			190 krpm		
$\dot{m}$ [g/s]		40	50	60	40	50	60	40	50	60
UMF_{p_2}		1.004	1.003	1.002	1.004	1.003	1.002	1.004	1.003	1.001
UPC_{p_2} [%]		57.631	61.780	63.746	71.209	72.859	73.966	78.699	79.630	79.712
UMF_{p_5}		1.004	1.002	1.001	1.002	1.001	1.001	1.002	1.001	1.000
UPC_{p_5} [%]		42.369	38.220	36.254	28.790	27.141	26.034	21.301	20.370	20.288
$UMF_{T_{02}}$	1×10^{-4}	2.230	1.370	0.821	2.110	1.390	0.839	2.110	1.460	0.695
$UPC_{T_{02}}$ [%]	1×10^{-6}	1.450	0.590	0.219	1.620	0.713	0.264	1.780	0.857	0.196
$UMF_{T_{05}}$	1×10^{-4}	1.810	0.944	0.524	1.040	0.634	0.365	0.754	0.496	0.240
$UPC_{T_{05}}$ [%]	1×10^{-6}	0.787	0.227	0.710	0.269	0.100	0.329	0.136	0.059	0.014
$UMF_{\dot{m}}$	1×10^{-4}	0.849	0.856	0.593	2.150	1.510	0.948	2.720	1.930	0.909
$UPC_{\dot{m}}$ [%]	1×10^{-5}	0.179	0.254	0.171	1.470	0.923	0.497	2.590	1.600	0.558

Table 3.6: *Uncertainty magnification factors (UMFs) and uncertainty percentage contributions (UPCs) for the stage total-to-total isentropic efficiency.*

Quantity		120 krpm			160 krpm			190 krpm		
$\dot{m}$ [g/s]		40	50	60	40	50	60	40	50	60
UMF_{p_2}		6.688	4.326	3.696	2.368	2.179	2.065	1.687	1.620	1.611
UPC_{p_2} [%]		50.039	46.883	46.568	51.420	51.757	52.473	55.587	56.086	58.574
UMF_{p_5}		6.682	4.322	3.694	2.363	2.176	2.063	1.682	1.617	1.610
UPC_{p_5} [%]		36.787	29.003	26.484	20.790	19.280	18.469	15.045	14.347	14.908
$UMF_{T_{02}}$		11.244	10.207	9.281	5.914	5.575	5.293	4.285	4.129	3.815
$UPC_{T_{02}}$ [%]		7.201	13.299	15.006	16.448	17.313	17.532	18.338	18.521	16.736
$UMF_{T_{05}}$		11.241	10.205	9.280	5.912	5.574	5.292	4.283	4.127	3.815
$UPC_{T_{05}}$ [%]		5.972	10.815	11.942	11.342	11.650	11.527	11.030	11.046	9.782
$UMF_{\dot{m}}$	1×10^{-4}	5.650	3.690	2.190	5.080	3.280	1.950	4.570	3.110	1.460
$UPC_{\dot{m}}$ [%]	1×10^{-5}	0.156	0.193	0.125	1.060	0.656	0.353	1.830	1.130	0.410

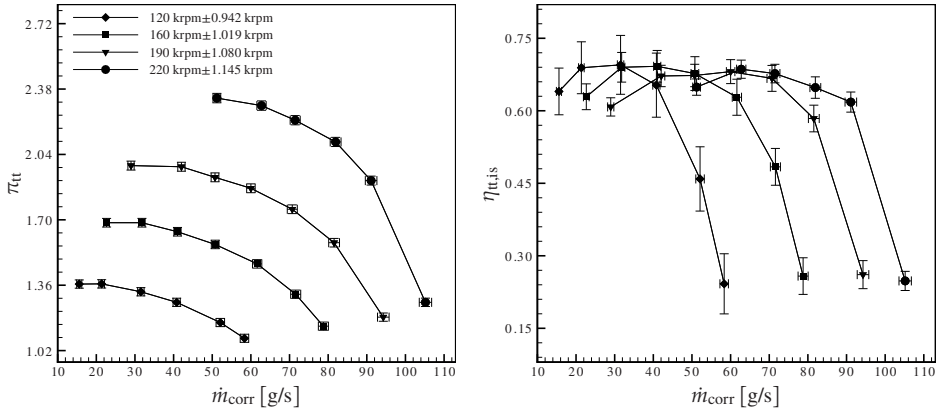

(a) *Total-to-total pressure ratio.* **(b)** *Total-to-total isentropic efficiency.*

Figure 3.7: *Performance maps of the centrifugal compressor adopted for the recuperated micro gas turbine developed by Micro Turbine Technology B.V., with reduced uncertainties due to improved static pressure measurements.*

the temperature uncertainty influence on the efficiency uncertainty increases at increasing rotational speed, for both $UPC_{T_{02}}$ and $UPC_{T_{05}}$. The same trend is noticeable for UPC_{p_2}, while the UPC_{p_5}-values diminish as the speed augments. The comparison between the UPCs for the pressure and those for the temperature shows also that the latter are smaller than the former, such that the thermocouple uncertainties produce smaller uncertainties in the efficiency than the pressure transmitters uncertainties. As for the pressure ratio, the contribution of the mass flow rate uncertainty is negligible.

The results of the uncertainty propagation analysis allow to find out that the pressure transmitters play the most important role in defining the final results uncertainties. Therefore, in order to reduce them, the accuracy of the static pressure measurements should be improved. This could be achieved (see Table 3.1) by reducing the measuring range of the pressure transmitters, such that the full scale would be lower, and by improving the accuracy of the transmitters themselves. A reduced pressure transmitters full scale would also improve the accuracy of the analog input module utilized for the static pressure measurements (see Table 3.2). Furthermore, although their contribution on the pressure ratio and efficiency uncertainties is lower than that of the pressure transmitters, improving the accuracy of the thermocouples would also lead to reduced uncertainties of the final results.

Figure 3.7 shows the performance maps of the centrifugal compressor in case the pressure transmitters full scale would be reduced to 1.2 bar and 4 bar at the compressor inlet and outlet, respectively. The uncertainties of the pressure ratio and efficiency would decrease noticeably at all rotational speeds and mass flow rates. The uncertainties of the mass flow rate would be lower as well.

Table 3.7 summarizes the average uncertainties of the calculated performance quantities at all rotational speeds, due to improved static pressure measurements. The average uncertainties of the corrected mass flow rate are 11.8%, 19.0%, 21.8%, and 23.1% lower

Table 3.7: *Average uncertainties of the corrected mass flow rate* ($\dot{m}_{corr}$)*, corrected rotational speed* (N_{corr})*, stage total-to-total pressure ratio* (π_{tt})*, and stage total-to-total isentropic efficiency* ($\eta_{tt,is}$)*, due to improved static pressure measurements.*

Quantity	120 krpm	160 krpm	190 krpm	220 krpm
$\dot{m}_{corr}$	2.69%	2.01%	1.83%	1.73%
N_{corr}	0.78%	0.63%	0.57%	0.52%
π_{tt}	1.68%	1.49%	1.33%	1.20%
$\eta_{tt,is}$	10.77%	6.57%	4.73%	3.65%

than the values shown in Table 3.4, at 120, 160, 190, and 220 krpm, respectively. The average uncertainties of the compressor stage total-to-total pressure ratio decrease by 54.5%, 57.9%, 61.0%, and 63.6%, while those of the total-to-total isentropic efficiency decrement by 42.0%, 45.6%, 47.4%, and 48.7%. The uncertainties of the corrected rotational speed did not change, because they are not affected by static pressure measurements.

3.5 Conclusions

An experimental set-up called μTURCO-rig, which is capable of providing the performance maps of very small, high-speed centrifugal compressors, has been designed, commissioned, and built. The main features of the μTURCO-rig and the most important experimental results can be summarized as follows:

- The compressor impeller is driven by a turbine powered by pressurized air coming from a buffer tank, pressurized in turn by two screw compressors. The shaft speed is varied by a turbine control valve, while further equipment (e.g., compressor throttle, inlet and outlet pipes, oil lubrication system) necessary to operate the test-rig was also integrated into the set-up, as well as the instrumentation and data acquisition system.

- The test-rig is robust, reliable, and versatile, as it can accomodate impellers with diameters up to 20 mm, and rotational speeds up to 220 krpm.

- An initial experimental campaign allowed to obtain the preliminary performance maps of the compressor stage currently adopted for the MTT micro gas turbine, at a rotational speed as high as 220 krpm.

- The aerodynamic performance of the micro turbine compressor has been quantified by means of a series of experiments carried out at four different corrected rotational speeds (i.e., 120, 160, 190, and 220 krpm), from high to low mass flow rates. The

surge condition was identified when the typical sound emitted by the vibrating compressor blades was heard.

- The highest estimated stage total-to-total isentropic efficiency is approximately 0.7 at all rotational speeds, while the maximum measured stage total-to-total pressure ratio is equal to 2.3 at 220 krpm.
- The results of these experiments have been summarized in the form of performance maps, and have also been used for the validation of the numerical models described in Chaps. 2 and 4.
- The uncertainty propagation analysis has been carried out, according to the methodology briefly described here, and the results have been displayed in the form of error bars in the performance maps, and in tables.
- The results of the uncertainty propagation analysis show that the static pressure uncertainty highly influences both the pressure ratio and efficiency uncertainties. In particular, the uncertainty of the compressor inlet static pressure is preponderant with respect to that of the outlet static pressure.
- Substituting the actual pressure transmitters with ones having better accuracy and lower full scale would therefore reduce the uncertainties of the final results. For example, the uncertainties of the corrected mass flow rate, stage total-to-total pressure ratio, and stage total-to-total isentropic efficiency could be on average 18.9%, 59.3%, and 45.9% lower than those calculated with the current pressure transmitters.
- Also the total temperature uncertainty contributes to the efficiency uncertainty, but to a lower degree than the static pressure uncertainty. The mass flow rate uncertainty does not have any impact at all on the pressure ratio and efficiency uncertainties.
- The μTURCO-rig will also be used in the future to experimentally verify newly designed configurations which aim to improve the micro turbine compressor performance, or other very small centrifugal compressors.

"The world's an exciting place when you know CFD."

John N. Shadid.

4

Numerical aerodynamic analysis

This chapter presents the numerical study performed with a commercial computational fluid dynamics code which solves the three-dimensional Reynolds averaged Navier-Stokes equations. Steady-state simulations have been carried to approximate the real, time-dependent flow physics with satisfactory results and shorter computational time with respect to an unsteady approach. The analysis allowed to acquire further knowledge about the compressor flow structure, performance, and loss mechanisms, and to understand the tip clearance influence on the compressor flow field and performance.

Excerpts of this chapter appeared in:
Olivero M., Javed A., Pecnik R., Colonna P., and van Buijtenen J. P., 2011, "Study on the Tip Clearance Effects in the Centrifugal Compressor of a Micro Gas Turbine by Means of Numerical Simulations," *Proc. International Gas Turbine Congress 2011*, IGTC2011-0233.
Olivero M., Javed A., and van Buijtenen J. P., 2010, "Aerodynamic Analysis of a Micro Turbine Centrifugal Compressor," *Proc. ASME Turbo Expo 2010*, GT2010-23112.

4.1 Introduction

Computational fluid dynamics (CFD) has been extensively used in recent years for the analysis of the flow through rotating turbomachinery, and nowadays has become an essential tool for the design of all types of turbomachinery.

Although it is not an exact science, since the results of its application can be uncorrect due to numerical and modelling errors, unknown boundary conditions and geometric details, and wrong assumptions about the flow steadiness [62], CFD has been fully integrated in the early phases of the design process because of the high costs associated with experiments.

This is particularly true for centrifugal compressors, which experience viscous, turbulent, unsteady, and three-dimensional (3D) flows, whose measurements could be extremely expensive or even impossible to realise. As a consequence, CFD is required for a better understanding of these flow phenomena, and provides fundamental advancements in analysing the flow field inside a centrifugal compressor.

This chapter describes the numerical investigation of the centrifugal compressor adopted by the micro turbine under development at Micro Turbine Technology B.V. (MTT) by means of a commercial CFD code which solves the 3D Reynolds averaged Navier-Stokes (RANS) equations. The analysis has been performed by using a steady-state model, which approximates the real, time-dependent flow physics with satisfactory results and shorter computational time with respect to an unsteady approach.

The simulations have allowed understanding the most significant flow phenomena of the compressor flow field (e.g., supersonic relative Mach number at the tip of the impeller blades, and impeller secondary flow structures), and the influence of the impeller tip clearance on the compressor performance and flow field.

4.2 Computational method

4.2.1 Geometry and grid generation

The 3D impeller geometry has been created with a geometry creation tool specialized for turbomachinery blades [8], which allowed defining the curves for the hub, shroud, and blade profiles (Fig. 4.1).

At first, the impeller has been modeled without considering the tip clearance, in order to simplify the creation of the geometry and the following grid generation. As a consequence, to avoid complications and uncertainties in the CFD computations due to the tip clearance, in the simulated geometry the blade has been extended up to the shroud. Furthermore, a 13.45-mm-long stationary inlet duct has been placed in the numerical domain, upstream of the impeller, in order to reduce the effect of the inlet boundary condition on the potential field of the blade. The volute has not been included in the computational domain because its geometric details were not available.

Figure 4.2a shows the structured grid of an impeller passage containing a full and a splitter blade, which has been generated with a meshing tool tailored for the CFD analysis

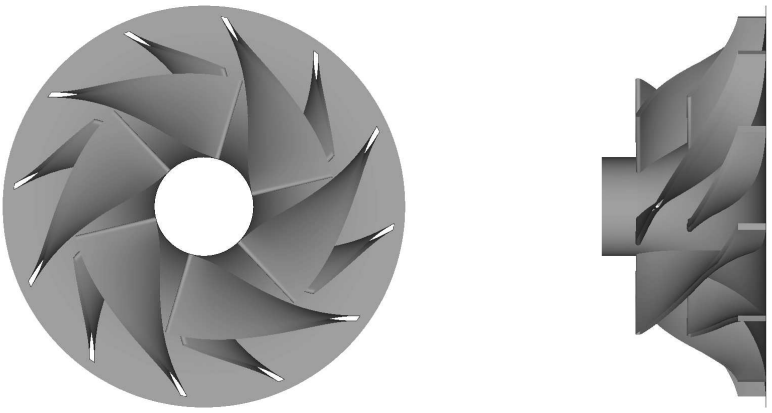

(a) *Front view.* **(b)** *Side view.*

Figure 4.1: *The impeller geometry created for the computational fluid dynamics analysis.*

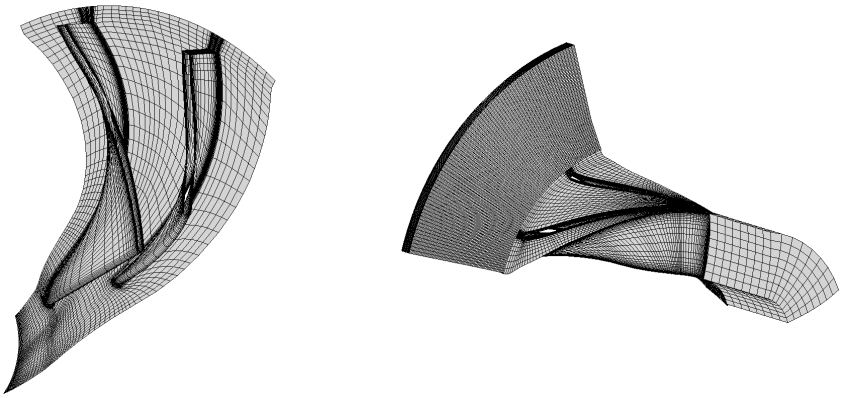

(a) *The impeller hub and blades.* **(b)** *The whole domain.*

Figure 4.2: *The domain grid for the computational fluid dynamics analysis.*

Table 4.1: *Grid cell number of the components of the computational domain.*

Inlet duct	Impeller	Diffuser	Total
512	161,568	122,400	284,480
512	321,984	320,000	642,496
512	638,080	633,600	1,272,192

of turbomachinery blade rows [10]. The adopted topology is based on a H-Grid method, whereby an O-Grid is added around the blades to increase the grid orthogonality in that region. The grids of the inlet duct and the vaneless diffuser (Fig. 4.2b) have been generated using a multi-purpose grid generator for unstructured grids [90]. To resolve the boundary layer on the impeller and vaneless diffuser walls, the dimensionless wall distance y^+ of the first grid node off the wall has been set equal to 1.

Overall, for the case without tip clearance, the computational domain grid has 642,496 hexahedral elements. The choice of the cell number is the consequence of a grid sensitivity analysis performed at the micro turbine design point (i.e., $\dot{m}$ = 50 g/s and N = 240 krpm), and summarized in Table 4.2, which compares for three grid sizes (see Table 4.1) total and static pressures, total and static temperatures, and absolute and relative velocities calculated at the impeller inlet, at the impeller blades leading and trailing edges, and at the diffuser inlet and outlet. For the impeller, the largest deviation is equal to 3.3%, is calculated for the absolute velocity between the baseline and the fine grids, and occurs at the blades leading edge. The average difference between the baseline grid and the coarse and fine ones is equal to 0.35% at the impeller inlet and blades leading edge, then it increases to 0.63% at the impeller blades trailing edge. For the diffuser, the largest deviation is calculated for the static pressure between the baseline and the finer grids, is equal to 2.3%, and occurs at the inlet. The average difference between the baseline grid and the coarse and fine ones is equal to 0.76% at the inlet and decreases to 0.63% at the outlet. For both the impeller and diffuser, in general the differences between the coarse and the baseline grids are negligible, wherelse they are slightly larger between the baseline and fine grids.

The numerical computations have been simplified by neglecting the clearance gap. However, tip clearances have a significant impact on compressors performance and such influence is even more remarkable for small turbomachinery. Thus, including the clearance gap between the blades tip and the shroud was the following step to improve the accuracy of the CFD simulations, and analyze the dependence of the compressor performance on the clearances. In particular, a 0.375-mm-tip-clearance has been measured with a calliper, with the compressor standing still in ambient air, as the difference between the shroud and the blade tip diameters at the inducer. Due to thermal expansion, impeller tip deflection, shaft bending, and inertia effects, the tip clearance in running conditions is lower than that measured and therefore not exactly known. As a consequence, it has been assumed to be constant from the leading to the trailing edge of the impeller blades, and three other dif-

Table 4.2: *Impeller and diffuser flow parameters comparison for the grid sensitivity analysis. Total* (p_0) *and static* (p) *pressures, total* (T_0) *and static* (T) *temperatures, and absolute* (C) *and relative* (W) *velocities are compared at the impeller inlet, at the impeller blades leading and trailing edges, and at the diffuser inlet and outlet for three grid sizes. The values have been normalized by those relative to the 642,496-cell grid.*

# cells	p	p_0	T	T_0	C	W
Impeller inlet						
284,480	1.000	1.000	1.000	1.000	1.000	1.000
642,496	1.000	1.000	1.000	1.000	1.000	1.000
1,272,192	0.997	1.001	0.999	1.000	1.033	1.005
Impeller blades leading edge						
284,480	0.999	1.000	1.000	1.000	0.994	1.002
642,496	1.000	1.000	1.000	1.000	1.000	1.000
1,272,192	0.998	1.000	0.999	1.000	1.022	1.008
Impeller blades trailing edge						
284,480	0.998	1.000	0.999	1.002	1.003	1.012
642,496	1.000	1.000	1.000	1.000	1.000	1.000
1,272,192	1.019	1.010	1.000	0.998	1.005	0.981
Diffuser inlet						
284,480	0.991	0.996	0.999	1.000	1.012	/
642,496	1.000	1.000	1.000	1.000	1.000	/
1,272,192	1.023	1.012	1.001	0.998	1.012	/
Diffuser outlet						
284,480	0.991	0.991	0.999	0.999	0.994	/
642,496	1.000	1.000	1.000	1.000	1.000	/
1,272,192	1.016	1.013	0.999	0.998	0.995	/

Table 4.3: *Simulated tip clearance values. The relative tip clearance is calculated as the ratio of the tip clearance to the blade height at the impeller outlet* ($RC = c/b_2$).

c [mm]	0.052	0.130	0.182	0.375
RC [%]	2.0	5.0	7.0	14.4

ferent values of tip clearance have been studied (see Table 4.3). In the table, the relative tip clearance is calculated as the ratio of the tip clearance to the blade height at the impeller outlet ($RC = c/b_2$). In the numerical domain, the tip clearance has been changed by reducing the blade height from the case with no tip clearance, in order not to affect the operating condition, thus the velocity triangles, and keep the flow passage area constant. For the four cases, the impeller grid cell number has increased to 426,674 hexahedral elements, because 10 cells have been added in the spanwise direction in the tip clearance area. In the literature, a lower cell number for even larger clearance gaps has also been used [110, 143], while Weiss *et al.* [273] stated that a three-cell layer in the clearance gap is sufficient for accurate prediction of clearance flows. Moreover, the turbulence model in the adopted CFD code automatically switches on the wall functions for higher values of y^+.

4.2.2 Numerical aspects and boundary conditions

The computational analysis has been performed by means of the commercial CFD code which solves the 3D RANS equations using a finite-volume-based method [9]. The convergence of the steady-state simulations has been set to 1×10^{-5} for the root mean square residuals of all the equations and has been controlled through a physical timescale option. In the current analysis, the timescale factor has been calculated as $1/\omega$, where ω is the angular velocity expressed in rad/s. The mass, momentum, energy, and turbulence equations have been solved with a high-resolution advection scheme. Furthermore, mass-flow-averaged total properties and area-averaged static properties [52] have been used for monitoring purposes during the simulations and for the post-processing of the results.

The definition of the boundaries of the computational domain is shown in Fig. 4.3. At the inlet, total pressure (i.e., 101,325 Pa) and temperature (i.e., 293.15 K) have been specified, while the direction has been set normal to the inlet plane. The turbulence intensity at the inlet has been kept at 5%, which is the recommended value when no information about the inlet turbulence is available. At the outlet, a mass flow rate has been imposed at the design point, but a static pressure has been specified at off-design operating conditions.

The working fluid for the simulations is air and its thermodynamic properties are obtained with the ideal gas equation of state, with a molar mass of 28.96 kg/kmol. A zero-pressure polynomial equation with four coefficients has been applied to describe the specific heat capacity, since a thermally perfect gas would better approximate the behaviour of the specific heat capacity at constant pressure (c_p) in comparison to a calorically perfect

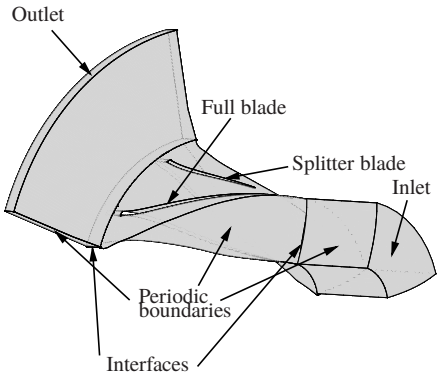

Figure 4.3: *The domain boundaries for the computational fluid dynamics analysis.*

gas. This is due to the fact that the latter exhibits constant c_p and c_v (i.e., the specific heat capacity at constant volume), while the former is characterized by thermodynamic and chemical equilibrium; specific gas constant R as function of c_p and c_v only; internal energy, enthalpy, and specific heat capacities as functions of temperature only. Sutherland's law has been used for the dynamic viscosity and the thermal conductivity.

The total energy model has been switched on to include the heat transfer and the shear stress transport $k-\omega$ (SST $k-\omega$) turbulence model [181, 182] has been adopted. This model was developed to overcome the deficiencies of the standard $k-\omega$ model developed by Wilcox [278–280] and the baseline $k-\omega$ model introduced by Menter [181, 182]. The latter combines the advantages of the $k-\omega$ and the $k-\epsilon$ models, but still fails to properly predict the onset and amount of flow separation from smooth surfaces, because it does not account for the transport of turbulent shear stress, leading to an overprediction of the eddy viscosity. On the contrary, the SST $k-\omega$ model accounts for the transport of the turbulent shear stress and gives highly accurate predictions of the onset and the amount of flow separation under adverse pressure gradients by including the transport effects into the formulation of the eddy viscosity. This in turns gives an improvement in terms of flow separation predictions, as demonstrated in many test cases [19, 20].

The lateral faces of the domain have been specified as rotational periodic boundaries and the walls have been modeled as adiabatic and smooth. The impeller shroud has been specified as counter-rotating, such that the relative motion between the rotating impeller and the stationary shroud is captured. The no-slip condition has been imposed on all walls, apart from the inlet duct shroud and hub, where the free-slip condition has been used, in order not to account for losses in this portion of the domain.

For the steady-state simulations, the frozen rotor approach has been used at the interface between the stationary and rotating components. In this model, the frame of reference is changed, but the relative orientation of the components across the interface is fixed, such that the two frames of reference are connected to each other with a fixed relative position

throughout the calculation. When the frame changes, the appropriate equation transformations are made and the fluxes are scaled by the pitch change. This kind of analysis requires the least amount of computational effort, but the transient effects at the interface are not modeled, thus the losses occurring as the flow is mixed between stationary and rotating components are not accounted for.

4.3 Results and discussion

The first part of the section deals with the 0%-relative-tip-clearance configuration. The comparison between the experimental and numerical results is firstly described, then the analysis of the compressor flow field follows. The second part of the section deals with the investigation of the tip clearance influence on the compressor performance. The CFD results are firstly compared to the experimental data, then the tip clearance influence on the performance and flow field is described.

4.3.1 The case without tip clearance

Comparison between experimental and numerical results

Figure 4.4 shows the comparison between the numerical results and the experimental data (see Chap. 3) at 120, 160, 190, and 220 krpm, and varying mass flow rate, respectively. The experimental value for the design point has been provided by MTT. Since the volute has not been included in the numerical domain, the one-dimensional (1D) model introduced in Chap. 2 has been used to take into account the realistic effects of diffusion and losses in this component. In the figure, the stage total-to-total pressure ratio and isentropic efficiency are plotted as a function of the corrected mass flow rate at four corrected rotational speeds.

Before describing in detail the comparison performed here, it is important to highlight the main assumptions taken to create the CFD domain, since they are likely to be the cause of the differences between experimental and numerical results. Eventual discrepancies might then be explained by the absence of

- The long pipe located at the compressor inlet in the μTURCO-rig.
- The heat transfer through the compressor walls, since the computations have been performed adiabatically.
- The tip clearance, which would affect somehow the maximum mass flow rate and reduce the pressure ratio and efficiency.
- The surface roughness, because smooth walls have been used in the CFD domain.
- The leakage between the impeller back disk and the diffuser.

The CFD simulations capture the pressure ratio trend, but they overpredict it, at all rotational speeds (Fig. 4.4a). The deviation between numerical and experimental results

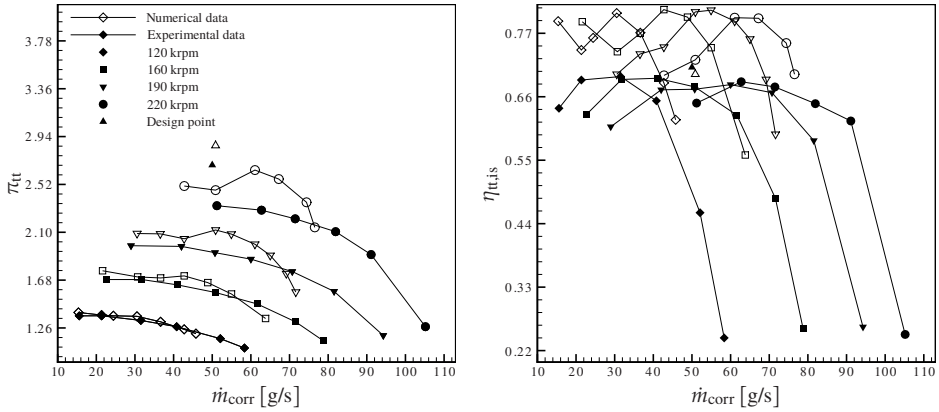

(a) *Total-to-total pressure ratio.* **(b)** *Total-to-total isentropic efficiency.*

Figure 4.4: *Comparison of stage total-to-total pressure ratio and isentropic efficiency between numerical (hollow symbols) and experimental (closed symbols) results at 120, 160, 190, and 220 krpm, and varying mass flow rate, respectively, and at the micro turbine design point (i.e., $\dot{m}$ = 50 g/s and N = 240 krpm), for the case without tip clearance.*

increases with increasing speed at low mass flow rates, at which a better agreement is however noticed up to the speed-line corresponding to 220 krpm. Particularly, at the lowest mass flow rate, the discrepancy between computations and measurements increases from 1.8% at 120 krpm to 6.4% at 220 krpm. On the other hand, the numerical computations anticipate the choking condition, in that the lowest pressure ratio is reached by the CFD model at a lower mass flow rate, at all rotational speeds. By comparing the lowest pressure ratio obtained through the numerical model with the closest experimental datum, it can be seen that the deviation in terms of mass flow rate decreases with increasing speed. The difference increases from −12.9% at 120 krpm to −4.5% at 220 krpm. At the design point, the CFD model overpredict the experimental value by 6.0%.

The numerical computations are also able to capture the efficiency trend at all rotational speeds (Fig. 4.4b), although they overpredict the efficiency with respect to the experimental values. This is not true at the design point, since the CFD value is 1.7% lower than the experimental one. Further on, contrarily to what was seen for the pressure ratio, at low mass flow rates the deviation between CFD and experimental values decreases from 17.7% at 120 krpm to 11.2% at 220 krpm. By increasing the mass flow rate, once again the numerical model anticipate the choking condition, such that in general the largest deviations are seen at off-design conditions at all speeds. Further on, the CFD simulations show that the compressor best-efficiency-point is of the same magnitude for all speeds and occurs very close to the mass flow rate at which it is calculated with the experimental data at 120 and 160 krpm, while it occurs at a lower mass flow rate at 190 and 220 krpm. The difference between numerical and experimental values is −8.0% for the former and 19.0% for the latter.

The numerical simulations are thus capable of capturing the characteristic curves of

the overall compressor performance, though some difficulties are faced in identifying the choking condition, because with increasing speed the CFD computations anticipate it with respect to the experiments. However, for this analysis, the limitations of the frozen rotor approach and of the turbulence model, especially at off-design conditions, must be taken into account. Particularly, the use of a steady-state model can give misleading results for operating conditions far from the design point, where the flow can strongly recirculates at the impeller-diffuser interface, and eventually the turbulence model might not satisfy completely the calculations. The 1D code used to calculate the flow properties at the volute outlet could also lead to errors, since it is an approximation employed to account for the losses in this component.

Since the MTT micro turbine will operate at the design point or in its proximity for most of the time, it can be concluded that the CFD results are sufficiently reliable.

Flow field analysis

Figure 4.5 shows the relative Mach number, meridional velocity, and normalized entropy contours on different sections normal to the meridional direction, at the micro turbine design point. The shown sections are located at eight streamwise positions, from 20 to 90% of the impeller meridional length, separated by a 10%-step.

The relative Mach number is illustrated in Fig. 4.5a. A region of supersonic relative Mach number can be seen at the full blade leading edge, on the suction side. It extends normal to the blade in the pitchwise (i.e., tangential) direction, but it also grows in the spanwise (i.e., from the impeller hub to shroud) direction, from the full blade tip to about 1/4 of the full blade height. At the design point, the meridional component of the absolute velocity is high, due to a relative high mass flow rate. As a consequence, the relative flow angle is lower than the blade angle, leading to a positive angle of incidence, which forces the flow to accelerate as it enters the blade rows. The region of high velocity is then followed by an area of low relative Mach number, which grows along the streamwise (i.e., from the impeller inlet to outlet) direction both in the spanwise and in the pitchwise directions. In particular, the relative Mach number decelerates more rapidly in the impeller passage between the full blade suction side and the splitter blade pressure side. By moving towards the impeller outlet, the region of low velocity increases in thickness from the shroud. The maximum extension from shroud to hub occurs at the full blade trailing edge. On the contrary, at the splitter blade trailing edge the relative Mach number is below unity, but the region of low relative Mach number generated from the full blade suction side interacts with the splitter blade as well. When this area encounters the splitter blade leading edge, a thin region of low velocity is created on the splitter blade suction side. Its thickness increases in the spanwise direction towards the splitter blade trailing edge, where it has the maximum extension.

Figure 4.5b shows the meridional velocity, which is the absolute velocity component that represents the mass flow rate, through the continuity equation. Similarly to what has been noticed for the relative Mach number, a low-velocity region developing from the shroud can be observed on the suction sides of both the full and splitter blades, although it is larger for the former. At the trailing edge it extends from the shroud down to the hub.

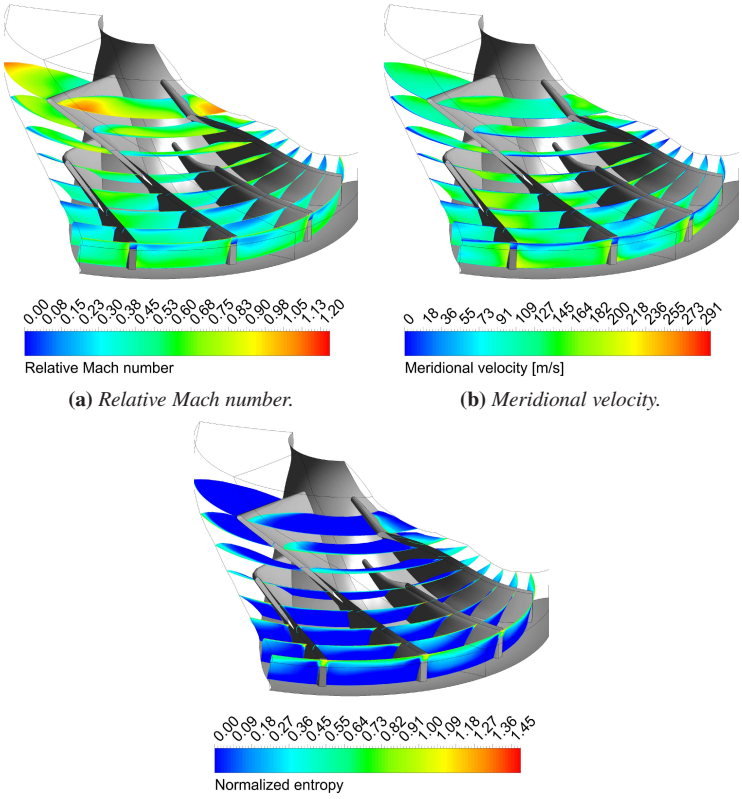

(a) *Relative Mach number.* **(b)** *Meridional velocity.*

(c) *Normalized entropyy.*

Figure 4.5: *Relative Mach number, meridional velocity, and normalized entropy contours on eight impeller sections normal to the meridional direction, at the micro turbine design point (i.e., $\dot{m}$ = 50 g/s and N = 240 krpm), for the case without tip clearance. The entropy has been normalized by the air specific gas constant* $(R = 287\ J/kg{\cdot}K)$.

The highest meridional velocity occurs near the hub on the suction sides.

As a consequence of the wake development at the shroud/suction side, losses are expected to be generated in this part of the impeller. Figure 4.5c illustrates the entropy generation in the impeller bladed passages. The entropy has been normalized by the air specific gas constant $(R = 287\ J/kg{\cdot}K)$. On each of the sections shown in the figure, the losses productions concentrates in the proximity of the shroud, while at the full blade leading edge it corresponds to the high-relative Mach number region visible in Fig. 4.5a. The entropy production is largest at the blades trailing edge, very close to the shroud.

Since the highest loss production has been found close to the shroud, a detailed insight of this region is given in Fig. 4.6, which shows the relative Mach number and static pressure contours on a section located at 90% of the impeller spanwise direction.

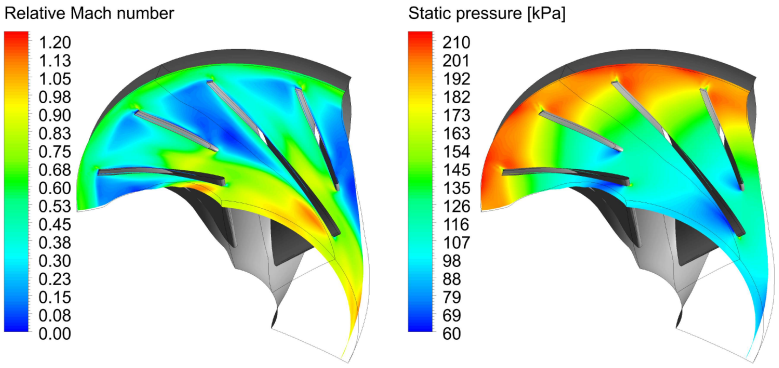

(a) *Relative Mach number.* **(b)** *Static pressure.*

Figure 4.6: *Relative Mach number and static pressure contours on a section located at 90% of the impeller spanwise direction, at the micro turbine design point (i.e., $\dot{m}$ = 50 g/s and N = 240 krpm), for the case without tip clearance.*

As visible in Fig. 4.6a, the relative Mach number is supersonic at the full blade leading edge, where a big region of high velocity develops on the suction side, and extends upstream normal to the suction side. At the splitter blade leading edge the relative Mach number is about 0.8. On the suction sides of both blades, the relative Mach number then decreases in the streamwise direction. A large wake develops right behind the high-velocity region visible on the full blade, but on the splitter side the low-velocity region is more visible only further downstream.

Figure 4.6b shows that an area of low static pressure is visible on the full blade suction side and at the splitter blade leading edge. The static pressure increases on the splitter blade pressure side from the leading to the trailing edges, while for the full blade it is constant up to about half length, then starts increasing towards the trailing edge. A very small region of high static pressure is also visible at the full blade leading edge. This can explain the large difference between the static pressure on the full blades suction and pressure sides, in proximity of the full blades leading edge. On the other hand, the static pressure difference between the splitter blades sides is lower.

Finally, the calculated static pressure recovery coefficient of the vaneless diffuser (see Eq. 5.1) is equal to 0.47. It is thus located at the lower end of the ranges documented in the literature [137, 151], since less than 50% of the high kinetic energy available at the diffuser inlet is converted into static pressure.

4.3.2 The case with tip clearance

Comparison between experimental and numerical results

Figure 4.7 illustrates the tip clearance influence on the compressor stage performance at 220 and 240 krpm, and varying mass flow rate, respectively. The comparison at the

two rotational speeds has not been plotted on the same graph in order to have a better visualization of the results. The case without tip clearance has been included as well to calculate the performance drop with increasing tip clearance. The experimental results at 220 krpm and varying mass flow rate, and at the micro turbine design point are also shown in Fig. 4.7.

The performance drop with increasing tip clearance at both rotational speeds can be noticed from Fig 4.7, although the values for the 2%-relative-tip-clearance are very close to those of the case without clearance, especially at low mass flow rates.

The tip clearance influence is stronger on the pressure ratio than on the efficiency, as a consequence of a lower influence on the temperature, but in both cases the differences increase with increasing mass flow rate and tip clearance.

In particular, the deviation with respect to the 0%-relative-tip-clearance increases with increasing mass flow rate, showing thus a stronger influence close to the choking condition for all the tip clearances. This trend is more visible at 240 krpm. On the contrary, close to the surge condition the deviations from the case without tip clearance are lower, and are almost of the same order of magnitude for both speeds.

The following correlation between tip clearance and efficiency drop has been published as an empirical formula [233]

$$-\frac{\Delta\eta}{\eta} = \frac{2ac}{b_1 + b_2}, \tag{4.1}$$

where a is a constant, c is the clearance gap, and b_1 and b_2 are the blade height at the leading and trailing edges, respectively. Eckert and Schnell [69] chose $a = 0.9$, while Pfleiderer [206] recommended $a = 1.5 \div 3.0$. The average line calculated by Pampreen [201] roughly agrees with the equation given by Eckert and Schnell, provided that $b_1/b_2 = 4$ and $\eta = 0.8$. In this case, the stage total-to-total isentropic efficiency decrement at design point can be estimated with $a = 1.67$, provided that $\eta = 0.699$ and $b_1/b_2 = 3.19$. The value for a is then within the interval suggested by Pfleiderer [206].

The comparison described here confirms thus that the values of tip clearance chosen for the analysis are plausible, since the deviation between computational and experimental results is generally in a good range of confidence, although at design point the numerical results are lower than the experimental data, even for the 0%-relative-tip-clearance. However, the computational study cannot be utilized to estimate the tip clearance in running conditions, because the CFD results do not show a constant relationship with the test data, at the different tip clearance values. Such analysis should then be carried out through an experimental campaign, whose results might solidify the CFD results shown here.

Flow parameters at the impeller outlet

Figure 4.8 shows the tip clearance influence on the flow parameters at the impeller outlet, at the micro turbine design point. The velocities have been normalized by the blade speed at the impeller blades trailing edge ($U_{TE} = 465$ m/s), while pressures and temperatures have been normalized by the total pressure and temperature specified at the CFD domain inlet (see Sec 4.2.2).

Since the tip clearance has been changed by trimming the blade, in order not to change

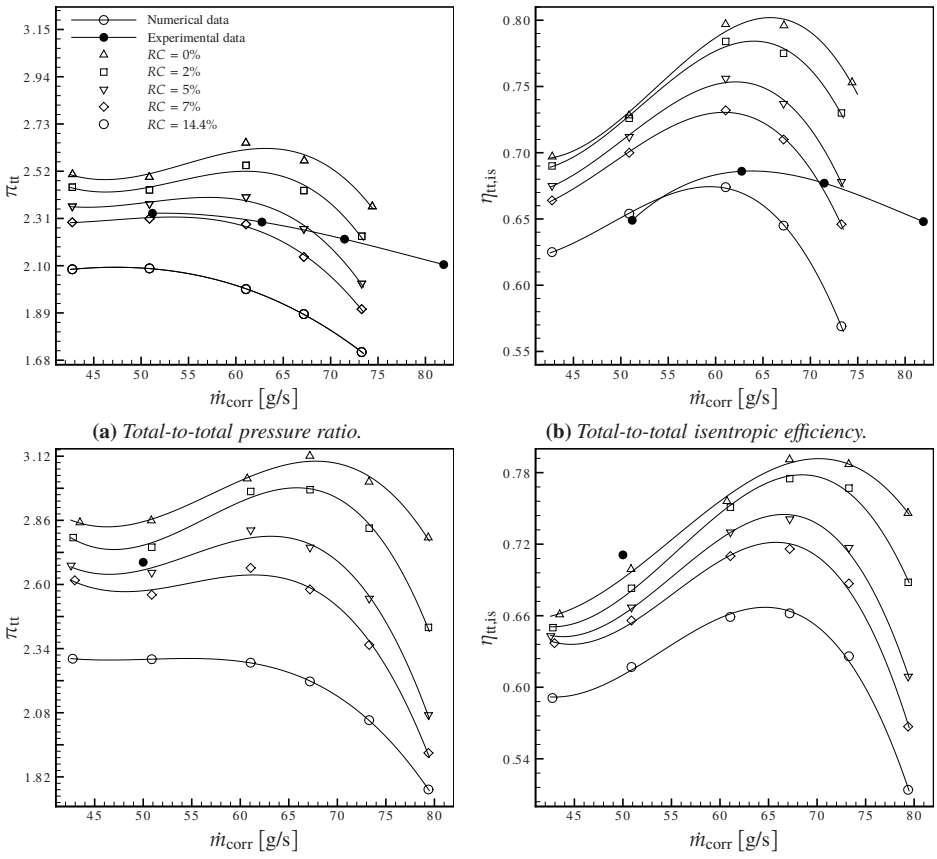

(a) *Total-to-total pressure ratio.*

(b) *Total-to-total isentropic efficiency.*

(c) *Total-to-total pressure ratio.*

(d) *Total-to-total isentropic efficiency.*

Figure 4.7: *Tip clearance influence on the stage total-to-total pressure ratio and isentropic efficiency at 220 (above) and 240 (below) krpm, and varying mass flow rate, respectively. The relative tip clearance* (RC) *is calculated as the ratio of the tip clearance to the blade height at the impeller outlet. The experimental results at 220 krpm and varying mass flow rate, and at the micro turbine design point (i.e.,* $\dot{m}$ *= 50 g/s and* N *= 240 krpm) are also shown.*

the flow passage area, an increase in clearance gap causes the blade to be shorter. For constant mass flow rate and rotational speed and negligible density change, the meridional velocity therefore increases with increasing tip clearance, as does the tangential velocity, although the tip clearance influence is small for both components (Fig. 4.8b). By increasing the tip clearance from 0 mm to 0.375 mm, the meridional and the tangential velocities increase by 16.1% and 11.2%, respectively.

This translates into the relative velocity increment, and in the absolute velocity decrease with increasing tip clearance, though the former shows an increase rate steeper than the decrement of the latter (Fig. 4.8a). By cutting down the blade to achieve the highest tip clearance, the absolute velocity drops by 5.1% while the relative velocity increases by 12.1%. Furthermore, the steepest increase of the relative velocity occurs by doubling the tip clearance from 0.182 to 0.375 mm, wherelse at lower clearance gaps the slope is flatter. The same trend is visible for the absolute velocity.

Consequently, the absolute flow angle is slightly influenced by the tip clearance, since the tangential and meridional velocities increase with the same slope, while the relative flow angle decreases noticeably with increasing tip clearance (Fig. 4.8c). The flow direction at the diffuser seems thus to be influenced only to a small extent by the tip clearence.

Furthermore, both the total and static pressures decrease with increasing tip clearance, although the total pressure shows a steeper descent slope as a consequence of the decrease in absolute velocity (Fig. 4.8d). The pressures decrease linearly with increasing clearance gap, while the temperatures show a faster descent from the 5%-relative-tip-clearance (Fig. 4.8e). The total and static temperatures decrease both as the gap becomes larger, but their decrement is slower than for the pressures. Particularly, the slope is 0.42% and 0.35% for the total and static temperature, respectively, and it increases to 4.3% and 2.6% for the total and static pressures, respectively.

The impeller total-to-total isentropic efficiency is shown in Fig. 4.8f, where the linear correlation between tip clearance change and efficiency drop can be seen as well. As a result of the numerical simulations performed for this investigation, the latter relationship is $\Delta\eta = -0.53RC$, which indicates a steeper decrement than that found in the literature, such as $\Delta\eta = -0.30RC$ [139, 201], $\Delta\eta = -0.35RC + 0.01$ for $RC > 0.03$ [189] and $\Delta\eta = -0.25RC$ for $RC < 0.1$ [233]. The efficiency decreases with increasing tip clearance, and the deficit can be calculated by means of Eq. 4.1 if $a = 1.37$, provided that $\eta = 0.804$ and $b_1/b_2 = 3.19$. In this case a is 9.5% lower then the left-hand side margin of the range proposed by Pfleiderer [206].

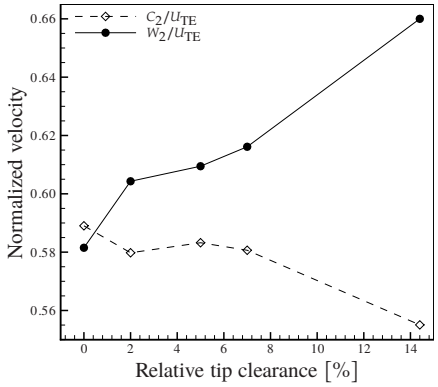

(a) *Absolute* (C_2) *and relative* (W_2) *velocity.*

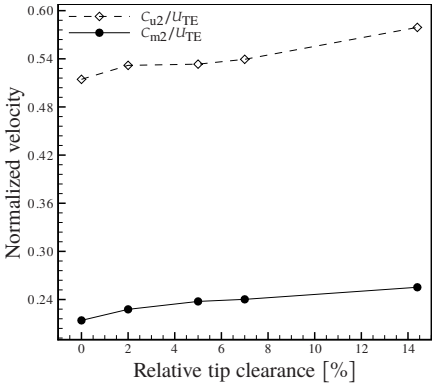

(b) *Tangential* (C_{u2}) *and meridional* (C_{m2}) *velocity.*

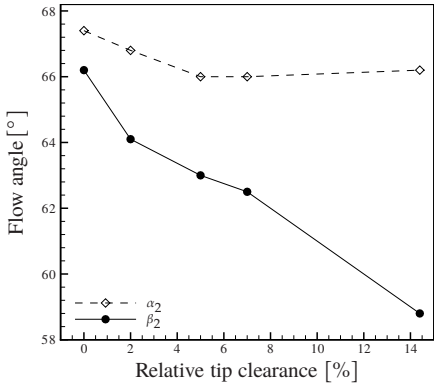

(c) *Absolute* (α_2) *and relative* (β_2) *flow angle.*

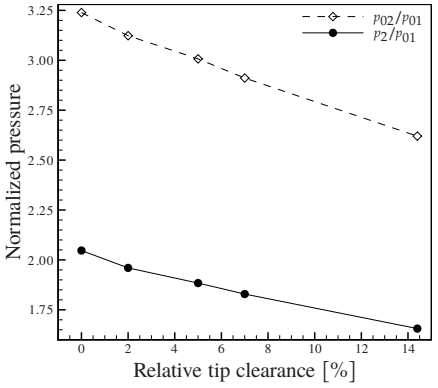

(d) *Total* (p_{02}) *and static* (p_2) *pressure.*

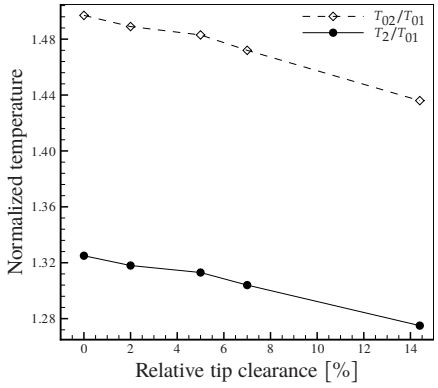

(e) *Total* (T_{02}) *and static* (T_2) *temperature.*

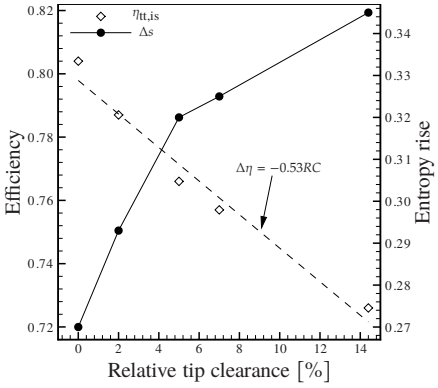

(f) *Total-to-total isentropic efficiency* $(\eta_{tt,is})$ *and entropy rise* (Δs).

Figure 4.8: *Tip clearance influence on the impeller outlet flow parameters at the micro turbine design point (i.e.,* $\dot{m}$ *= 50 g/s and* N *= 240 krpm). The relative tip clearance is calculated as the ratio of the tip clearance to the blade height at the impeller outlet. The velocities have been normalized by the blade speed at the impeller blades trailing edge* $(U_{TE}$ *= 465 m/s). Pressures and temperatures have been normalized by the total pressure and temperature specified at the computational domain inlet* $(p_{01}$ *= 101,325 Pa and* T_{01} *= 293.15 K).*

Figure 4.8f illustrates the entropy rise at the impeller outlet, that is defined as [94]

$$\Delta s = \frac{\gamma}{\gamma - 1} \ln\left(\frac{T}{T_{01}}\right) - \ln\left(\frac{p}{p_{01}}\right), \tag{4.2}$$

where γ is the ratio of the specific heat capacities, and p_{01} and T_{01} are the total pressure and temperature at the impeller inlet. The static pressure p and the static temperature T have been calculated at the impeller outlet. The entropy raises more by increasing tip clearances, but it does so at a slower rate as the clearances become larger, as a consequence of a steeper decrease in total temperature at higher clearances. In particular, the entropy increases by 1% for every tip clearance percent if $RC \leq 5\%$, but the slope diminishes to 0.26% for $5\% \leq RC \leq 14.4\%$.

Impeller streamwise distribution of the flow parameters

Figure 4.9 shows the tip clearance influence on the impeller streamwise distribution of the flow parameters, at the micro turbine design point. The streamwise direction follows the impeller side, is based on the meridional coordinate, and is normalized so that it ranges from 0 at the inlet to 1 at the outlet. The full blade leading and trailing edges are located at 0.18- and 0.94-stream, and are indicated by *LE* and *TE* in the figure, respectively. The splitter blade leading edge is placed around 0.4-stream, but it is not shown there. The velocities have been normalized by the blade speed at the impeller blades trailing edge (U_{TE} = 465 m/s), while pressures and temperatures have been normalized by the total pressure and temperature specified at the CFD domain inlet (see Sec 4.2.2).

The absolute and relative velocities are illustrated in Fig. 4.9a. As expected, the former increases from inlet to outlet, but only at about 0.75-stream the tip clearance starts to influence the velocity field, such that the absolute velocity decreases with increasing tip clearance closer to the trailing edge. The relative velocity decreases quickly right downstream of the full blade leading edge, then again close to the splitter blade leading edge, but at a less steep slope. This does not hold for the 14.4%-relative-tip-clearance case, for which the relative velocity is almost constant along the majority of the bladed passage. In all cases, the relative velocity increases with increasing tip clearance, but downstream of the trailing edge the tip clearance influence smoothens out, as visible for the absolute velocity as well.

Figure 4.9b shows the velocity components. The meridional velocity increases firstly at the full blade leading edges and secondly at the splitter blade leading edge, then it decreases from 0.5-stream to the impeller outlet, at a faster rate for lower tip clearances. The tangential velocity steeply decreases between the full and splitter blades leading edges, then with a flatter slope from 0.4-stream to about 0.6-stream and from there to about 0.85-stream it has a constant trend. This is not true for the case with the highest tip clearance, for which the tangential velocity increases right after the descent phase. For both velocity components the effect of the tip clearances is stronger from about 0.35-stream, and in both cases it increases with increasing tip clearances.

The pressures and temperatures ratios are depicted in Figs. 4.9c and 4.9d, respectively.

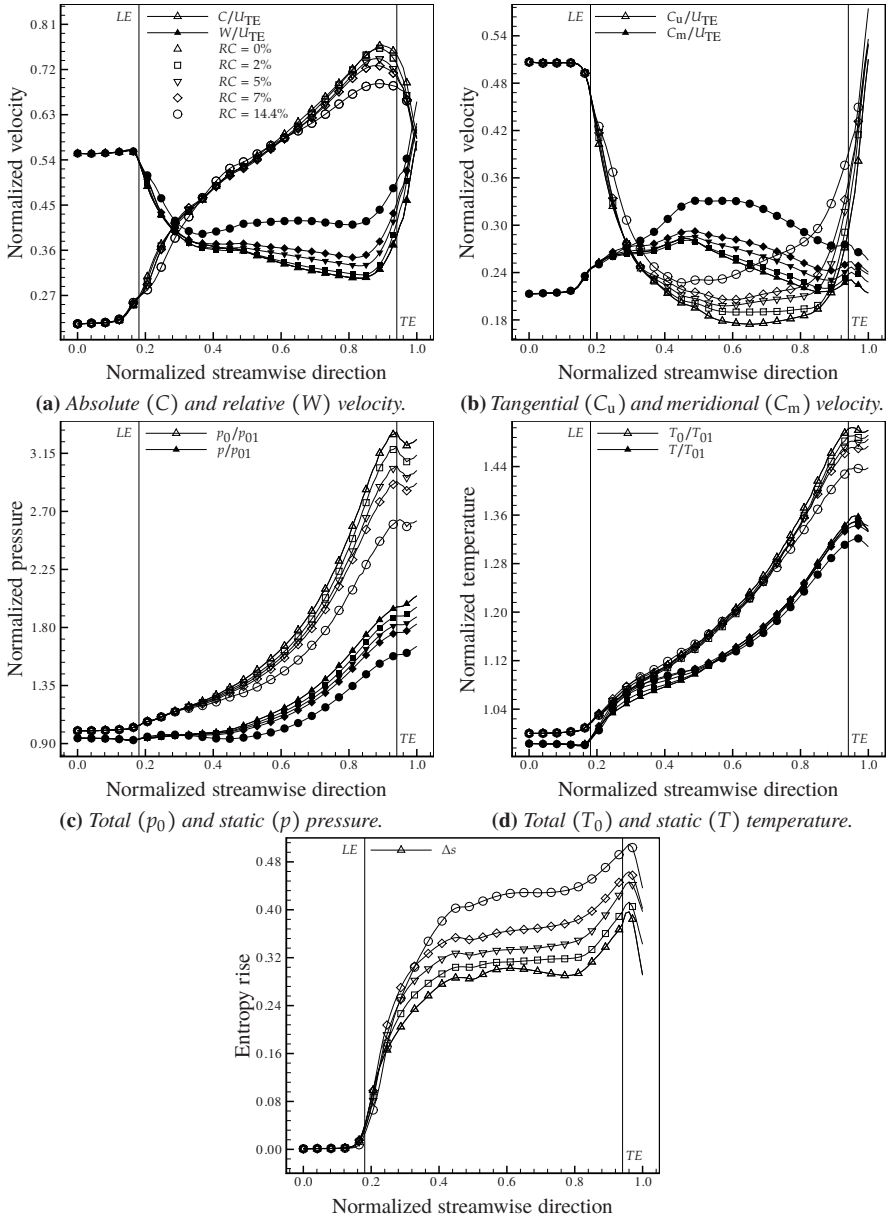

(a) *Absolute* (C) *and relative* (W) *velocity.*

(b) *Tangential* (C_u) *and meridional* (C_m) *velocity.*

(c) *Total* (p_0) *and static* (p) *pressure.*

(d) *Total* (T_0) *and static* (T) *temperature.*

(e) *Entropy rise.*

Figure 4.9: *Tip clearance influence on the impeller streamwise distribution of flow parameters at the micro turbine design point (i.e.,* $\dot{m}$ *= 50 g/s and* N *= 240 krpm). The relative tip clearance* (RC) *is calculated as the ratio of the tip clearance to the blade height at the impeller outlet. The velocities have been normalized by the blade speed at the impeller blades trailing edge* $(U_{TE}$ *= 465 m/s). Pressures and temperatures have been normalized by the total pressure and temperature specified at the computational domain inlet* $(p_{01}$ *= 101,325 Pa and* T_{01} *= 293.15 K). LE and TE are the full blades leading and trailing edges, respectively.*

The tip clearances influence is larger for the total and static pressures and it can be noticed only from mid-stream to the impeller outlet. On the other hand, the total and static temperature are less influenced by the clearance gaps, whose effects are visible very close to the trailing edge, especially for the total temperature. In all the four cases, the values decrease with increasing tip clearances. Furthermore, as a possible consequence of the high-velocity leakage flow present in the region between the trailing edge and the impeller outlet, the total pressure distribution flattens downstream of the trailing edge, as do both temperatures. This does not hold for the static pressure, which continuously rises from inlet to outlet.

Figure 4.9e shows that the entropy rise (Eq. 4.2) grows in the streamwise direction, with higher levels for larger tip clearance. In particular, a very steep growth occurs downstream of the full blade trailing edge, then the rate is less steep to 0.4-stream, and from there to about 0.8-stream it seems to be almost constant. In the last 20% of the streamwise direction, the entropy rise is again stronger across the trailing edge.

Spanwise distribution of the flow parameters at the impeller blades trailing edge

Figure 4.10 illustrates the tip clearance influence on the spanwise distribution of the flow parameters at the impeller blades trailing edge, at the micro turbine design point. The spanwise direction follows the impeller width within the end-walls (i.e., from hub to shroud) and is normalized so that it ranges from 0 at the hub to 1 at the shroud. The velocities have been normalized by the blade speed at the impeller blades trailing edge (U_{TE} = 465 m/s), while the pressures and temperatures have been normalized by the total pressure and temperature specified at the CFD domain inlet (see Sec 4.2.2).

The absolute and relative velocities are shown in Fig. 4.10a. The absolute velocity slightly increases from hub to 0.7-span, then it decreases rapidly up to the shroud. The influence of the tip clearance is more noticeable from about 0.7-span, from where the absolute velocity decreases more rapidly with increasing tip clearance. The relative velocity has an opposite behaviour, but the tip clearance effect is visible along the whole spanwise direction, especially close to the end-walls.

Figure 4.10b illustrates the velocity components. The tangential velocity shows a distribution similar to that of the relative velocity and from 0.65-span the tip clearance influence is stronger. The meridional velocity distribution is influenced by the blockage of the flow passage, as a consequence of a thicker boundary layer due to tip clearance leakage flow and mixing. The meridional velocity thus decreases closer to the shroud, while it has higher values near the hub, to preserve mass conservation. In particular, a very low meridional velocity at the shroud might cause flow reversal, if the low-momentum flow would not overcome the pressure gradient.

The relative flow angle increases constantly from hub to shroud, although the difference between the values at the two end-walls is not large, while the absolute flow angle increases from hub to 0.15-span, then decreases to mid-span and increases again up to the shroud, where a highly tangential flow can be noticed (Fig. 4.10c).

The static pressure shows a flat distribution from hub to shroud, while the total pressure decreases mostly from 0.7-span to the shroud (Fig. 4.10d). The same occurs to the

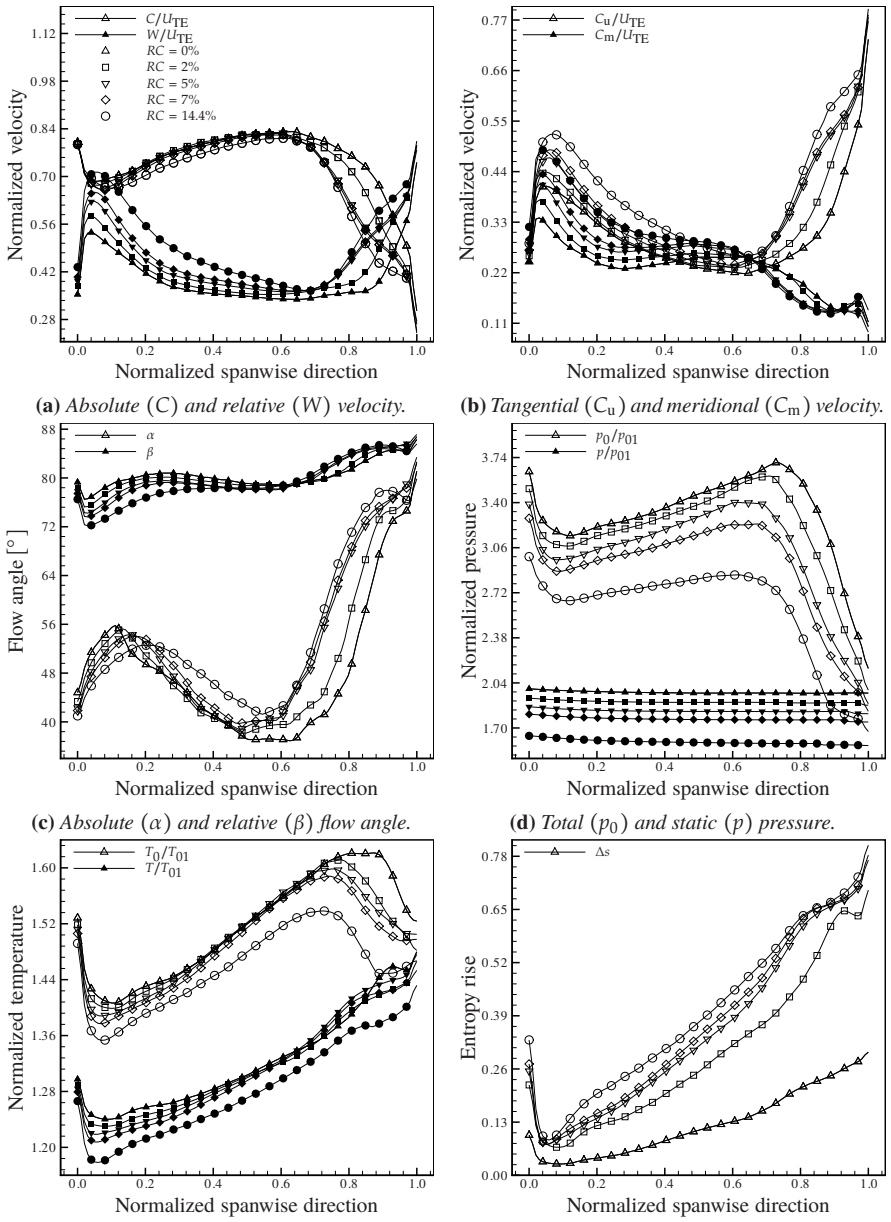

(a) *Absolute* (C) *and relative* (W) *velocity.*

(b) *Tangential* (C_u) *and meridional* (C_m) *velocity.*

(c) *Absolute* (α) *and relative* (β) *flow angle.*

(d) *Total* (p_0) *and static* (p) *pressure.*

(e) *Total* (T_0) *and static* (T) *temperature.*

(f) *Entropy rise.*

Figure 4.10: *Tip clearance influence on the spanwise distribution of flow parameters at the impeller blades trailing edge, at the micro turbine design point (i.e.,* $\dot{m}$ *= 50 g/s and* N *= 240 krpm). The relative tip clearance* (RC) *is calculated as the ratio of the tip clearance to the blade height at the impeller outlet. The velocities have been normalized by the blade speed at the impeller blades trailing edge* $(U_{TE}$ *= 465 m/s). Pressures and temperatures have been normalized by the total pressure and temperature specified at the computational domain inlet* (p_{01} *= 101,325 Pa and* T_{01} *= 293.15 K).*

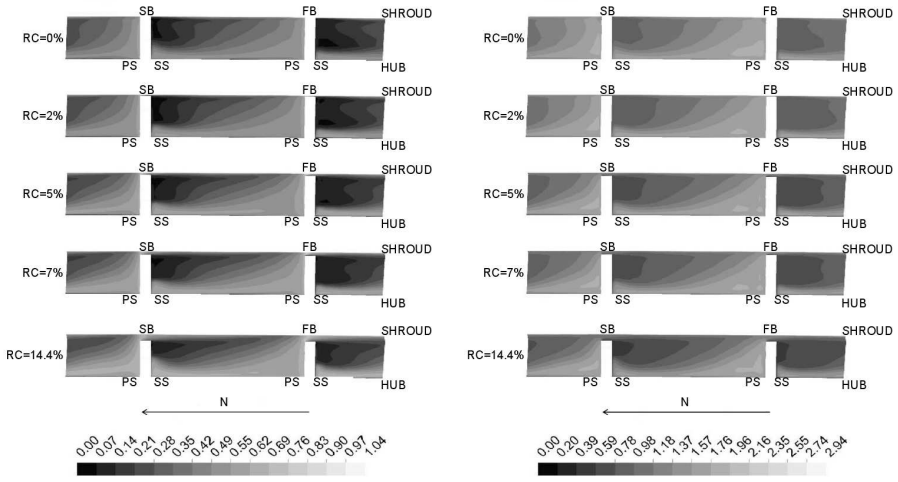

(a) *Relative velocity.* **(b)** *Relative total pressure.*

Figure 4.11: *Tip clearance influence on the relative velocity and relative total pressure at the impeller blades trailing edge, at the micro turbine design point (i.e., $\dot{m}$ = 50 g/s and N = 240 krpm). The relative tip clearance (RC) is calculated as the ratio of the tip clearance to the blade height at the impeller outlet. The relative velocity has been normalized by the blade speed at the impeller blades trailing edge (U_{TE} = 465 m/s). The relative total pressure has been normalized by the total pressure specified at the computational domain inlet (p_{01} = 101,325 Pa). FB and SB are the full and splitter blades. PS and SS are the pressure and suction sides. The rotational speed N indicates the direction of rotation.*

total temperature, which means that the leakage flow affects there the work transfer, while the static temperature increases almost linearly in the spanwise direction (Fig. 4.10e). For both total and static pressure and both total and static temperature, the highest values are seen at the lowest tip clearances.

The entropy rise from hub to shroud is show in Fig. 4.10f. Entropy increases almost linearly between the end-walls and the tip clearance influence is identified, as the the entropy levels are higher in presence of larger clearance gaps. However, the deviations among the cases with tip clearances are low, and even negligible close to hub and shroud.

Flow field at the impeller blades trailing edge

Figure 4.11 shows the contours of the relative velocity and relative total pressure at the impeller blades trailing edge, at the micro turbine design point. The relative velocity has been normalized by the blade speed at the impeller blades trailing edge (U_{TE} = 465 m/s), while the relative total pressure has been normalized by the total pressure specified at the CFD domain inlet (see Sec 4.2.2).

The classical jet-wake structure can be seen in Fig. 4.11a, which illustrates the normal-

ized relative velocity field. For the case without tip clearance, the wake region is located at the shroud/suction side corner and on the full blade suction side it is larger than on the splitter blade suction side. As the tip clearance increase, the wake region becomes larger in the pitchwise (i.e., tangential) direction for both the full and splitter blades and the flow velocity near the shroud increases, because the tip clearance leakage flow becomes stronger in the pitchwise direction as the tip clearance increases, thus the low-speed flow is pushed towards the pressure side. Furthermore, the high-speed leakage flow mixes with the low-speed flow, such that the average velocity in the wake region increases. In the spanwise direction, the wake region has a constant width on the full blade suction side, while it becomes smaller on the splitter blade suction side, as a consequence of the fact that the normalized relative velocity increases in the hub/suction side corner, so that the jet and wake regions are divided diagonally from the hub/suction side to the shroud/pressure side corner. On the full blade suction side this distribution is more marked at higher tip clearances.

The normalized relative total pressure contours are shown in Fig. 4.11b to investigate the loss characteristics, since the classical jet-wake theory [56, 135] states that impeller losses occur in the wake region. The normalized relative total pressure flow field is similar to that of the normalized relative velocity, and the low pressure can be seen in the wake region, which enlarges both in the spanwise and pitchwise directions with increasing tip clearance.

4.4 Conclusions

In this chapter, a commercial CFD code which solves the 3D RANS equations has been used to acquire further knowledge about the compressor flow structure, and tip clearance influence on the compressor performance. The investigations have been performed at the micro turbine design point (i.e., $\dot{m}$ = 50 g/s and N = 240 krpm).

At first, the computational domain did not include any clearance gap, in order to simplify the impeller geometry and grid generation. The numerical results have been compared with the experimental data and such comparison showed good agreement, especially at the design point and at low mass flow rates. On the contrary, some discrepancies have been highlighted at high mass flow rates.

From the compressor flow field analysis, the following can be concluded:

- The supersonic relative Mach number in the inducer causes the development of a low-velocity region on the full blade suction side. This area grows from shroud to hub and has its maximum extension in the spanwise direction at the full blades trailing edge.

- On the splitter blades suction side, the relative Mach number is lower and the low-velocity region smaller. Therefore, at the impeller outlet the wake due to the full blades is larger than that due to the splitter blades.

- The largest loss production occurs in proximity of the shroud and has its maximum

extension in the spanwise direction in correspondance of the large wake developed from the full blades suction side.

- The calculated static pressure recovery coefficient of the vaneless diffuser is equal to 0.47. It is thus located at the lower end of the ranges documented in the literature, since less than 50% of the high kinetic energy available at the diffuser inlet is converted into static pressure.

Furthermore, the tip clearance influence on the performance and flow field of the centrifugal compressor have been studied. Four different values of tip clearance have been used. The following can be concluded:

- The stage total-to-total pressure ratio and isentropic efficiency decrease by 13.4% and 5.6%, respectively, for every 10%-increase of tip clearance. Equation 4.1 can be used to calculate the stage total-to-total isentropic efficiency drop with $a = 1.67$, provided that $\eta = 0.699$ and $b_1/b_2 = 3.19$. Furthermore, the decrease of the impeller total-to-total isentropic efficiency due to increasing tip clearance can be estimated with Eq. 4.1, provided that $a = 1.37$, $\eta = 0.804$, and $b_1/b_2 = 3.19$.

- The values of total and static pressures and temperatures at the impeller outlet decrease with increasing tip clearance, although the pressures decrease linearly with increasing clearance gap, while the temperatures are more influenced at higher clearances. The velocity drop is more noticeable when the clearance gaps are large, wherelse the velocity components are influenced only marginally by increasing tip clearances.

- The entropy grows with increasing clearances, but the rate is slower as the clearances become larger, as a consequence of a steeper decrease of the total temperature at higher gaps.

- In the impeller streamwise direction, the total and static flow properties are affected by the increasing tip clearance especially closer to the blades trailing edge. On the other hand, the tip clearance influences the velocities along the whole streamwise direction, but its influence is lower at the impeller outlet. The entropy is larger at higher tip clearances, and a steep increment is noticeable right behind the full blades leading edge.

- At the outlet, the strongest tip clearance effects are observed close to the shroud due to the leakage flow in that region. The static pressure has a constant distribution from hub to shroud, while the static temperature linearly increases in that direction. The magnitude of the properties is generally lower for higher clearance gaps.

- As observed for the case without tip clearance, a wake is visible in the shroud/suction side corner. With increasing tip clearance, it enlarges and is pushed towards the pressure side, because the tangential tip clearance leakage flow strengthens at higher tip clearances. Due to a velocity increase at the hub/pressure side corner with increasing tip clearance, the jet and wake structures are divided diagonally and a deficit of

relative total pressure is visible in the wake. As a consequence, losses increase with increasing tip clearance.

“There are many paths to the top of the mountain, but the view is always the same.”

Chinese proverb.

5

The role of the diffuser

In this chapter, the influence of the diffuser on the compressor performance is described. Firstly, an overview of the impeller outlet flow phenomena is given, in order to identify their effects on the downstream flow field. A brief description of the two main categories of diffusers (i.e., vaneless and vaned) follows. Finally, the most important design parameters of a vaned diffuser are highlighted.

5.1 Introduction

In a centrifugal compressor, the energy is transferred to the fluid by the impeller blades. Although impellers are designed for very good diffusion within the bladed passages, up to 50% of the energy transferred to the fluid remains available at the impeller outlet as kinetic energy [4, 130, 136–138, 153, 171, 262]. As a consequence, for the centrifugal compressor stage to be efficient, that kinetic energy has to be converted into static pressure as much as possible.

In a centrifugal compressor stage the diffuser is located downstream of the impeller and upstream of the volute. A complicated flow field develops in the impeller and strong fluctuations in the velocity and flow angle in the circumferential and axial directions can be seen at the impeller outlet [56, 66, 161, 162]. In particular, a jet-wake flow pattern exists at the impeller outlet. The jet or primary flow can be considered isentropic and is typically located on the blades pressure side. On the contrary, the wake or secondary flow carries turbulence and losses, and usually gathers at the shroud/suction side corner. As a consequence, the velocity of the flow leaving the impeller will be higher on the pressure side and on the hub, due to recirculation and separation. As the impeller rotates, the velocity entering the diffuser will then vary from that on the suction side to that on the pressure surface, as well as from that at the shroud to that at the hub. Furthermore, at high pressure ratios, the tangential velocity will be high, eventually leading to transonic and turbulent flow, while shock waves and boundary layer separation might occur as well. The flow at the diffuser inlet is thus highly unsteady, viscous, three-dimensional (3D), and non-uniform, and the pressure non-uniformity caused by the volute further influences the diffuser flow [14, 88, 101, 111, 245, 267]. Further on, both the impeller and volute affect the diffuser flow field and its performance, thus a diffuser should not be designed without considering the other two elements. At the same time, the diffuser has a challenging task in matching together the two elements of the compressor stage.

Centrifugal compressors can be equipped with either a vaneless or a vaned diffuser (Fig. 5.1). Broadly speaking, those fitted with vaneless diffusers have a wider operating range, but lower efficiency and pressure recovery, whereas those mounting a vaned diffuser exhibit higher pressure recovery and efficiency, but a narrower operating range. A vaneless diffuser is thus used whenever a large operating range is needed and manufacturing costs have to be kept low, wherelse vaned diffusers are typically used in high-pressure-ratio centrifugal compressors and in applications where the need to vary the flow rate is not a priority.

The two most important parameters to evaluate the performance of a diffuser are the static pressure recovery coefficient (CP) and the total pressure loss coefficient (K), which are defined as

$$CP = \frac{p_5 - p_2}{p_{02} - p_2}, \tag{5.1}$$

$$K = \frac{p_{02} - p_{05}}{p_{02} - p_2}, \tag{5.2}$$

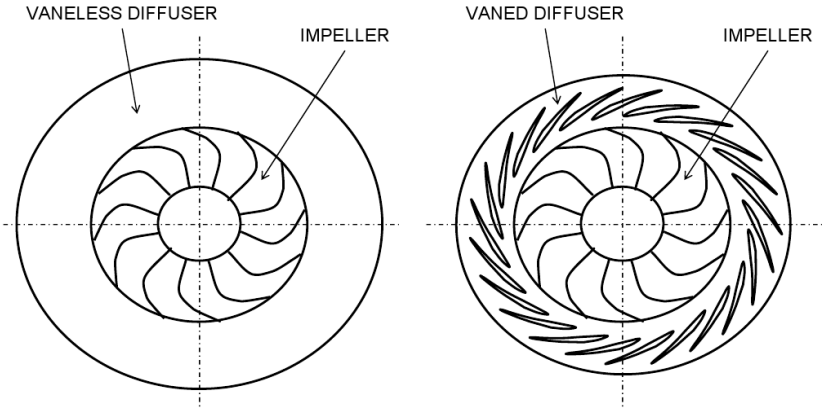

(a) *Vaneless diffuser.* **(b)** *Vaned diffuser.*

Figure 5.1: *Typical diffusers for a centrifugal compressor.*

where subscripts 2 and 5 indicate the diffuser inlet and outlet, respectively, while subscript 0 represents the total condition. According to Kim *et al.* [151], vaneless diffusers typically have a static pressure recovery coefficient in the range from 0.45 to 0.6, and vaned diffusers in the range from 0.55 to 0.70. Japikse and Baines [137] claim that typical values of pressure recovery can range from 0.3-0.4 up to 0.8-0.9, although high-performance diffusers more commonly exhibit pressure recovery from 0.6 to 0.7.

In the following, an overview of the flow phenomena which occur at the impeller outlet, and therefore affect the flow field in the downstream diffuser, is given. Subsequently, the vaneless and vaned diffusers are briefly described. Finally, the most important design parameters of a vaned diffuser are highlighted.

5.2 The flow at the impeller outlet

The flow in a centrifugal impeller experiences a diffusing process through a highly curved, rotating passage. The high- and low-momentum flows are separated into clearly distinguished high- and low-energy flows because of rotation, Coriolis forces, blade curvature, boundary layer development, and tip clearance effects. The low-momentum flow is typically swept into the shroud/suction side corner, while the isentropic core (i.e., the high-momentum flow) constitutes the rest of the flow field.

The possibility of a separated flow, referred to as a “neutral zone”, was firstly considered in the early 1920’s by Carrard [34, 35], while in 1932 Fischer and Thoma [89] showed the existence of a separated flow through flow visualization and measurements in a water centrifugal pump. By using dye injected into the impeller passage, the authors noticed regions of very low momentum flow occupying a large portion of the passage on the blades suction side (i.e., the trailing surface).

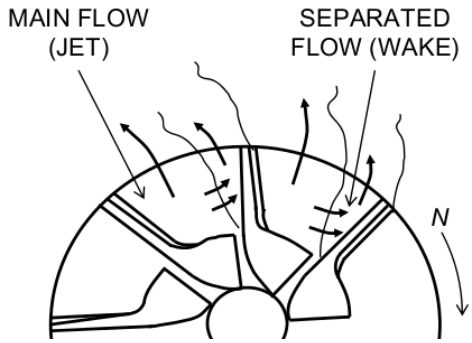

Figure 5.2: *The idealized jet-wake model. The rotational speed N indicates the direction of rotation.*

Despite this evidence, fully attention was drew to separation in centrifugal impellers only thanks to the work presentend in 1960 by Dean and Senoo [56], who named this phenomenon the "jet-wake" model (Fig. 5.2). According to the authors, most of the flow leaves the impeller in the jet, which is almost free-loss in the relative frame of reference, wherelse the wake has a lower velocity, with even lower relative total pressure, but it may occupy a much larger passage area. In the authors' work, the flow was assumed to be two-dimensional (2D), the jet and wake divided the passage in the tangential direction, and the wake gathered on the blades suction side.

Evidence of the existence of a strongly non-uniform impeller flow was also given by the work of Fowler [91], in which a huge impeller rotated slowly with an observer sitting in the hub. A few years later, Moore [185, 186] published his work on a rotating diffuser, and was able to prove the existence of a separated region on the suction side.

The most important information about impeller flows came from the laser measurements performed by Eckardt [66–68], which allowed to remove the ambiguities of interpreting experimental data taken outside the impeller. Eckardt [66] performed detailed measurements at the outlet of a radial (i.e., with no backsweep) impeller with high-frequency measuring systems. The results showed pronounced jet-wake patterns, as a consequence of a region near the shroud/suction side corner with low mass flow and high losses, and one on the pressure side with lower losses. The flow distortions caused by the impeller wakes were also observed in the vaneless diffuser, up to a radius ratio (i.e., the ratio between the radius of any given location in the diffuser and the impeller outlet radius) higher than that predicted by theoretical models.

In a following work [67], Eckardt carried out laser velocimeter measurements of the velocity flow field in an impeller with no backsweep rotating at 18,000 rpm, that was designed to deliver a pressure ratio equal to 3 at a mass flow rate equal to 7.2 kg/s. Figure 5.3a shows the meridional velocity at five sections along the streamwise direction (i.e., the direction which follows the impeller surface and is based on the meridional coordinate). Those experimental results refer however to a pressure ratio equal to 2.1, at 5.31 kg/s and 14,000 rpm. Right behind the inducer (plane 2) there are no irregularities in the flow, but some emerge close to the shroud at plane 3. The irregularity is then noticeable as a region

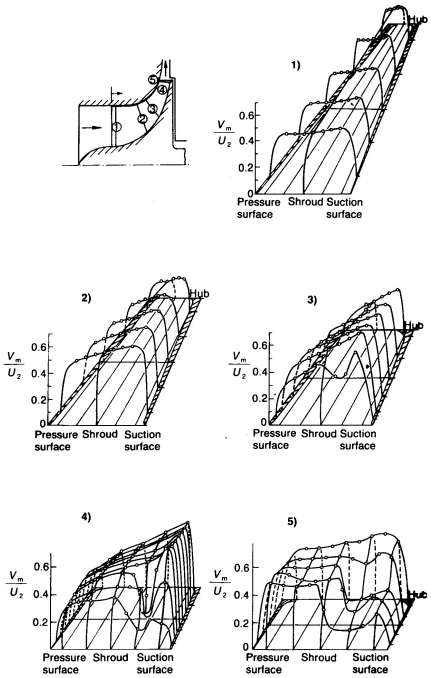

(a) *2.1-pressure-ratio impeller without backsweep, rotating at 14,000 rpm with mass flow rate equal to 5.31 kg/s. Adapted from Ref. [67].*

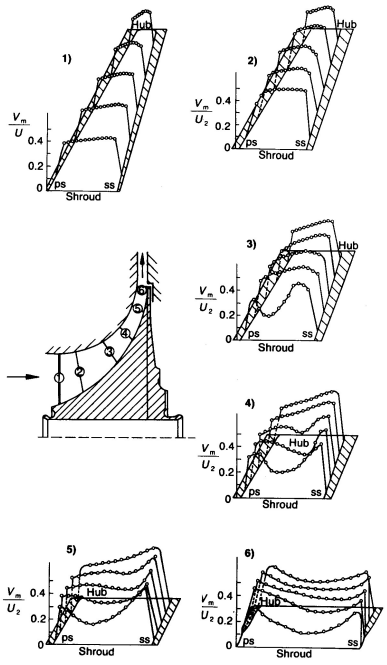

(b) *4.7-pressure-ratio impeller with 30°-backsweep, rotating at 22,345 rpm with mass flow rate equal to 4 kg/s. Adapted from Ref. [162].*

Figure 5.3: *Measurements of the meridional velocity* (V_m) *in two centrifugal impellers.* V_m *has been normalized by the blade speed at the impeller outlet* (U_2)*, and is shown on different sections normal to the meridional direction.*

of loss on plane 4, where it has moved to the shroud/suction side corner. The separated area then grows and flattens as the flow moves towards the impeller outlet (plane 5), where it can be recognized as a wake.

Eckardt [68] further presented experimental data concerning an impeller similar to the previous one, but with a backsweep angle equal to 30°. The velocity field is similar to that of the original impeller, thus with the separation starting at the shroud and growing in size towards the impeller outlet. However, in this case, at the best efficiency point, the author noticed less migration of the wake to the suction side, not even at the impeller outlet. Flow separation occurred at the choking condition only.

In order to study the wake formation and development, Johnson and Moore [144–146] measured the three mutually perpendicular velocity components and the rotary total pressure. They found that the wake flow was due to the accumulation of low relative total pressure flow at the shroud/suction side corner of the impeller passage, and to the convection of low relative total pressure fluid by secondary flows (i.e., flows normal to the

primary flow parallel to the blades walls). The authors identified the adverse static pressure gradient between the inlet and outlet of the axial to radial impeller bend, near the shroud/suction side corner, as the cause of that accumulation. They also showed that the mass flow rate influenced the position of the wake at the impeller outlet. The wake moved from the suction side to the shroud/suction side, corner and then to the shroud when the mass flow rate increased from low to high values. It was concluded that the secondary flows contribute to the wake formation and have a strong influence on the location of the wake at the impeller outlet. since they depend on the mass flow rate as well.

Inoue and Cumpsty [118] showed that with increasing radius the tangential velocity profile did not vary as significantly as the radial velocity across the spanwise direction, while the circumferential distortions of the radial velocity in the vaneless diffuser were still visible at a radius ratio equal to 1.3. However, those distortions decreased rapidly with radius, as a consequence of the energy transfer between the jet and wake regions.

Krain [162] performed laser-2-focus measurements to study the behaviour of a new backswept impeller of his own design. The design point pressure ratio was equal to 4.7, at a mass flow rate of about 4 kg/s and a rotational speed equal to 22,345 rpm. The meridional view of that impeller is sketched in Fig. 5.3b, where the large and smoothly varying radius of curvature on the shroud is noticeable. This is due to a small inducer diameter in relation to the impeller outlet diameter, such that the shroud profile is very different from that on the impeller tested by Eckardt [67], which can be see in Fig. 5.3a. Figure 5.3b shows the meridional velocity distributions measured at six sections along the streamwise direction. In this case, at the impeller outlet (plane 6) the meridional velocity did not exhibit a feature that could be described as a wake, but rather a region of reduced velocity near the shroud, which led to a smoother impeller outlet flow. The big difference between these measurements and those performed by Eckardt [67] is that in the latter case the low-velocity region remained close to the shroud, did not grow nor deepen, and did not migrate to the shroud/suction side corner.

Mounts and Brasz [187] developed a 3D Navier-Stokes algorithm to study the unsteady flow field interaction between the impeller and vaneless diffuser of a centrifugal compressor. The results showed that the initial dynamic variations in velocity and flow angle quickly disappeared with increasing diffuser radius, while the dynamic fluctuations in the static pressure originating from the impeller blade loading did not reduce appreciably with radius.

Hathaway *et al.* [104, 105] studied the flow field of a low-speed centrifugal compressor using laser anemometry. The results obtained were in good agreement with those showed in previous works. The authors found that the low-momentum fluid moved from the blade surfaces outward to the blade tip. The flow which moved up to the pressure and suction sides was entrained into the tip clearance jet and transported towards the shroud/pressure side corner of the passage, contributing then to the formation of the low-momentum wake typical of unshrouded centrifugal impellers.

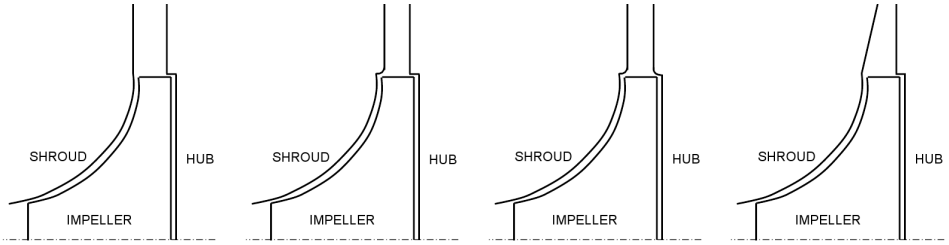

(a) *Unpinched.* **(b)** *Shroud pinch.* **(c)** *Hub and shroud pinch.* **(d)** *Constant area diffuser.*

Figure 5.4: *Different types of the inlet geometry for a vaneless diffuser.*

5.3 The vaneless diffuser

In its simplest configuration, a vaneless diffuser consists of two parallel walls which form a radial annular passage from the impeller outlet radius to some diffuser outlet radius. The fluid is thus allowed to flow along the radial direction, such that the kinetic energy can be converted into static pressure. Different inlet configurations are possible (Fig. 5.4), and generally some degrees of pinch (i.e., a reduction of the diffuser height) are used to stabilize the flow which enters the diffuser.

Figure 5.5 shows the velocity triangles in a vaneless diffuser at the inlet (station 2) and at an arbitrary location (station *a*). For an isentropic flow, the angular momentum of the fluid entering the diffuser will remain constant, such that

$$C_{u2} r_2 = C_{u,a} r_a, \tag{5.3}$$

where C_u and r are the tangential velocity and the radius, respectively. From the continuity equation yields

$$\dot{m} = C_{m2} \rho_2 A_2 = C_{m,a} \rho_a A_a, \tag{5.4}$$

where C_m is the meridional velocity, A is the flow passage area, and ρ is the flow density. For a diffuser with constant height b, the flow passage areas at the diffuser inlet (A_2) and at any arbitrary location (A_a) are defined as

$$A_2 = 2\pi r_2 b, \tag{5.5}$$
$$A_a = 2\pi r_a b. \tag{5.6}$$

Substituting Eqs. 5.5 and 5.6 in Eq. 5.4 yields

$$C_{m2} \rho_2 r_2 = C_{m,a} \rho_a r_a. \tag{5.7}$$

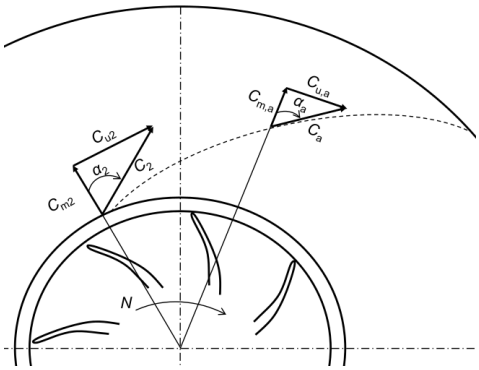

Figure 5.5: *Velocity triangles at the inlet of a vaneless diffuser (station 2), and at an arbitrary location within the vaneless diffuser (station a). C and α are the absolute flow velocity and angle, while C_u and C_m are the tangential and meridional components of the absolute velocity. The rotational speed N indicates the direction of rotation.*

The absolute flow angles at the diffuser inlet (α_2) and at any arbitrary location (α_a) are then given by

$$\tan(\alpha_2) = \frac{C_{u2}}{C_{m2}}, \tag{5.8}$$

$$\tan(\alpha_a) = \frac{C_{u,a}}{C_{m,a}} = \frac{C_{u2} r_2 \rho_a r_a}{C_{m2} r_2 \rho_a r_a} = \frac{C_{u2}\rho_a}{C_{m2}\rho_2}. \tag{5.9}$$

For given diffuser inlet conditions, Eq. 5.9 finally reduces to

$$\tan(\alpha_a) = \text{const} \times \rho_a. \tag{5.10}$$

From Eq. 5.10 yields that for an isentropic, incompressible flow in a vaneless diffuser of constant height, the absolute flow angle is constant, leading to the so-called logarithmic spiral path. On the other hand, for compressible flows the density changes with pressure and temperature in such a way that the absolute flow angle increases in the radial direction with increasing radius, so that the flow turns more than the simple logarithmic spiral, giving rise to increased friction losses. These losses can be especially high for diffusers with large radius-to-width ratios, like those employed in low-flow or high-pressure applications. Vaneless diffusers are thus practical for centrifugal compressors with pressure ratios of approximately 2.5, and are rarely used in compressors with pressure ratios above 3.5 [136]. Came and Robinson [31] claimed that for pressure ratios above 3 a vaned diffuser is more or less mandatory.

The major characteristic of a vaneless diffuser is the lack of a throat. Therefore, there is no real possibility of diffuser choking, leading then to a wide range of operating conditions. Furthermore, the absence of vanes does not generate a vane-driven vibratory coupling between the impeller and the diffuser, which can lead to the impeller blades and

diffuser vanes excitation, and eventually to possible fatigue failure. Vaneless diffusers are also simple and cheap to manufacture, and are more tolerant to erosion and fouling. Moreover, the dependence between losses and mass flow rate is relatively low when compared to vaned diffusers, for which losses at off-design conditions might rapidly rise due to incidence and shocks. Further on, vaneless diffusers offer no perturbation to the flow, and do not produce unfavourable pressure waves. Thus, they are often mounted on centrifugal compressors if a stable operating margin and low noise emissions are desired. Centrifugal compressors equipped with vaneless diffusers are mainly used in the process and refrigeration industries, and in automotive turbochargers.

5.4 The vaned diffuser

The fluid through a vaneless diffuser describe a long path, which can even be as long as 360°, resulting then in high friction losses. The path length cannot be easily reduced, as a large diffuser outlet radius is necessary to achieve the required amount of diffusion through the conservation of angular momentum. As a consequence, the commonly adopted approach to shorten the flow path is to insert diffuser vanes.

The principle of vaned diffusers is thus to provide additional reduction of the tangential velocity over the vaneless concept by reducing the angular momentum. The inlet tangential velocity can be decreased by 50%, leading to an effective reduction of the radial extent by half, when compared to a vaneless diffuser, such that vaned diffusers are advantageous when small size is fundamental. The additional diffusion achieved by a vaned diffuser over a vaneless configuration can then significantly reduce the losses occurring in the downstream components of the compressor stage.

In a vaned diffuser, there is usually a vaneless gap between the impeller outlet and the vanes leading edge. It reduces the circumenferential pressure gradient at the diffuser inlet, smoothens out the velocity variations between the impeller blades and the diffuser vanes, and reduces the Mach number at the diffuser vanes leading edge, in order to avoid shocks or overspeeding on the vane profile. In the vaneless space, the flow describes a logarithmic spiral path to the vanes leading edge, after which it reaches the semivaneless space. The throat area, which is very critical in that controls the choking condition of the compressor stage, is located right downstream of the semivaneless space. Afterwards, the flow is constrained by the vaned passages and finally enters the downstream component.

Diffuser vanes reduce the tangential velocity more rapidly than in a vaneless space, therefore leading to an increased diffusion rate and a reduced flow path length. Losses are thus reduced, leading to more efficient compressor stages. According to Osborne [199], at design point centrifugal compressors fitted with vaned diffusers can exhibit efficiency values up to 7% higher than those having vaneless diffusers, while Boyce [27] states that the difference can be as high as 4%. However, their flow range is highly influenced by the diffuser vanes. If the mass flow rate is changed at constant rotational speed, the absolute flow angle at the impeller outlet will vary, affecting the incidence losses at the diffuser vanes leading edges, which will increase if the absolute flow angle will depart from the vane leading edge angle. As a consequence, the efficiency of compressors mounting vaned

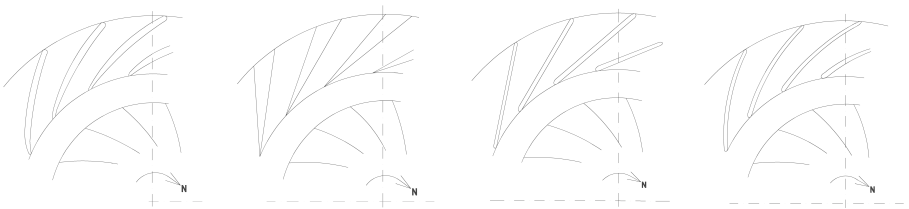

(a) *Airfoil type.* **(b)** *Channel type.* **(c)** *Flat-plate type.* **(d)** *Thin spiral type.*

Figure 5.6: *Different types of a vaned diffuser. The rotational speed N indicates the direction of rotation.*

diffusers will degrade more rapidly at off-design conditions, such that the efficient operating range of a centrifugal compressor is usually limited in presence of vaned diffusers.

The most common designs for a vaned diffuser make use of profiled vanes and straight centerline channels. The profiled configurations can vary from vanes having simple straight walls (Fig. 5.6c), through logarithmic spirals (Fig. 5.6d), to complex profiles based on airfoils tested in axial compressors (Fig. 5.6a). A fourth category is that of channel diffusers (Fig. 5.6b), which capture the oncoming flow and force it from an angular motion to a linear one, along the path of the diffuser. In a channel diffuser the point of minimum geometric area (i.e., the throat) is usually located right at the diffuser vanes leading edge. Channel diffusers are normally employed for operations at high Mach numbers, and make use of the principle of straight-line diffusion to reduce losses and hence improve the compressor stage efficiency. Japikse [136] and Japikse and Baines [138] stated that the airfoil diffuser is classically perceived as delivering performance levels and operating ranges in between those of the vaneless and channel diffusers, although this is too much of a generalisation and in general there is no clear indication of one type of vaned diffuser being superior to the other.

Vaned diffusers can be divided into two further families on the basis of the so-called solidity

$$\sigma = c/s, \tag{5.11}$$

where c is the chord length and s is the pitch, which represents the distance between the leading edge of two successive diffuser vanes. Vaned diffusers can be either conventional if the solidity is higher than one or low-solidity when it is lower than unity. One of the earliest works on low-solidity vaned diffusers (LSVDs) for a radial impeller has been presented by Sutton [257], who performed a test on a centrifugal pump, while the first reference of a LSVD applied to a compressor was given in a Japanese patent by Senoo [231]. In a LSVD, there are less and smaller vanes, and the distance between them is large, such that no geometric throat appears. This leads to the extension of the flow range towards higher flow rates. LSVDs are then a good compromise between vaneless and vaned diffusers, since they have better pressure recovery than the former and wider flow range than the latter.

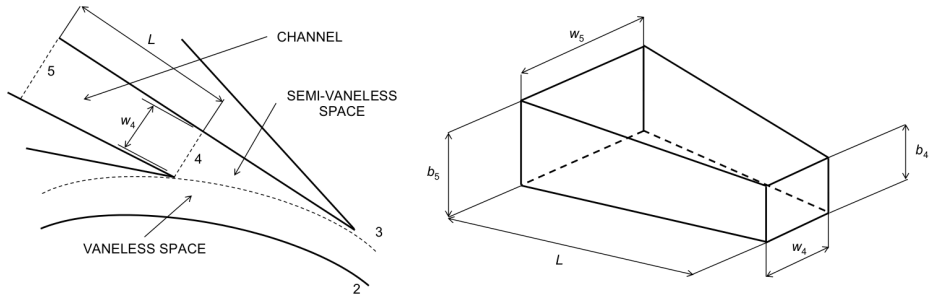

(a) *Two-dimensional view.* **(b)** *Three-dimensional view.*

Figure 5.7: *Essential features of the geometry of a vaned diffuser. L, b, and w are the diffuser vane length, height, and width, respectively. Stations 2 and 5 represent the diffuser inlet and outlet, while stations 3 and 4 are located at the diffuser vane leading edge and at the diffuser throat.*

5.5 Design parameters for vaned diffusers

The performance of vaned diffusers depends upon both geometric and flow parameters. Regardless of the type of vaned diffuser, among the former one can find the divergence angle, the length-to-width ratio, the area ratio, the diffuser height, the vane profile, the vane leading edge shape, the vane number, and the inlet radius ratio. The main flow parameters which influence vaned diffusers performance are the incidence angle and the throat blockage.

The essential features of a vaned diffuser are summarized in Fig. 5.7 for a channel diffuser. The nomenclature shown in the figure helps understanding the following description of the design parameters for a vaned diffuser.

5.5.1 Divergence angle

The influence of the divergence angle (2θ) has been investigated by many researchers who conducted extensive analisys of 2D straight channel diffusers [32, 156, 214, 223, 224]. Their common conclusion was that at a small divergence angle ($2\theta < 8°$) the flow deceleration was controlled by the effective flow area (i.e., geometric area minus boundary layer blockage). However, decreasing the divergence angle resulted in longer diffusers for a constant area ratio, leading to thicker boundary layers. Thus, separation could eventually occur after that a large deceleration had taken place in a long diffuser, but still resulted in high pressure recovery. If the divergence angle was larger ($8° < 2\theta < 20°$), separation occurred near the diffuser channel inlet for a small area ratio, resulting in a much lower pressure recovery, since no diffusion took place downstream of the separation point.

Further tests on channel diffusers were performed by Clements and Artt [41]. They found that a compressor stage mouting a channel diffuser with $2\theta = 12°$ produced a pressure recovery coefficient that was 4% higher than the case with $2\theta = 4°$. It was also found

that the pressure recovery increased with increasing divergence angle up to 12°, while any further increase in the divergence angle did not have any significant effect on the pressure recovery. Furthermore, an increase in the divergence angle caused the flow range to decrease, while the throat blockage at surge decreased with an increase in the divergence angle. The authors thus concluded that the narrower flow range with divergence angle increase could be due to the separation of thick boundary layers caused by a large adverse pressure gradient.

5.5.2 Length-to-width ratio

The length-to-width ratio (LWR) is the ratio of the channel length to the throat width. Maximum diffusion in a straight channel usually occurs in long diffusers ($LWR = 15$) with small openings ($2\theta = 8°$), and in short diffusers ($LWR = 4$) with large divergence angle ($2\theta = 20°$). It is however important to remember that the static pressure rises with the diffuser length until friction losses become predominant, and boundary layer growth prevents any further deceleration of the flow.

Clements and Artt [42] showed that most of the channel pressure rise occurred in the first half of the channel, while the latter half contributed only to a small portion. They also showed that a similar pressure recovery could be attained by reducing the channel length and replacing it with a downstream vaneless space. Their conclusions indicated that there was an optimum value of LWR, beyond which performance improvements were small. Moreover, the low pressure recovery in the latter part of the channel was caused by unstable boundary layers growth, whose blockage prevented any further effective area increase. The authors concluded as well that high levels of throat blockage could contribute to channel boundary layers instability, since a thick boundary layer usually separates much earlier than a thin one. Thus, as the channel throat blockage increases, the point of separation will move towards the diffuser throat, resulting in a lower LWR.

5.5.3 Area ratio

The area ratio (AR) is the ratio of the areas calculated at the diffuser outlet and throat. Yoshinaga *et al.* [284] tested sixteen different configurations of vaned diffusers and concluded that as the AR became greater than 2, the effectiveness (i.e., the ratio of the actual pressure rise to that which would be achieved in an ideal case) and pressure recovery of the vaned diffusers decreased. Furthermore, from their work it can be seen that both the AR and pressure recovery of vaned diffusers were higher than those of vaneless diffusers. As a consequence, for given inlet flow conditions, there is an optimum AR beyond which the diffuser effectiveness does not show any improvement. As the AR increases, either the divergence angle or the LWR increase. If the former increases, the vanes become highly loaded and the flow separates, resulting in a reduced pressure recovery. If the latter increases, the boundary layers thickens and the AR is reduced, such that the gain in the pressure recovery is low.

5.5.4 Diffuser height

The information that can be found in the literature about the influence of the diffuser height on the diffuser performance is limited. Stein and Rautenberg [254] showed that the compressor stage efficiency improved by reducing the vaned diffusers height. The authors showed that an 11%-height decrease led to a 4%-efficiency increase. At the same time, decreasing the passage height caused a shift in the choking condition towards lower mass flow rates, thus reducing the compressor operating range.

The efficiency increase and the mass flow rate decrease are generally more pronounced at higher rotational speeds than at lower speeds with narrower passages. Because of a high variation of the flow angle in the spanwise direction at the impeller outlet, reduction of the height at high speeds has an equalizing effect on the flow angle, which leads to improved flow conditions at the diffuser vanes leading edge. Furthermore, reducing the height seems to be favorable for good matching of the compressor components, while the surge point of a compressor with a vaned diffuser can be pushed to the same value as if the compressor had a vaneless diffuser.

5.5.5 Vane profile

Among the geometric configurations commonly used in a vaned diffuser, the vane profile does not seem to have a significant impact on the diffuser efficiency, neither in subsonic nor in supersonic conditions. There is also little evidence that the shape of the profile has a large effect on the diffuser flow, although Kmecl *et al.* [157, 158] proved that using proper aerodynamic profiles was effective in reducing losses.

Dean [54] and Rodgers [217] already observed that the shape of the vane did not matter very much in terms of diffuser performace. On the contrary, the influence of the vane profile on the pressure recovery is more evident according to its lift coefficient, while a different profile can significantly influence the behavior of the machine near the stall and choking conditions.

Smith [241] compared the static pressure recovery and total pressure loss coefficients for thin spiral and airfoil cascade vaned diffusers (Fig. 5.8). The author concluded that the latter had better efficiency and pressure recovery. Due to a longer vane guide from the leading edge to the throat, the spiral vaned diffuser also had a smaller stall-free range at high Mach numbers.

Pampreen [200] performed tests on conventional vaned diffusers (CVDs) and tandem cascade diffusers. He observed that the diffuser outlet Mach number with the latter arrangement was lower than with the former one, and that the stall-free range was much larger when tandem cascade diffusers were utilized. The latter also reduced losses by about 10% compared to the CVDs. Pampreen further noticed that the slit between the two rows in the tandem cascade diffusers helped in moving the low-momentum flow from the suction surface of the first row vanes to the main flow, thanks the high-momentum flow on the pressure surface. Therefore, cascade diffusers had a smaller overall size than CVDs, for given inlet and outlet diffuser conditions.

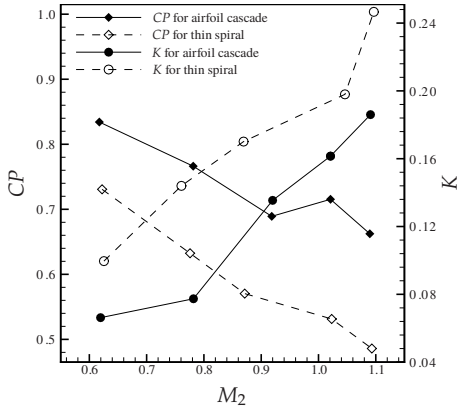

Figure 5.8: *Comparison of static pressure recovery* (CP) *and total pressure loss* (K) *coefficients for thin spiral and airfoil cascade vaned diffusers. The different operating conditions are represented by the varying impeller outlet Mach number* (M_2)*. Data taken from Ref. [241].*

5.5.6 Vane leading edge shape

The effects of the vane leading edge shapes on the diffuser performance were analyzed by Yoshinaga *et al.* [284], who cut rectangular and triangular sections from the vane leading edge in order to match the vane inlet angle with the flow angle along the vane height (Fig. 5.9). The authors noticed that in the former case the stage efficiency decreased (Figs. 5.10a and 5.10b), whereas in the latter it slightly improved at design point (Figs. 5.10c and 5.10d). On the other hand, the cuts on the leading edges did not bring any improvement in terms of the pressure ratio.

Bammert *et al.* [17] tested three different vane shapes (i.e., cambered vanes, straight channel vanes, and twisted vanes) and saw that the performance of the stage equipped with twisted vanes was shifted towards higher mass flow rates at low speeds, as compared to the two other designs. The authors also found that this stage generally reached better efficiencies. In particular, the efficiency increased at low speed by 4% and 3%, in comparison with the cambered vane and the straight channel diffusers, respectively. At higher speeds, the stage with twisted vanes had a wider operating range than the other two. Furthermore, the cambered vane diffuser showed the smallest pressure recovery.

Casartelli *et al.* [36] analyzed the vane leading edge geometry of a standard circular arc vaned through numerical and experimental studies. The results showed that the stage performance could be improved by reducing the total pressure losses, increasing the static pressure rise, and providing a more stable operating range.

5.5.7 Vane number

The vane number (Z_D) has a direct influence on the diffuser size and efficiency. A large vane number reduces the diffuser outlet diameter and leads to a smaller divergence

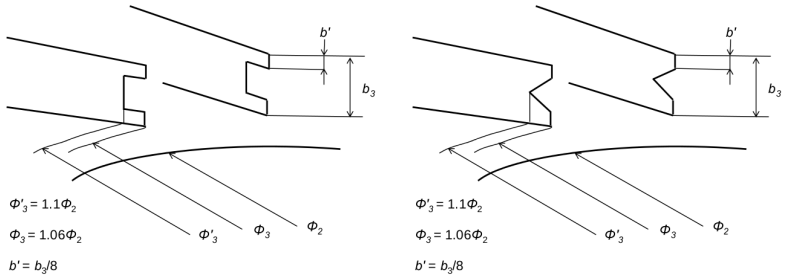

(a) *Ten vanes with rectangular cut.* **(b)** *Eleven vanes with triangular cut.*

Figure 5.9: *Different shapes of the vane leading edge for a vaned diffuser. ϕ_2, ϕ_3, and ϕ_3' are the diameters at the impeller outlet diameter, at the diffuser vane leading edge, and at the diffuser vane leading edge cut, respectively. b_3 is the diffuser height at the vane leading edge. b' is the height of the diffuser cut at the vane leading edge. Data taken from Ref. [284].*

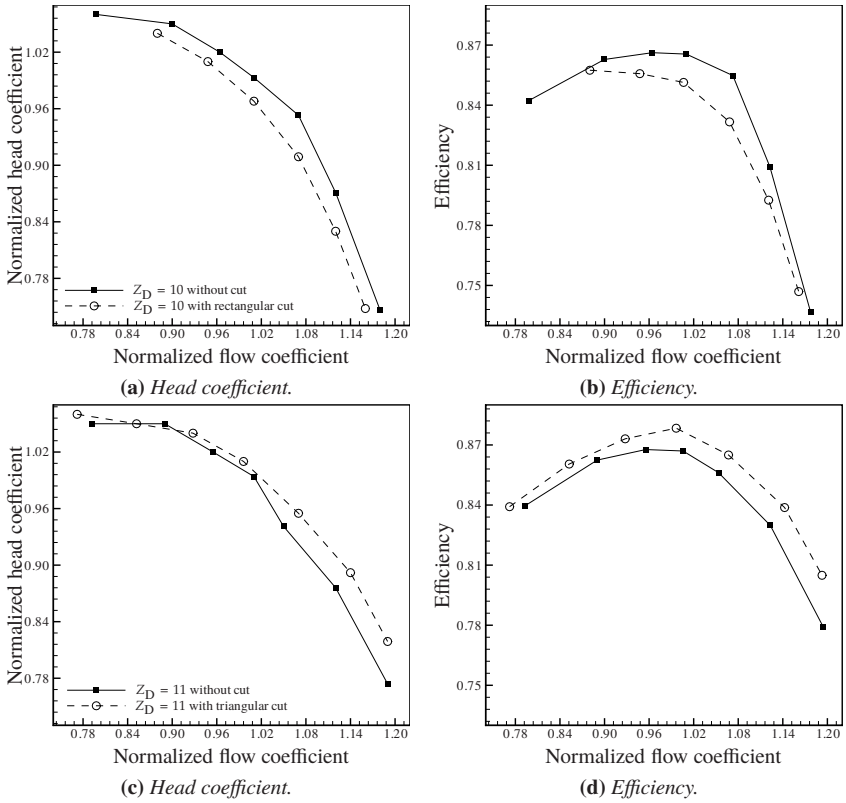

(a) *Head coefficient.* **(b)** *Efficiency.*

(c) *Head coefficient.* **(d)** *Efficiency.*

Figure 5.10: *The influence of the vane leading edge shape on the performance of a vaned diffuser. Two vaned diffusers having ten vanes (above) and eleven vanes (below) are compared. The flow and head coefficients have been normalized by the values at design point. Data taken from Ref. [284].*

angle, while the efficiency increases to the point at which increased friction and blockage overcome the advantage of a more gradual diffusion. Furthermore, a too high vane number can have a strong negative impact on the compressor characteristics at low rates, and if several vane passages share the flow coming out of one impeller passage the uneven velocity distribution can result in alternate vaned passages being either starved or choked. This unstable situation leads to flow reversal in the vaned passages and eventually to compressor surge. Thus, a more uniform flow can be achieved if the diffuser passage number is lower than the impeller passage number [4] and the number of vanes for the diffuser should ideally be less than the number of impeller blades (Z_I), in order to avoid the possibility that large wakes from the impeller blades would sweep around the vaneless space and block off individual vaned diffuser passages [27]. Further on, the selection of the vane number should be based on the effects of the incidence angle necessary to provide maximum flow range and to avoid the vibrational problems that could be encountered due to the impeller blades and diffuser vanes interaction. Both aerodynamic and reasonance have then to be kept in mind for such a choice, for which Boyce [27] claims that Z_D should be the minimum necessary to realize the required throat area, while for Aungier [13] the preferred choice is $Z_D = Z_I \pm 1$, but $10 \leq Z_D \leq 20$ is required. If the final selection cannot be in that range, then the criterion $|Z_D - Z_I| \geq 8$ has to be fulfilled.

Dean [55] indicated that the number of vanes employed in a vane island diffuser could vary between 8 and 60, while Yoshinaga *et al.* [284] suggested that it should be limited to 27.

Japikse [132] compared two pipe diffusers with 17 and 34 pipes, respectively. The stage with 17 pipes had a highly larger operating range, but produced slightly less pressure rise at the design point. By measuring the static pressure on the end-walls, Japikse concluded that the wider range was due to the presence of strong shocks, such that at high speeds the flow from the impeller outlet to the diffuser throat would cross two shocks with an accelerating region in between, leading to a stable situation.

Rodgers [217] performed tests with varying vane numbers with constant throat area. He found that the changes in the flow range were minor, and that the overall pressure recovery depended on the bladed passage performance. The stage performance comparison of a high-efficiency, low pressure ratio stage with 13- and 12-vane channel diffusers with the same throat area were virtually unchanged. Thus, the vane number did not seem to have a great effect on the performance of the vaned diffuser as long as the throat area was kept constant.

Several works concerning tests of LSVDs with different solidities and vane numbers were presented in the late 1990's [5, 6, 76–78, 154]. In all cases, the incidence angle was set to $-2°$ and flat plate vanes were used. It was shown that an increase in solidity decreased the operating range, but led to a better pressure recovery. The increase of the vane number led to a lower vane turning angle (i.e., the difference between the vane angle at the leading and trailing edges) when the solidity was kept constant, and improved the surge margin, because shorter vanes allowed a higher positive incidence angle due to the smaller turning angle. A lower vane number resulted also in better efficiencies at high rotational speeds, because of a higher turning angle, which reduced the flow path.

Eynon and Whitfield [85] tested five different LSVDs with 6, 8, and 10 vanes, solidity

equal to 0.69, and three different vane turning angles. No major changes in performance were noticed when the vane number varied, but increasing it led to a slightly narrower operating range at high flow rates.

He and Tourlidakis [107] performed numerical simulation of four circular arc vaned diffusers placed in a high-speed centrifugal compressor stage for turbocharger applications. Three vaned diffusers had 11, 22, and 33 vanes and an inlet radius ratio equal to 1.07, while the fourth one had 22 vanes and an inlet radius ratio equal to 1.15. The authors noted that the peak efficiency changed when the vane number was changed, but it was not clear whether it increased or decreased with respect to the vane number. Close to the surge condition, when the vane number decreased, the pressure recovery coefficient increased in all the four cases, if the mass flow rate was kept constant. They also concluded that the flow through the vaneless and semivaneless space was more uniform with a lower vane number, because of a lower adverse pressure gradient in that region.

Jaatinen *et al.* [131] tested three circular arc vaned diffusers having a fixed vane leading edge position, and 15 and 23 vanes. Two values of the vane turning angle were chosen, while the incidence angle was equal to -8° at the design point. The authors showed that an increase in the number of vanes seemed to narrow down the operating range by moving the choke limit towards lower mass flow rates, whereas the increase of the vane turning angle had an opposite effect, due to changes in the throat area.

5.5.8 Inlet radius ratio

In proximity of the diffuser inlet, it is important to reduce the vibration and noise generation, due to the impeller-diffuser interaction. At the same time, there is often the need to keep the size of the compressor stage as small as possible. Consequently, there is a strong incentive to decrease the inlet radius ratio, which normally can be as low as 1.05 [51]. However, in case of a supersonic flow coming out of the impeller, some designers increase the vaneless space upstream of the diffuser vane, so that the Mach number decrease to the subsonic condition before meeting the vane leading edge, though this could require an inlet radius ratio as high as 1.25 [51]. In any case, there seems to be no particular merit in doing so, since in axial geometries a very high static pressure rise, without serious losses, can be achieved even at low-supersonic regimes. An alternative for supersonic conditions would be to keep the radius ratio low and make use of thin and sharp diffuser vane leading edges.

Jiang and Yang [142] analyzed the effects of the radial distance between the impeller outlet and the diffuser vanes leading edge on a blower stage efficiency. A 4%-increase in efficiency was achieved by relocating the vanes from a radius ratio equal to 1.1 to a value of 1.2. Better mixing of circumferential distortions was also achieved as the radius ratio increased from 1.05 to 1.2. Furthermore, the authors showed that the lowest total pressure loss coefficient was achieved when the radius ratio increased from 1.15 to 1.2, for a vane setting angle (i.e., the vane angle at the leading edge) equal to $+12^\circ$.

Rodgers [217] investigated the performance of four centrifugal compressors stages with different radius ratios. The best performance was achieved with a radius ratio equal to 1.125, while the worst condition occured at a radius ratio of 1.035. The existence of an

optimum radius ratio between the diffuser vane leading edge and the impeller outlet radii for the maximum stage total-to-static pressure ratio was then confirmed experimentally by the author, and later the same conclusion was drawn by and Clements and Artt [40], who found out that the optimum stage performance was obtained when the radius ratio was in the range from 1.06 to 1.10.

Thanks to 3D, unsteady numerical simulations, also Shum *et al.* [234] concluded that there was an optimum radial gap between the impeller outlet and diffuser vanes leading edges, because with decreasing radius the increase in losses would overtake the benefits of a smaller blockage achieved with a smaller radial gap.

Justen *et al.* [148] carried out unsteady pressure measurements on a highly loaded centrifugal impeller followed by a 23-vane channel diffuser. The investigations were performed at operating speeds equal to 60%, 70%, and 80% of the design rotational speed, and radius ratios equal to 1.06 and 1.10. The pressure fluctuations revealed that the semi-vaneless space, especially closer to the vane suction side, was influenced by the unsteady interaction between the impeller and diffuser. This unsteadiness did not decay even with the larger radial gap.

Ziegler *et al.* [285, 286] studied the impeller-diffuser interaction as function of the radius ratio through laser-2-focus velocimeter measurements. For a diffuser with a vane setting angle equal to +16.5°, the radial gap varied from 1.04 to 1.18, while for that having a vane setting angle equal to +12.5°, the vanes leading edge radius varied from 1.06 to 1.18 times the impeller outlet radius. The compressor map showed higher total pressure ratio and efficiency with smaller radial gaps. In the latter cases, the impeller showed slightly higher work input and its efficiency hardly changed, while the flow field at the diffuser outlet seemed to be more uniform. The authors explained this phenomenon being a consequence of the unloading of the diffuser vane pressure side, which is usually highly loaded. Due to lower Mach numbers at the diffuser outlet with smaller radius ratios, the total pressure loss in the collector was smaller as well. Thus, the authors concluded that small radial gaps should be usually recommended, when a wide operating range was not a priority.

Other researchers [118, 227] presented investigations varying the inlet radius ratio, but it seems that the corresponding recommendations to find the optimum radial gap do not exist yet, despite the numerous works about this topic. Particularly, this could be due to the large number of contradicting parameters influenced by the inlet radius ratio. For example, although the Mach number at the vanes leading edge decreases if the radial gap is extended, the flow path in the vaneless space is significantly longer. This allows then for a further growth of the boundary layer thickness, which thereby increases the throat blockage and in turns decrements the performance of the downstream vaned passages. It is thus even more difficult to attribute the found effects to single causes. A variation of the radial gap has a high practical relevance as well, because it is a design parameter which affects pressure ratio, efficiency, operating range, mechanical loading, noise emissions, and size of a centrifugal compressor.

5.5.9 Throat blockage

In case of an impeller followed by a vaned diffuser, it is the latter which determines the operating range of the centrifugal compressor stage. In the choking condition, since a vaned diffuser is typically designed with a throat area smaller than that of the impeller, the diffuser throat area will determine the maximum mass flow rate. Particularly, the flow decrease at higher mass flow rates results from the formation of an aerodynamic throat area, known as the throat blockage, due to the boundary layer development. Blockage is then considered in connection with the mass flow capacity of the vaned diffuser throat, but it affects the diffuser pressure rise as well.

Studies of 2D channel diffusers have shown the influence of inlet blockage on the maximum achievable pressure rise. Runstadler and Dean [223] and Runstadler *et al.* [225] showed the dependence of the maximum pressure rise coefficient for a two-dimensional diffuser on the aspect ratio (AS, defined as the vane height-to-throat width ratio) and throat blockage. Their work was conducted for a throat Mach number equal to one. The authors found out that the AS was a relevant variable and that the maximum pressure recovery coefficienct was achieved for values of AS close to unity. However, the dominant flow variable which most influenced the maximum pressure rise was the blockage, whose increase caused a rapid drop in the pressure rise.

Kenny [149] showed results about the effectiveness of cambered vane and pipe diffusers. He showed that the effectiveness was around 80% for very small throat blockage, but dramatically dropped to 55% at the maximum blockage equal to 0.2.

Throat blockage is thus crucial in evaluating the diffuser pressure rise. It is desirable to keep it low and if the pressure rise between the impeller outlet and the diffuser throat is large, the throat blockage will be large as well and will then lead to a small pressure rise in the vaned passage downstream of the throat. This conclusion was drawn by Dean [55] and successively confirmed by Rodgers [217], who performed a very wide range of tests and claimed that nearly 3/4 of the static pressure rise occured upstream of the throat. Rodgers also found a strong influence of the blockage on the pressure rise. Similar conclusions were shown by Japikse [132] at high speeds. The small pressure rise downstream of the diffuser throat was due to the high velocity as a consequence of the blockage increase.

5.5.10 Incidence angle

The incidence angle at the diffuser vane leading edge is another significant parameter which influences the operating range of a centrifugal compressor equipped with a vaned diffuser. The diffuser vane incidence angle is defined as

$$i_3 = \alpha_{3v} - \alpha_3, \tag{5.12}$$

where α_{3v} is the vane angle and α_3 is the flow angle. Both angles are measured from the tangential direction.

At constant rotational speed, as the mass flow rate is reduced from the design value, the meridional velocity decreases accordingly while the tangential velocity will increase. As a consequence, the flow angle at the vane leading edge is inclined at a larger value

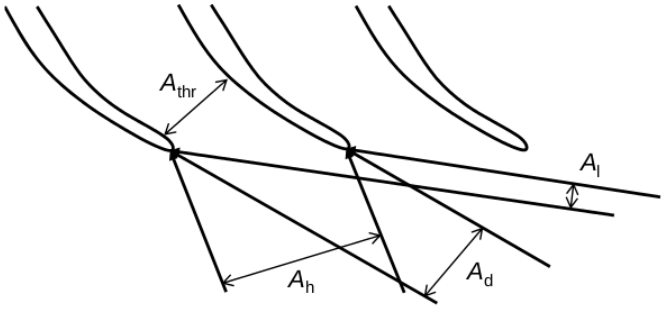

Figure 5.11: *Variation of incidence angle with varying mass flow rate, at the vane leading edge of a vaned diffuser. A_{thr} is the throat area; A_d is the flow passage area at design point; A_l is the flow passage area at a mass flow rate lower than design; A_h is the flow passage area at a mass flow rate higher than design.*

from the radial direction. The reduction in mass flow rate is thus perceived by the diffuser vane as a positive incidence. At low flow rates, the throat area will then increase, causing flow deceleration and thereby an increase in the static pressure rise in the vaneless space upstream of the throat (Fig. 5.11). The diffuser vanes stall may eventually be the ultimate consequence of such phenomena. Conversely, a mass flow rate larger than the design one causes the meridional velocity to increase and forces the flow into a more radial direction. A negative incidence angle is thus seen by the diffuser vane. At the same time, the throat area will decrease, causing a flow acceleration and a significant reduction in pressure recovery. This will eventually lead to the compressor stage choking. Furthermore, at high flow rates the boundary layer will tend to be thin because the flow is generally accelerating, and as the flow rate is reduced the boundary layer thickness will increase and the performance of the diffuser will be reduced.

Dean [54] studied the impact of the vane incidence angle on the flow range and observed that it could be changed by several degrees without visible effects on the performance of high pressure ratio machines.

Rodgers [217] carried out experiments on a single-stage centrifugal compressor equipped with channel diffusers and showed fairly small variations in performance when the vane angle at the leading edge changed up to +5°.

Sorokes and Welch [246, 247] investigated the effect of the setting angle in LSVDs with a solidity equal to 0.7. The setting angle was varied to give an incidence angle in the range ±10°. With a large setting angle, high incidence occurred at high flow rates and consequently the efficiency was poor in the choking condition. At low flow rates, the efficiency exceeded that of a vaneless diffuser and the surge margin was reduced.

Hohlweg *et al.* [112] tested a CVD and three LSVDs downstream of a high-speed air compressor and a low-speed nitrogen compressor. The solidity of the LSVDs was kept constant but the incidence angle varied. The authors found out that for the high-speed compressor the LSVD with the highest negative incidence (−4.1°) had the best overall performance and its flow range exceeded by 30% that of the CVD. On the contrary, the

LSVD with the highest positive incidence (+0.3°) had significantly lower efficiency and stability than the CVD. The best efficiency was obtained with an incidence angle equal to −1.9°, but it was lower than the efficiency of the CVD. The authors concluded that even higher negative incidence angles could improve the LSVD stability, at the expenses of a decline in efficiency, while positive incidence angles was not a good choice when designing LSVDs.

By studying previous works [30, 102, 106, 112, 232, 246, 247], Engeda [77] concluded that the flow range tended to increase as the incidence angle became more negative, up to a certain value, showing then that there was an optimum incidence angle at which the highest flow range could be achieved. He also noticed that there was a trend of peak efficiency at an incidence angle around −2°.

The same value of incidence angle was also used by Turunen-Saaresti [262], who performed a numerical study on five different LSVDs coupled with a high-speed centrifugal impeller. Flat plate vanes, vanes with circular arc camberline but constant thickness distribution, and vanes with circular arc camberline and NACA 65-Series thickness distribution were modelled. Generally, the LSVDs achieved good performance over a wide range of incidence angles, and only very high negative or positive incidence angles deteriorated the efficiency.

Other values of incidence angles were applied as well in the design and analysis of vaned diffuser. Stahlecker and Gyarmathy [250] performed laser Doppler velocimetry measurements on a single stage high subsonic centrifugal compressor with a vaned diffuser having 24 circular arc vanes, placed such that the incidence was zero.

Justen *et al.* [148] carried out unsteady pressure measurements on a highly loaded centrifugal compressor impeller followed by a diffuser with 23 wedge vanes. The investigations were performed at three different operating speeds and two values of radius ratios were employed, both combined with two setting angles equal to +14.5° and +16.5° from the tangential direction.

The setting angle was further decreased to +12.5° by Ziegler *et al.* [285, 286], who performed laser-2-focus velocimeter measurements on the same experimental set-up used by Justen *et al.* to study the impeller-diffuser interaction as function of the radial gap between the impeller outlet and the diffuser vanes leading edge.

Boyce [27] claimed that the diffuser vanes should be set at an incidence angle equal to −4°, in order to accomodate the variation in flow angle along the vanes leading edge.

Jaatinen *et al.* [131] studied experimentally three vaned diffusers having a very large negative incidence (−8°) at the design condition and concluded that designing vaned diffusers with such high negative values at the design point improved the performance at low mass flow rates, without deteriorating the performance at the design condition, compared to a vaneless diffuser.

5.6 Summary

There are many geometric and flow parameters to be considered for vaned diffusers design, irrespective of the family to which they belong to. Some of them (e.g., 2θ, LWR,

AR, and throat blockage) are however more closely related to the design of 2D straight channel diffusers. At the same time, there is no definitive indication about which vaned diffuser type delivers the best performance, while it is clear that the profiled category has indeed the advantage of a smaller diffuser outlet diameter.

Other parameters (e.g., the diffuser height and, more generally, the shape of the meridional channel) are relevant in determining the thermodynamic state of the flow along the diffuser, therefore the nature and stability of the profile and end-walls boundary layers. However, there is a lack of information in the literature about the influence of the diffuser height on the diffuser performance.

Furthermore, the shape of the profile does not seem to influence the diffuser efficiency in a very significant way, even if the use of proper aerodynamic airfoils has proven to be effective in reducing the losses. On the other hand, as far as the pressure recovery is concerned, the influence of the shape is more evident according to the actual lift coefficient of the profile. Moreover, a different profile geometry can significantly influence the behavior of the centrifugal compressor stage at off-design conditions.

Experimental results show that vaned diffusers having a long chord exhibit a higher peak efficiency and pressure recovery, despite their large volutes. The length of the chord also highly influences the compressor operating range, since it can be related to the appearance of a throat in the separated flow field at partial loads.

The occurrence of a throat is also controlled by the diffuser vane number, so that the operating range is reduced when the solidity is high and increased, especially toward the choking condition, when LSVDs are employed. Further on, the vane number has a direct influence on the compressor stage size and efficiency, although it is worth noting that its reduction does not have a significant impact on the peak efficiency until the vane number goes below a certain minimum value.

The length of the radial vaneless gap between the impeller outlet and the diffuser vanes leading edge is relevant in determining the size of the diffuser throat at off-design conditions, and thus the size of the compressor stage, in reducing the vibrations and noise due to the impeller-diffuser interaction, and in reducing the Mach number at the vanes leading edge. However, on the one hand, experimental results show negligible variations in peak efficiency among configurations having different gaps. On the other hand, contradicting results have been found about the relationship between the inlet radius ratio and the diffuser efficiency. Therefore, it seems that the corresponding recommendations to find the optimum radial gap do not exist yet, despite the numerous works about this topic.

Furthermore, the diffuser vanes incidence angle can influence the position of the optimal operating condition, and can thus determine the optimal mass flow rate, pressure recovery, and efficiency. As a consequence, isolating the influence of this parameter from all the others might not be an easy task, especially because a change in it can affect the status of the flow passing through the compressor stage. However, the optimal matching between an impeller and a vaned diffuser is achieved only with a specific value of incidence angle, departing from which might lead to a dramatic reduction of the compressor stage performance.

In conclusion, in view of the vaned diffusers optimization which will be discussed in Chap. 6, the relative position of the diffuser vanes between the inlet and outlet, their incli-

nation with respect to the radial direction at the leading and trailing edges, and the vane number has been selected as the variables for vaned diffusers design. The vane profile has been kept constant and consists of a circular arc camberline with constant thickness distribution.

"It is not the strongest of the species that survives, nor the most intelligent that survives. It is the one that is the most adaptable to change."

Charles Darwin.

6

Vaned diffusers optimization

In this chapter, the optimization of vaned diffusers has been performed by coupling a genetic algorithm firstly to a in-house computational fluid dynamics code which solves the two-dimensional Euler equations, and secondly to a commercial code which solves the three-dimensional Reynolds averaged Navier-Stokes equations. In the latter case, a metamodel has been used to reduce the computational costs. The position of the vanes between the diffuser inlet and outlet, their inclination with respect to the radial direction at the leading and trailing edges, the diffuser vane number, and the diffuser outlet radius have been selected as design variables. The maximization of the static pressure recovery and the minimization of the total pressure losses have been chosen as objective functions.

Excerpts of this chapter appeared in:

Olivero M., Pasquale D., Ghidoni A., and Rebay S., 2012. "Three-Dimensional Turbulent Optimization of Vaned Diffusers for Centrifugal Compressors Based on Metamodel-Assisted Genetic Algorithms," submitted for publication to Optim. Eng.

Olivero M., Pasquale D., Ghidoni A., Pecnik R., Rebay S., and van Buijtenen J. P., 2011, "Aerodynamic Shape Optimization of a Vaned Diffuser for a Micro Turbine Centrifugal Compressor," *Proc. 2011 International Conference on Evolutionary and Deterministic Methods for Design, Optimization and Control with Applications to Industrial and Societal Problems.*

6.1 Introduction

Vaned diffusers (VDs) design usually relies on experimental data and on the engineer's experience. These aspects however represent a limit when a VD has to be employed in small-size centrifugal compressors, since a solid design procedure has not been developed yet. Recently, the coupling of computational fluid dynamics (CFD) codes with optimization techniques has however gained interest in turbomachinery, and proved to be helpful to overcome the weakness of designing a VD on the basis of empirical correlations. Nevertheless, not many studies on this topic can be found in the literature.

Benini and Tourlidakis [23] performed a three-dimensional (3D) design optimization of VDs for centrifugal compressors, by coupling a multi-objective genetic algorithm (MOGA) with a commercial CFD code. The authors ignored the impeller-diffuser interaction in their study, and assumed uniform flow conditions at the diffuser inlet. They evaluated the effectiveness of the optimization method by comparing the efficiency and pressure recovery of an existing VD with those of optimized diffusers.

Micheli *et al.* [183] redesigned the VD of a centrifugal compressor through a CFD code coupled firstly to a MOGA, and secondly to a non-linear Nelder-Mead Simplex method. In the former case, the diffuser static pressure recovery coefficient and the total-to-total isentropic efficiency were optimized, wherelse in the latter case only the static pressure recovery coefficient was used as objective function. The optimization has been carried out at the compressor design point, and yielded one optimized geometry having better pressure recovery, and another with higher efficiency.

Benini and Toffolo [22] presented the constrained optimization of a diffuser apparatus, consisting of radial and deswirl cascades. The optimization has been performed through a MOGA interfaced to a parametric code for the geometries generation, and to a CFD code for evaluating the candidates. The maximum pressure rise has been achieved with the lower stagger angle of the radial profile, while the total pressure losses have been minimized with the lower camber of the deswirl profile.

Wang *et al.* [271] performed the optimization of VDs for high-speed centrifugal compressors by means of a 3D CFD turbulent flow analysis, a genetic algorithm, and a Kriging surrogate model, which substituted the time-consuming numerical computations and accelerated the optimization procedure. The objective was the largest decrement of the total pressure losses, while maintaining the static pressure recovery. For the given operating condition, the total pressure losses were reduced by 5.5%, while the static pressure recovery was increased by 2.6%.

Xi *et al.* [282] carried out the design optimization of the VD for a 100-kW micro turbine centrifugal compressor. A forward-loaded diffuser and a conventional airfoil one have been redesigned by means of 3D CFD calculations and a surrogate model, which considerably accelerated the optimization process. The optimization aimed at the maximum stage total-to-static isentropic efficiency. The CFD predictions showed that the latter was improved at design and off-design conditions.

Kim *et al.* [152] optimized both the impeller and diffuser of a centrifugal compressor by means of the response surface method. Higher total pressure ratio, pressure recovery, and efficiency were obtained with respect to the original design, since the total pressure

losses decreased dramatically.

In this chapter, at first a preliminary VD has been designed on the basis of a classical procedure and empirical correlations found in the literature. Subsequently, in order to optimize the VD and to further increase its performance, an optimization strategy in combination with a CFD tool has been built into an optimization environment which includes several algorithms, design of experiments (DOE) techniques, and metamodels [116].

Firstly, a single-objective optimization problem has been solved by coupling an optimization method to an in-house CFD code [49] which solves the two-dimensional (2D) Euler equations, over a domain which includes the vaned diffuser only.

Secondly, a multi-objective optimization problem has been solved by coupling the same optimization method to a commercial CFD package [9] which solves the 3D Reynolds averaged Navier-Stokes (RANS) equations, over a domain which includes both the impeller and the vaned diffuser. In this case, a metamodel has been utilized to speed up the optimization procedure by reducing the computational costs. Furthermore, the 3D multi-objective optimization has been performed with two different centrifugal impellers (i.e., the current impeller and a larger one).

Before presenting and discussing the results of the 2D and 3D optimizations, an overview of the general optimization problem is given, followed by the description of the optimization techniques adopted in this dissertation.

6.2 General statement of the optimization problem

An optimization problem can be mathematically formulated as

$$\text{minimize} \qquad f(\mathbf{x}), \tag{6.1}$$

$$\text{subject to} \qquad g_j(\mathbf{x}) \le 0 \qquad j = 1 \dots l, \tag{6.2}$$

$$h_k(\mathbf{x}) = 0 \qquad k = 1 \dots m, \tag{6.3}$$

$$x_{p,\min}(\mathbf{x}) \le x_p \le x_{p,\max}(\mathbf{x}) \qquad p = 1 \dots n, \tag{6.4}$$

$$\text{where} \qquad \mathbf{x} = \begin{Bmatrix} x_1 \\ x_2 \\ \vdots \\ x_n \end{Bmatrix}. \tag{6.5}$$

The vector $\mathbf{x}$ contains the n design variables (i.e., the parameters that can vary during the design process) and is thus named the design vector. The objective function is $f(\mathbf{x})$ and represents the criterion chosen for comparing the different designs and for selecting the best one. Equations $g_j(\mathbf{x})$ and $h_k(\mathbf{x})$ are the inequality and equality constraints, respectively. Inequality constraints (Eq. 6.2) represent certain specified functional and/or other requirements that have to be fulfilled, wherelse equality constraints (Eq. 6.3) indicate relationships between the design variables that can be used to reduce their number. A good choice of the design variables can however eliminate $h_k(\mathbf{x})$. Equation 6.4 represents the range within which the design variables are defined.

The problem stated in Eqs. from 6.1 to 6.5 is called a constrained optimization problem. However, some optimization problems do not involve any constraints and can be stated as

$$\text{minimize} \qquad f(\mathbf{x}), \tag{6.6}$$

$$x_{\mathrm{p,min}}(\mathbf{x}) \le x_{\mathrm{p}} \le x_{\mathrm{p,max}}(\mathbf{x}) \qquad p = 1 \dots n, \tag{6.7}$$

$$\text{where} \qquad \mathbf{x} = \begin{Bmatrix} x_1 \\ x_2 \\ \vdots \\ x_{\mathrm{n}} \end{Bmatrix}. \tag{6.8}$$

The abovementioned problem represents a single-objective optimization formulation, because it considers the minimization of one objective function only, thus only one design vector $\mathbf{x}$ minimizes the latter. However, some applications requires the simultaneous minimization of several objective functions $f_{\mathrm{i}}(\mathbf{x})$, leading to a so-called multi-objective optimization problem

$$\text{minimize} \qquad f_{\mathrm{i}}(\mathbf{x}) \qquad i = 1 \dots r, \tag{6.9}$$

$$\text{subject to} \qquad g_{\mathrm{j}}(\mathbf{x}) \le 0 \qquad j = 1 \dots l, \tag{6.10}$$

$$h_{\mathrm{k}}(\mathbf{x}) = 0 \qquad k = 1 \dots m, \tag{6.11}$$

$$x_{\mathrm{p,min}}(\mathbf{x}) \le x_{\mathrm{p}} \le x_{\mathrm{p,max}}(\mathbf{x}) \qquad p = 1 \dots n, \tag{6.12}$$

$$\text{where} \qquad \mathbf{x} = \begin{Bmatrix} x_1 \\ x_2 \\ \vdots \\ x_{\mathrm{n}} \end{Bmatrix}. \tag{6.13}$$

In this case, conflicting objective functions might exist, such that none of the feasible solutions allows the simultaneous minimization of all of them. Therefore, the solution to the problem is a family of design variables known as the Pareto front. An example of the Pareto front for two objectives f_1 and f_2, which both have to be minimized, is given in Fig. 6.1. Each solution which belongs to the front is optimal in that the first objective cannot be improved without leading to a decrement of the second one. In particular, design D_1 is dominated by design D_2 since the values of both its objectives are higher than those of D_2. However, design D_3 is not dominated by design D_2, and vice versa, because an improvement of f_1, by going from design D_2 to design D_3, will lead to a deterioration of f_2. If no other design can be found to improve both objectives, designs D_2 and D_3 belong to the Pareto front.

A simple way to handle this problem is to convert a multi-objective function into a single-objective one by considering a "pseudo-objective function" $\tilde{f}(\mathbf{x})$ as the weighted sum of each individual objective

$$\tilde{f}(\mathbf{x}) = \sum_{i=1}^{n} w_{\mathrm{i}} f_{\mathrm{i}}(\mathbf{x}), \tag{6.14}$$

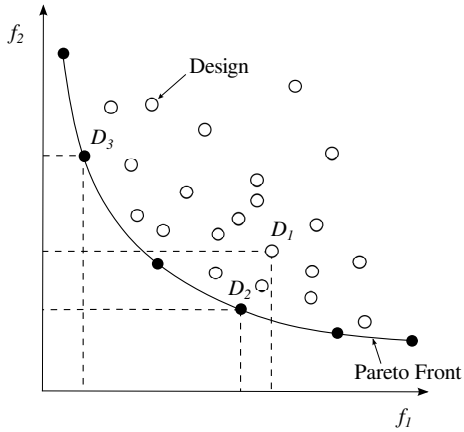

Figure 6.1: *An example of the Pareto front in the case of the minimization of two objective functions f_1 and f_2. Design D_1 is dominated by designs D_2 and D_3, which are thus Pareto optimal solutions.*

where $w_i \geq 0$ are the weighting coefficients representing the relative importance of the i-th objective function $f_i(\mathbf{x})$. It is usually assumed that the sum of all the coefficients has to be equal to 1 [43, 160]. The main difficulty with this approach is however the selection of the weights, since the solution can vary significantly as they change, and since very little is usually known about how to choose them. In any case, solving a problem with the objective function given by Eq. 6.14 will yield to a single solution for a given weight vector $\mathbf{w} = \{w_1, w_2, \ldots, w_n\}$, such that if multiple solutions are desired, the problem must be solved multiple times with different weight combinations.

This concept is illustrated in Fig. 6.2a in the case of the minimization of two objective functions f_1 and f_2. By fixing the weights w_1 and w_2, all the designs that yield the same value of the objective function $\tilde{f}(\mathbf{x}) = w_1 f_1 + w_2 f_2 = const$ lie on the same straight line. Since during the optimization process $\tilde{f}(\mathbf{x})$ has to decrease, in the limiting case the straight line will be tangent to the Pareto front, such that only one optimal design can be found. Figure 6.2b shows the influence of different weights. By changing the weighting coefficients w_i of the objective function $\tilde{f}(\mathbf{x})$, different Pareto optimal solutions can be found.

6.3 Optimization problems and solution techniques

According to Rao [210], optimization problems can be classified on the basis of the existence/absence of constraints, the number of objective functions to be optimized, the nature of the design variables involved, the physical structure of the problem considered, the nature of the expressions used for the objective functions and constraints, the values allowed for the design variables, and the separability of the objective and constraint functions. For a detailed analysis of the different categories, the reader is directed to the work

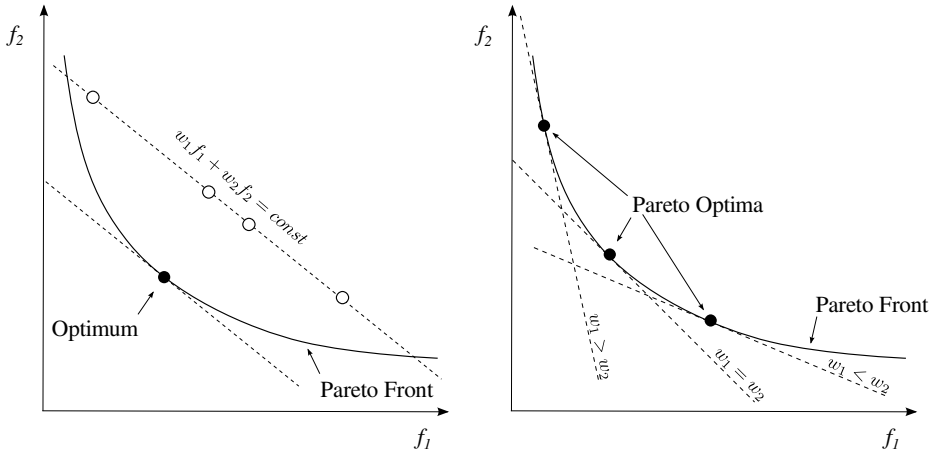

(a) *Only one optimal design is found if w_1 and w_2 are fixed.*

(b) *Influence of different weighting coefficients w_i on the optimal solutions.*

Figure 6.2: *Conversion of a multi-objective optimization problem (i.e., two objective functions f_1 and f_2 to be minimized) into a single-objective optimization problem.*

of Rao [210].

Various optimization techniques are available to find the solution of the different optimization problems listed above. A thorough description of such strategies has been provided by Rao [210], while only a brief overview will be given here.

Generally, optimization methods can be either local or global. In the former case, the starting point is a known configuration, whose design variables are perturbed in such a way that the direction followed leads to a performance improvement, thanks to knowledge available beforehand. In the latter case, a set of several designs are simultaneously compared to each other, combined, and altered to obtain a new set of designs whose performance is optimized.

Another well-known distinction classifies the optimization techniques into stochastic and deterministic methods. In a stochastic (or probabilistic or non-deterministic) optimization problem, the design variables are randomly created and used, wherelse a deterministic (or analitical) method does not involve any randomness in the solution of the optimization problem. Stochastic methods have the ability to work with noisy objective functions with no assumptions on continuity, existence of derivatives, and unimodality. They allow as well for a direct implementation of constraints and multiple objectives, but need a vast number of evaluations to obtain the optimum, even for a small number of design variables. Deterministic methods require some gradient information about the objective function, which increases the computational costs. Further on, they require continuous objective functions, have worse performance in a noisy environment, and are prone to local minima entrapment.

Classical optimization strategies (e.g., non-linear, linear, geometric, quadratic, inte-

ger, and dynamic programming [210]), which are useful in finding the optimum solution of continuous and differentiable functions, are local, deterministic methods. These methods are analytical techniques that make use of differential calculus in locating the optimum points, which are then sought by proceeding in an iterative manner from an initial solution.

On the other hand, in recent years some optimization methods that are conceptually different from the traditional mathematical programming techniques have been developed. They are generally global, stochastic strategies, as they require only the objectives functions to be evaluated, and not the derivatives to be calculated. These methods are labeled as modern or non-traditional optimization methods, and are based on certain characteristics and behavior of biological, molecular, swarm of insects, and neurobiological systems. Some of them are simulated annealing, evolutionary algorithms, particle swarm optimization, ant colony optimization, fuzzy optimization, and neural-network-based methods [210].

6.4 Evolutionary algorithms

Optimization problems are often characterized by mixed continuous-discrete variables and discontinuous and non-convex design spaces. Applying standard non-linear programming techniques in these cases would be inefficient and computationally expensive and, in most cases, a relative optimum that is close to the starting point would be found. Evolutionary algorithms (EAs) are well suited for solving such problems, since they can find the global optimum solution with a high probability.

Although EAs were firstly presented in a systematic fashion by Holland [113], the basic ideas of analysis and design based on the concepts of biological evolution can be found in the work of Rechenberg [211, 212]. Philosophically, EAs are based on Darwin's theory of evolution, whereby populations of individuals evolve over a search space and adapt to the environment by the use of different mechanisms such as mutation, cross-over, and selection. Individuals with a higher fitness have more chance to survive and/or get reproduced.

EAs differ from previous methods since

- A population of design vectors called individuals is used to start the procedure, instead of a single design point. EAs are therefore less likely to local minima entrapment.

- The derivatives are not used in the search procedure, because EAs only evaluate the objective functions.

- The search method is naturally applicable for solving both discrete and integer programming problems, as well as for cases with continuous design variables.

- The objective function value corresponding to a design vector plays the role of fitness in natural genetics.

- In every new generation, a new set of individuals is produced by using random parents selection and cross-over from the parents. Although randomized, EAs are not simple random search techniques, but efficiently explore the new combinations with the available knowledge.

The two most popular evolutionary techniques are genetic algorithms (GAs) and differential evolution. The former is illustrated in the following section, because it has been used in this work.

6.4.1 Genetic algorithms

Genetic algorithms [15, 97] are global optimization algorithms based on the mechanisms of natural selection and use the "survival-of-the-fittest" concept to obtain the optimum. GAs are widely used in turbomachinery optimization and show a very attractive potential in seeking for the global optimum solution in very broad design spaces, without the risk of being trapped in the vicinity of local solutions. Furthermore, they are robust, flexible, and easy to implement because they only require the evaluation of the objective functions for a given set of design variables.

The solution of an optimization problem by GAs starts with a population consisting of a fixed number of individuals (i.e, the design vectors), each one represented by a string of binary (or floating) numbers, analogously to the chromosomes of living creatures.

Each design vector is then evaluated to find its fitness value and the population is subsequently "perturbed" by three operators (i.e., reproduction, cross-over, and mutation) to produce a new population of design vectors. The new population is further evaluated to find the fitness values and tested for the convergence of the process. One cycle of reproduction, cross-over, and mutation, followed by the evaluation of the fitness values, is known as a generation. If the convergence criterion is not satisfied, a new population is iteratively created by means of the three operators and evaluated for the fitness values. The procedure is continued through several generations until the convergence criterion is satisfied and the process is terminated. The details of the three operations of GAs are given below, while Fig. 6.3 shows a flow-chart of the working principles of a standard GA, where t denotes the number of generations.

Reproduction The reproduction operator, also called the selection operator, is the first to be applied in a GA and selects good strings of the population, based on a probabilistic procedure, to insert their multiple copies in the mating pool. In a commonly used reproduction operator, a string is selected from the mating pool with a probability proportional to its fitness.

The implementation of the selection process can be understood by imagining a roulette-wheel with its circumference divided into segments, one for each string of the population, with the segment lengths proportional to the fitness of the strings. By spinning the roulette wheel n times (n being the population size) and selecting, each time, the string chosen by the roulette-wheel pointer, a mating pool of size n is obtained. Since the segments of the circumference of the wheel are marked according to the fitness of the various strings of

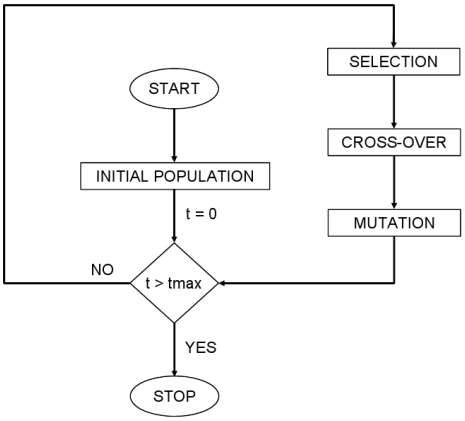

Figure 6.3: *The flow-chart of the working principles of a standard genetic algorithm, where t denotes the number of generations.*

the original population, strings with a higher fitness value will be selected more frequently to be copied into the mating pool, thus strings with high fitness values in the population, probabilistically, get more copies in the mating pool. Note that no new strings are formed in the reproduction stage, but only the existing strings in the population get copied to the mating pool. The reproduction stage ensures that highly fit individuals live and reproduce, wherelse less fit individuals die. GAs indeed simulate the principle of survival-of-the-fittest as encountered in nature. Although this algorithm seems to be elaborate, in some cases it is affected by slow convergence to the optimum [150]. In addition, the population of the roulette-wheel selection will be less diverse due to the more elitist selection.

Tournament and ranking [15, 98] are other selection techniques implemented into EAs. In the tournament selection, s individuals are chosen randomly from the population and the best among them is selected as the first parent. The second parent is selected in the same way. The parameter s is called the tournament size and the larger it is, the more elitist the selection will be, while low values allow less fit parents to be selected, resulting in a more diverse population. Binary tournaments, for which $s = 2$, are the most common. Note that the entire optimization strategy rests only on retaining the best out of two randomly selected individuals. Although this is a very simple selection rule, it has proven to be very effective. Ranking assigns selection probabilities solely based on the individuals rank, ignoring the absolute fitness values.

Cross-over After reproduction, the cross-over operator is implemented to create new strings by exchanging information among strings of the mating pool. Many cross-over operators have been used in the literature, but in most cases two individual strings are randomly selected from the mating pool previously generated and some of their portions are exchanged between the strings. In the commonly used process, known as a single-point cross-over operator, a cross-over site is randomly selected along the string length and the

binary digits lying on the right-hand side of the cross-over site are swapped between the two strings. The two selected strings are known as parent strings, and the generated strings are known as child strings.

Since the cross-over operator combines substrings from parent strings having good fitness values, the created child strings are expected to have better fitness values, if an appropriate cross-over site is selected. However, the appropriate cross-over site is not known a priori, but randomly chosen, such that the child strings may or may not be as good as (or better than) their parent strings in terms of their fitness values. Therefore, the effect of cross-over may be useful or detrimental, so it is desirable not to use all the strings of the mating pool in cross-over, but to preserve some of the good strings of the mating pool as part of the population in the next generation. In practice, a cross-over probability is used in selecting the parents for cross-over. In most GAs, a probability around 0.7-0.9 is given to the cross-over operation [268], in order to have a small chance to the parents to move into the new generation without reproducing.

Mutation The cross-over is the main operator by which new strings with better fitness values are created for the new generations, while the mutation operator changes the binary digit 1 to 0, and vice versa, with a specific small mutation probability p_{m}. Typical values for the mutation probability can be around 0.001-0.008 [268]. Several methods can be used for implementing the mutation operator. In the single-point mutation, a mutation site is randomly selected along the string length and the binary digit at that site is then changed from 1 to 0 or 0 to 1 with probability p_{m}. In the bit-wise mutation, each bit (binary digit) in the string is considered one at a time in sequence and the digit is changed from 1 to 0 or 0 to 1 with a probability p_{m}.

During the evolutionary process, it is possible that the best individual is lost by mutation or cross-over. To prevent this loss of valuable information for the evolution, most genetic algorithms use the elitism strategy. In case the best individual of the new generation is worse than that of the previous generation, the latter one will replace a randomly selected individual of the new generation. In this way, the best individual prevails or can be replaced by a better one.

6.4.2 Metamodels

Due to the population-based approach, GAs require hundreds or thousands evaluations during the optimization process. This number can increase even more depending on the complexity of the optimization problem, such that the use of GAs may become unrealistic if the evaluations are computationally expensive, like in the case of CFD simulations.

In order to reduce the computational costs due to the fluid dynamics computations, metamodels can be used to assist the GAs during the optimization process without altering the quality of the final result [96]. A metamodel performs the same task of the CFD tool with a very low computational cost, has no relation with the physical phenomena involved in the real problem, and bases its knowledge on a database. A set of wisely chosen designs are mainly analyzed by means of the CFD computations, so that a series of input/

output relations is generated. The parameters of the metamodels are then tuned in order to maximize the accuracy of those set of samples, and the model becomes able to make predictions also for other individuals. However, it can be very inaccurate especially in regions of the design space which are far from the designs that have been already analyzed. As a consequence, how the optimization algorithm deals with the inaccuracy of the model is the most crucial aspect of the implementation of the metamodel into the optimization system.

Many metamodels exist, such as artificial neural networks, radial basis functions, response surface methods, and Kriging methods, but in this work the latter have been used, because of their ability to generate accurate global approximations of a design space [226]. These metamodels are extremely flexible thanks to the wide range of spatial correlation functions that can be chosen to obtain the approximation, such that Kriging models can approximate linear and non-linear functions equally well. Furthemore, Kriging models can either "honor the data", by providing an exact interpolation of the data, or "smooth the data", in the presence of numerical noise [50]. Another advantage of Kriging metamodels is that the error of an estimated value can be obtained as a by-product of the prediction of the objective functions [170, 268].

The theory behind Kriging models was developed by Matheron [177] on the basis of the work of Krige [163, 164], a South-African mining engineer who developed a method to elaborate maps of mineral concentrations from scattered samples. A few years later, Kriging models were introduced in the field of statistics to include the correlations that existed between the residuals of a linear estimator [99]. Therefore, many references are available about the use of Kriging techniques in geostatistics [100, 147] and in spatial statistics [50, 215, 253], providing many details on the development and use of such models in these disciplines. More recently, Kriging metamodels became of interest for accelerating optimization processes [3, 93, 141, 170, 176, 236–238, 249].

The mathematical formulation of a Kriging model is given as

$$y(\mathbf{x}) = p(\mathbf{x}) + Z(\mathbf{x}), \tag{6.15}$$

where $y(\mathbf{x})$ is the unknown function of interest, $p(\mathbf{x})$ is a known polinomial function, and $Z(\mathbf{x})$ is the realization of a Gaussian random process with zero-mean, variance σ^2, and non-zero covariance [226, 239]. The vector $\mathbf{x} = (x_1, x_2, \ldots, x_{n_s})$ represents the set of the n_s sample points.

The function $p(\mathbf{x})$ is a polinomial regression function which provides a "global" approximation of the design space. The regression function can be assumed either constant, linear, or quadratic. Although many authors [141, 226, 239] chose a constant value for $p(\mathbf{x})$, a quadratic regression function has been adopted in this work, since it is more accurate than the other two, on the basis of several error metrics. The regression function is defined as

$$p(\mathbf{x}) = \sum_i a_{ii} x_i^2 + \sum_{i,j} a_{ij} x_i x_j + \sum_i a_i x_i, \tag{6.16}$$

where a_{ii}, a_{ij}, and a_i are the coefficients of the polinomials, determined through least-square regression. The latter minimizes the sum of the squares of the deviations between

the predicted values and the actual ones. The coefficients can be found by means of

$$\mathbf{A} = [X'X]^{-1} X'y, \tag{6.17}$$

where X is the design matrix of the sample data points, X' is its transpose, and y is a column vector that contains the values of the response at each sample point.

The term $Z(\mathbf{x})$ creates "localized" deviations, so that the Kriging model can interpolate the n_s sampled data points. The covariance matrix of $Z(\mathbf{x})$ is given by

$$\mathrm{cov}\left[Z\left(x^i\right), Z\left(x^j\right)\right] = \sigma^2 \mathbf{R}, \tag{6.18}$$

where $\mathbf{R} = \left[R(x^i, x^j)\right]$ is an $n_s \times n_s$ symmetric, positive definite matrix with ones along the diagonal, and off-diagonal elements given by $R(x^i, x^j)$, which is the correlation function between any two sample points x^i and x^j. A variety of correlation functions exist [226], but here the Gaussian correlation function has been used. It has the form

$$R(x^i, x^j) = \prod_{k=1}^{n} \exp\left(-\tau_k \left|x_k^i - x_k^j\right|^2\right), \tag{6.19}$$

where n is the number of design variables, τ_k are the unknown correlation parameters used to fit the model, and x_k^i and x_k^j are the k-th components of the sample points x^i and x^j. In same cases, using a single correlation parameter yields to good results [226], but here a different τ_k for each design variable has been utilized.

6.5 Geometry definition

A vane profile with a circular arc camberline [248] has been adopted for this optimization work. The choice of such a simple geometry has been based on manufacturing and economic reasons, which are fundamental when considering the very small dimensions of the turbocharger centrifugal compressor investigated here. Furthermore, this configuration can be considered as a first step in the design and optimization of VDs which will later involve more complex vane profiles.

Figure 6.4 shows the geometry of the circular arc VD. The camberline is defined by the radius of curvature (r_c) and the chord length (c). The vane angles at the leading (α_{3v}) and trailing (α_{4v}) edges are connected to each other by the vane turning angle (VTA). The leading and trailing edges radii are r_3 and r_4, wherelse the diffuser inlet and outlet are located at r_2 and r_5, respectively. The stagger angle is represented by θ. Furthermore, a constant thickness distribution equal to 1 mm has been applied to the camberline in order to define the pressure and suction sides, wherelse the vane profile is represented by the use of two non-uniform rational B-spline (NURBS) curves. Although the camberline consists of a circular arc, the NURBS approach has been utilized in view of future optimization works involving airfoil-shaped diffuser vanes.

For the 2D optimization problem, the VD has to fit into the available vaneless space of the current centrifugal compressor, between r_2 = 19.5 mm and r_5 = 33 mm. The chosen

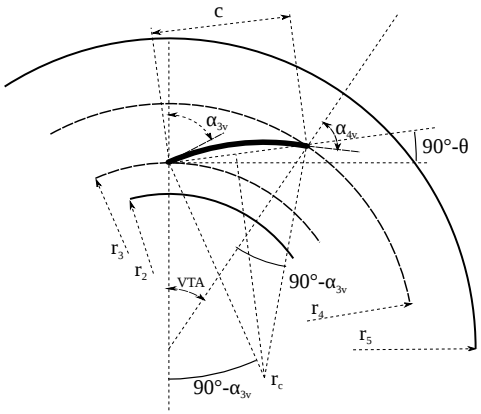

Figure 6.4: *Details of the circular arc vaned diffuser. The camberline is defined by the radius of curvature* (r_c) *and the chord length* (c)*. The vane angles at the leading* (α_{3v}) *and trailing* (α_{4v}) *edges are connected to each other by the vane turning angle* (VTA)*. The leading and trailing edges radii are* r_3 *and* r_4*, respectively, while the diffuser inlet and outlet are located at* r_2 *and* r_5*, respectively. The stagger angle* θ *is shown as well.*

design variables are then the radius ratios at the diffuser vane leading $(RR_3 = r_3/r_2)$ and trailing $(RR_4 = r_4/r_2)$ edges, the vane angle at the leading edge (α_{3v}), the vane turning angle, and the vane number (Z_D).

For the 3D optimization problem, the radius ratio at the diffuser outlet $(RR_5 = r_5/r_2)$ has been chosen as a sixth design variable, in order to minimize the friction losses that can be generated in the vaneless space between the vanes leading edge and the outlet. The decision is also supported by the fact that vaned diffusers are usually more compact than vaneless diffusers, because the presence of the vanes provides further reduction in the tangential velocity in comparison with vaneless designs.

Table 6.1 shows the ranges of variation for the design variables for both the 2D and 3D optimization problems, while Table 6.2 lists the corresponding values of the preliminary VD designs for the current $(D_{p,c})$ and larger $(D_{p,l})$ impellers. The works of Rodgers [217], Inoue and Cumpsty [118], and Cumpsty [51] have been used to define RR_3, while RR_4 has been set according to a formula given by Aungier [13]. The latter reference has been utilized as well to choose Z_D, wherelse α_{3v} and VTA have been specified following the works of Engeda [77] and Eynon and Whitfield [85], respectively. The outlet radius ratio RR_5 corresponds to that of the vaneless diffuser.

6.6 Two-dimensional Euler single-objective optimization

The optimization method coupled to a 2D Euler solver aims to find a combination of the diffuser design variables which assures, at the micro turbine design point (i.e., $\dot{m}$ = 50 g/s and N = 240 krpm), the maximum static pressure recovery with the minimum amount

Table 6.1: *Range of definition of the design variables for the two- and three-dimensional optimization problems. RR_3 and RR_4 are the radius ratios at the diffuser vane leading and trailing edges, RR_5 is the radius ratio at the diffuser outlet, α_{3v} is the vane angle at the leading edge, VTA is the vane turning angle, and Z_D is the vane number.*

	RR_3	RR_4	RR_5	$\alpha_{3v}\,[^\circ]$	$VTA\,[^\circ]$	Z_D
Minimum	1.05	1.20	1.25	60.0	5	7
Maximum	1.15	1.67	1.95	80.0	20	21

Table 6.2: *Design variables of the preliminary vaned diffuser for the current ($D_{p,c}$) and larger ($D_{p,l}$) impellers. RR_3 and RR_4 are the radius ratios at the diffuser vane leading and trailing edges, RR_5 is the radius ratio at the diffuser outlet, α_{3v} is the vane angle at the leading edge, VTA is the vane turning angle, and Z_D is the vane number.*

	RR_3	RR_4	RR_5	$\alpha_{3v}\,[^\circ]$	$VTA\,[^\circ]$	Z_D
$D_{p,c}$	1.10	1.62	1.69	72.5	10	13
$D_{p,l}$	1.15	1.67	1.69	74.5	10	13

of total pressure losses. Although Euler calculations have been performed, the total pressure loss coefficient has been considered as well, to take into account the eventual presence of shocks, which might occur in the present simulations, because of transonic Mach numbers.

The two objective functions CP (see Eq. 5.1) and K (see Eq. 5.2) cannot be simultaneously satisfied, since maximum static pressure rise will be achieved through high blade loading on the diffuser vane profiles, resulting in higher total pressure losses, while minimum total pressure losses will be obtained using the so-called low-solidity vaned diffusers, which have lower friction losses and do not alter too much the flow direction.

Here, the optimization problem involving two conflicting objective functions has been combined into the minimization of the following objective function

$$f(\mathbf{x}) = w_1(1 - CP) + w_2 K. \tag{6.20}$$

In order to investigate to which extent the different weights would lead to different optimized geometries, three combinations of w_1 and w_2 have been chosen, such that the following three objective functions have been minimized separately

$$\varphi_1 = 0.5(1 - CP) + 0.5K, \tag{6.21}$$

$$\varphi_2 = 0.75(1 - CP) + 0.25K, \tag{6.22}$$

$$\varphi_3 = 0.25(1 - CP) + 0.75K. \tag{6.23}$$

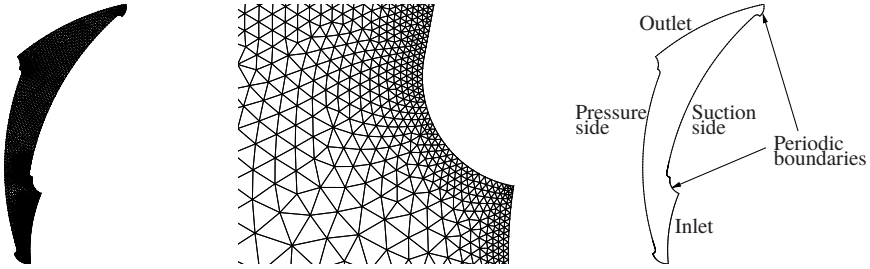

(a) *The grid in the whole domain.* **(b)** *A close-up view of the grid at the vane leading edge.* **(c)** *The boundaries.*

Figure 6.5: *The grid and the boundaries of the computational domain for the two-dimensional Euler single-objective optimization.*

The optimization is driven by an implementation of the non-dominated sorting genetic algorithm II developed by Deb *et al.* [57, 58]. A population of 20 individuals has been chosen. According to van den Braembussche, the solution quality is maximum in the range from 11 to 20 [266], while Rao stated that the population size should be usually taken in the range from $2n$ to $4n$ [210], where n is the number of design variables. The GA computed the evolution of the individuals over 65 generations to ensure the achievement of the global optimum. The probabilities of cross-over and mutation have been specified equal to 0.8 and 0.01, respectively, while elitism has been used. The initial population of the GA, which counts 200 individuals, has been generated by means of a random allocation.

6.6.1 Computational method

Grid generation

The grid generator consist of a fully automated 2D unstructured grid algorithm based on the advancing-Delaunnay strategy [95]. The spacing is defined using a metric field, which is computed on the boundaries analyzing their curvature. In the domain, the spacing is controlled through a background grid, which is utilized to interpolate the boundary value of the metric at any other point of the domain to be discretized. This approach can lead to the creation of discontinuities or large gradients in the metric definition, limited by the use of a spring analogy based algorithm, which allows propagating and regularizing the metric field. The computational domain grid of the preliminary vaned diffuser (Figs. 6.5a and 6.5b) consists of about 7,200 triangular elements, and the same cell number has been used in all the numerical simulations.

Numerical aspects and boundary conditions

The GA has been coupled to an in-house CFD code [49], which solves the 2D Euler equations by means of a hybrid finite element/finite volume approach in which the finite

Table 6.3: *The objective function* $(f(\mathbf{x}))$ *and diffuser performance parameters* (CP, K) *of the preliminary* $(D_{p,c})$ *and optimized* $(\varphi_1, \varphi_2, \varphi_3)$ *vaned diffusers computed for the two-dimensional Euler single-objective optimization.*

	$D_{p,c}$	φ_1	Δ[%]	$D_{p,c}$	φ_2	Δ[%]	$D_{p,c}$	φ_3	Δ[%]
$f(\mathbf{x})$	0.084	0.075	−11.4	0.115	0.091	−20.7	0.054	0.053	−3.3
CP	0.855	0.884	+3.4	0.855	0.891	+4.1	0.855	0.884	+3.3
K	0.024	0.034	+40.3	0.024	0.036	+47.3	0.024	0.031	+29.2

volume metric quantities are computed using the standard linear Lagrange polynomials basis functions of the finite element method [229]. The spatial approximation of the Euler flow equations is constructed by means of a high-resolution finite volume method suitable for general unstructured and hybrid grids, while the first-order scheme is the well-known Roe's approximate Riemann solver [220]. This class of discretization schemes is particularly well suited for the computation of high Mach number flows. The in-house CFD code adopts an implicit time integration scheme, which computes steady-state solutions in a much more efficient way with respect to conventional explicit schemes.

The boundary conditions of the computational domain are shown in Fig. 6.5c. The CFD simulations have been performed with uniform inlet flow conditions, obtained by solving the 3D RANS equations across the current centrifugal impeller and the downstream vaneless diffuser [196]. At the inlet, total pressure (i.e., 359 kPa) and temperature (i.e., 448 K) have been specified, while an absolute flow angle equal to 74.2° has been set. At the outlet, the static pressure has been constantly changed to achieve a mass flow rate equal to 50 g/s. The symmetry condition has been applied on the vane wall. The solutions advance in time until the L^2-norm of the residuals is reduced to 10^{-8} times with respect to the first iteration.

6.6.2 Results and discussion

In this section, the results of the three single-objective optimization problems are discussed. Firstly, the objective functions which are the solution to the three optimization problems are analyzed. Secondly, the optimized vaned diffusers corresponding to the solution to the three optimization problems are studied in depth.

The comparison between the single-objective functions calculated for the preliminary and the optimized geometries is shown in Fig. 6.6 and in Table 6.3. The objective functions values for the three optimized diffusers decreased by 11.4%, 20.7%, and 3.3% for φ_1, φ_2, and φ_3, respectively. In all cases, CP is higher than that of the preliminary diffuser, but K has increased as well.

Figure 6.7a shows the three objective functions for the 20 individuals of the population, for each generation. In total, about 1,200 individuals have been analysed for each

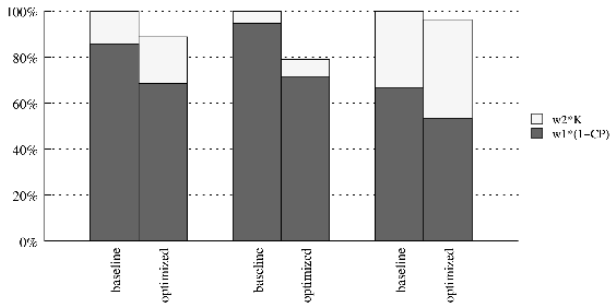

Figure 6.6: *Objective function comparison between preliminary and optimized vaned diffusers for the two-dimensional Euler single-objective optimization. From left to right, the objective functions are φ_1, φ_2, and φ_3, respectively.*

objective function. In all cases, a higher dispersion of individuals can be seen during the first generations. This indicates that the GA has searched through a wider space, but this dispersion weakens as the generations pass by, although it is still noticeable for φ_1, such that a clear path towards the optimal solution is found. Further on, when CP and K are given the same two weights (i.e., φ_1), more time is needed for the GA to find the trend towards the optimum. On the contrary, if one objective function dominates the other because of a higher weight, the population tends to the optimal solution at a faster pace.

Figure 6.7b illustrates the best individual of every generation, for each objective function. It is interesting to notice that, despite the larger dispersion of the values previously seen, the best individual for φ_1 has already been found at the second generation, while it took more time for φ_2 and φ_3 (56 and 20 generations, respectively). At the same time, as a consequence of what has been mentioned above, the figure shows that for φ_2 and φ_3 the best individual of each generation is very close to the global minimum.

Figures from 6.7c to 6.7f illustrate the leading and trailing edge radius ratios and vane angles computed for all the evaluations, for the three objective functions. The vane number is not shown because the trend to the optimum value has been found very quickly for the three objective functions. The spread of the Z_D-values was thus visible only in the early phases of the optimization cycle. The range within which the vane number varied was however narrow (from 9 to 13 vanes), eventually because only integers were allowed, and since the vane number could be less important if Euler calculations are performed. For φ_2 and φ_3 the vast majority of the individuals had 13 vanes, while for φ_1 the vane number was equal to 12 in most cases. For both radius ratios (Figs. 6.7c and 6.7d) and both vane angles (Figs. 6.7e and 6.7f), the values are more dispersed at the very beginning of the optimization cycle, and further tend to the optimum, while the individuals reproduce. The tendency of RR_3 and α_{3v} is to go towards different values for φ_1, φ_2, and φ_3, respectively, although the path towards optimized values is easily noticed for the three objective functions. In general, the design variables which represent the leading edge position and inclination seem to be more important than the trailing edge position and inclination, since

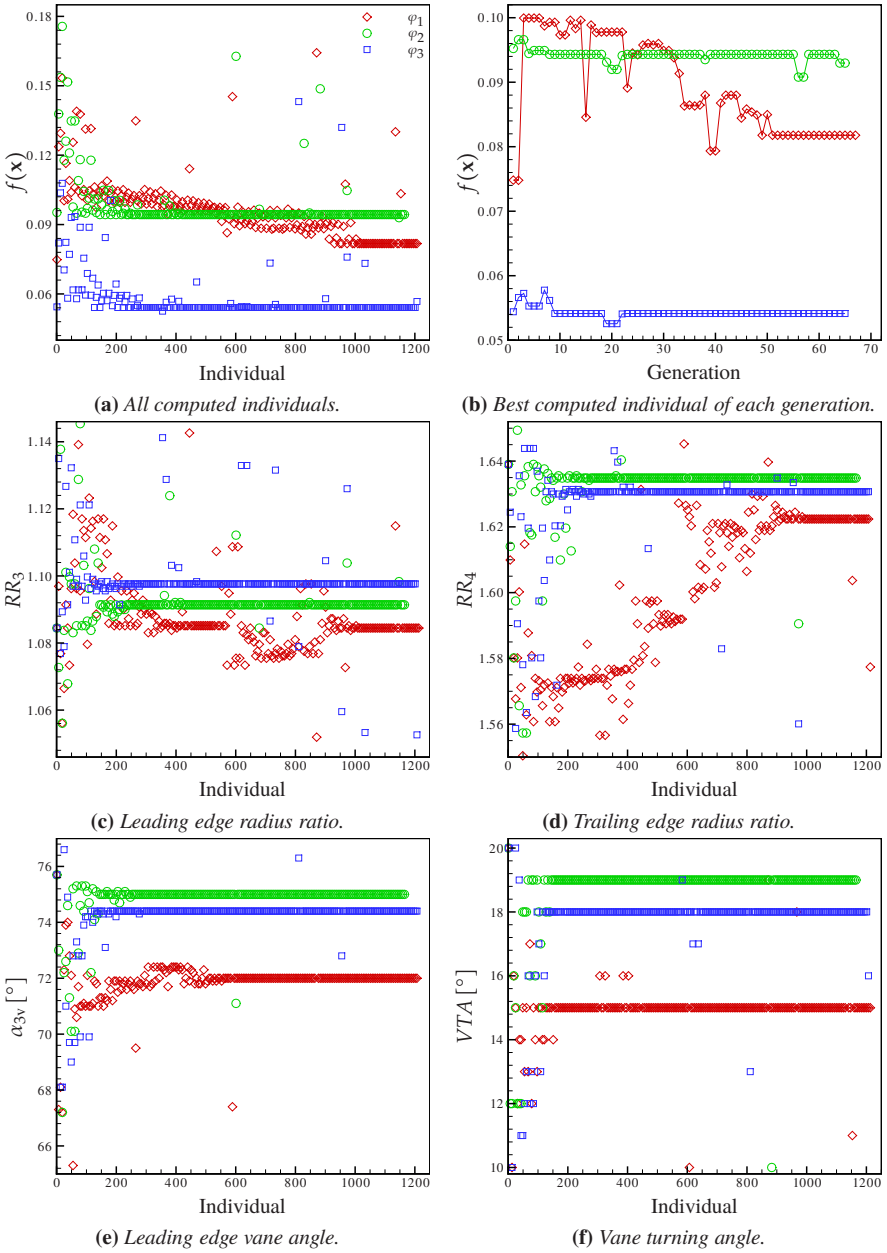

(a) *All computed individuals.*

(b) *Best computed individual of each generation.*

(c) *Leading edge radius ratio.*

(d) *Trailing edge radius ratio.*

(e) *Leading edge vane angle.*

(f) *Vane turning angle.*

Figure 6.7: *The objective function* $(f(\mathbf{x}))$ *and the design variables* $(RR_3,\ RR_4,\ \alpha_{3v},\ VTA)$ *computed for the optimized vaned diffusers* $(\varphi_1,\ \varphi_2,\ \varphi_3)$*, for the two-dimensional Euler single-objective optimization.*

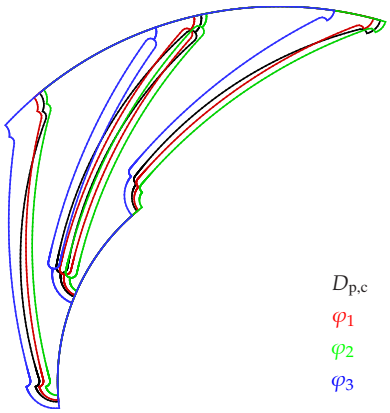

Figure 6.8: *CGeometry comparison between preliminary* $(D_{p,c})$ *and optimized* $(\varphi_1, \varphi_2, \varphi_3)$ *vaned diffusers for the two-dimensional Euler single-objective optimization.*

Table 6.4: *Design variables of the preliminary* $(D_{p,c})$ *and optimized* $(\varphi_1, \varphi_2, \varphi_3)$ *vaned diffusers computed for the two-dimensional Euler single-objective optimization.* RR_3 *and* RR_4 *are the radius ratios at the diffuser vane leading and trailing edges,* α_{3v} *is the vane angle at the leading edge,* VTA *is the vane turning angle, and* Z_D *is the vane number.*

	RR_3	RR_4	$\alpha_{3v}\,[^\circ]$	$VTA\,[^\circ]$	Z_D
$D_{p,c}$	1.100	1.620	72.5	10	13
φ_1	1.083	1.636	75.4	19	13
φ_2	1.053	1.635	75.0	19	13
φ_3	1.141	1.643	74.4	18	13

RR_4 and VTA exhibit a trend to move towards similar values. Thus, the values of RR_3 and α_{3v} seem to be influenced more by the different weights used in the three objective functions, whereas RR_4 and VTA seem to be influenced to a lower extent by the different w_i. Furthermore, in the case of φ_1, the design variables are further from the optima found for φ_2 and φ_3. Particularly, the trend is to allow vanes which are closer to diffuser inlet, in order to maximize the pressure recovery, and more aligned to the flow, in order to minimize the losses. At the trailing edge, on the other hand, the compromise between short or long vanes is found to be satisfactory only after about 40 generation. Generally, it is however difficult to separate the contribution of each design variable to the objective function, since the minimum value of the latter is given by a geometry which is a combination of all the five parameters.

Figure 6.8 shows a graphical comparison between the preliminary $(D_{p,c})$ and opti-

mized (φ_1, φ_2, φ_3) vaned diffusers. The shorter vane in the case of φ_3 and the leading edge closer to the diffuser inlet for φ_2 can be identified. A further comparison between the design variables of the preliminary and optimized geometries is given in Table 6.4. All the solutions have a blade number equal to 13, but differences are seen in the vane angles and radius ratios. Particularly, the closer the vane leading edge to the diffuser inlet is, the higher CP is, while K is reduced by moving the vane further from the inlet. At the oulet, the optimized solutions have a more radial vane and similar vane angles. The same behaviour can be noticed for the radius ratio, such that the position of the vane trailing edge is almost the same in all cases. It also valuable to notice that for φ_1 a solution with 13 vanes has been found, although the clear trend to move to 12 vanes mentioned before. The combination of the design variables, and not each of them separately considered, is therefore of utmost importance for the optimized solution.

Figure 6.9a shows the Mach number contours of the preliminary and optimized vaned diffusers. The latter allow the velocity to decrease more steeply, i.e., closer to the leading edge. In other words, on the suction side the Mach number decreases to about 0.2 in the first half of the vane, for the optimized cases, while the same value is reached further downstream in the preliminary configuration. Close to the diffuser inlet, the highest velocity can be seen for φ_2, for which more importance was given to the pressure recovery, which imposed the vane to be closer to the inlet. On the contrary, the lowest values are obtained for φ_3, which optimized the geometry with a higher weight for K, allowing the vane to be further from the inlet. The wakes at the trailing edges could be caused by a too coarse grid.

The area around the vane leading edge is magnified in Fig. 6.10. A shock normal to the vane pressure side is visible for the preliminary design, for which the highest Mach number reaches about 1.58. The Mach number drops below unity for φ_1 and φ_3, and it is surprising that these two geometries have a similar velocity field on the suction side, despite different weights given to the two objective functions. On the other hand, when CP is given the highest priority (φ_2), the Mach number is still supersonic and around 1.25, due to the proximity of the leading edge to the diffuser inlet.

Figure 6.9b shows the static pressure contours of the preliminary and optimized vaned diffusers. The static pressure has been normalized by the total pressure at CFD domain inlet (p_{02} = 359 kPa). As one would expect based on the previous discussion, the optimized configurations perform better in terms of static pressure rise. Their static pressure fields are similar, but one difference can be highlighted by looking at the values close to the leading edge. There, the highest values are reached for φ_3, because of the longer distance between the diffuser inlet and the vanes. Thus, although overall the best performance in terms of pressure recovery is obtained in the case of φ_2, which was given the highest importance in that respect, locally at the leading edge the geometry generated for φ_3 performs better. Allowing the flow velocity to further decrease from the inlet to the vane leading edge, by placing the latter further downstream, is then beneficial in terms of local behaviour, but the overall performance might require the vane to be closer.

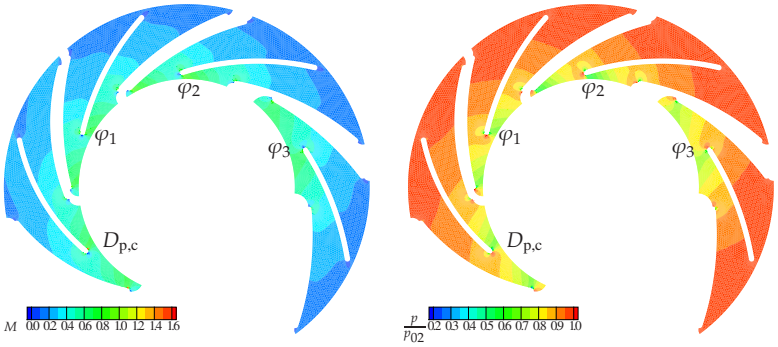

(a) *Mach number.* **(b)** *Static pressure.*

Figure 6.9: *Mach number and static pressure contours of the preliminary* $(D_{p,c})$ *and optimized* $(\varphi_1, \varphi_2, \varphi_3)$ *vaned diffusers for the two-dimensional Euler single-objective optimization. The static pressure has been normalized by the total pressure at the computational domain inlet* $(p_{02} = 359\ kPa)$.

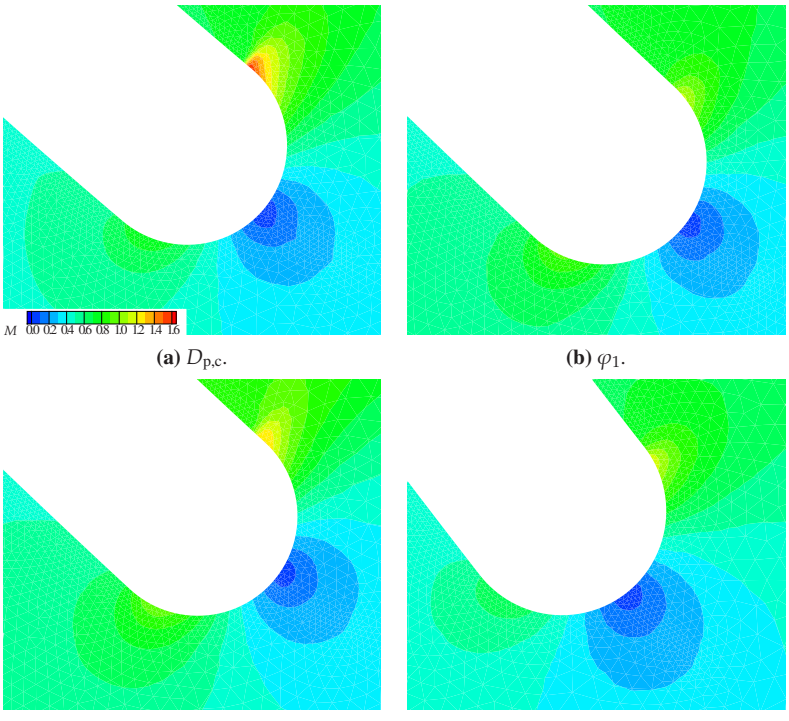

(a) $D_{p,c}$. **(b)** φ_1.

(c) φ_3. **(d)** φ_3.

Figure 6.10: *Mach number contours at the vane leading edge of the preliminary* $(D_{p,c})$ *and optimized* $(\varphi_1, \varphi_2, \varphi_3)$ *vaned diffusers for the two-dimensional Euler single-objective optimization.*

6.7 Three-dimensional RANS multi-objective optimization

The optimization previously performed does not take into account the complexity of the flow field at the diffuser inlet, and the viscous effects. The velocity of the flow leaving the impeller will be higher on the pressure side and on the hub, due to recirculation and separation, therefore the velocity entering the diffuser will vary from that on the suction side to that on the pressure side, and from that at the shroud to that at the hub. Furthermore, at high pressure ratios, the flow will have a high tangential velocity, and will be transonic and turbulent, with the eventual presence of shock waves and boundary layer separation. The flow at the diffuser inlet is thus highly unsteady, viscous, 3D, and non-uniform.

As a consequence, in order to account for those flow phenomena, the second phase of the optimization work has been performed by coupling the GA previously used to a CFD code which is able to solve the 3D RANS equations, over a domain which includes both the impeller and the vaned diffuser.

The performance of the centrifugal compressor having a vaned diffuser has been assessed by evaluating across the whole domain the static pressure recovery and the total pressure losses, which have been quantified through the total-to-static pressure pressure ratio π_{ts} and the total-to-total isentropic efficiency $\eta_{tt,is}$, respectively. The two objective functions have been minimized separately and simultaneously, such that the following constrained multi-objective optimization problem has been solved

$$\text{minimize} \qquad \varphi_1 = 1/\pi_{ts} = \frac{p_{01}}{p_5}, \tag{6.24}$$

$$\varphi_2 = 1 - \eta_{tt,is} = 1 - \frac{\left(\frac{p_{05}}{p_{01}}\right)^{\frac{\gamma-1}{\gamma}} - 1}{\frac{T_{05}}{T_{01}} - 1}, \tag{6.25}$$

$$\text{subject to} \qquad \psi = \frac{\int_{A_{out}} \operatorname{sgn}(\mathbf{v}\cdot\mathbf{n})\,\mathrm{d}A}{A_{out}} \geq 0.95, \tag{6.26}$$

$$\text{where} \qquad \operatorname{sgn}(x) = \begin{cases} 1 & \text{if } x > 0 \\ 0 & \text{if otherwise} \end{cases}, \tag{6.27}$$

and where p_{01} and T_{01} are the total pressure and temperature at the compressor inlet; p_{05}, T_{05}, and p_5 are the total pressure and temperature and the static pressure at the diffuser outlet; $\mathbf{v}$ is the velocity vector; $\mathbf{n}$ is a vector normal to the outlet area A_{out}. The constraint ψ has been introduced in order to minimize the backflow at the diffuser outlet, since flow separation on the vane suction side, and consequent recirculation, are expected for a large number of geometries.

The optimization has been performed at the micro turbine design point, and is driven by a GA which is an implementation of the non-dominated sorting genetic algorithm II developed by Deb *et al.* [57, 58]. A metamodel has been used to assist the GA during the optimization process to reduce the computational costs. In the present work, the optimization

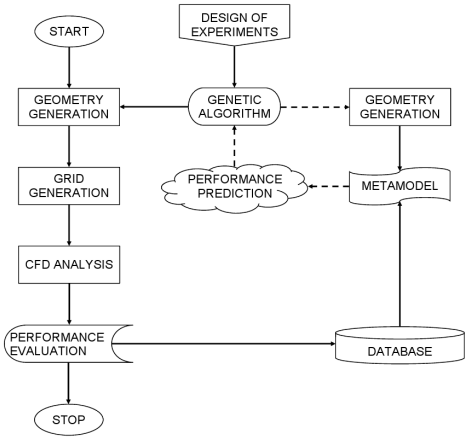

Figure 6.11: *The layout of the optimization procedure based on an off-line metamodel-assisted genetic algorithm.*

is performed by the use of a so-called "off-line trained metamodel" technique [207, 269]. This technique utilizes the metamodel as an evaluation tool during all the evolutionary process. After several generations, the evolution is stopped and the best individual is analyzed by the CFD tool. The difference between the value predicted by the metamodel and that calculated with the CFD code is a direct measure of the metamodel accuracy. Often, at the beginning of the optimization process, that difference is expectedly large. As soon as the new evaluated individual is added to the training database, the metamodel will be more accurate in the region of the design space where the evolutionary algorithm was previously predicting the best individual. This feedback is the most valuable part of the algorithm as it makes the system self-learning.

Figure 6.11 illustrates the layout of the implemented optimization procedure. The main components are the geometry generator, the CFD tool, and the optimization blocks (i.e., the GA, the metamodel, the initial database, and the DOE). In this work, a Kriging metamodel with a quadratic regression function and a Gaussian correlation function has been selected. For each geometry tested during the optimization process, φ_1, φ_2, and ψ have been estimated by a dedicated metamodel.

For every optimization cycle, the metamodel-assisted GA computed the evolution of 48 individuals over 2000 generations. The population size has been chosen as a function of the number of design variables [210, 266]. The probabilities of cross-over and mutation have been specified equal to 0.75 and 0.015, respectively, while elitism has been used. The initial population of the GA has been generated by means of a Latin hypercube sampling strategy [258, 283]. By minimising a potential energy function, this technique is able to spread the generated points as uniformly as possible within the design space, ensuring that all its portions are represented. The number of initial individuals is selected on the basis of the number of design variables of the problem.

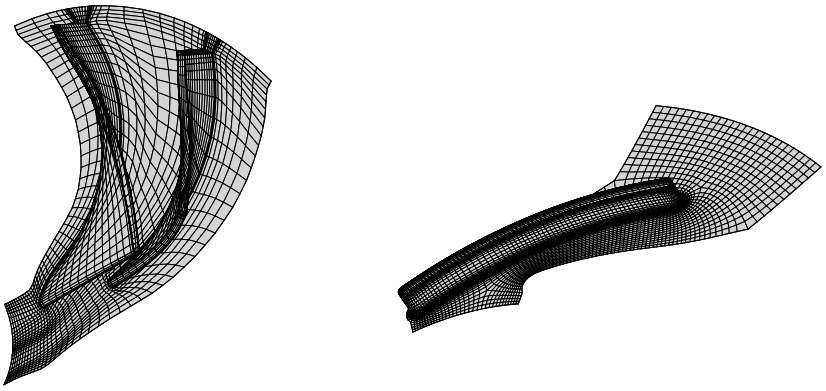

(a) *Impeller hub and blades grids.* **(b)** *Diffuser hub and vane grids.*

Figure 6.12: *The grid of the computational domain for the three-dimensional Reynolds averaged Navier-Stokes multi-objective optimization.*

6.7.1 Computational method

Geometry and grid generation

The 3D impeller geometry has been created with a geometry creation tool specialized for turbomachinery blades [8]. The impeller has been modeled without considering the tip clearance, while a 13.45-mm-long stationary inlet duct has been placed upstream of the impeller, in order to reduce the effect of the inlet boundary condition on the potential field of the blade. At the diffuser outlet, the computational domain has been extended further downstream to ensure that the outlet boundary condition does not affect the flow field around the diffuser vane trailing edge. The volute has not been included in the computational domain.

The structured grids of an impeller passage containing a full and a splitter blade, and of the vaned diffuser containing one vane have been generated with a meshing tool tailored for the CFD analysis of turbomachinery blade rows [10], while the grid of the inlet duct has been generated using a multi-purpose grid generator for unstructured grids [90].

A very coarse grid of about 42,000 elements has been generated for the impeller (Fig. 6.12a), since only the flow properties at the impeller outlet (i.e., the diffuser inlet) were necessary to be known, wherelse there was no interest in a detailed impeller flow field investigation. The cell number has been obtained on the basis of a grid sensitivity analysis performed at the micro turbine design point. Total and static pressures and temperatures, and the absolute velocity have been calculated at the impeller inlet and outlet, and compared for four grid sizes. The latter are the 42,000-element grid utilized in the optimization work, and the three grid sizes (i.e., 284,480, 642,496, and 1,272,192 cells) employed in Chap. 4. At the impeller outlet, the total and static temperatures and the absolute velocity are about 1% lower for the chosen grid size, while the total and static pressures are about

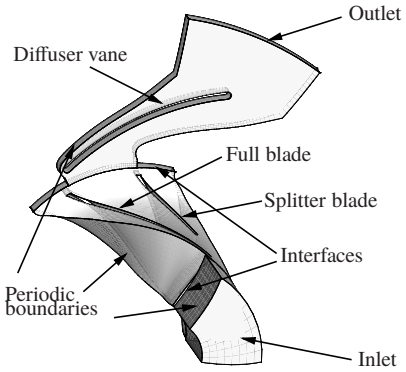

Figure 6.13: *The boundaries of the computational domain for the three-dimensional Reynolds averaged Navier-Stokes multi-objective optimization.*

5% lower. At the impeller inlet, the flow properties obtained with the chosen cell number are on average 0.2% higher than those calculated with the other three grid sizes.

Furthermore, the choice of a coarse impeller grid was also sustained by the work of Tsuei *et al.* [261], who investigated the influence of a large number of computing options by comparing experimental and numerical results for seven turbomachines, including centrifugal compressors. By using two commercial CFD codes, and following a hypothesis formulated by Denton [61], the authors concluded that most of the important effects in a turbomachinery bladed passage may be captured using a coarse grid of only 30,000 nodes, since almost all of their numerical results regarding the efficiency and pressure ratio agreed well with the test data.

On the other hand, no guidelines can be found in the literature about the grid generation for VDs. At the same time, various cell numbers have been used in the works listed in Sec. 6.1. Here, a grid of about 164,000 elements has been created for the VD (Fig. 6.12b), on the basis of a grid sensitivity analysis performed at the micro turbine design point. Total and static pressures and temperatures, absolute velocity, and velocities components, have been calculated at the diffuser inlet and outlet and at the vanes leading and trailing edges, and compared for three grid sizes. The differences between the coarse (~80,000 elements) and the baseline (~164,000 elements) grids are negligible, wherelse they are slightly larger between the baseline and fine (~328,000 elements) grids.

Furthermore, the VD grid has been created through an automatic topology and meshing optimized feature, which enables the creation of high-quality grids with minimal effort. Furthermore, in order to resolve the boundary layer on the diffuser vanes and end-walls, the dimensionless wall distance y^+ of the first grid node off the wall has been set equal to 1.

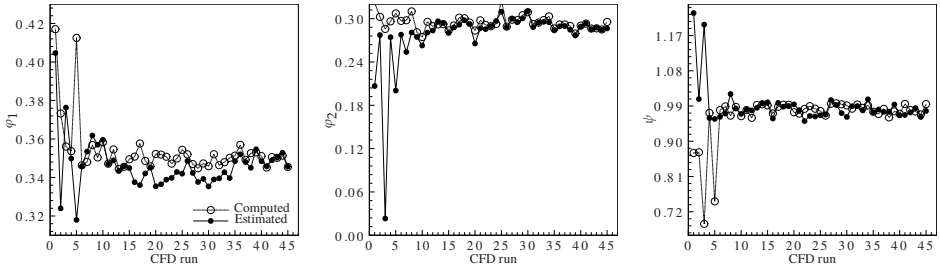

(a) φ_1. **(b)** φ_2. **(c)** ψ.

Figure 6.14: *Comparison between computed and estimated objective functions* (φ_1, φ_2) *and constraint* (ψ) *for one individual of the Pareto front, for the three-dimensional Reynolds averaged Navier-Stokes multi-objective optimization with current impeller.*

Numerical aspects and boundary conditions

The computational analysis has been performed by means of a commercial CFD code which solves the 3D RANS equations using a finite-volume-based method [9]. Details about the numerical schemes and the boundaries conditions (Fig. 6.13) utilized for the CFD simulations can be found in Sec. 4.2.2.

Contrarily to what has been adopted for the numerical aerodynamic analysis described in Chap. 4, in this optimization work for the steady-state simulations a mixing plane approach has been used at the interface between the rotating impeller and the stationary vaned diffuser. This approach performs a circumferential averaging of the fluxes through bands on the interface, and steady-state solutions are then obtained in each reference frame. Stage averaging between blade passages accounts for time average interaction effects, but neglects transient interaction effects, thus the losses which occur as the flow is mixed between the two components are not accounted for.

6.7.2 Results and discussion

In this section, the results of the 3D RANS multi-objective optimization problem are presented for both the current and the larger impellers. The behaviour of the optimization technique is firstly analyzed, then the comparison between the preliminary and optimized vaned diffusers follows.

Current impeller

The metamodel-assisted GA creates a Pareto front based on the values predicted by the metamodels. This front is made of several optimal individuals, among which five geometries, equally spaced along the Pareto front, are extracted, analyzed by means of the CFD tool, and added to the DOE for the successive cycles. The optimization process has been stopped after 45 optimization cycles, when the differences between the computed and the estimated values became negligible.

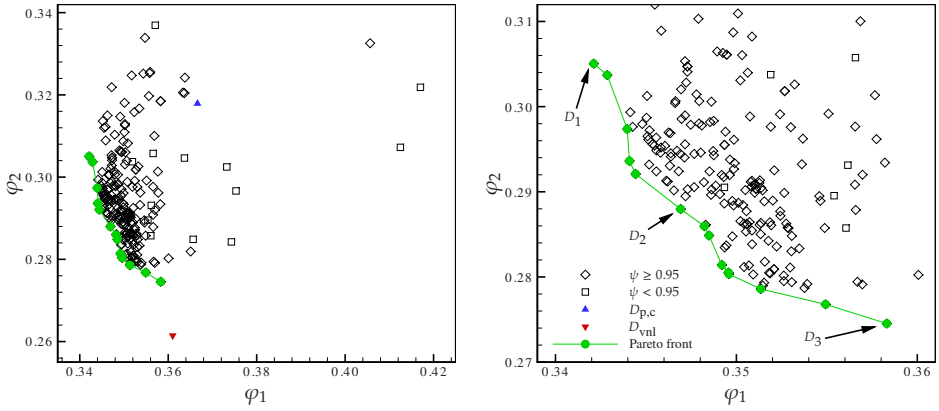

(a) *A global view.* **(b)** *A close-up view around the Pareto front.*

Figure 6.15: *The objective functions* (φ_1, φ_2) *of all the individuals, the Pareto front, the preliminary vaned diffuser* $(D_{p,c})$*, and the vaneless diffuser* (D_{vnl})*, for the three-dimensional Reynolds averaged Navier-Stokes multi-objective optimization with current impeller. The individuals showing the best static pressure recovery* (D_1)*, best efficiency* (D_3)*, and intermediate performance* (D_2) *are also illustrated. The indivuals fulfilling the constraint* $(\psi \geq 0.95)$ *and those which do not* $(\psi < 0.95)$ *are shown with two different symbols.*

Figure 6.14 shows the deviations between the computed and estimated values for φ_1, φ_2, and ψ, for one individual among the five extrapolated from the Pareto front. During the first iterations of the optimization process, the deviations between the predicted and the CFD-based values are large, but they significantly decrease with increasing number of CFD runs. This is the consequence of the increasing number of samples present in the DOE, resulting in more accurate predictions of the metamodels. Only about 10 cycles for φ_2 and ψ were necessary to obtain a good agreement between the metamodels and the CFD values, wherelse more CFD runs were required for φ_1.

Figure 6.15a shows the objective functions of all the geometries evaluated with the CFD tool. Two different symbols have been given to the individuals which satisfy the constraint $(\psi \geq 0.95)$, and to those which do not $(\psi < 0.95)$. The latter represent only 6% of all the individuals. The preliminary and vaneless configurations have been included in the figure as well. The trade-off between the static pressure recovery and total pressure losses is visible, as the majority of the individuals are clustered at low values of φ_1 and φ_2. However, most of them are distributed within a small range for φ_1 $(0.34 \leq \varphi_1 \leq 0.36)$, while the range for φ_2 is larger $(0.28 \leq \varphi_1 \leq 0.32)$. Furthermore, it can be noticed that the preliminary diffuser exhibited very low static pressure recovery and efficiency, such that most of the geometries have better performance than those of the preliminary design. On the other hand, the comparison with the vaneless diffuser leads to different conclusions. Apart from thirteen individuals (including the preliminary), all the geometries have lower values of φ_1, resulting thus in a better static pressure recovery. However, all the vaned diffusers show worse efficiencies than that of the vaneless configuration. Therefore, these

Table 6.5: *The objective functions (φ_1, φ_2) and constraint (ψ) of the preliminary ($D_{p,c}$), vaneless (D_{vnl}), and optimized (D_1, D_2, D_3) vaned diffusers for the three-dimensional Reynolds averaged Navier-Stokes multi-objective optimization with current impeller.*

	φ_1	φ_2	ψ
$D_{p,c}$	0.367	0.318	0.947
D_{vnl}	0.361	0.261	1.000
D_1	0.342	0.305	0.972
$\Delta_{p,c}$ [%]	−6.7	−4.0	+2.6
Δ_{vnl} [%]	−5.2	+16.7	−2.8
D_2	0.347	0.288	0.991
$\Delta_{p,c}$ [%]	−5.4	−9.4	+4.6
Δ_{vnl} [%]	−3.9	+10.1	−0.9
D_3	0.358	0.275	0.964
$\Delta_{p,c}$ [%]	−2.3	−13.6	+1.8
Δ_{vnl} [%]	−0.7	+5.0	−3.6

conclusions hold as well for the fourteen geometries of the Pareto front, which is magnified in Fig. 6.15b. Among the optimal solutions, three interesting configurations can be identified, namely the individual with the best static pressure recovery (D_1), that having the best efficiency (D_3), and one showing intermediate performance (D_2).

The comparison between the two objective functions and the constraint for the preliminary ($D_{p,c}$), vaneless (D_{vnl}), and optimized (D_1, D_2, D_3) geometries is shown in Table 6.5. As noticed in Fig. 6.15a, the three optimized configurations perform better than the preliminary design in terms of both φ_1 and φ_2. The highest deviations are calculated between D_1 and $D_{p,c}$ for φ_1 (−6.7%), and between D_3 and $D_{p,c}$ for φ_2 (−13.6%). D_1, D_2, and D_3 exhibit as well as better fulfillment of the constraint, as they have higher values of ψ. On the contrary, although they all have better static pressure recovery than the vaneless configuration (with decreasing performance in that respect from D_1 to D_3), they perform worse in terms of total pressure losses when compared to D_{vnl} (with decreasing performance in that respect from D_3 to D_1). As a consequence, for such low-pressure ratio impeller the addition of diffuser vanes in the vaneless space does not lead to an improved compressor efficiency, although the static pressure recovery is higher.

Larger impeller

An alternative strategy is thus proposed by considering that in the automotive field it is common practice [16, 109, 272] to manufacture different centrifugal impellers by trimming down the blades trailing edge radius (r_{TE}) from the largest geometry. As a consequence, several impellers are considered to belong to same family, since they differ only by r_{TE},

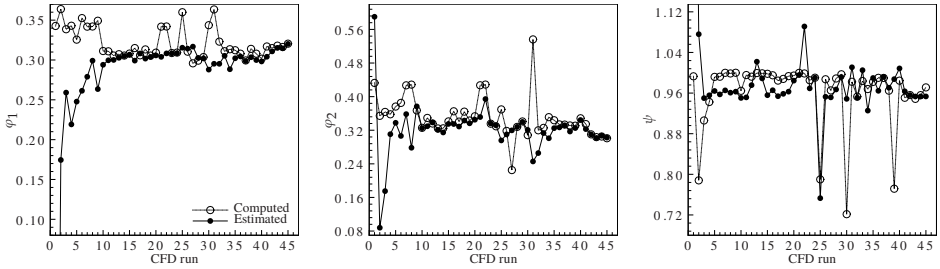

(a) φ_1. **(b)** φ_2. **(c)** ψ.

Figure 6.16: *Comparison between computed and estimated objective functions* (φ_1, φ_2) *and constraint* (ψ) *for one individual of the Pareto front, for the three-dimensional Reynolds averaged Navier-Stokes multi-objective optimization with larger impeller.*

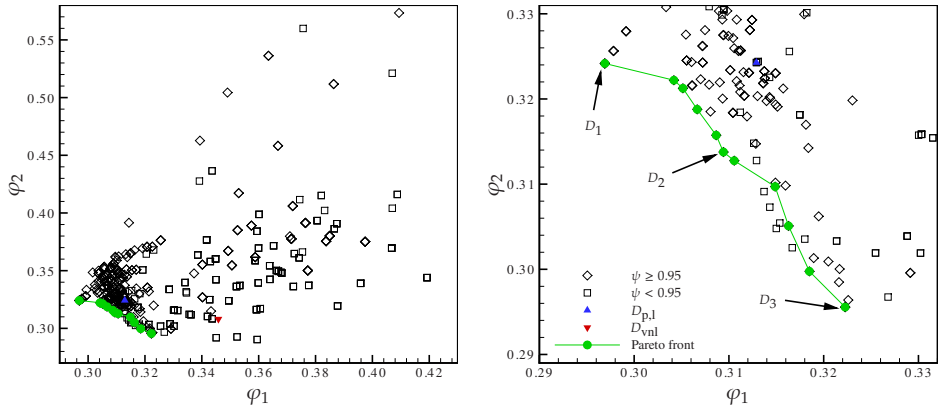

(a) *A global view.* **(b)** *A close-up view around the Pareto front.*

Figure 6.17: *The objective functions* (φ_1, φ_2) *of all the individuals, the Pareto front, the preliminary vaned diffuser* $(D_{p,c})$*, and the vaneless diffuser* (D_{vnl})*, for the three-dimensional Reynolds averaged Navier-Stokes multi-objective optimization with larger impeller. The individuals showing the best static pressure recovery* (D_1)*, best efficiency* (D_3)*, and intermediate performance* (D_2) *are also illustrated. The indivuals fulfilling the constraint* $(\psi \geq 0.95)$ *and those which do not* $(\psi < 0.95)$ *are shown with two different symbols.*

which leads to different flow capacities and pressure ratios, wherelse the other geometric details are intact.

By looking at Figs. 3.1c and 3.1d, it can be seen that a 1-mm margin is still available between the impeller blades trailing edge and the impeller outlet. Therefore, an impeller having an r_{TE}-value equal to 19.5 mm would still fit within the same impeller outlet radius, could be easily mounted on the same turbocharger as the current one, and could be manufactured with very low costs.

Furthermore, a larger r_{TE} implies a higher pressure ratio, at constant rotational speed,

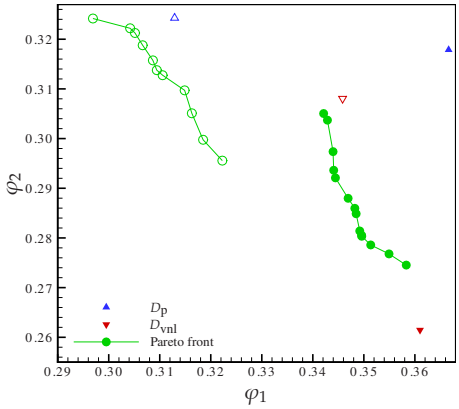

Figure 6.18: *The objective functions* (φ_1, φ_2) *of the Pareto front, the preliminary vaned diffuser* (D_p)*, and the vaneless diffuser* (D_{vnl}) *computed with the current (closed symbols) and larger (hollow symbols) impellers for the three-dimensional Reynolds averaged Navier-Stokes multi-objective optimization.*

as a consequence of a higher tangential velocity at the impeller outlet. However, this leads to a longer flow path in the vaneless diffuser, and in turn to higher friction losses. Consequently, at a larger impeller outlet the effect of the guided diffusion process might be beneficial because the dynamic head to recover is higher, due to a higher impeller outlet tangential velocity.

Therefore, in order to assess whether this solution is feasible, a second 3D RANS multi-objective optimization process has been carried out with a larger impeller (i.e., r_{TE} = 19.5 mm). All the components of the optimization strategy are however the same as those previously described throughout Sec. 6.7.

Figure 6.16 shows the deviations between the computed and estimated values for φ_1, φ_2, and ψ, for one individual among the five extrapolated from the Pareto front. The deviation is high in the early stages of the optimization process, as the predicted values understimate the calculated ones, then it significantly decreases after about 10 cycles for φ_1 and about 20 cycles for φ_2 and ψ.

Figure 6.17a shows all the individuals evaluated with the CFD tool, and the Pareto front which has been created at the end of the optimization process. Two different symbols have been given to the individuals which satisfied the constraint $(\psi \geq 0.95)$, and to those which did not $(\psi < 0.95)$. The latter represent about 40% of all the computed individuals. The preliminary and vaneless configurations have been included in the figure as well. All the individuals are distributed within wide ranges for both objective functions, such that the conflict between φ_1 and φ_2 cannot be underestimated. However, the trend towards the minimization of both objective functions is visible, as the majority of the individuals are clustered at low values of φ_1 and φ_2. This spread might also be the consequence of the broad ranges assigned to the design variables. The preliminary diffuser exhibited a good behaviour with respect to the pressure recovery, but had a very low efficiency. Further-

more, most of the individuals performed better than the vaneless configuration in terms of pressure recovery, while only a few had better efficiency. Figure 6.17b illustrates a closer view around the Pareto front. The front is made of eleven individuals, among which three critical configurations can be identified. D_1 is the individual with the lowest φ_1, D_3 is the one with the best efficiency, and D_2 exhibits intermediate performance. In Fig. 6.17b five individuals located on the left-hand side of the Pareto front are noticeble. They have been disregarded because did not fulfill the constraint.

Figure 6.18 shows the comparison of the Pareto front and the preliminary (D_{p}) and vaneless (D_{vnl}) configurations for the 3D RANS multi-objective optimization with the current and larger impellers. The value of φ_1 for the larger impeller and vaneless diffuser is 4.2% lower than that of the current impeller and vaneless diffuser, but the φ_2-value increases by 17.8%. The same vaneless diffuser allows then for a slightly better static pressure recovery in the case of higher tangential velocities at the impeller outlet, at the expense of a dramatic reduction of the total-to-total isentropic efficiency. Subsequently, in the case of the larger impeller, the substitution of the vaneless diffuser with a vaned one further improves the static pressure recovery, but leads to additional friction losses which decrease φ_2. On the contrary, if the current impeller is employed, the preliminary vaned diffuser performs worse than the vaneless configuration in terms of both φ_1 and φ_2. Furthermore, the Pareto front computed with the larger impeller is located at the left, top corner of the figure, exhibiting thus lower values of φ_1 (i.e., better static pressure recovery) and higher values of φ_2 (i.e., worse efficiency), when compared to the Pareto front computed with the current impeller. However, three individuals of the front show better efficiency than the vaneless diffuser, but in the case of the current impeller the Pareto front is above the vaneless configuration, at its left. As a consequence, the use of vaned diffusers with a low-pressure pressure ratio compressor is beneficial only in terms of static pressure recovery, while a reduction of the friction losses, leading to increased efficiencies, can be achieved only in the case of high dinamic heads available at the diffuser inlet, due to larger impellers.

Table 6.6 shows the comparison between the two objective functions (φ_1 and φ_2) and constraint (ψ) calculated for the preliminary ($D_{\mathrm{p,l}}$), vaneless (D_{vnl}), and optimized (D_1, D_2, D_3) geometries. Both D_1 and D_2 have better pressure recovery than the preliminary configuration (φ_1 is 5.1% and 1.1% lower, respectively), while the value of φ_1 for D_3 is 3.0% higher. Furthermore, the three optimized geometries exhibit higher values of the constraint function with respect to the preliminary configuration. The optimized designs show also higher static pressure recovery than the vaneless diffuser, as confirmed by the values of φ_1. Conversely, the use of a vaned diffuser has a drawback in terms of stage efficiency. D_3 is the only configuration that performs better than the vaneless diffuser (4.1%-decrease for φ_2), but D_1 and D_2 have worse performance. Consequently, the efficiency of this centrifugal compressor featuring a larger impeller and a vaneless diffuser can be indeed increased by using a vaned diffuser.

Table 6.7 shows the values of the total-to-static pressure ratio (π_{ts}), total-to-total isentropic effiency ($\eta_{\mathrm{tt,is}}$), static pressure recovery coefficient (CP), and total pressure loss coefficient (K) for the preliminary ($D_{\mathrm{p,l}}$), vaneless (D_{vnl}), and optimized (D_1, D_2, D_3) geometries. This comparison allows for a distinction upon the diffuser and compressor

Table 6.6: *The objective functions* (φ_1, φ_2) *and constraint* (ψ) *of the preliminary* ($D_{\mathrm{p,c}}$), *vaneless* (D_{vnl}), *and optimized* (D_1, D_2, D_3) *vaned diffusers for the three-dimensional Reynolds averaged Navier-Stokes multi-objective optimization with larger impeller.*

	φ_1	φ_2	ψ
$D_{\mathrm{p,l}}$	0.313	0.324	0.923
D_{vnl}	0.346	0.308	1.000
D_1	0.297	0.324	0.972
$\Delta_{\mathrm{p,l}}$ [%]	−5.1	0.0	+5.3
Δ_{vnl} [%]	−14.2	+5.2	−2.8
D_2	0.309	0.314	0.992
$\Delta_{\mathrm{p,l}}$ [%]	−1.1	−3.2	+7.4
Δ_{vnl} [%]	−10.5	+1.9	−0.8
D_3	0.322	0.296	0.975
$\Delta_{\mathrm{p,l}}$ [%]	+3.0	−8.6	+5.6
Δ_{vnl} [%]	−6.8	−4.1	−2.5

Table 6.7: *Compressor* (π_{ts}, $\eta_{\mathrm{tt,is}}$) *and diffuser* (CP, K) *performance parameters for the preliminary vaned diffuser* ($D_{\mathrm{p,l}}$), *vaneless diffuser*(D_{vnl}), *and optimized vaned diffusers* (D_1, D_2, D_3), *computed for the three-dimensional Reynolds averaged Navier-Stokes multi-objective optimization with larger impeller.*

	π_{ts}	$\eta_{\mathrm{tt,is}}$	CP	K
$D_{\mathrm{p,l}}$	3.196	0.676	0.554	0.327
D_{vnl}	2.892	0.692	0.482	0.216
D_1	3.368	0.676	0.612	0.319
$\Delta_{\mathrm{p,l}}$ [%]	+5.4	0.0	+10.5	−2.4
Δ_{vnl} [%]	+16.5	−2.3	+27.0	+47.7
D_2	3.232	0.686	0.596	0.278
$\Delta_{\mathrm{p,l}}$ [%]	+1.1	+1.6	+7.6	−15.0
Δ_{vnl} [%]	+11.8	−0.8	+23.7	+28.7
D_3	3.103	0.704	0.549	0.235
$\Delta_{\mathrm{p,l}}$ [%]	−2.9	+4.5	−0.9	−28.1
Δ_{vnl} [%]	+7.3	+1.8	+13.9	+8.8

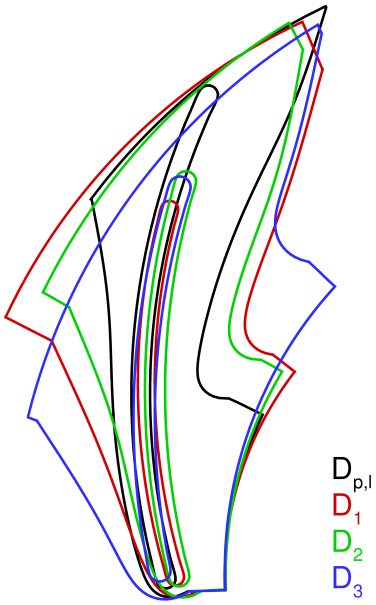

Figure 6.19: *Geometry comparison between preliminary* ($D_{\mathrm{p,l}}$) *and optimized* (D_1, D_2, D_3) *vaned diffusers for the three-dimensional Reynolds averaged Navier-Stokes multi-objective optimization with larger impeller.*

performance. In accordance with the previous results, D_1 and D_2 have higher values of π_{ts} than $D_{\mathrm{p,l}}$, while the value obtained with D_3 is lower. This is reflected as well by the comparison between the *CP*-values. On the contrary, some differences can be noticed about the relationship between the total pressure loss coefficient and the efficiency. The three optimized configurations exhibit lower *K*-values than the preliminary diffuser, with the highest difference calculated for D_3 (-28.1%), but the deviations in terms of efficiency values are one order of magnitude lower. In general, a lower total pressure loss coefficient leads to a higher efficiency, although this is not true for D_1. Furthermore, when comparing the vaneless diffuser with the optimized vaned geometries, it can be noticed that the latter have higher π_{ts} than the former, with decreasing deviations from D_1 ($+16.5\%$) to D_3 ($+7.3\%$), as a consequence of a better static pressure recovery within the diffuser. However, another conclusion can be drawn when comparing K and $\eta_{\mathrm{tt,is}}$. The optimized geometries show very high values of the total pressure loss coefficient in comparison to the value of D_{vnl} ($+47.7\%$, $+28.7\%$, and $+8.8\%$ for D_1, D_2, and D_3, respectively), but this does not yield to a worse efficiency in the case of D_3. This optimized configuration has an efficiency which is 1.8% higher than that of the vaneless design, although it has a 8.8% higher total pressure loss coefficient.

Figure 6.19 shows a graphical comparison between the preliminary design and the three optimized configurations, while the corresponding design variables are summarized

Table 6.8: *Design variables of the preliminary ($D_{p,l}$) and optimized (φ_1, φ_2, φ_3) vaned diffusers computed for vaned diffusers for the three-dimensional Reynolds averaged Navier-Stokes multi-objective optimization with larger impeller. RR_3 and RR_4 are the radius ratios at the diffuser vane leading and trailing edges, RR_5 is the radius ratio at the diffuser outlet, α_{3v} is the vane angle at the leading edge, VTA is the vane turning angle, and Z_D is the vane number.*

	RR_3	RR_4	RR_5	$\alpha_{3v}\,[^\circ]$	$VTA\,[^\circ]$	Z_D
$D_{p,l}$	1.150	1.670	1.692	74.5	10.0	13
D_1	1.139	1.611	1.825	72.9	10.9	9
D_2	1.110	1.489	1.621	75.2	10.4	11
D_3	1.149	1.441	1.511	78.4	10.2	8

in Table 6.8. The optimized designs have less vanes than the preliminary, but while D_3 has eight vanes according to the minimization of total pressure losses, D_2 has eleven vanes, in contrast to the nine vanes of D_1. Increasing the vane number is therefore not a guarantee of a higher pressure recovery. The latter is however achieved with longer haves, as in the case of D_1. This configuration exhibits as well the largest space downstream of the vanes trailing edge, such that the highest pressure recovery is a combination of the velocity decrease both in the vaned passages and in the second vaneless space. On the contrary, the efficiency is maximized with a large first vaneless space, short vanes, and a small second vaneless space. Further on, the optimized designs exhibit different vane angles at the leading edge, wherelse the values of VTA are very similar. D_2 show more radial vanes, while the vanes of D_3 are more tangential at the trailing edge.

In the following, the flow field of the preliminary and optimized geometries will be analyzed by means of the Mach number, static pressure, and total pressure contours on a section located at the diffuser mid-span.

Figure 6.20 shows the Mach number contours. A supersonic Mach number of about 1.27 is visible for D_1, which exhibits a shock on the vane pressure side, very close to the leading edge. This leads to a velocity decrease on the vane suction side, where D_1 has the lowest average velocities in comparison to the other geometries. However, the lowest peak Mach numbers have been found in the preliminary diffuser and in D_3, whose vanes are located the furthest from the diffuser inlet. Furthermore, D_1 does not exhibit the low-velocity region which is visible in the preliminary configuration on the vane suction side. This area can still be noticed for D_2 at about mid-chord, and for D_3 to a very small extent. However, in the two optimized geometries flow separation and recirculation on the vanes suction side does not occur.

Figure 6.21 shows the contours of static pressure, normalized by the total pressure at the CFD domain inlet (p_{01} = 101,325 Pa). Compared to the preliminary design, D_1 has the highest pressure rise in the vaned passage. On the vane pressure side, the isobars are very close to each others, and rapidly increase in magnitude from the leading to the trailing

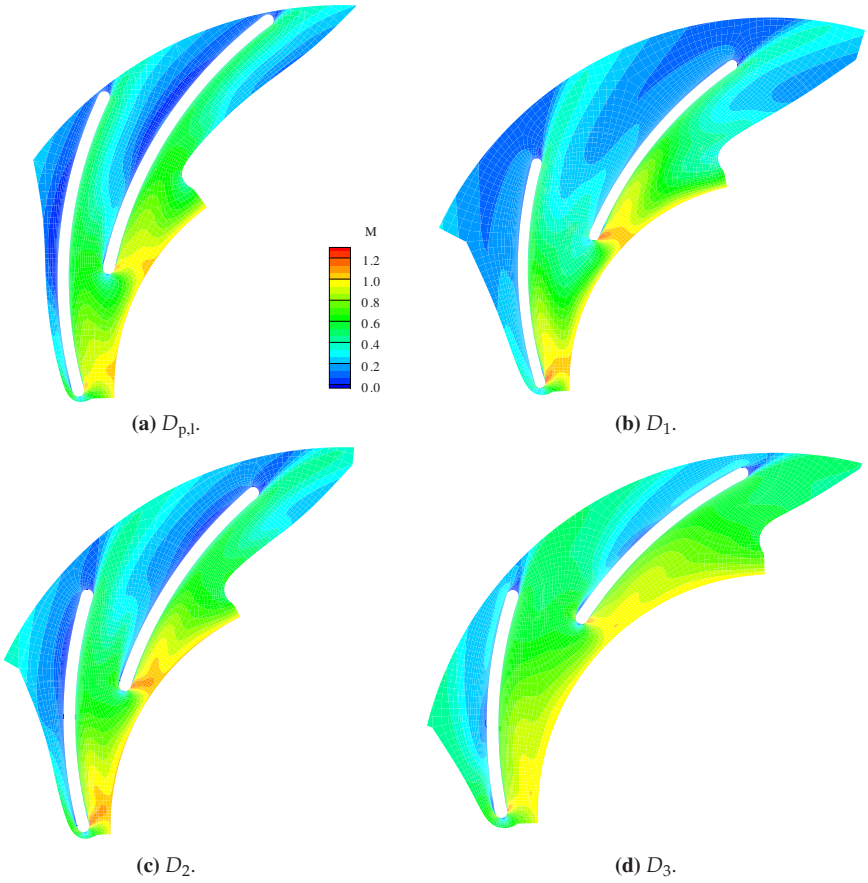

(a) $D_{\mathrm{p,l}}$. **(b)** D_1.

(c) D_2. **(d)** D_3.

Figure 6.20: *Mach number contours of the preliminary* $(D_{\mathrm{p,l}})$ *and optimized* (D_1, D_2, D_3) *vaned diffusers for the three-dimensional Reynolds averaged Navier-Stokes multi-objective optimization with larger impeller. The contours are shown on a section located at 50% of the diffuser spanwise direction.*

edges. On the other hand, the worst static pressure recovery has been obtained with D_3, because of very short vanes. D_2 is better than D_3 in terms of static pressure recovery, but worse than D_1.

Figure 6.22 shows the contours of the total pressure, normalized by the total pressure at CFD domain inlet (p_{01} = 101,325 Pa). For all the four vaned diffusers, the total pressure is minimum approximately in correspondance of the low-velocity pools seen in Fig. 6.20. As a consequence, the wakes which are visible on the vanes suction side are the source of the losses within the diffuser. The optimized design D_3 has the highest total pressure in the proximity of the vanes leading edge, which in turn gives the lowest losses in the downsteam vaned passages, maximizing thus φ_2. The highest total pressure losses in the vaned

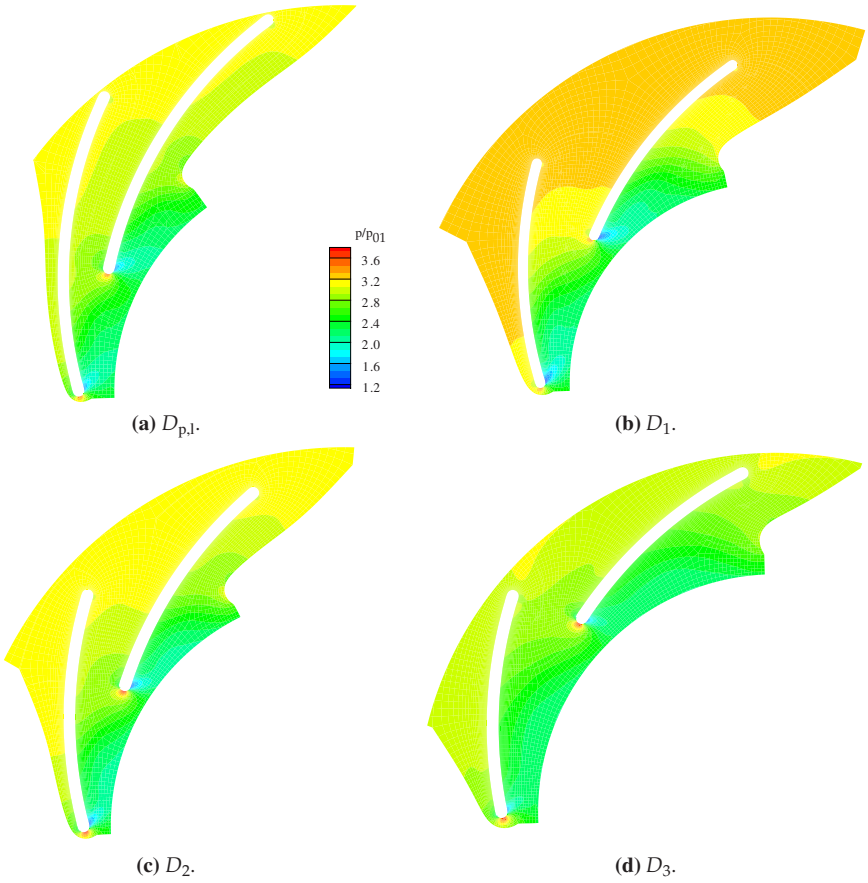

(a) $D_{p,1}$. **(b)** D_1.

(c) D_2. **(d)** D_3.

Figure 6.21: *Static pressure contours of the preliminary* ($D_{p,1}$) *and optimized* (D_1, D_2, D_3) *vaned diffusers for the three-dimensional Reynolds averaged Navier-Stokes multi-objective optimization with larger impeller. The contours are shown on a section located at 50% of the diffuser spanwise direction. The static pressure has been normalized by the total pressure specified at the computational domain inlet* (p_{01} = *101,325 Pa*).

passage are visible in D_1, whose efficiency is equal to that of the preliminary diffuser.

6.8 Conclusions

This chapter describes the optimization of vaned diffusers, which has been firstly performed by coupling a GA to a in-house 2D Euler CFD code, in order to test the developed optimization strategy through a fast solution of the optimization problem. The optimization has been carried out at the micro turbine design point (i.e., $\dot{m}$ = 50 g/s and N = 240

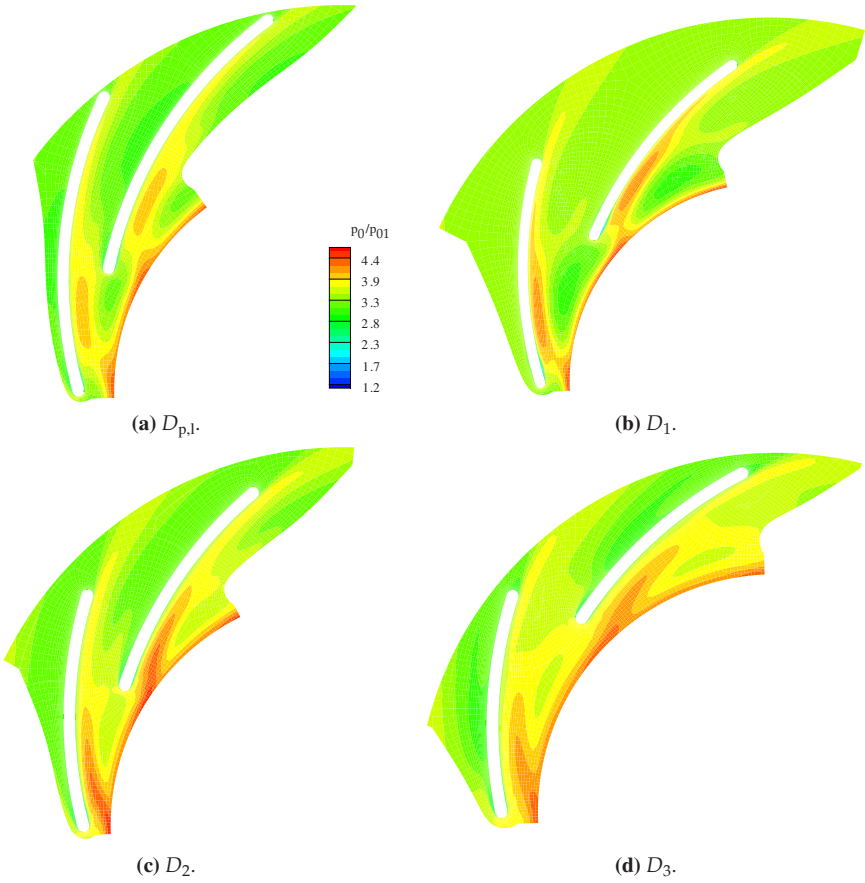

(a) $D_{p,l}$. **(b)** D_1.

(c) D_2. **(d)** D_3.

Figure 6.22: *Total pressure contours of the preliminary* $(D_{p,l})$ *and optimized* (D_1, D_2, D_3) *vaned diffusers for the three-dimensional Reynolds averaged Navier-Stokes multi-objective optimization with larger impeller. The contours are shown on a section located at 50% of the diffuser spanwise direction. The total pressure has been normalized by the total pressure specified at the computational domain inlet* $(p_{01} = 101{,}325\ Pa)$.

krpm).

The static pressure recovery and the total pressure losses have been chosen as objective functions. The multi-objective problem has been reduced to a single-objective one by minimizing an equation which is the weighted sum of the two objective functions $1 - CP$ and K. Therefore, three objective functions, having different weights given to the two objectives, have been optimized.

The relative position of the vanes between the diffuser inlet and outlet, their inclination with respect to the radial direction at the leading and trailing edges, and the vane number have been selected as design variables.

The following can be concluded regarding the 2D Euler single-objective optimization problem:

- The values of the three objective functions are lower than the corresponding values calculated for the preliminary design. They all have higher static pressure recovery coefficient, but higher total pressure loss coefficient as well. The increase in the pressure recovery is mainly due to the reduction below unity of the Mach number.

- The choice of the weights given to each objective function influences the optimized solution. Thus, a vane closer to the diffuser inlet has been designed if the pressure recovery is given a higher priority, while the vane is located further downstream when the static pressure recovery coefficient is considered less important.

- The preliminary and the three optimized geometries have the same vane number, while it has been found out that the vane leading edge position and inclination are more important than those at the trailing edge. As a consequence, at the trailing edge the radius ratios and vane angles of the optimized geometries are very similar to each other, while at the leading edge the radius ratio shows a wider variety. Its pattern is to be smaller for increasing the pressure recovery and higher for achieving lower total pressure losses.

The simulations performed in the first phase of the optimization do not take into account neither the complexity of the flow field at the diffuser inlet, nor the effects of the flow conditions on the diffuser losses. The velocity of the flow leaving the impeller will be higher on the pressure side and on the hub, due to recirculation and separation. As the impeller rotates, the velocity entering the diffuser will then be varying from that on the suction side to that on the pressure surface, as well as from that at the shroud to that at the hub. Furthermore, at high pressure ratios, the flow will have a high tangential component of velocity and will be transonic and turbulent, with the eventual presence of shock waves and boundary layer separation. Therefore, the flow at the diffuser inlet is highly unsteady, viscous, 3D, and non-uniform. phenomena.

As a consequence, in the second step of the optimization the GA has been coupled to a commercial 3D RANS CFD code, in order to account for the viscous effects and the impeller-diffuser interaction. The GA has been assisted by a Kriging metamodel, to reduce the computational costs. The performance of the centrifugal compressor having a vaned diffuser has been assessed by evaluating across the compressor stage the static pressure recovery and the total pressure losses. The former has been quantified through the total-to-static pressure pressure ratio, while the latter have been quantified through the total-to-total isentropic efficiency. The two objective functions have been minimized separately and simultaneously, such that a constrained multi-objective optimization problem has been solved. Furthermore, the diffuser outlet radius has been used as a sixth design variable, in order to minimize the friction losses between the vanes trailing edge and the diffuser outlet. Also in this case the optimization has been carried out at the micro turbine design point.

The 3D RANS multi-objective optimization has been performed with two different

centrifugal impellers (i.e., the current impeller and a larger one). A larger impeller outlet diameter implies a higher pressure ratio, at constant rotational speed, as a consequence of a higher tangential velocity at the impeller outlet. However, this leads to a longer flow path in the vaneless diffuser, and in turn to higher friction losses. Consequently, at a larger impeller outlet the effect of the guided diffusion process might be beneficial because the dynamic head to recover is higher, due to a higher impeller outlet tangential velocity.

The solution of the 3D RANS multi-objective optimization problem with the current impeller led to a Pareto front made of fourteen individuals, among which one that maximizes the static pressure recovery (D_1), one that maximizes the efficiency (D_3), and one showing intermediate performance (D_2) have been identified. By comparing them to the preliminary and vaneless configurations, it can be concluded that the efficiency of the latter cannot be improved through a vaned diffuser, although the optimized geometries perform better than the preliminary design. The presence of the diffuser vanes is indeed beneficial in terms of static pressure recovery, but the high total pressure losses overcome the increase in static pressure, leading to lower efficiencies.

The solution of the 3D RANS multi-objective optimization problem with the larger impeller led to a Pareto front made of eleven individuals, among which D_1, D_2, and D_3 have been extrapolated as before. The following can be concluded regarding this optimization:

- D_1 and D_2 perform better than the preliminary design in terms of static pressure recovery, while D_3 does not. The three optimized geometry exhibit the same efficiency, or better, compared to the preliminary geometry. The ideal best vaned diffuser would couple the static pressure recovery level of D_1 (-5.1% for φ_1), with the total pressure losses level of D_3 (-8.6% for φ_2).

- The three optimized geometry show better pressure recovery than the vaneless configuration as well, but differences are noticed in terms of total pressure losses, since they all feature higher total pressure loss coefficients. However, D_3 exhibits a better efficiency ($+1.8\%$) than the vaneless diffuser. The performance of this high-pressure ratio centrifugal compressor featuring a vaneless diffuser can thus be improved by the addition of diffuser vanes. Furthermore, in this case the diffuser outlet radius is 12% shorter than that of the vaneless configuration.

- Long diffuser vanes increase the static pressure recovery, while shorter ones, coupled with small a vaneless space at the diffuser outlet, has a positive effect on the efficiency. The influence of the diffuser vane number on the pressure recovery and efficiency could not be properly assessed.

- The optimized geometries cause less backflow than the preliminary configuration, as a consequence of higher average Mach numbers, and due to the absence of flow recirculation on the vanes suction side. In all cases, the loss production occurs in correspondance of the low-velocity regions present in the flow field.

“Enough research will tend to support your conclusions.”

Arthur Bloch.

7

Conclusions and perspectives

This chapter draws the conclusions regarding the work presented in this dissertation, while recommendations are suggested for future research activities.

7.1 Conclusions

Distributed generation (DG) is one of the options for a more efficient and sustainable use of fossil fuels as energy sources. Among the various technologies which are currently proposed for DG, micro combined heat and power (μCHP) could play a very relevant role, because it positively integrates technological as well as cultural and institutional components, related to the potential for reducing the ecological impact of electricity conversion.

Micro gas turbines offer many potential advantages in comparison to other conversion technologies suitable for μCHP applications, and usually adopt radial-flow components for the turbomachinery, since they offer minimum surface and end-wall losses, and provide the highest efficiency. Centrifugal compressors also provide very high pressure ratio per stage, are less expensive to manufacture, and are similar in terms of design and volume flow rate to those adopted for automotive turbochargers.

Thanks to the evolution experienced by automotive turbochargers in the past seventy years, the use of single-shaft radial turbomachinery for micro turbines allows thus for simple designs, satisfiying aerothermodynamic constraints, and relatively low production costs. Nevertheless, micro turbines performance can be improved through suitable modifications of turbocharger technology, especially considering that turbochargers usually employ centrifugal compressors with vaneless diffusers in order to maximize the flow range and minimize production costs, wherelse gas turbines require higher efficiency and pressure ratio for a much narrower operating range.

In this study, the recuperated micro gas turbine developed by the Dutch company Micro Turbine Technology B.V. (MTT) has been utilized as an illustrative example. The MTT micro turbine delivers electrical and thermal power output up to 3 and 14 kW, respectively, and will be primarily applied in μCHP units for domestic dwellings. The turbomachinery consists of a commercial off-the-shelf automotive turbocharger, made of a centrifugal compressor, a radial turbine, and oil-lubricated bearings. A cycle study of the MTT recuperated micro gas turbine has been carried out in order to assess the impact of the centrifugal compressor performance on the system performance. The analysis proved that the system net electrical conversion efficiency can increase by about 2% for every 1%-increase in the compressor isentropic efficiency.

In line with the objectives of this research as stated in Chap. 1, the main conclusions of the work presented in this dissertation are summarized as follows:

- A fully automated optimization methodology has been developed by integrating an optimization algorithm, a geometry generator, a grid generator, a computational fluid dynamics (CFD) solver, and a post processor. This methodology can be used for the optimization of turbomachinery components, but has been applied here to the design and optimization of vaned diffusers for the exemplary micro compressor. The optimized vaned diffusers led to increased static pressure recovery, but the compressor efficiency was lower than that of the vaneless configuration, because of larger total pressure losses.

- The test-rig, which has been designed and built for the automatic acquisition of the performance maps of very small centrifugal compressors, proved to be robust,

reliable, and versatile. An experimental campaign has been carried out in order to quantify the aerodynamic performance of the MTT compressor, and the test data have been used to validate the results of numerical analyses. The test-rig will also be a useful tool in the development of future, new designs which aim at improving the micro turbine compressor performance, and will be utilized to test other micro centrifugal compressors for a variety of different applications.

- A new one-dimensional (1D) method for the assessment of the performance (i.e., stage total-to-total pressure ratio and isentropic efficiency; impeller inlet and outlet velocity triangles; impeller internal, external, and mixing losses; vaneless diffuser losses; volute losses) of very small centrifugal compressors has been developed on the basis of two very well-known design methodologies, namely the single- and two-zone model. This novel tool combines the advantages of the two, since it distinguishes between high- and low-momentum flows within the impeller bladed passages as possible with the two-zone model, and allows evaluating the impeller loss mechanisms, as possible with the single-zone model.

Furthermore, in line with the chapters of the dissertation, more detailed results are summarized as follows:

- One-dimensional performance analysis:
  - The numerical results computed by the 1D tool have been validated against the experimental results obtained with the test-rig, at 190 and 220 krpm, and varying mass flow rate, respectively.
  - The comparison shows a good agreement, since the model is able to capture the pressure ratio and efficiency trends. However, in proximity of the choking condition the difference between the numerical and test data is higher.
  - At the micro turbine design point (i.e., $\dot{m}$ = 50 g/s and N = 240 krpm), the model overpredicts the pressure ratio, but underpredicts the efficiency, while it has been calculated that the skin friction losses contribute to the largest efficiency decrease, followed by the mixing losses, and the vaneless diffuser losses.
- Experimental set-up:
  - The performance maps of the MTT micro turbine compressor have been obtained at a rotational speed as high as 220 krpm, but rotational speeds up to 240 krpm (i.e., the micro turbine design point) are deemed within reach with suitable improvements of the compressor test-rig.
  - The highest measured total-to-total isentropic efficiency of the current compressor stage is equal to 0.695±0.112 at 120 krpm, 0.692±0.063 at 160 krpm, 0.681±0.049 at 190 krpm, and 0.686±0.037 at 220 krpm. The maximum measured stage total-to-total pressure ratio is equal to 2.33±0.08 at 220 krpm.

  - The uncertainty of the measured static pressures highly influences the uncertainty of both the stage total-to-total pressure ratio and isentropic efficiency. Particularly, the uncertainty of the static pressure at the compressor inlet is preponderant with respect to that of the static pressure at the outlet.
  - Substituting the actual pressure transmitters with instruments having better accuracy and lower full scale would reduce the uncertainties of the final results. For example, decreasing the full scale would reduce the average uncertainties of the pressure ratio and efficiency from 3.5% and 11.7%, to 1.4% and 6.5%, respectively.

- Numerical aerodynamic analysis at the micro turbine design point:

  - The supersonic relative Mach number at the impeller blades tip causes the flow to separate, and the following development of a low-velocity region on the blades suction side. The wake which develops at the impeller outlet due to the flow separation is larger on the full blades suction side than on the suction side of the splitter blades, and leads to the generation of high losses in proximity of the shroud.
  - The calculated static pressure recovery coefficient of the vaneless diffuser of the actual compressor stage is equal to 0.47. It is thus located at the lower end of the ranges documented in the literature, since less than 50% of the high kinetic energy available at the diffuser inlet is converted into static pressure.
  - For every 1%-increase of the impeller tip clearance, the stage total-to-total pressure ratio and isentropic efficiency decrease by 1.3% and 0.6%, respectively. The impeller efficiency drop due to the impeller tip clearance is two times larger than the loss documented in the literature for larger centrifugal impellers.

- Vaned diffusers optimization at the micro turbine design point:

  - For the MTT micro compressor, the efficiency of the simulated most efficient optimized vaned diffuser is 1.9% lower than that of the vaneless diffuser. The vaned diffuser however exhibits a 7.4%-higher static pressure recovery.
  - Subsequently, an impeller with larger diameter, which delivers a higher pressure ratio at the same rotational speed, has been considered, since the effects of a guided diffusion process might be beneficial because of a higher dynamic head to recover. The efficiency and static pressure recovery of the simulated most efficient optimized vaned diffuser are respectively 1.8% and 16.6% higher than those of the vaneless configuration. The outlet diameter of the vaned diffuser is 12% smaller than that of the vaneless diffuser.
  - The length of the diffuser vanes is a trade-off between static pressure recovery and total pressure losses. The influence of the diffuser vane number on the static pressure recovery and efficiency could not be properly assessed.

7.2 Perspectives

The work described in this dissertation left many open issues of interest for future research activities:

- One-dimensional performance analysis:
  - The 1D model has to be tested with other small centrifugal compressors, in order to further solidify its role as an efficient method to analyze these turbomachines.
  - Further CFD simulations are required in order to improve the capability of the 1D approach to properly quantify the diffusion parameters, the relationship between the secondary flow mass and area fractions, and the tangential velocity factor.
- Experimental set-up:
  - Further experiments of the exemplary compressor stage in proximity of the choking condition have to be performed at all rotational speeds.
  - In order to reach a higher rotational speed in the test-rig, the turbine which drives the compressor has to be powered by a more reliable and controllable power source (e.g., an electric motor).
  - Additional measurements within the single components of the exemplary compressor stage have to be carried out, in order to quantify their performance, and to acquire further knowledge about the flow phenomena which occur there.
  - The impeller tip clearance has to be measured in running conditions, in order to establish an experimental correlation between the tip clearance and the efficiency drop, and to validate the numerical results.
- Numerical aerodynamic analysis:
  - The inlet pipe located upstream of the compressor in the test-rig, as well as the volute, have to be included in the computational domain, in order to achieve a better insight on the flow field in all the stage components, and of their mutual influence.
  - A deeper analysis of the tip clearance influence on the impeller and diffuser (either vaneless or vaned) flow fields has to be carried out.
- Vaned diffusers optimization:
  - Thanks to the available ever increasing computational power and to the use of metamodels, the simultaneous optimization of the impeller and the vaned diffuser can be carried out, in order to achieve a new aerodynamic design which will significantly increase the compressor stage performance.

- The impeller tip clearance has to be included in the computational domain for the simultaneous impeller and vaned diffuser optimization, in order to assess its effects on the performance of the vaned diffuser and compressor stage.
- The geometric variables wich define the diffuser vane leading edge shape and the diffuser vane profile shape have to be included in the group of design variables, in order to account for the variation of the flow angle in the spanwise direction, and to obtain "more aerodynamic" vane shapes.
- A so-called "multi-point" optimization has to be carried out, in order to optimize the vaned diffusers for a wider range of operating conditions, so to avoid abrupt decrements of the compressor performance when the micro turbine operates at part-load conditions.
- Unsteady CFD investigations of the best vaned diffuser obtained through the optimization work can be performed, in order to analyze the impeller-vaned diffuser interaction.

Bibliography

[1] ABB, Baden, Switzerland, 2011, *Netherlands Energy Efficiency Report*.

[2] Ackermann, T., Andersson, G., and Soder, L., 2001, "Distributed Generation: a Definition," Electr. Power Syst. Res., **57**: 195–204.

[3] Ahmed, M. Y. M. and Qin, N., 2009, "Comparison of Response Surface and Kriging Surrogates in Aerodynamic Design Optimization of Hypersonic Spiked Blunt Bodies," *Proc. 13th International Conference on Aerospace Sciences & Aviation Technology*, ASAT-13-AE-15.

[4] Amineni, N. K., 1996, "Design and Development of Advanced Vaned Diffusers for Centrifugal Compressors," Ph.D. thesis, Michigan State University, U.S.A.

[5] Amineni, N. K. and Engeda, A., 1997, "Pressure Recovery in Low Solidity Vaned Diffusers for Centrifugal Compressors," *Proc. ASME Turbo Expo 1997*, 97-GT-472.

[6] Amineni, N. K., Engeda, A., Hohlweg, W. C., and Direnzi, G. L., 1996, "Performance of Low Solidity and Conventional Diffusers Systems for Centrifugal Compressors," *Proc. ASME Turbo Expo 1996*, 96-GT-155.

[7] Angelino, G., Gaia, M., and Macchi, E., 1984, "A Review of Italian Activity in the Field of Organic Rankine Cycles," *ORC-HP-Technology Working Fluid Problems*, Verlag des Dereins Deutscher Ingenieure, Düsseldorf, Germany, vDI Berichte 539.

[8] ANSYS, Inc., Canonsburg, U.S.A., 2010, *ANSYS BladeGen User's Guide*, release 13.0.

[9] ANSYS, Inc., Canonsburg, U.S.A., 2010, *ANSYS CFX-Pre, Post, and Solver Manager User's Guide*, release 13.0.

[10] ANSYS, Inc., Canonsburg, U.S.A., 2010, *ANSYS TurboGrid User's Guide*, release 13.0.

[11] ASME, New York, U.S.A., 2006, *Test Uncertainty PTC 19.1 - 2005*.

[12] Aungier, R. H., 1995, "Mean Streamline Aerodynamic Performance Analysis of Centrifugal Compressors," J. Turbomach.-Trans. ASME, **117**(3): 360–366.

[13] Aungier, R. H., 2000, *Centrifugal Compressors: a Strategy for Aerodynamic Design and Analysis*, ASME Press, New York, U.S.A.

[14] Ayder, E. and Van Den Braembussche, R. A., 1994, "Numerical Analysis of the Three-Dimensional Swirling Flow in Centrifugal Compressor Volutes," J. Turbomach.-Trans. ASME, **116**(3): 462–468.

[15] Bäck, T., 1996, *Evolutionary Algorithms in Theory and Practice: Evolution Strategies, Evolutionary Programming, Genetic Algorithms*, Oxford University Press, New York, U.S.A. and Oxford, U.K.

[16] Baines, N. C., 2005, *Fundamentals of Turbocharging*, Concepts NREC, White River Junction, U.S.A.

[17] Bammert, K., Jansen, M., and Rautenberg, M., 1983, "On the Influence of the Diffuser Inlet Shape on the Performance of a Centrifugal Compressor Stage," *Proc. ASME Turbo Expo 1983*, 83-GT-9.

[18] Barber-Nichols Inc., Arvada, U.S.A., 2011, *Mini-Brayton Power Source*, internal report.

[19] Bardina, J. E., Huang, P. G., and Coakley, T. J., 1997, "Turbulence Modeling Validation," *Proc. 33rd AIAA/ASME/SAE/ASEE Joint Propulsion Conference & Exhibit*, AIAA 1997-2121.

[20] Bardina, J. E., Huang, P. G., and Coakley, T. J., 1997, "Turbulence Modeling Validation, Testing, and Development," Tech. Rep. TM 110446, NASA, U.S.A.

[21] Baxi Heating U.K. Ltd., U.K., *http://www.baxi.co.uk/products/ecogen.htm*, accessed on June 29th, 2012.

[22] Benini, E. and Toffolo, A., 2003, "Centrifugal Compressor of a 100 kW Microturbine: Part 3 - Optimization of Diffuser Apparatus," *Proc. ASME Turbo Expo 2003*, GT-2003-38154.

[23] Benini, E. and Tourlidakis, A., 2001, "Design Optimization of Vaned Diffusers for Centrifugal Compressors Using Genetic Algorithms," *Proc. 15th AIAA Computational Fluid Dynamics Conference*, AIAA 2001-2583.

[24] Bevington, P. R. and Robinson, D. K., 2003, *Data Reduction and Error Analysis for the Physical Sciences*, McGraw-Hill, Inc., New York, U.S.A., 3rd ed.

[25] Bini, R. and Manciana, E., 1996, "Organic Rankine Cycle Turbogenerators for Combined Heat and Power Production from Biomass," *Proc. 3rd Munich Discussion Meeting on "Energy Conversion from Biomass Fuels: Current Trends and Future Systems"*.

[26] Bohn, D., 2005, "Micro Gas Turbine and Fuel Cell - A Hybrid Energy Conversion System with High Potential," *Micro Gas Turbines*, RTO-EN-AVT-131-13, RTO of NATO, France.

[27] Boyce, M. P., 2003, *Centrifugal Compressors: a Basic Guide*, PennWell Corporation, Tulsa, U.S.A.

[28] Brown, W. B., 1947, "Friction Coefficients in a Vaneless Diffuser," Tech. Rep. TN 1311, NACA, U.S.A.

[29] Busemann, A., 1928, "Das Förderhöhenverhältnis Radialer Kreisel-Pumpen mit Logarithmisch-Spiraligen Schaufeln," ZAMM-Z. Angew. Math. Mech., **8**(5): 372–384.

[30] Camatti, M., Betti, D., and Giachi, M., 1995, "Vaned Diffusers Development Using Numerical and Experimental Techniques," *Proc. 1995 ASME International Mechanical Engineering Congress & Exposition*, 95-WA/PID-4.

[31] Came, P. M. and Robinson, C. J., 1999, "Centrifugal Compressor Design," Proc. Inst. Mech. Eng. Part C-J. Eng. Mech. Eng. Sci., **213**(2): 139–155.

[32] Carlson, J. J., Johnston, J. P., and Sagi, C. J., 1967, "Effects of Wall Shape on Flow Regimes and Performance in Straight, Two-Dimensional Diffusers," J. Basic. Eng., **89**: 151–160.

[33] Carno, J., Cavani, A., and Liinanki, L., 1998, "Micro Gas Turbine for Combined Heat and Power in Distributed Generation," *Proc. ASME Turbo Expo 1998*, 98-GT-309.

[34] Carrard, A., 1923, "Sur le Calcul des Rows Centrifuges," La Technique Moderne, **XV**(3): 65–71.

[35] Carrard, A., 1923, "Sur le Calcul des Rows Centrifuges," La Technique Moderne, **XV**(4): 100–104.

[36] Casartelli, E., Saxer, A. P., and Gyarmathy, G., 1999, "Numerical Flow Analysis of a Subsonic Vaned Radial Diffuser with Leading Edge Redesign," J. Turbomach.-Trans. ASME, **121**: 119–1226.

[37] Central Intelligence Agency, Langley, U.S.A., 2011, *CIA - The World Factbook*.

[38] Clark, D. J., Jansen, M. J., and Montague, G. T., 2004, "An Overview of Magnetic Bearing Technology for Gas Turbine Engines," Tech. Rep. NASA/TM-2004-213177, NASA, U.S.A.

[39] CleanEnergy AB, Sweden, *http://www.cleanergy.com/chp-Engines/*, accessed on June 29th, 2012.

[40] Clements, W. and Artt, D., 1989, "The Influence of Diffuser Vane Leading Edge Geometry on the Performance of a Centrifugal Compressor," *Proc. ASME Turbo Expo 1989*, 89-GT-163.

[41] Clements, W. W. and Artt, D. W., 1987, "Influence of Diffuser Channel Geometry on the Flow Range and Efficiency of a Centrifugal Compressor," Proc. Inst. Mech. Eng. Part A-Power Process Eng., **201**(A2): 145–152.

[42] Clements, W. W. and Artt, D. W., 1988, "The Influence of Diffusers Channel Length-Width Ratio on the Efficiency of a Centrifugal Compressor," Proc. Inst. Mech. Eng. Part A-Power Process Eng., **202**(A3): 163–169.

[43] Coello Coello, C. A., 1999, "A Comprehensive Survey of Evolutionary-Based Multiobjective Optimization Techniques," Knowl. Inf. Syst., **1**(3): 269–308.

[44] COGEN Europe, Brussels, Belgium, 2010, *Cogeneration as the Foundation of Europe's 2050 Low-Carbon Energy Policy*.

[45] Coleman, H. W. and Steele, W. G., 1987, "Some Considerations in the Propagation of Systematic and Random Errors into an Experimental Result," Experimental Uncertainty in Fluid Measurements, ASME FED, **58**: 57–62.

[46] Coleman, H. W. and Steele, W. G., 1995, "Engineering Application of Experimental Uncertainty Analysis," AIAA J., **33**(10): 1888–1896.

[47] Coleman, H. W. and Steele, W. G., 2009, *Experimentation and Uncertainty Analysis for Engineers*, John Wiley & Sons, Inc., New York, U.S.A., 3rd ed.

[48] Colijn, M., 2006, "Micro Cogeneration in the Netherlands," *Micro Cogeneration: Towards Decentralized Energy Systems*, edited by Pehnt, M., Cames, M., Fischer, C., Praetorius, B., Schneider, L., Schumacher, K., and Voß, J.-P., Springer, Berlin, Germany.

[49] Colonna, P. and Rebay, S., 2004, "Numerical Simulation of Dense Gas Flows on Unstructured Grids with an Implicit High Resolution Upwind Euler Solver," Int. J. Numer. Meth. Fl., **46**(7): 735–765.

[50] Cressie, N. A. C., 1993, *Statistics for Spatial Data*, John Wiley & Sons, Inc., New York, U.S.A.

[51] Cumpsty, N. A., 1989, *Compressor Aerodynamics*, Longman Scientific & Technical, Essex, U.K.

[52] Cumpsty, N. A. and Horlock, J. H., 2006, "Averaging Nonuniform Flow for a Purpose," J. Turbomach.-Trans. ASME, **128**(1): 120–129.

[53] de Jong, A., van Gastel, M., Bakker, E.-J., Jeeninga, J., H. Dam, van Wolferen, H., Rooijers, F., Koot, M., Schlatmann, S., Seebregts, A., Menkveld, M., Boerakker, Y., Harmsen, R., and Turkstra, J. W., 2008, "Energie- en CO_2-Besparingspotentieel van Micro-wkk in Nederland (2010-2030)," Tech. rep., CE Delft, Cogen Projects, ECN, Ecofys, Gasunie Engineering & Technology, and TNO, The Netherlands.

[54] Dean, R. C., 1971, "On the Unresolved Fluid Dynamics of the Centrifugal Compressor," *Advanced Centrifugal Compressors*, ASME.

[55] Dean, R. C., 1974, "The Fluid Dynamic Design of Advanced Centrifugal Compressors," *Lecture Series 1974*, Von Kármán Institute for Fluid Dynamics, Belgium.

[56] Dean, R. C. and Senoo, Y., 1960, "Rotating Wake in Vaneless Diffusers," J. Basic Eng., **82**: 563–574.

[57] Deb, K., Agrawal, S., Pratap, A., and Meyarivan, T., 2000, "A Fast Elitist Non-Dominated Sorting Genetic Algorithm for Multi-Objective Optimization: NSGA-II," *Proc. Parallel Problem Solving from Nature VI Conference*.

[58] Deb, K., Pratap, A., Agarwal, S., , and Meyarivan, T., 2002, "A Fast and Elitist Multiobjective Genetic Algorithm: NSGA-II," Evol. Comput., **6**(2): 182–197.

[59] Delta Energy & Environment, Edinburgh, U.K., 2011, *Delta Market Projections: European Combined Mini & Micro CHP Annual Sales Can Reach 600,000 by 2020*.

[60] Dentice d'Accadia, M., Sasso, M., Sibilio, S., and Vanoli, L., 2003, "Micro-Combined Heat and Power in Residential and Light Commercial Applications," Appl. Therm. Eng., **23**(10): 1247–1259.

[61] Denton, J. D., 1994, "Designing in Three Dimensions," *Turbomachinery Design Using CFD*, AGARD-LS-195, AGARD.

[62] Denton, J. D., 2010, "Some Limitations of Turbomachinery CFD," *Proc. ASME Turbo Expo 2010*, GT2010-22540.

[63] Dorer, V. and Weber, A., 2009, "Energy and CO_2 Emissions Performance Assessment of Residential Micro-Cogeneration Systems with Dynamic Whole-Building Simulation Programs," Energy Convers. Manage., **50**(3): 648–657.

[64] Dunn, S., 2000, *MicroPower: The Next Electrical Era*, Worldwatch Institute, Washington, U.S.A.

[65] Duvia, A., Guercio, A., and Rossi di Schio, C., 2011, "Technical and Economic Aspects of Biomass Fuelled CHP Plants Based on ORC Turbogenerators Feeding Existing District Heating Networks," *Proc. 1st International Seminar on ORC Power Systems*.

[66] Eckardt, D., 1975, "Instantaneous Measurements in the Jet-Wake Discharge Flow of a Centrifugal Compressor Impeller," J. Eng. Power-Trans. ASME, **97**(3): 337–346.

[67] Eckardt, D., 1976, "Detailed Flow Investigations within a High-Speed Centrifugal Compressor Impeller," J. Fluids Eng.-Trans. ASME, **98**(3): 390–402.

[68] Eckardt, D., 1980, "Flow Field Analysis of Radial and Backswept Centrifugal Compressor Impellers. Part 1: Flow Measurements Using a Laser Velocimeter," *Performance Prediction of Centrifugal Pumps and Compressors*, ASME, U.S.A.

[69] Eckert, B. and Schnell, E., 1961, *Axial- und Radial-Kompressoren*, Springer-Verlag, Berlin, Germany, 2nd ed.

[70] El-Khattam, W. and Salama, M. M. A., 2004, "Distributed Generation Technologies, Definitions and Benefits," Electr. Power Syst. Res., **71**: 119–128.

[71] Energy and Environmental Analysis, Inc. and Exergy Partners Corp., 2004, *Industrial Application Guide For Innovative Combined Heat and Power*.

[72] Energy for Sustainable Development Ltd., Corsham, U.K., 2001, *The Future of CHP in the European Market - The European Cogeneration Study - Final Publishable Report*.

[73] Energy for Sustainable Development Ltd., Corsham, U.K., 2001, *The Future of CHP in the European Market - The European Cogeneration Study - Publishable Summary*.

[74] Energy Information Administration, Washington, U.S.A., 1999, *Natural Gas 1998: Issues and Trends*.

[75] Energy Technology Systems Analysis Program, Paris, France, 2010, *Gas Fired Power Plants*.

[76] Engeda, A., 1996, "Performance of Different Diffusers for Centrifugal Compressors," ASME FED, **238**: 589–594.

[77] Engeda, A., 1997, "Design of a Range of Low Solidity Vaned Diffusers for Centrifugal Compressors," *Proc. 1997 ASME International Mechanical Engineering Congress & Exposition*, 97-WA/PID-4.

[78] Engeda, A., 1998, "Design and Investigation of Four Low Solidity Vaned Diffusers to Assess the Effect of Solidity and Vane Number," *Proc. ASME Turbo Expo 1998*, 98-GT-252.

[79] Etheridge, D. M., Steele, L. P., Langenfelds, R. L., Francey, R. J., Barnola, J.-M., and Morgan, V. I., 1998, "Historical CO_2 Records from the Law Dome DE08, DE08-2, and DSS Ice Cores," *Trends: a Compendium of Data on Global Change*, Carbon Dioxide Information Analysis Center, Oak Ridge National Laboratory, U.S.Department of Energy, Oak Ridge, U.S.A.

[80] The European Association for the Promotion of Cogeneration, Brussels, Belgium, 2001, *A Guide to Cogeneration*.

[81] European Union, Brussels, Belgium, 1997, *Energy for the Future: Renewable Sources of Energy*, COM(97) 599 final.

[82] European Union, Brussels, Belgium, 2004, *Directive on the Promotion of Cogeneration Based on a Useful Heat Demand in the Internal Energy Market*, COM 2004/8/EC.

[83] European Union, Brussels, Belgium, 2008, *20 20 by 2020 Europe's Climate Change Opportunity*, COM(2008) 30 final.

[84] European Union Committee, London, U.K., 2008, *The EU's Target for Renewable Energy: 20% by 2020 Volume I: Report*.

[85] Eynon, P. A. and Whitfield, A., 1997, "The Effect of Low-Solidity Vaned Diffusers on the Performance of a Turbocharger Compressor," Proc. Inst. Mech. Eng. Part C-J. Eng. Mech. Eng. Sci., **211**(5): 325–339.

[86] Faber, A., Valente, M., and Janssen, P., 2010, "Exploring Domestic Micro-Cogeneration in the Netherlands: an Agent-Based Demand Model for Technology Diffusion," Energ. Policy, **38**(6): 2763–2775.

[87] FaberMaunsell, London, U.K., 2002, *Mini and Micro CHP - Market Assessment and Development Plan*.

[88] Fatsis, A., Pierret, S., and Van Den Braembussche, R. A., 1997, "Three-Dimensional Unsteady Flow and Forces in Centrifugal Impellers with Circumferential Distortion of the Outlet Static Pressure," J. Turbomach.-Trans. ASME, **119**(1): 94–102.

[89] Fischer, K. and Thoma, D., 1932, "Investigation of the Flow Conditions in a Centrifugal Pump," Trans. ASME, **54-58**: 141.

[90] FLUENT, Inc., Lebanon, U.S.A., 2007, *GAMBIT User's Guide*, release 2.4.6.

[91] Fowler, H. S., 1968, "The Distribution and Stability of Flow in a Rotating Channel," J. Eng. Power-Trans. ASME, **90**: 229–236.

[92] Fuel Cell Today, Royston, U.K., 2011, *The Fuel Cell Today Industry Review 2011*.

[93] Gano, S. E. and Renaud, J. E., 2005, "Hybrid Variable Fidelity Optimization by Using a Kriging-Based Scaling Function," AIAA J., **43**: 2422–2430.

[94] Garrison, L. and Cooper, N., 2009, "Visualization and Post-Processing of Centrifugal Compressor Computational Fluid Dynamics Flow Fields," *Proc. ASME Turbo Expo 2009*, GT2009-60165.

[95] Ghidoni, A., Pelizzari, E., Rebay, S., and Selmin, V., 2006, "3D Anisotropic Unstructured Grid Generation," Int. J. Numer. Meth. Fl., **51**(9-10): 1097–1115.

[96] Giannakoglou, K. C., 2002, "Design of Optimal Aerodynamic Shapes Using Stochastic Optimization Methods and Computational Intelligence," Prog. Aeros. Sci., **38**(1): 43–76.

[97] Goldberg, D. E., 1989, *Genetic Algorithms in Search, Optimization and Machine Learning*, Addison-Wesley, Reading, U.S.A.

[98] Goldberg, D. E. and Deb, K., 1991, "A Comparison of Selection Schemes Used in Genetic Algorithms," *Foundations of Genetic Algorithms*, Morgan Kaufmann, U.S.A.

[99] Goldberger, A. S., 1962, "Best Linear Unbiased Prediction in the Generalized Linear Regression Model," J. Am. Stat. Assoc., **57**(298): 369–375.

[100] Goovaerts, P., *Geostatistics for Natural Resources Evaluation*, Oxford University Press, Oxford, U.K.

[101] Hagelstein, D., Hillewaert, K., Van Den Braembussche, R. A., Engeda, A., Keiper, R., and Rautenberg, M., 2000, "Experimental and Numerical Investigation of the Flow in a Centrifugal Compressor Volute," J. Turbomach.-Trans. ASME, **122**(1): 22–31.

[102] Harada, H. and Goto, M., 1993, "Numerical and Experimental Studies of Single and Tandem Low-Solidity Cascade Diffusers in a Centrifugal Compressor," *Proc. ASME Turbo Expo 1993*, 93-GT-108.

[103] Harrison, J., 2004, "Micro Combined Heat & Power (CHP) for Housing," *Proc. 3rd International Conference on Sustainable Energy Technologies*.

[104] Hathaway, M. D., Chriss, R. M., Wood, J. R., and Strazisar, A. J., 1993, "Experimental and Computational Investigation of the NASA Low-Speed Centrifugal Compressor Flow Field," J. Turbomach.-Trans. ASME, **115**(3): 527–542.

[105] Hathaway, M. D., Chriss, R. M., Wood, J. R., and Strazisar, A. J., 1993, "Experimental and Computational Investigation of the NASA Low-Speed Centrifugal Compressor Flow Field," Tech. Rep. TM 4481, NASA, U.S.A.

[106] Hayami, H., Senoo, Y., and Utsunomiya, K., 1990, "Application of a Low-Solidity Cascade Diffuser to Transonic Centrifugal Compressor," J. Turbomach.-Trans. ASME, **112**(1): 25–29.

[107] He, N. and Tourlidakis, A., 2001, "Analysis of Diffusers with Different Number of Vanes in a Centrifugal Compressor Stage," *Proc. ASME Turbo Expo 2001*, 2001-GT-0321.

[108] Hexis AG, Switzerland, *http://www.hexis.com/en/system-Data*, accessed on June 29th, 2012.

[109] Hiereth, H. and Prenninger, P., 2007, *Charging the Internal Combustion Engine*, Springer, Wien, Austria.

[110] Hildebrandt, A. and Genrup, M., 2007, "Numerical Investigation of the Effect of Different Back Sweep Angle and Exducer Width on the Impeller Outlet Flow Pattern of a Centrifugal Compressor with Waneless Diffuser," J. Turbomach.-Trans. ASME, **129**(2): 421–433.

[111] Hillewaert, K. and Van Den Braembussche, R. A., 1999, "Numerical Simulation of Impeller-Volute Interaction in Centrifugal Compressors," J. Turbomach.-Trans. ASME, **121**(3): 603–608.

[112] Hohlweg, W. C., Direnzi, G. L., and Aungier, R. H., 1993, "Comparison of Conventional and Low Solidity Vaned Diffusers," *Proc. ASME Turbo Expo 1993*, 93-GT-98.

[113] Holland, J. H., 1975, *Adaption in Natural and Artificial Systems*, University of Michigan Press, Ann Arbor, U.S.A.

[114] Honda Motor Company, Ltd., Japan, *http://world.honda.com/Power/cogenerator*, accessed on June 29th, 2012.

[115] Houwing, M., 2010, "Smart Heat and Power: Utilizing the Flexibility of Micro Cogeneration," Ph.D. thesis, Technische Universiteit Delft, The Netherlands.

[116] iChrome Ltd., Bristol, U.K., 2010, *Nexus Graphical User Interface Manual*.

[117] IdaTech, LLC., U.S.A., *http://www.idatech.com/products-and-services-product-lineup.asp*, accessed on June 29th, 2012.

[118] Inoue, M. and Cumpsty, N. A., 1984, "Experimental Study of Centrifugal Impeller Discharge Flow in Vaneless and Vaned Diffusers," J. Eng. Gas. Turb. Power-Trans. ASME, **106**(2): 455–467.

[119] Intergovernmental Panel on Climate Change, Geneva, Switzerland, 2000, *Emissions Scenarios - Summary for Policymakers*.

[120] Intergovernmental Panel on Climate Change, Geneva, Switzerland, 2001, *Climate Change 2001: the Physical Science Basis*.

[121] Intergovernmental Panel on Climate Change, Geneva, Switzerland, 2007, *Climate Change 2007: Synthesis Report - Summary for Policymakers*.

[122] Intergovernmental Panel on Climate Change, Geneva, Switzerland, 2007, *Climate Change 2007: the Physical Science Basis*.

[123] International Energy Agency, Paris, France, 2002, *Distributed Generation in Liberalised Electricity Markets*.

[124] International Energy Agency, Paris, France, 2008, *Energy Technologies Perspectives 2008 - Scenarios & Strategies to 2050*.

[125] International Energy Agency, Paris, France, 2008, *The Netherlands 2008 Review*.

[126] International Energy Agency, Paris, France, 2010, *CO_2 Emissions from Fuel Combustion Highlights*.

[127] International Energy Agency, Paris, France, 2010, *World Energy Outlook 2010*.

[128] International Organization for Standardization, Geneva, Switzerland, 1993, *Guide to the Expression of Uncertainty in Measurement*.

[129] Invernizzi, C., Iora, P., and Silva, P., 2007, "Bottoming Micro-Rankine Cycles for Micro-Gas Turbines," Appl. Therm. Eng., **27**(1): 100–110.

[130] Jaatinen, A., 2009, "Performance Improvement of Centrifugal Compressor Stage with Pinched Geometry or Vaned Diffusers," Ph.D. thesis, Lappeenranta University of Technology, Finland.

[131] Jaatinen, A., Grönman, A.-P., Turunen-Saaresti, T., and Backman, J. L. H., 2010, "Experimental Study of Vaned Diffusers in Centrifugal Compressor," *Proc. ASME Turbo Expo 2010*, GT2010-22883.

[132] Japikse, D., 1980, "The Influence of Diffusers Inlet Pressure Fields on the Range and Durability of Centrifugal Compressor Stages," *Centrifugal Compressors, Flow Phenomena and Performance*, AGARD.

[133] Japikse, D., 1982, "Advanced Diffusion Levels in Turbocharger Compressor and Component Matching," *Turbocharging and Turbochargers*, C45/82, Mechanical Engineering Publications Limited for the Institution of Mechanical Engineers.

[134] Japikse, D., 1984, "A Critical Evaluation of Three Centrifugal Compressors with Pedigree Data Sets: Part 5 - Studies in Component Performance," J. Turbomach.-Trans. ASME, **109**(1): 1–9.

[135] Japikse, D., 1985, "Assessment of Single- and Two-Zone Modeling of Centrifugal Compressors. Studies in Component Performance: Part 3," *Proc. ASME Turbo Expo 1985*, 85-GT-73.

[136] Japikse, D., 1996, *Centrifugal Compressor Design and Performance*, Concepts ETI, Inc., Wilder, U.S.A.

[137] Japikse, D. and Baines, N. C., 1994, *Introduction to Turbomachinery*, Concepts ETI, Inc. and Oxford University Press, Norwich, U.S.A. and Oxford, U.K.

[138] Japikse, D. and Baines, N. C., 1998, *Diffuser Design Technology*, Concepts ETI, Inc. and Oxford University Press, Norwich, U.S.A. and Oxford, U.K.

[139] Japikse, D. and Goebel, J., 1979, "Turbocharger Compressor Performance Evaluation and Critical Flow Field Measurements," *SAE 1979 International Congress & Exposition*, 790315.

[140] Javed, A., Olivero, M., Pecnik, R., and Van Buijtenen, J. P., 2011, "Performance Analysis of a Microturbine Centrifugal Compressor from a Manufacturing Perspective," *Proc. ASME Turbo Expo 2011*, GT2011-46374.

[141] Jeong, S., Murayama, M., and Yamamoto, K., 2005, "Efficient Optimization Design Method Using Kriging Model," J. Aircraft, **42**(2): 413–420.

[142] Jiang, T. and Yang, T.-t., 1982, "Improved Vane-Island Diffusers at High Swirl," *Proc. ASME Turbo Expo 1982*, 82-GT-68.

[143] Jiao, K., Sun, H., Li, X., Wu, H., Krivitzky, E., Schram, T., and Larosiliere, L. M., 2009, "Numerical Simulation of Air Flow through Turbocharger Compressors with Dual Volute Design," Appl. Energy, **86**: 2494–2506.

[144] Johnson, M. W. and Moore, J., 1980, "The Development of Wake Flow in a Centrifugal impeller," J. Eng. Power-Trans. ASME, **102**(2): 382–390.

[145] Johnson, M. W. and Moore, J., 1983, "The Influence of Flow Rate on the Wake in a Centrifugal Impeller," J. Eng. Power-Trans. ASME, **105**(2): 33–39.

[146] Johnson, M. W. and Moore, J., 1983, "Secondary Flow Mixing Losses in a Centrifugal Impeller," J. Eng. Power-Trans. ASME, **105**(2): 24–32.

[147] Journel, A. G. and Huijbregts, C. J., 1978, *Mining Geostatistics*, Academic Press, New York, U.S.A.

[148] Justen, F., Ziegler, K. U., and Gallus, H. E., 1999, "Experimental Investigation of Unsteady Flow Phenomena in a Centrifugal Compressor Vaned Diffuser of Variable Geometry," J. Turbomach.-Trans. ASME, **121**(4): 763–771.

[149] Kenny, D. P., 1984, "The History and Future of the Centrifugal Compressor in Aviation Gas Turbine," *1st Cliff Garrett Turbomachinery Award Lecture*, SAE/SP-804/602, Society of Automotive Engineers, Inc., U.K.

[150] Kharbat, F., Bull, L., and Odeh, M., 2005, "Revisiting Genetic Selection in XCS Learning Classifier System," *Proc. IEEE Conference on Evolutionary Computations*.

[151] Kim, H.-W., Park, J.-I., Ryu, S.-H., Choi, S.-W., and Ghal, S.-H., 2009, "The Performance Evaluation with Diffuser Geometry Variations of the Centrifugal Compressor in a Marine Engine (70 MW) Turbocharger," J. Eng. Gas. Turb. Power-Trans. ASME, **131**: 012201–1–012201–7.

[152] Kim, S., Park, J., Ahn, K., and Baek, J., 2010, "Numerical Investigation and Validation of the Optimization of a Centrifugal Compressor Using a Response Surface Method," Proc. Inst. Mech. Eng. Part A-J. Power Energy, **224**(2): 251–259.

[153] Kim, W. J., 1998, "Design and Development of Low Solidity Vaned Diffusers for Centrifugal Compressors," Ph.D. thesis, Michigan State University, U.S.A.

[154] Kim, W. J. and Engeda, A., 1997, "Comparison of Pressure Recovery and Overall Performance of Different Diffusers for Centrifugal Compressors," *Proc. 1997 ASME Fluids Engineering Division Summer Meeting*, FEDSM97-3029.

[155] Kirkup, L. and Frenkel, R. B., 2006, *An Introduction to Uncertainty in Measurement Using the GUM (Guide to the Expression of Uncertainty in Measurement)*, Cambridge University Press, Cambridge, U.K.

[156] Kline, S. J., Abbott, D. E., and Fox, R. W., 1959, "Optimum Design of Straight-Walled Diffusers," J. Basic. Eng., **81**: 321–329.

[157] Kmecl, T., Harkel, R. T., and Dalbert, P., 1999, "Optimization of a Vaned Diffuser Geometry for Radial Compressors. Part I: Investigation of the Influence of Geometry Parameters on Performance of a Diffuser," *Proc. ASME Turbo Expo 1999*, 99-GT-437.

[158] Kmecl, T., Harkel, R. T., and Dalbert, P., 1999, "Optimization of a Vaned Diffuser Geometry for Radial Compressors. Part II: Optimization of a Diffuser Vane Profile in Low Solidity Diffusers," *Proc. ASME Turbo Expo 1999*, 99-GT-434.

[159] Kolanowski, B. F., 2004, *Guide to Microturbines*, The Fairmont Press, Inc. and Marcel Dekker, Inc., New York, U.S.A.

[160] Konak, A., Coitb, D. W., and Smith, A. E., 2006, "Multi-Objective Optimization Using Genetic Algorithms: A tutorial," Reliab. Eng. Syst. Safe., **91**: 992–1007.

[161] Krain, H., 1981, "A Study on Centrifugal Impeller and Diffuser Flow," J. Eng. Power-Trans. ASME, **103**(4): 688–697.

[162] Krain, H., 1987, "Swirling Impeller Flow," *Proc. ASME Turbo Expo 1987*, 87-GT-19.

[163] Krige, D. G., 1951, "A Statistical Approach to Some Basic Mine Valuation Problems on the Witwatersrand," J. S. Afr. I. Min. Metall., **52**(6): 119–139.

[164] Krige, D. G., 1951, "A Statistical Approach to Some Mine Valuations and Allied Problems at the Witwatersrand," Master's thesis, University of Witwatersrand, Republic of South Africa.

[165] Kumakura, H., Maekawa, H., and Murakami, K., 2004, "Development of Portable Gas Turbine Generator "Dynajet 2.6"," IHI Engineering Review, **37**(3): 113–115.

[166] Lakshminarayana, B., 1996, *Fluid Dynamics and Heat Transfer of Turbomachinery*, John Wiley & Sons, Inc., New York, U.S.A.

[167] Larjola, J., 1995, "Electricity from Industrial Waste Heat Using High-Speed Organic Rankine Cycle (ORC)," Int. J. Prod. Econ., **41**(1-3): 227–235.

[168] Layton, L., 2008, "Micro-Combined Heat and Power Systems," Tech. rep., PDHEngineer.com, Houston, U.S.A.

[169] Lee, R., 2010, "Combined Heat and Power in a Carbon-Constrained World," Proc. Inst. Civil Eng.-Energy, **163**: 31–39.

[170] Li, M., Li, G., and Azarm, S., 2008, "A Kriging Metamodel Assisted Multi-Objective Genetic Algorithm for Design Optimization," J. Mech. Des.-Trans. ASME, **130**(3): 031401–1–031401–10.

[171] Li, X., 2005, "Numerical Study of a High-Speed Miniature Centrifugal Compressor," Ph.D. thesis, University of Central Florida, U.S.A.

[172] Lymberopoulos, N., 2004, "Microturbines and Their Application in Bio-Energy," Tech. rep., Centre for Renewable Energy Sources, Pikermi Attiki, Greece.

[173] Macchi, E., 1977, "Design Criteria for Turbines Operating with Fluids Having a Low Speed of Sound," *Lecture Series 1977*, Von Kármán Institute for Fluid Dynamics, Belgium.

[174] Macchi, E. and Perdichizzi, A., 1981, "Efficiency Prediction for Axial-Flow Turbines Operating with Nonconventional Fluids," J. Eng. Power-Trans. ASME, **103**(4): 718–724.

[175] Marland, G., Boden, T. A., and Andres, R. J., 2008, "Global, Regional, and National Fossil-Fuel CO_2 Emissions," *Trends: a Compendium of Data on Global Change*, Carbon Dioxide Information Analysis Center, Oak Ridge National Laboratory, U.S.Department of Energy, Oak Ridge, U.S.A.

[176] Martin, J. D. and Simpson, T. W., 2005, "Use of Kriging Models to Approximate Deterministic Computer Models," AIAA J., **43**(4): 853–863.

[177] Matheron, G., 58, "Principles of Geostatistics," Econ. Geol., **1963**: 1246–1266.

[178] The MathWorks, Inc., Natick, U.S.A., 2012, *MATLAB Primer*, release 2012a.

[179] McDonald, C. F., 2000, "Low-Cost Compact Primary Surface Recuperator Concept for Microturbines," Appl. Therm. Eng., **20**(5): 471–497.

[180] McDonald, C. F., 2003, "Recuperator Considerations for Future Higher Efficiency Microturbines," Appl. Therm. Eng., **23**(12): 1463–1487.

[181] Menter, F. R., 1993, "Zonal Two-Equation $k-\omega$ Turbulence Models for Aerodynamic Flows," *Proc. 23rd Fluid Dynamics, PlasmaDynamics and Lasers Conference*, AIAA 1993-2906.

[182] Menter, F. R., 1994, "Two-Equation Eddy-Viscosity Turbulence Models for Engineering Applications," AIAA J., **32**(8): 1598–1605.

[183] Micheli, D., Pantarotto, S., and Pediroda, V., 2003, "Optimum-Shape Design of a Small Gas Turbine Centrifugal Compressor Diffusers," *Proc. 5th European Conference on Turbomachinery, Fluid Dynamics and Thermodynamics*.

[184] Ministerie van Volkshuisvesting, Ruimtelijke Ordening en Milieu, The Netherlands, 2007, *New Energy for Climate Policy: the 'Clean and Efficient' Program*.

[185] Moore, J., 1973, "A Wake and an Eddy in a Rotating, Radial-Flow Passage. Part 1: Experimental Observations," J. Eng. Power-Trans. ASME, **95**(3): 205–212.

[186] Moore, J., 1973, "A Wake and an Eddy in a Rotating, Radial-Flow Passage. Part 2: Flow Model," J. Eng. Power-Trans. ASME, **95**(3): 212–219.

[187] Mounts, J. S. and Brasz, J. J., 1992, "Analysis of Jet/Wake Mixing in a Vaneless Diffuser," *Proc. ASME Turbo Expo 1992*, 92-GT-418.

[188] Muley, A. and Sundén, B., 2003, "Advances in Recuperator Technology for Gas Turbine Systems," *Proc. 2003 ASME International Mechanical Engineering Congress and Exposition*, IMECE2003-43294.

[189] Musgrave, D. S., 1980, "The Prediction of Design and Off-Design Efficiency for Centrifugal Compressor Impellers," *Performance Prediction of Centrifugal Pumps and Compressors*, ASME.

[190] Muste, M., 2009, "Guidelines for the Assessment of Uncertainty of Hydrometric Measurements," Tech. rep., World Meteorological Organization, Switzerland.

[191] National Instruments Corporation, Austin, U.S.A., 2003, *LabVIEW User Manual*.

[192] Obernberger, I., Carlsen, H., and Biedermann, F., 2003, "State-of-the-Art and Future Developments Regarding Small-Scale Biomass CHP Systems with a Special Focus on ORC and Stirling Engine Technologies," *Proc. International Nordic BioEnergy 2003 Conference*.

[193] Oh, H. W., Yoon, E. S., and Chung, M. K., 1997, "An Optimum Set of Loss Models for Performance Prediction of Centrifugal Compressors," Proc. Inst. Mech. Eng. Part A-J. Power Energy, **211**(4): 331–338.

[194] Oh, H. W., Yoon, E. S., and Chung, M. K., 2002, "Systematic Two-Zone Modelling for Performance Prediction of Centrifugal Compressors," Proc. Inst. Mech. Eng. Part A-J. Power Energy, **216**(1): 75–88.

[195] Olivero, M., Javed, A., Pecnik, R., Colonna, P., and Van Buijtenen, J. P., 2011, "Study on the Tip Clearance Effects in the Centrifugal Compressor of a Micro Gas Turbine by means of Numerical Simulations," *Proc. International Gas Turbine Congress 2011*, IGTC2011-0233.

[196] Olivero, M., Javed, A., and Van Buijtenen, J. P., 2010, "Aerodynamic Analysis of a Micro Turbine Centrifugal Compressor," *Proc. ASME Turbo Expo 2010*, GT2010-23112.

[197] Onovwiona, H. I. and Ugursalb, V. I., 2006, "Residential Cogeneration Systems: Review of the Current Technology," Renew. Sust. Energ. Rev., **10**: 389–431.

[198] Organ, A. J., 1997, *The Regenerator and the Stirling Engine*, The Harvill Press Ltd., London, U.K.

[199] Osborne, C., 1979, "Turbocharging the Internal Combustion Engine," Tech. rep., Fluid Dynamics Institute, U.S.A.

[200] Pampreen, R. C., 1972, "The Use of Cascade Technology in Centrifugal Compressor Vaned Diffuser Design," J. Eng. Power-Trans. ASME, **94**(3): 187–192.

[201] Pampreen, R. C., 1973, "Small Turbomachinery Compressor and Fan Aerodynamics," J. Eng. Power-Trans. ASME, **95**(3): 251–256.

[202] Pehnt, M., 2006, "Micro Cogeneration Technology," *Micro Cogeneration: Towards Decentralized Energy Systems*, edited by Pehnt, M., Cames, M., Fischer, C., Praetorius, B., Schneider, L., Schumacher, K., and Voß, J.-P., Springer, Berlin, Germany.

[203] Pehnt, M. and Fischer, C., 2006, "Environmental Impacts of Micro Cogeneration," *Micro Cogeneration: Towards Decentralized Energy Systems*, edited by Pehnt, M., Cames, M., Fischer, C., Praetorius, B., Schneider, L., Schumacher, K., and Voß, J.-P., Springer, Berlin, Germany.

[204] Pepermans, G., Driesen, J., Haeseldonckx, D., Belmans, R., and D'haeseleer, W., 2005, "Distributed Generation: Definition, Benefits and Issues," Energ. Policy, **33**: 787–798.

[205] Pfleiderer, C., 1924, *Die Kreiselpumpen für Flüssigkeiten und Gase*, Springer, Berlin, Germany.

[206] Pfleiderer, C., 1961, *Die Kreiselpumpen*, vol. 5, Springer-Verlag, Berlin, Germany.

[207] Pierret, S. and Van Den Braembussche, R. A., 1999, "Turbomachinery Blade Design Using a Navier-Stokes Solver and Artificial Neural Network," J. Turbomach.-Trans. ASME, **121**(2): 326–332.

[208] Pilavachi, P. A., 2002, "Mini- and Micro-Gas Turbines for Combined Heat and Power," Appl. Therm. Eng., **22**: 2003–2014.

[209] PowerPlus Technologies GmbH, Germany, *http://www.powerplus-systeme.de/produkte/kraft-waerme-kopplung*, accessed on June 29th, 2012.

[210] Rao, S. S., 2009, *Engineering Optimization - Theory and Practice*, John Wiley & Sons, Inc., Hoboken, U.S.A., 4th ed.

[211] Rechenberg, I., 1965, *Cybernetic Solution Path of an Experimental Problem*, Royal Aircraft Establishment, Farnborough, U.K.

[212] Rechenberg, I., 1973, *Evolutionsstrategie: Optimierung Technischer Systeme nach Prinzipien der Biologischen Evolution*, frommann-Holzboog, Stuttgart, Germany.

[213] Remeha B.V., The Netherlands, *http://www.remeha.com/products/micro-chp*, accessed on June 29th, 2012.

[214] Reneau, L. R., Johnston, J. P., and Kline, S. J., 1967, "Performance and Design of Straight, Two-Dimensional Diffusers," J. Basic. Eng., **March 1967**: 141–150.

[215] Ripley, B. D., 1981, *Spatial Statistics*, John Wiley & Sons, Inc., New York, U.S.A.

[216] Roberts, S., 2008, "Effects of Climate Change on the Built Environment," Energ. Policy, **36**(12): 4552–4557.

[217] Rodgers, C., 1982, "Performance of Centrifugal Compressor Channel Diffusers," *Proc. ASME Turbo Expo 1982*, 82-GT-10.

[218] Rodgers, C., 1997, "Turbochargers to Small Gas Turbines?" *Proc. ASME Turbo Expo 1997*, 97-GT-200.

[219] Rodgers, C., 2000, "25-5 kWe Microturbine Design Aspects," *Proc. ASME Turbo Expo 2000*, 2000-GT-626.

[220] Roe, P. L., 1981, "Approximate Riemann Solvers, Parameter Vectors, and Difference Schemes," J. Comput. Phys., **43**(2): 357–372.

[221] Rohne, K. H. and Banzhaf, M., 1991, "Investigation of the Flow at the Exit of an Unshrouded Centrifugal Impeller and Comparison with the "Classical" Jet-Wake Theory," J. Turbomach.-Trans. ASME, **113**: 654–659.

[222] Ross, A., 1981, *Stirling Cycle Engines*, Solar Engines, Phoenix, U.S.A., 2nd ed.

[223] Runstadler, P. W. and Dean, R. C., 1969, "Straight Channel Diffusers Performance at High Inlet Mach Numbers," J. Basic Eng., **91**: 397–422.

[224] Runstadler, P. W. and Dolan, F. X., 1973, "Further Data on the Pressure Recovery Performance of Straight-Channel, Plane-Divergence Diffusers at High Subsonic Mach Numbers," J. Fluids Eng.-Trans. ASME, **95**(3): 373–384.

[225] Runstadler, P. W., Dolan, F. X., and Dean, R. C., 1975, "Diffuser Data Book," Tech. Rep. TN-186, Creare, Inc., U.S.A.

[226] Sacks, J., Welch, W. J., Mitchell, T. J., and Wynn, H. P., 1989, "Design and Analysis of Computer Experiments," Stat. Sci., **4**(4): 409–435.

[227] Salvage, J. W., 1999, "Development of a Centrifugal Compressor with a Variable Geometry Split-Ring Pipe Diffuser," J. Turbomach.-Trans. ASME, **121**(2): 295–303.

[228] Schumacher, E. F., 1973, *Small is Beautiful: Economics as if People Mattered*, Blond & Briggs, London, U.K.

[229] Selmin, V., 1993, "The Node-Centered Finite Volume Approach: Bridge Between Finite Differences and Finite Elements," Comput. Method. Appl. M., **102**(1): 107–138.

[230] SenerTec GmbH, Germany, *http://www.senertec.de/index.php?id=&L=1*, accessed on June 29th, 2012.

[231] Senoo, Y., 1978, "Japanese Patent Application Disclosure," 119411/78.

[232] Senoo, Y., Hayami, H., and Ueki, H., 1983, "Low Solidity Tandem Cascade Diffusers for Wide Range Centrifugal Clowers," *Proc. ASME Turbo Expo 1983*, 83-GT-3.

[233] Senoo, Y. and Ishida, M., 1987, "Deterioration of Compressor Performance Due to Tip Clearance of Centrifugal Impellers," J. Turbomach.-Trans. ASME, **109**(1): 55–61.

[234] Shum, Y. K. P., Tan, C. S., and Cumpsty, N. A., 2000, "Impeller-Diffusers Interaction in a Centrifugal Compressor," J. Turbomach.-Trans. ASME, **122**(4): 777–786.

[235] Simader, G. R., Krawinkler, R., and Trnka, G., 2006, "Micro CHP Systems: State-of-the-Art," Tech. rep., Austrian Energy Agency.

[236] Simpson, T. W., 1998, "Comparison of Response Surface and Kriging Models in the Multidisciplinary Design of an Aerospike Nozzle," Tech. Rep. NASA/CR-1998-206935, NASA, U.S.A.

[237] Simpson, T. W., Mauery, T. M., Korte, J. J., and Mistree, F., 1998, "Comparison of Response Surface and Kriging Models for Multidisciplinary Design Optimization," *Proc. 7th AIAA/U.S.A.F/NASA/ISSMO Symposium on Multidisciplinary Analysis and Optimization*, AIAA-98-4755.

[238] Simpson, T. W., Mauery, T. M., Korte, J. J., and Mistree, F., 2001, "Kriging Models for Global Approximation in Simulation-Based Multidisciplinary Design Optimization," AIAA J., **39**(12): 2233–2241.

[239] Simpson, T. W., Peplinski, J., Koch, P. N., and Allen, J. K., 2001, "Metamodels for Computer-Based Engineering Design: Survey and Recommendations," Eng. Comput., **17**(2): 129–150.

[240] Slowe, S., 2006, "Micro-CHP: Global Industry Status and Commercial Prospects," *Proc. 23rd World Gas Conference*.

[241] Smith, V. J., 1970, "A Review of the Design Practice and Technology of Radial Compressor Diffusers," *Proc. ASME Turbo Expo 1970*, 70-GT-116.

[242] Soares, C., 2007, *Microturbines - Applications for Distributed Enegy Systems*, Butterworth-Heinemann, Amsterdam, The Netherlands.

[243] Society of Automotive Engineers, Inc., Warrendale, U.S.A., 1995, *Supercharger Testing Standard*, SAE J1723 Issued AUG95.

[244] Society of Automotive Engineers, Inc., Warrendale, U.S.A., 1995, *Turbocharger Gas Stand Test Code*, SAE J1826 Reaf. MAR95.

[245] Sorokes, J. M., Borer, J. C., and Koch, J. M., 1998, "Investigation of the Circumferential Static Pressure Non-Uniformity Caused by Centrifugal Compressor Discharge Volute," *Proc. ASME Turbo Expo 1998*, 98-GT-326.

[246] Sorokes, J. M. and Welch, J. P., 1991, "Centrifugal Compressor Performance Enhancement through the Use of a Single-Stage Development Rig," *Proc. 20th Turbomachinery Symposium*.

[247] Sorokes, J. M. and Welch, J. P., 1992, "Experimental Results on a Rotatable Low Solidity Vaned Diffusers," *Proc. ASME Turbo Expo 1992*, 92-GT-19.

[248] Spraker, W. A., Young, M. Y., and Silvey, J. P., 1994, "A One-Dimensional Design Method for a Turbocharger Compressor Vaned Diffusers," *Turbocharging and Turbochargers*, C484/016/94, Mechanical Engineering Publications Limited for the Institution of Mechanical Engineers.

[249] Srivastava, A., Hacker, K., Lewis, K., and Simpson, T., 1999, "Development of a Kriging Based Surrogate Approximation Method for Large-Scale Systems," Tech. rep., State University of New York at Buffalo, Buffalo, U.S.A.

[250] Stahlecker, D. and Gyarmathy, G., 1998, "Investigations of Turbulent Flow in a Centrifugal Compressor Vaned Diffuser by 3-Component Laser Velocimetry," *Proc. ASME Turbo expo 1998*, 98-GT-300.

[251] Stanitz, J. D., 1952, "One-Dimensional Compressible Flow in Vaneless Diffusers of Radial and Mixed Flow Centrifugal Compressors, Including Effects of Friction, Heat Transfer and Area Change," Tech. Rep. TN 2610, NACA, U.S.A.

[252] Stanitz, J. D., 1952, "Some Theoretical Aerodynamic Investigations of Impellers in Radial and Mixed-Flow Centrifugal Compressors," Trans. ASME, **74**: 473–497.

[253] Stein, M. L., *Interpolation of Spatial Data: Some theory of Kriging*, Springer-Verlag, New York, U.S.A.

[254] Stein, W. and Rautenberg, M., 1985, "Flow Measurements in Two Cambered Vane Diffusers with Different Passage Widths," *Proc. ASME Turbo Expo 1985*, 85-GT-46.

[255] Stirling Systems Ltd., Switzerland, *http://www.stirling-systems.com/en/produkt.html*, accessed on June 29th, 2012.

[256] Stodola, A., 1927, *Steam and Gas Turbines*, McGraw-Hill, Inc., New York, U.S.A.

[257] Sutton, E., 1968, "The Performance and Flow Conditions within a Radial Diffusers Fitted with Short Vanes," Tech. Rep. 946, British Hydromech. Res. Assn., U.K.

[258] Tang, B., 1993, "Orthogonal Array-Based Latin Hypercubes," J. Am. Stat. Assoc., **88**(424): 1392–1397.

[259] Technische Universiteit Delft, Delft, The Netherlands, *Cycle-Tempo*.

[260] Technische Universiteit Delft, Delft, The Netherlands, *FluidProp*.

[261] Tsuei, H.-H., Oliphant, K., and Japikse, D., 1999, "The Validation of Rapid CFD Modeling for Turbomachinery," *Proc. Inst. Mech. Eng. Conference on CFD Technical Developments and Future Trends*.

[262] Turunen-Saaresti, T., 2004, "Computational and Experimental Analysis of Flow Field in the Diffusers of Centrifugal Compressors," Ph.D. thesis, Lappeenranta University of Technology, Finland.

[263] Urieli, I. and Berchowitz, D. M., 1984, *Stirling Cycle Engine Analysis*, Adam Hilger Ltd., Bristol, U.K.

[264] U.S. Environmental Protection Agency and Combined Heat and Power Partnership, U.S.A., 2008, *Catalog of CHP Technologies*.

[265] U.S.Department of Energy, Washington, U.S.A., 2007, *The Potential Benefits of Distributed Generation and Rate-Related Issues That May Impede Their Expansion*.

[266] Van Den Braembussche, R. A., 2010, "Tuning of Optimization Strategies," *Strategies for Optimization and Automated Design of Gas Turbine Engines*, RTO-EN-AVT-167-15, RTO of NATO, France.

[267] Van Den Braembussche, R. A., Ayder, E., Hagelstein, D., Rautenberg, M., and Keiper, R., 1999, "Improved Model for the Design and Analysis of Centrifugal Compressor Volutes," J. Turbomach.-Trans. ASME, **121**(3): 619–625.

[268] Verstraete, T., 2008, "Multidisciplinary Turbomachinery Component Optimization Considering Performance, Stress and Internal Heat Transfer," Ph.D. thesis, Von Kármán Institute for Fluid Dynamics, Belgium.

[269] Verstraete, T., Alsalihi, Z., and Van Den Braembussche, R. A., 2007, "Multidisciplinary Optimization of a Radial Compressor for Micro Gas Turbine Applications," *Proc. ASME Turbo Expo 2007*, GT2007-27484.

[270] Visser, W. P. J., Shakariyants, S. A., and Oostveen, M., 2011, "Development of a 3 kW Microturbine for CHP Applications," J. Eng. Gas. Turb. Power-Trans. ASME, **133**(4): 042301–1–042301–8.

[271] Wang, Z., Zi, G., and Wang, X., 2006, "Aerodynamic Design Optimization of Vaned Diffusers for Centrifugal Compressors Using Kriging Model," *Proc. Asian Joint Conference on Propulsion and Power 2006*, AJCPP2006-22023.

[272] Watson, N. and Janota, M. S., 1982, *Turbocharging the Internal Combustion Engine*, The Macmillan Press Ltd., London and Basingstoke, U.K.

[273] Weiß, C., Grates, D. R., Thermann, H., and Niehuis, R., 2003, "Numerical Investigation of the Influence of the Tip Clearance on Wake Formation Inside a Radial Impeller," *Proc. ASME Turbo Expo 2003*, GT2003-38279.

[274] Whisper Tech Ltd., New Zealand, *http://www.whispergen.com/main/acwhispergen*, accessed on June 29th, 2012.

[275] Whitfield, A. and Baines, N. C., 1990, *Design of Radial Turbomachines*, Longman Scientific & Technical, Essex, U.K.

[276] Whitfield, A. and Wallace, F. J., 1975, "Performance Prediction for Automotive Turbocharger Compressors," Proc. Inst. Mech. Eng., **189**(12): 59–67.

[277] Wiesner, F. J., 1967, "A Review of Slip Factors for Centrifugal Impellers," J. Eng. Power-Trans. ASME, **89**: 558–572.

[278] Wilcox, D. C., 1988, "Multiscale Model for Turbulent Flows," AIAA J., **26**(11): 1311–1320.

[279] Wilcox, D. C., 1988, "Reassessment of the Scale-Determining Equation for Advanced Turbulence Models," AIAA J., **26**(11): 1299–1310.

[280] Wilcox, D. C., 2006, *Turbulence Modeling for CFD*, DCW Industries, Inc., London, U.K., 3rd ed.

[281] World Alliance for Decentralized Energy, Edinburgh, U.K., 2003, *Guide to Decentralized Energy Technologies*.

[282] Xi, G., Wang, Z., Zhang, C., and Yuan, M., 2008, "Aerodynamic Optimization Design of Vaned Diffusers for the 100kW Micro Gas Turbine's Centrifugal Compressor," *Proc. ASME Turbo Expo 2008*, GT2008-50440.

[283] Ye, K. Q., 1998, "Orthogonal Column Latin Hypercubes and Their Application in Computer Experiments," J. Am. Stat. Assoc., **93**(444): 1430–1439.

[284] Yoshinaga, Y., Gyobu, I., Mishina, H., Koseki, F., and Nishida, H., 1980, "Aerodynamic Performance of a Centrifugal Compressor with Vaned Diffusers," J. Fluids Eng.-Trans. ASME, **102**: 486–493.

[285] Ziegler, K. U., Gallus, H. E., and Niehuis, R., 2003, "A Study on Impeller-Diffuser Interaction - Part I: Influence on the Performance," J. Turbomach.-Trans. ASME, **125**: 173–182.

[286] Ziegler, K. U., Gallus, H. E., and Niehuis, R., 2003, "A Study on Impeller-Diffuser Interaction - Part II: Detailed Flow Analysis," J. Turbomach.-Trans. ASME, **125**: 183–192.

Acknowledgements

When I look back at the five-plus years passed from my first day of work at the Process & Energy Department, I feel like they flew in a blink of an eye. Many people are "responsible" for that, for many different reasons.

First of all, I want to express my deepest gratitude to my supervisor, Jos van Buijtenen. When I walked into his office to seek for a Master thesis subject at the end of 2005, I was a young student enjoying his Erasmus experience. Today I leave the office as a researcher. Thank you Jos, for the guidance you gave me since then, during the up's of my work, when you always kept me anchored to the ground, and during the down's, when you put me back on track with a few words. Thank you for the discussions we had, during which I was mostly listening at first, but after I learned to be the leading actor. I thank you as well for our more personal talks, with which I hope I have convinced you that Italy is far better than France for your holidays with the caravan.

I am infinitely grateful to my co-supervisor, Piero Colonna. He made me aware of what being a PhD student means, by forcing me to focus on my own goals as researcher, though they might seem less interesting and worthy to others. Piero, thank you very much for your continuous support: you have always been the first to congratulate me for my achievements, yet at the same time you were reminding me of what was next. The relentless passion that you show for your work has often been a strong source of inspiration for me, and without it I would not be the scientist I am today. I also thank you for the great effort you put in these latest weeks, because your final review lifted this dissertation to the high quality level I think it shows now. I only regret that during the several, long conversations we had since we first met, we never talked about history, a subject we are both fond of.

Many thanks as well to Rene Pecnik, who, unfortunately for me, took office at P&E on the very same day I arrived at Università degli Studi di Brescia (Italy) as a visiting PhD student. Despite the long-distance cooperation, his critical eye has always surprised and inspired me, to the point that I consider his ability in this respect as being at the very heart of the quality of a researcher. Rene, one day I will reach your high standard as well!

All of this would not have been possible without the financial support of Micro Turbine Technology B.V. Particulary, my thanks go to Wilfried Visser, Savad Shakariyants, Mark Oostveen, and Nicholas George for the useful discussions.

I wish to thank Stefano Rebay, Antonio Ghidoni, and David Pasquale for the supervision and cooperation during my stay in Brescia. Chapter 6 of this dissertation is the wonderful result of our joint efforts! I also thank Antonio and David, as well as Andrea, for the *aperitivi* and dinners, which helped me in surviving in a "foreign" city. Roberto,

thank you very much for all the time you spent fixing my bike. Shame on me, as I lived for so long in the Netherlands!

Many other people at P&E have proved to be precious resources. Eveline, Helma, Ilona, Judith, Leslie, thank you for lifting the burden of bureaucratic "stuff" off of my shoulders more than once. Andre, Daniel, Jan, Jasper, Martijn, Rein, thanks a lot for the help you gave me while building the experimental facility. Also Esteban Valencia Torres contributed to its development, when I supervised him during his Master thesis. Esteban, thank you for the great deal of things you made me learn about uncertainty propagation analysis!

During my PhD I shared the office with several people, but only Bart has been there from day one. Bart, thank you for being the living proof of how a PhD student should live: working hard for a few hours a day, then getting enjoyment from many hobbies when the office doors are shut! Ik betreur alleen maar dat in de afgelopen jaren jouw Italiaans veel beter ontwikkeld is dan mijn Nederlands.

When he started his PhD at the end of 2008, Adeel saved me from weeks of loneliness, as I was the only presence in the office in that period. Dude, the laughs we had while talking about *Snatch* and *South Park* are some of the unforgettable moments of my life in Delft. There have not been always laughter and spare time, but countless discussions about our work as well: they often helped me in quickly finding the balance between the "good and bad sides" of my ideas, and I hope they were beneficial to you as much as they were to me. Adeel, thanks a bunch for the pleasant talks we have had during these years, and for introducing me to the amazing taste of *biryani*, which is currently and undoubtedly my favourite international dish, second only to the Italian ones. One day I will enjoy a plate filled with *biryani* in Pakistan, *in sha' Allah*!

Let me thank as well Michel, Sowande, and Theo, my other room-mates: I know that standing my mood changes and loud voice has not been an easy task!

Several other characters crossed my path at P&E and surroundings. In the last months of my stay in Delft, I thought of Gianluca and Laura as my "Delft parents", since most of the people who started their PhD when I did were leaving the department, while they were still there. We shared weekday dinners and Sunday lunches; we complained about the bad quality of Dutch food; we had some drinks downtown; we talked about personal successes and troubles, good and bad workdays; we (I obviously mean Gianluca and I!) sweat together on the football pitch. Well, I will never finish to thank you both for being true friends!

Emile and Eleonora, thank you for taking care of me as a little brother, and for making me feel at home every time I was with you two. Sooner or later we will again see each other up there in Switzerland.

Jacopo and Mahsa, I am sure that one day you will happily live in Italy, with neither *broodje kaas* nor *bitterballen*, and with shops that stay open later than 6:30 pm. Jacopo, thank you for the endless talks about football (too bad you support A.C. Milan!), Berlusconi (will he ever and forever step back?), and the many qualities which contribute to Italy's greatness among the rest of Europe, and yet keep "Italian brains" abroad. Mahsa, thank you for the delicious chocolate chakes, the chitchats, and for being the only one who noticed my very good mood every time I was expecting Luisella to arrive in Delft.

Thank you Ryan, for being my mate when I finally decided to go back to the gym, for the advices you gave me about being an independent researcher, and for those that pumped my ego!

Daniele, Giacomo, our friendship dates back to our Erasmus times in 2005, and still endures: who would have thought so?

Gabriele, when I arrived in Delft on March the 3rd, 2007, you literally opened the door of the house that we shared for one year. Back then we did not know each other, and since then we both lived in many other places: I believe that is a record!

Albert, Aylin, Bernardo, Carsten (my cycling-mate), Christian, Elif, Emiliano, Ernesto (the Colombian Italian), Francesco (my first Delft mentor), Jelan, John (the Dutch Italian), Marcin, Marco (my second Delft mentor), Marta, Martina, Miguel, Richard L., Sara, Sergio, Stefano (the Sardinian walking camera): thanking you is way too less in comparison to the happy moments we had together!

When I left home headed to the Netherlands, in the summer of year 2005, I did not have any clue at all that such departure would turn into my PhD experience, and would keep me in Delft for almost five years. My most heart-felt thank goes then to my parents, who always encouraged my choices, never turned their backs, even when my decisions were wrong, and made this possible, because they paid for my studies after all! Mamma, papà, non avete idea di quanto mi renda felice sapere che siete così orgogliosi di me, perchè avete svolto un incredibile lavoro nel forgiare la persona che sono oggi! Non posso non citare Elena, la mia sorellina, i cui successi mi riempono di orgoglio, e mia zia Adry, il mio "confessore": grazie di tutto!

One person is still missing from the list. Life is strange, and often gives you "funny" opportunities when you least expect them. I met Luisella when I applied for the PhD position, and she always knew I was eagerly looking forward to go back to Delft. Nevertheless, when I was about to leave, we decided to "give it a try". "It" became our story, despite at that time none but us would bet in its favour. The long-distance relationship we are still in has been very challeging and difficult at times, yet very exciting and rewarding. Lui, grazie per esser sempre stata presente quando più ne avevo bisogno; per tutti i sorrisi che mi fai spuntare, e per quelli che mi offri; per il soffio di pazzia che hai portato nella mia noiosa vita da ingegnere; per la pazienza che spesso mostri con la persona "difficile" che a volte so di essere; perchè sei la persona più importante della mia vita. Non vedo l'ora che arrivi aprile 2013!

Mattia Olivero
Brescia, September the 22nd, 2012

About the author

Mattia Olivero was born on April the 18th, 1982 in Carmagnola (TO), Italy. In Italy, after being awarded with his high school diploma by Liceo Classico & Scientifico G. B. Bodoni in 2001, he started his studies in aerospace engineering at Politecnico di Torino. There, he obtained his "Laurea" (i.e., BSc) in October 2004, and his "Laurea specialistica" (i.e., MSc) in October 2006. From September 2005, he spent one year at the Technische Universiteit Delft as Erasmus student. There, he followed several MSc courses at the faculty of aerospace engineering, and completed his MSc thesis at the faculty of mechanical engineering. In March 2007, he started his doctoral research in the field of turbomachinery for micro cogeneration applications. During this period, he spent a few months as a visiting PhD student at Università degli Studi di Brescia (Italy), and coached several MSc students. From October 2011 to September 2012 he worked as a research fellow at Università degli Studi di Brescia, and he is currently employed at EnginSoft TO s.r.l. (Italy) as a CFD engineer.

Publications

Olivero M., Pasquale D., Ghidoni A., and Rebay S., 2012. "Three-Dimensional Turbulent Optimization of Vaned Diffusers for Centrifugal Compressors Based on Metamodel-Assisted Genetic Algorithms," submitted for publication to Optim. Eng.

Javed A., Pecnik R., Olivero M., and van Buijtenen J. P., 2012, "Effects of Manufacturing Noise on Microturbine Centrifugal Impeller Performance," J. Eng. Gas. Turb. Power-Trans. ASME, **134**(10): 1023029–1–102302–9.

Javed A., Pecnik R., Olivero M., and van Buijtenen J. P., 2012, "Effects of Manufacturing Noise on Microturbine Centrifugal Impeller Performance," *Proc. ASME Turbo Expo 2012*, GT2012-69500.

Olivero M., Javed A., Pecnik R., Colonna P., and van Buijtenen J. P., 2011, "Study on the Tip Clearance Effects in the Centrifugal Compressor of a Micro Gas Turbine by Means of Numerical Simulations," *Proc. International Gas Turbine Congress 2011*, IGTC2011-0233.

Javed A., Yang S.-Y., Olivero M., Pecnik R., and van Buijtenen J. P., 2011, "Performance Evaluation of a Microturbine Centrifugal Compressor Using a Novel Approach," *Proc.*

International Gas Turbine Congress 2011, IGTC2011-0144.

Olivero M., Pasquale D., Ghidoni A., Pecnik R., Rebay S., and van Buijtenen J. P., 2011, "Aerodynamic Shape Optimization of a Vaned Diffuser for a Micro Turbine Centrifugal Compressor," *Proc. 2011 International Conference on Evolutionary and Deterministic Methods for Design, Optimization and Control with Applications to Industrial and Societal Problems*.

Javed A., Olivero M., Pecnik R., and van Buijtenen J. P., 2011, "Performance Analysis of a Microturbine Centrifugal Compressor From a Manufacturing Perspective," *Proc. ASME Turbo Expo 2011*, GT2011-46374.

Javed A., Olivero M., and van Buijtenen J. P., 2010, "Investigation on the Two-Zone Flow Phenomenon in a Microturbine Centrifugal Compressor Using CFD," *Proc. 5th International Conference on The Future of Gas Turbine Technology*.

Olivero M., Javed A., and van Buijtenen J. P., 2010, "Aerodynamic Analysis of a Micro Turbine Centrifugal Compressor," *Proc. ASME Turbo Expo 2010*, GT2010-23112.

Javed A., Olivero M., and van Buijtenen J. P., 2010, "Development of 1D Performance Analysis Tool for a Microturbine Radial Compressor Using CFD," *Proc. V European Conference on Computational Fluid Dynamics.*

Olivero M. and van Buijtenen J. P., 2009, "Design of a Vaned Diffuser to Enhance the Performance of a Micro Turbine Centrifugal Compressor," *Proc. XIX ISABE Conference*, ISABE-2009-1296.